

A comprehensive analysis of the DNA damage response by mass spectrometry- based proteomics

Dissertation

Zu Erlangung des Grades
Doktor der Naturwissenschaften

Am Fachbereich Biologie
der Johannes Gutenberg-Universität Mainz

vorgelegt von
Matthias Ostermaier
Geboren 18.08.1987
in Bad Saulgau, Deutschland

Mainz, Mai 2021

Dekan:

1. Gutachterin:

2. Gutachter:

Tag der mündlichen Prüfung:

Preface

Summary

The integrity of the human genome is continuously challenged by external agents and endogenous sources. To maintain genome stability, eukaryotic cells utilize protective mechanisms of the DNA damage response (DDR), which encompass a wide range of signaling and repair pathways. These are coordinated by dynamic changes in posttranslational modifications (PTMs), among which phosphorylation and ubiquitination play a central role. Although the DDR has been intensively investigated, a comprehensive analysis systematically comparing the cellular responses to different types of DNA damage is still lacking.

To this end, we established a reproducible and efficient workflow for multiplexed proteome and PTM analyses by mass spectrometry. This permitted to investigate cellular responses to 11 different DNA damage-inducing agents, resulting in one of the largest proteomic datasets on the DDR with ~450,000 data points. These included curated information on nearly 8,500 proteins, 24,000 phosphopeptides, 2,200 diglycine-lysine (diGly)-modified peptides, and 6,400 chromatin-associated proteins for each of the treatment conditions. Our data enabled to distinguish common from treatment-specific effects and linked protein modification to protein localization. Finally, we have created the DNA Damage Response dataBase (DDRBase), which provides easy access to these data to the scientific community.

Based on the proteomic screens, we identified a role of the HECT-type E3 ubiquitin ligase UBE3A (also known as E6AP) in the DDR. Loss of UBE3A negatively influenced DNA damage signaling, reduced double-strand break repair, led to genomic instability, and induced cell cycle arrest. We further showed that ATM and ATR phosphorylate UBE3A on serine 218, which mediates its nuclear translocation in response to DNA damage. Disruption of UBE3A phosphorylation inhibited its translocation and sensitized cells to genotoxic stress. Additionally, the ubiquitination activity of UBE3A was reduced in response to DNA damage.

By interactome and DiGly remnant analysis, we identified several putative UBE3A interactors and/or substrates, revealing a connection of UBE3A with the proteasome and the DNA replication machinery. In line with this, we verified the catalytic subunit of POL δ (POLD1) as a UBE3A substrate and implicated UBE3A in the regulation of proteasome activity. We found that hydroxyurea disrupted the interaction of UBE3A with the proteasome, which was associated with decreased ubiquitination of the proteasome receptor RPN10, and increased catalytic activity of the proteasome.

Ultimately, we hope that our DDRBase will become a valuable resource for the DNA damage community that allows extraction of protein-specific information, easy comparison between different treatment conditions, and the identification of novel repair factors, as exemplified for UBE3A.

Zusammenfassung

Das menschliche Genom ist ununterbrochen DNA-schädigenden Quellen ausgesetzt. Um die Stabilität des Genoms aufrechtzuerhalten, nutzen eukaryotische Zellen die Schutzmechanismen der DNA-Schadensreaktion (engl. DDR), die ein breites Spektrum an Signal- und Reparaturwegen umfassen. Diese werden durch dynamische Veränderungen von posttranslationalen Modifikationen (PTMs) koordiniert, unter denen Phosphorylierung und Ubiquitinierung eine zentrale Rolle spielen. Obwohl intensiv an der DDR geforscht wird, fehlt es an Studien, die systematisch die zelluläre Antwort auf verschiedene Arten von DNA-Schäden untersuchen und vergleichen.

Zu diesem Zweck haben wir einen reproduzierbaren und effizienten Arbeitsablauf für Multiplex-Proteom- und PTM-Analysen mittels Massenspektrometrie etabliert. Dies hat es uns gestattet, die zellulären Antworten auf 11 verschiedene DNA-schädigende Substanzen zu untersuchen, und führte mit knapp 450.000 Datenpunkten zu einem der größten proteomischen Datensätze über die DDR. Insgesamt haben wir Daten zu fast 8.500 Proteinen, 24.000 Phosphopeptiden, 2.200 Diglycin-Lysin (diGly)-modifizierten Peptiden und 6.400 Chromatin-assoziierten Proteinen für die einzelnen Behandlungsbedingungen zusammengestellt. Diese haben es uns ermöglicht, gemeine von behandlungsspezifischen Effekten zu unterscheiden und Proteinmodifikation mit Proteinlokalisierung zu verknüpfen. Weiterhin haben wir die DNA Damage Response dataBase (DDRBase) erstellt, die der wissenschaftlichen Gemeinschaft einen einfachen Zugang zu diesen Daten bietet.

Basierend auf unserer Datenbank haben wir die HECT-Typ E3-Ubiquitin-Ligase UBE3A (auch bekannt als E6AP) als einen neuen Faktor in der DDR identifiziert. Der Verlust von UBE3A behindert die Signalisierung von DNA-Schäden, reduziert die Reparatur von Doppelstrangbrüchen, führt zu Instabilität des Genoms und induziert Zellzyklusarrest. Des Weiteren zeigen wir, dass UBE3A als Reaktion auf DNA-Schäden von den Kinase ATM und ATR an Serin 218 phosphoryliert wird, was die Translokation von UBE3A in den Nukleus zur Folge hat. Die Unterdrückung der Phosphorylierung hemmt die Translokation und sensibilisiert die Zellen für genotoxischen Stress. Zusätzlich wird die Ubiquitinierungsaktivität von UBE3A durch die Induktion von DNA-Schäden verringert.

Mittels Interaktom- und DiGly-Restanalyse haben wir mehrere mutmaßliche UBE3A-Interaktoren und/oder -Substrate identifiziert, die eine starke Verbindung von UBE3A zum Proteasom und der DNA-Replikationsmaschinerie aufzeigen. In Übereinstimmung hiermit haben unsere Untersuchungen die katalytische Untereinheit von POL δ (POLD1) als neues UBE3A-Substrat verifiziert und UBE3A als Regulator der Proteasom-Aktivität impliziert. Wir haben herausgefunden, dass Hydroxyharnstoff die Interaktion von UBE3A mit dem Proteasom stört, was mit einer verminderten Ubiquitinierung des Proteasomrezeptors RPN10 und einer erhöhten katalytischen Aktivität des Proteasoms einhergeht.

Abschließend hoffen wir, dass unsere DDRBase zu einer wertvollen Ressource für die Forscher der DDR wird, die die Extraktion von protein-spezifischen Informationen, den einfachen Vergleich zwischen verschiedenen Behandlungsbedingungen und die Identifizierung neuartiger Reparaturfaktoren, wie am Beispiel von UBE3A gezeigt, ermöglicht.

Table of contents

Preface	III
Summary	V
Zusammenfassung	VII
Table of contents	IX
1 Introduction	1
1.1 DNA damage response	1
1.1.1 Endogenous and exogenous sources of DNA damage	2
1.1.2 DNA repair pathways	7
1.1.3 Posttranslational modifications in the DDR	12
1.1.4 The HECT-type ubiquitin ligase E6AP/UBE3A	16
1.2 Mass spectrometry-based proteomics	18
1.2.1 Sample preparation	18
1.2.2 Offline and online fractionation	19
1.2.3 Electrospray ionization	20
1.2.4 Mass-to-charge analysis	21
1.2.5 Tandem mass spectrometry and data acquisition	22
1.2.6 Peptide and protein identification	23
1.2.7 Peptide and protein quantification	23
1.3 Aim of the study	25
2 Results	26
2.1 A comprehensive analysis of the DNA damage response by mass spectrometry-based proteomics	26
2.1.1 Selection and evaluation of screening conditions	26
2.1.2 Establishment of a reproducible and efficient workflow for multiplexed proteome and PTM analysis	29
2.1.3 Laying the foundation for a comprehensive DDR database	32
2.1.4 Analysis of the cellular proteome	34
2.1.5 Analysis of protein phosphorylation	35
2.1.6 Analysis of protein ubiquitination	41
2.1.7 Analysis of the chromatin proteome	44
2.1.8 Integration of screening data	48
2.2 UBE3A - a new player in the DNA damage response	50
2.2.1 Proteasome subunits and associated proteins are differentially phosphorylated upon treatment with DNA damage-inducing agents	50
2.2.2 UBE3A is phosphorylated in an ATM/ATR-dependent manner	51
2.2.3 Depletion of UBE3A leads to genome instability and reduces DSB repair by homologous recombination	52

2.2.4	Proteasome subunits, and proteins involved in DNA replication and the DDR are putative UBE3A substrates.....	54
2.2.5	POLD1 is a substrate of UBE3A	57
2.2.6	UBE3A localization and activity is regulated in response to DNA damage.....	59
2.2.7	Hydroxyurea inhibits the interaction of UBE3A with the proteasome and modifies proteasome activity.....	61
3	Discussion.....	63
3.1	A comprehensive analysis of the DNA damage response by mass spectrometry.....	63
3.1.1	TMT workflow and technical considerations	67
3.2	UBE3A – A putative new player in the DDR.....	69
3.2.1	UBE3A regulates cell cycle progression, genome stability, and possibly DNA replication and repair	69
3.2.2	POLD1 is a substrate of UBE3A	72
3.2.3	DNA damage-dependent regulation of UBE3A	73
3.2.4	Hydroxyurea and UBE3A regulate proteasome activity.....	75
3.3	Concluding remarks	77
4	Materials and Methods	79
4.1	Lists of all consumables, machines, and software	79
4.2	Cell culture.....	85
4.2.1	Cell cultivation and passaging	85
4.2.2	Transfection of cells.....	85
4.2.3	Stable cell line production by lentivirus transduction.....	85
4.3	Methods for DNA modification and analysis	86
4.3.1	Gate-way cloning.....	86
4.3.2	Site-directed mutagenesis	86
4.3.3	CPEC cloning	86
4.4	Cell-based methods.....	87
4.4.1	Colony-forming assay.....	87
4.4.2	Cell viability assay.....	87
4.4.3	Immunofluorescence and confocal microscopy.....	88
4.4.4	TLR assay	88
4.4.5	Cell-cycle profiling.....	88
4.4.6	Neutral comet assay	88
4.4.7	Proteasome activity assay	89
4.5	Protein-specific methods.....	89
4.5.1	Cell lysis	89
4.5.2	Cell fractionation	89
4.5.3	SDS-PAGE and Western blotting.....	90
4.5.4	Pull-down using GFP-Trap agarose / Strep-Tactin sepharose	90
4.5.5	Expression and purification of recombinant proteins	90
4.5.6	Ubiquitination assay	91

4.5.7 GST Pull-down.....	91
4.5.8 iPOND.....	91
4.6 Mass spectrometry-based proteomics.....	92
4.6.1 In-gel digestion.....	92
4.6.2 Cell lysis and in-solution digest.....	92
4.6.3 TMT labeling.....	93
4.6.4 Phosphopeptide enrichment.....	93
4.6.5 DiGly-remnant enrichment.....	93
4.6.6 Micro-tip based strong cation exchange chromatography (Micro-SCX).....	94
4.6.7 Desalting and concentration of peptides.....	94
4.6.8 MS analysis.....	94
4.6.9 MS peptide identification.....	95
4.6.10 Data processing and visualization.....	95
5 Abbreviations.....	97
6 Appendix.....	103
7 References.....	Fehler! Textmarke nicht definiert.
8 Acknowledgments.....	139
9 Curriculum Vitae Matthias Ostermaier.....	141

1 Introduction

1.1 DNA damage response

DNA is the basic unit of inheritance. While genetic variation is an important driver of evolution, the perpetuation of life demands genetic stability. The integrity of the genome is continuously challenged by both external agents and endogenous sources. Unrepaired, lesions drive mutagenesis, genomic instability, and fuel the development of cancer. To counteract these outcomes, cells have developed mechanisms to detect the damage, signal its presence and promote its repair (Figure 1). This wide range of signaling, repair, tolerance, and cell death pathways are commonly known as the DNA damage response (DDR).

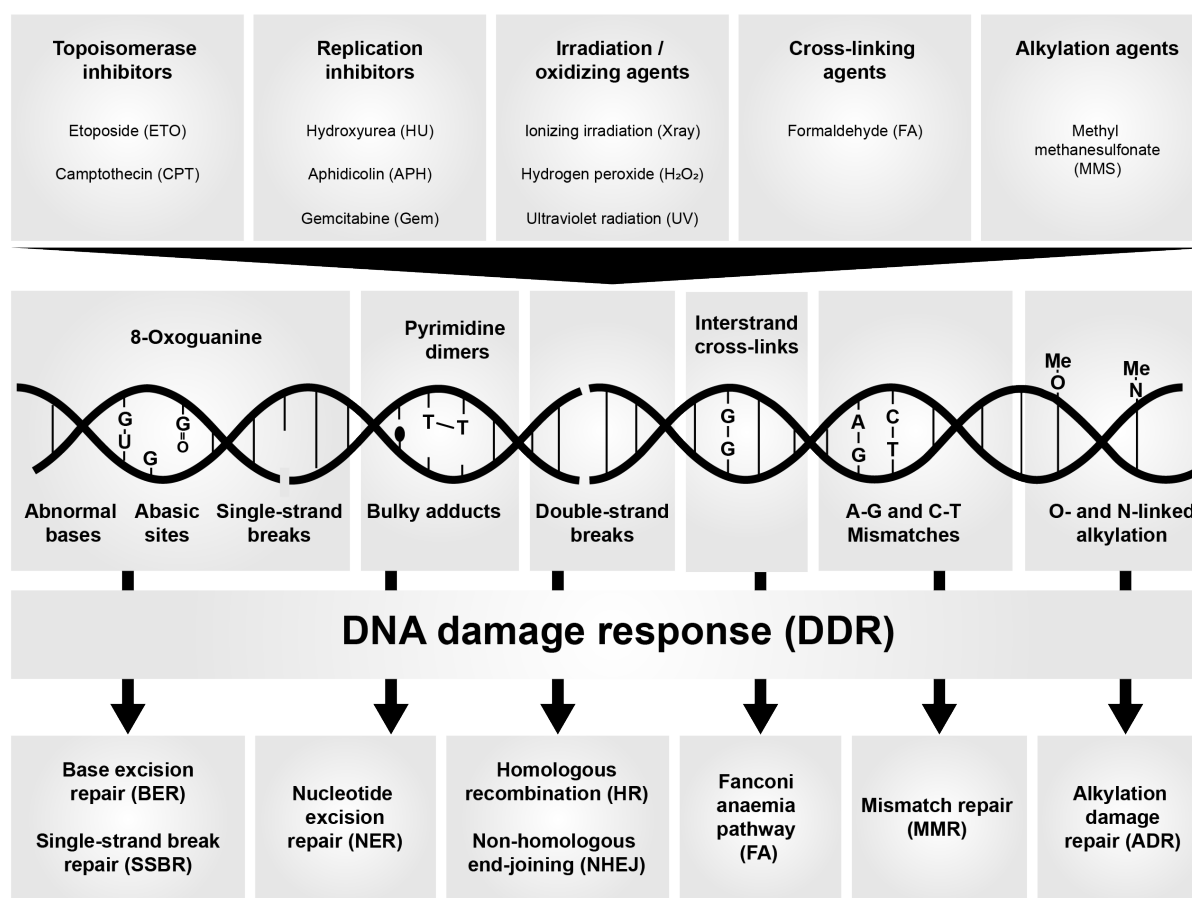


Figure 1: Exogenous sources of DNA damage, DNA lesions, and repair pathways. Exogenous sources of DNA damage (top) cause various types of DNA damage and lead to activation of the DDR (middle). DNA lesions can be repaired through various pathways (bottom). Adapted from Tasaki et al. [1].

1.1.1 Endogenous and exogenous sources of DNA damage

Each cell in the human body receives tens of thousands of DNA lesions per day [2]. Endogenous DNA damage arises from physiological processes such as mistakes during DNA replication or the reaction with molecules that are naturally present in our cells like water, or reactive oxygen species (ROS). Exogenous sources of DNA damage refer to environmental factors, including ionizing radiation (IR), ultraviolet (UV) radiation, and various chemicals [3].

Enzymatic reactions: replication and resolution of torsional stress

To maintain genetic integrity and preserve genetic continuity, human cells must accurately replicate the genomic DNA, encompassing approximately 3×10^9 bases. Replicative polymerases δ and ϵ (POL δ/ϵ) ensure insertion of the correct deoxynucleotide complementary to the template strand. This feat is achieved by (i) the thermodynamic stability of correct base pairing, (ii) the sensing of the correct shape and geometry of the incoming deoxynucleotides by the polymerase through an induced-fit mechanism, and (iii) the proofreading capability of the polymerase, which removes incorrectly incorporated deoxynucleotide triphosphates (dNTPs) through a 3'-5' exonuclease activity and improves the fidelity by two to three orders of magnitude [4–6]. Additionally, incorrectly incorporated dNTPs can be removed postreplicatively by the mismatch repair pathway (MMR). Yet, single base insertions, deletions, or base substitutions occur with a frequency of 10^{-6} to 10^{-8} per cell per generation [4–7]. A very frequent replication error (10^6 per cell per replication) is the incorporation of ribonucleotide triphosphate (NTPs), as the discrimination between NTPs and dNTPs is imperfect and because of the far greater abundance of NTPs levels in the cell. Especially, the reactive 2'-OH group poses a major threat to genome integrity. However, the removal of nucleotide monophosphates (NMPs) from DNA is carried out by dedicated RNases of the ribonucleotide excision repair (RER) pathway [8–10]. Additionally, insertions or deletions can accumulate through strand slippage during replication of repetitive sequences [11]. A different source of DNA damage originates from the action of topoisomerases. These enzymes remove torsional stress that is created through supercoiling during replication and transcription [12, 13]. For instance, topoisomerase I (TOP1) can create a temporary nick in double-stranded DNA (dsDNA), which allows the rotation of the DNA and the reduction of supercoiling. Mechanistically, this is achieved through a tyrosine in the catalytic center of TOP1, which creates a covalent bond with the 3'-phosphate in dsDNA through a nucleophilic attack and the formation of a phosphodiester bond. Once the 5'-hydroxylgroup of the incised DNA is aligned back with the tyrosine-DNA phosphodiester bond, TOP1 religates the breaks resolving the complex. Misalignment of the TOP1 cleavage complex (TOP1cc) leads to the formation of DNA lesions [12, 14]. Anti-cancer drugs like camptothecin (CPT) exert their poisoning effect by trapping the TOP1cc intermediate on DNA [15]. DNA double-strand breaks (DSBs) arise during transcription or when the replication fork collides with single-strand breaks (SSBs) and “runs off” [16, 17]. The TOP1cc can also be irreversibly trapped into so-called suicide complexes by aberrant DNA structures close to the incision site [18–21]. Repair of TOP1-associated DNA damage is

usually mediated through excision of the complexes by the tyrosyl DNA phosphodiesterase 1 (TDP1) and endonucleases [22, 23]. The underlying mechanisms are very similar e.g. for topoisomerase 2 (TOP2). TOP2 creates transient DSBs, allowing another DNA molecule to pass through. The TOP2 cleavage complex (TOP2cc) can be trapped by the drug etoposide (ETO) and removal of the trapped TOP2cc can be achieved with the help of tyrosyl DNA phosphodiesterase 1 (TDP2) [24].

Abasic sites

Apurinic / apyrimidinic or abasic (AP) sites are created through the break of the N-glycosyl bond that links the nucleic acid base to the sugar backbone. Spontaneous hydrolysis alone accounts for 10,000 AP sites per cell per day and is further elevated by exogenous damage agents, such as ROS and alkylating substances [2, 25, 26]. AP sites are also generated enzymatically as an intermediate within the base excision repair (BER) pathway or during the removal of the epigenetic mark 5-methylcytosine (5mC) [2, 27, 28]. Repair is mediated through factors of the BER, with the DNA-(apurinic or apyrimidinic site)endonucleases 1 and 2 (APE1/2) cleaving off the AP sites. When not repaired, AP sites lead to polymerase stalling, induce DNA strand breaks, as well as mutations through misincorporated bases opposite the missing base [29, 30].

Base deamination

Base deamination describes the loss of the exocyclic amino group of nucleotides and is a major source of mutagenesis in cells. Deamination of adenine (A), guanine (G), cytosine (C), and 5mC results in the decomposition products hypoxanthine, xanthine, uracil (U), and thymine (T), respectively (Figure 2B) [31, 32]. Spontaneous deamination is a very frequent event and is further catalyzed by exogenous sources (e.g. radiation). The presence of ROS can lead to further deamination products [33–37]. Cytosine and especially 5mC are the most frequently deaminated bases, explaining the high occurrence of CG-to-AT transitions. For instance, the deamination product of C is U, which in turn pairs incorrectly with A instead of G [3, 32, 38, 39]. Notwithstanding, deamination also fulfills physiological functions as it leads to somatic hypermutation during antibody development. In this case, deamination is actively carried out by deaminases like AID (activation-induced deaminase) [40, 41]. Deaminated bases are generally removed by glycosylases of the BER and factors of the MMR pathway [38, 42, 43].

Oxidative damage

ROS are a family of highly reactive, oxygen-containing molecules, including superoxide radicals ($\bullet\text{O}_2^-$), hydrogen peroxide (H_2O_2), and the hydroxyl radical ($\bullet\text{OH}$), that can react with amino acids, proteins, or lipids [44]. They are typical byproducts of mitochondrial respiration, where oxygen works as a terminal electron acceptor. Other endogenous sources include peroxisomes (contains H_2O_2), NADPH oxidase (production of superoxide radicals in cellular signaling and immune response), and the endoplasmic reticulum (during protein folding) [45–48]. Ionizing irradiation, chemotherapeutic drugs, or certain environmental agents can also lead to ROS production [49]. While low levels of ROS fulfill

Introduction

important functions in cellular signaling or the defense response to pathogens, excess of ROS can be detrimental to genomic stability [50]. ROS can react with both the DNA bases and the DNA backbone, producing approximately 100 different oxidative base lesions or 2-deoxyribose modifications [51–53].

Prominent examples formed by the hydroxyl radical are thymine glycol, 7,8 dihydro-8-oxoguanine (8-oxoG), formamidopyrimidine (Figure 2C). 8-oxoG is formed by hydroxylation of the C-8 in G. 8-oxoG is highly mutagenic as it pairs with A instead of C and can be further oxidized forming secondary DNA lesions [54–56]. Thymine glycol residues are generated from an attack on the C5/C6 double bonds of thymine. Similarly, formamidopyrimidine is formed by imidazole ring-opening in guanine and adenine. Although cells keep ROS levels in check by restricting ROS to certain compartments (mitochondria, peroxisomes) and by quenching ROS with the antioxidant enzymes superoxide dismutase, catalase, and peroxiredoxin it is estimated that each cell experiences about 2300 SSBs per cell per hour from ROS compromising the DNA backbone alone [57–62]. Therefore, oxidized bases are repaired by the BER pathway, while breaks in the DNA backbone are addressed by single-strand break repair (SSBR) or the double-strand break repair (DSBR) pathways [63, 64].

Ionizing radiation

IR refers to high-energy radiation in form of electromagnetic waves (X-rays, γ -rays) or particles (α -rays, β -rays, neutron, and proton beams) that carries sufficient energy to release electrons from atoms and molecules, thereby ionizing them. Sources are naturally occurring elements in water, soil, and air (e.g. radon), cosmic radiation, or medical devices. IR can be further classified according to its linear energy transfer (LET), which is the ratio of energy a charged particle transfers to atoms and molecules while passing through a substance. Consequently, high LET radiations (α -rays, neutrons, protons) produce higher damage in a system than low LET radiations (β -rays, γ -rays, x-rays). IR leads to DNA damage through direct or indirect means [65, 66]. Directly induced DNA breaks typically involve the loss of at least one nucleotide and display 3'-phosphate or 3'-phosphoglycolate ends, which cannot be directly religated [64, 67]. Repair of such breaks is mediated through factors of the SSBR pathway. For instance, AP endonucleases and TDPI remove 3'-phosphoglycolates, while polynucleotide kinase 3'-phosphatase (PNKP) hydrolyses 3'-phosphate groups [68–71]. DSBs may be formed through multiple closely positioned SSBs. In this case, lesions are repaired by DSBR pathways [72, 73]. Indirectly induced damage by IR is due to the production of ROS, for example through radiolysis of water molecules. Accounting for 65% of IR-induced DNA damage, the spectrum of IR-induced DNA lesions overlaps greatly with that of endogenous ROS production [74–76].

Ultraviolet light

UV can be classified according to its wavelength range. UV-C (190-290 nm) is the shortest wavelength and mostly absorbed by the ozone layer in the stratosphere. UV-B (290-320 nm) is also filtered out by the ozone layer and can be further absorbed by clouds. Only the lower energetic UV-A radiation (320-

400 nm) reaches the planet's surface almost unfiltered (95%) [77, 78]. Nonetheless, it is UV-C that is widely used in laboratories to investigate UV-induced DNA damage. This is due to UV-C's high energy content and the overlap with the energy absorption maximum of DNA at 260 nm, resulting in the strong formation of photoproducts. The most frequent photoproducts are helix distorting lesions formed through the dimerization of adjacent pyrimidine rings, resulting in cyclopurine dimers (CPDs), 6'-4'-photoproducts (6-4PPs), and Dewar valence isomers (DVIs) (Figure 2E). CPDs are formed through the covalent linkage of adjacent pyrimidines through a cyclobutane ring, whereas 6-4PPs are formed by covalent linkage of the C6 and the C4 of two adjacent pyrimidines. DVIs are derived from 6-4PPs as an intermediate [78–83]. These bulky lesions are major obstacles for transcription and translation but can be efficiently removed through the nucleotide excision repair (NER) pathway [84]. However, UV radiation can also lead to the formation of other minor photoproducts, DNA-protein crosslinks, and ROS [85]. Additionally, DNA damage can be mediated by so-called photosensitizers, which function as catalysts and are especially relevant for UV-A-induced lesions [86, 87].

Methylation/alkylation

Alkylation means the transfer of an alkyl group, such as methyl or ethyl groups, to another molecule. In cells, methylation mediated through methyltransferases is very common and can act as an epigenetic mark on DNA (e.g. 5mC) [88]. However, S-adenosylmethionine (SAM), which serves as a methyl donor, can spontaneously form approximately 4000 7-methylguanine (7mG), 600 3-methyladenine (3mA), and 20 O⁶-methyl-guanine (O⁶-mG) residues in a mammalian cell per day [3, 89] (Figure 2D). O⁶-mG leads to transition mutations, 3-mA inhibits DNA replication, and 7mG can undergo cleavage to AP sites or react to the replication inhibiting formamidopyrimidine. However, most exocyclic oxygens, ring nitrogens, backbone phosphates, and oxygens are susceptible to methylation to varying degrees [90–95]. Other sources of alkylating agents are amides and nitrosamines found in food, decaying matter, drinking water, nicotine metabolites, or certain industrial processes. In laboratories, methyl methanesulfonate (MMS), N-methyl-N-nitro-N-nitrosoguanidine (MNNG), and N-methyl-N-nitrosourea (MNU) are common alkylating agents. While MMS produces 7mG and 3mA, MNNG and MNU lead to O⁶-mG formation [92, 96, 97]. Alkylating agents also include bifunctional sulfur and nitrogen mustards carrying two reactive groups. Therefore, they can form DNA inter-strand, or DNA-protein crosslinks [98–101]. This principle is exploited in the chemotherapeutic drugs cyclophosphamide and cisplatin. Direct damage reversal (e.g. methyltransferases), BER, and inter-strand crosslink repair (ICL)/Fanconi anaemia repair pathways dealing with the removal of alkylation damage of DNA [97].

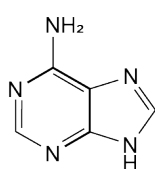
Other DNA damaging agents

Given the broad range of DNA damaging agents and the scope of this thesis, it is not possible to cover them all in detail. However, other sources of DNA damage worth mentioning are listed as we encounter them in everyday life: Environmental stresses (heat, cold, hypoxia). Butylparaben and bisphenol A

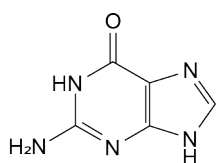
Introduction

(found in cosmetics, pharmaceuticals, food products). Food preservatives and additives (benzoate, sorbate, citric acid, phosphoric acid, brilliant blue, sunset yellow). Aromatic, polycyclic amines (found in coal, fuel, industrial dyes, cigarette smoke, pesticides, incomplete combustion products), and aflatoxin (from *Aspergillus flavus* and *parasiticus*). Although very different, the latter three are metabolized in the liver by the cytochrome P450 complex into a genotoxic form, which readily reacts to form DNA adducts [3, 102].

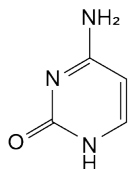
A Normal bases



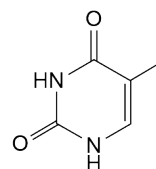
Adenine



Guanine

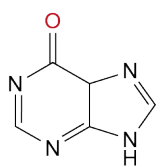


Cytosine

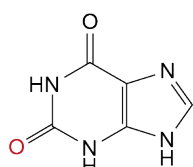


Thymine

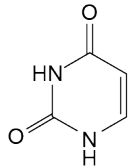
B Deaminated bases



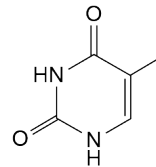
Hypoxanthine



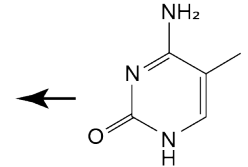
Xanthine



Uracil

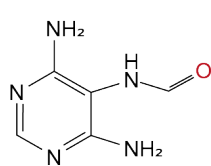


Thymine

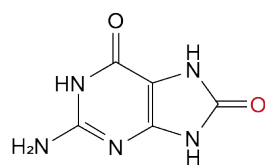


5-methylcytosine

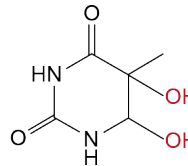
C Oxidized DNA bases



Formamidopyrimidine

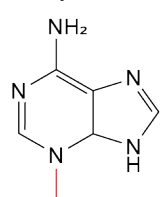


7,8 dihydro-8oxoguanine

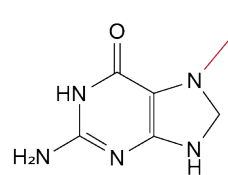


Thymine glycol

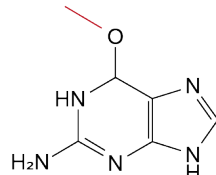
D Methylated bases



N3-methyladenine

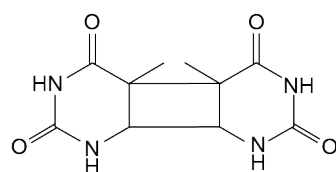


N7-methylguanine

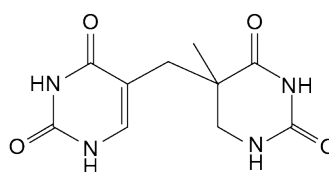


O⁶-methylguanine

E UV-induced bulky lesions



Cyclobutane pyrimidine



Pyrimidine (6-4) pyrimidone photoproduct

Figure 2: Normal DNA bases and common DNA base lesions. Structure of normal (A), deaminated (B), oxidized (C), and methylated bases (D). Thymine can be formed as a deamination product of 5-methylcytosine. Bulky lesions introduced by UV radiation (E). Adapted from Chatterjee and Walker [102].

1.1.2 DNA repair pathways

Mismatch repair

As discussed above, DNA replication is not an error-free process but can lead to mutations e.g. through misincorporations. The MMR pathway reduces this rate by 100-fold, via continuous scanning and repairing of the replicated DNA [4–6]. In *E.coli*, the daughter strand is distinguished from the parental DNA template strand by DNA adenine methylase (DAM) methylation of the bases [103]. In eukaryotic cells, this distinction is not completely understood yet. Although MMR is an evolutionarily conserved pathway, there are more distinctions between prokaryotes and eukaryotes. While the core factors of the MMR pathway in *E.coli* are the homodimers MutS and MutL, their homologs in human cells have diversified into heterodimeric complexes. MutS α , composed of MSH2 and MSH6, recognizes base mismatches and dinucleotide insertion-deletion loops (IDLs), which arise as a consequence of strand-slippage in repetitive sequences. MutS β (MSH2 + MSH3) on the other hand, binds to larger IDLs (~13 nucleotides (nts)) [104–106]. The other core components of the MMR pathway are homologs of MutL and form three different complexes: MutL α (MLH1 + PSM2) and MutL β (MLH1 + PSM1) and MutL γ (MLH1 + MLH3). Both MutS α/β and MutL α complexes possess ATPase activity.

The MMR process can be divided into four steps: lesion recognition, repair initiation, lesion excision, and DNA resynthesis. In the first step, mismatches are recognized by the MutS complexes. Upon mismatch binding, MutS exchanges ADP for ATP and undergoes a conformational change to a “sliding clamp”, which leads to the recruitment of MutL and the exposure of the mispair. The exact mechanism and role of the conformational change are still under debate [103, 107]. Upon its recruitment, MutL endonuclease activity leads to the incision of the error-containing DNA strand. The resulting nick serves as an entry point for exonuclease 1 (EXO1), which further degrades the mispair containing DNA strand. Finally, POL δ is recruited to resynthesize the DNA strand and ligase 1 (LIG1) to seal the strand break [103, 108]. MMR has also been implicated in microsatellite stability, meiotic and mitotic recombination (MSH4/5 specific), class-switch recombination, somatic hypermutation, DNA-damage signaling, apoptosis, and triplet-repeat expansion [108–111].

Base excision repair

Single base damage due to deamination, oxidation, alkylation, and abasic sites that do not impose significant helix distortions are repaired by the BER pathway [112]. The DNA lesions are recognized and excised by at least 11 different DNA glycosylases, leaving behind an AP site. These glycosylases can be either monofunctional, with only a glycosylase activity (MPG, MUTYH), or bifunctional with both glycosylase and β -lyase activity (NEIL1, NEIL2, NEIL3, NTHL1, OGG1) [113–115]. AP sites created by monofunctional glycosylases initiate the short-patch-repair pathway, while bifunctional glycosylases lead the long-patch repair pathway [112]. In the former, AP sites are removed by the endonuclease APE1, which cleaves 5' to the AP site, leaving behind a hydroxyl group at the 3'-end and a 5'-deoxyribose phosphate (5'-dRP). Next, POL β removes the 5'-dRP through its lyase activity (gap

Introduction

tailoring) and fills in the single nucleotide gap, while LIG1 or LIG3 together with XRCC1 seal the remaining break. In long patch repair, the AP site is tailored by the 3'-phosphodiesterase activity of APE1. Subsequently, either POL δ (non-proliferating cells) or POL ϵ (proliferating cells) insert new nucleotides in a strand-displacement manner, leading to the generation of a 5' flap. The flap is removed by flap endonuclease 1 (FEN1) and LIG1 mediates break ligation [116, 117]. The SSBR pathway is extremely similar to BER. However, recognition of ssDNA breaks is mediated by Poly(ADP-ribose) polymerase (PARP) family proteins, primarily PARP1 [118, 119].

Nucleotide excision repair

Photoproducts and bulky lesions (e.g. CPDs and 6-4PPs) formed by UV radiation, polycyclic aromatic hydrocarbons (e.g. benzo[a]pyrene adducts), or damage from chemotherapeutic agents (e.g. cisplatin) are removed by the NER pathway. NER can be split into two sub-pathways: the transcription-coupled NER (TC-NER) and the global genome NER (GG-NER), which differ in the mode of lesion recognition [120]. GG-NER scans the entire genome, including regions with no or low transcriptional activity. The damage sensor is XPC, coupled to the proteins RAD23A and CETN2, that recognizes transient ssDNA caused by disrupted base pairing. CPDs can also be recognized by the UV-DDB complex (DDB1 + DDB2), bending out and representing ssDNA to XPC [121–123].

TC-NER largely overlaps with GG-NER, but lesion recognition is dependent on active transcription. RNA polymerase II (POLII), stalled upon the encounter of a lesion, is recognized by UVSSA, USP7, and CSB. This leads to the recruitment of CSA, which initiates backtracking of POLII to make way for the incoming NER machinery [124, 125]. Once the damage is recognized, the transcription initiation factor IIIH (TFIIH) complex, comprised of ten different subunits, is required. This includes the helicases XPD (5'-3') and XPB (3'-5'), which unwind the DNA around the lesion, leading to the displacement of POLII in the case of TC-NER. Meanwhile, binding of RPA and XPA displaces XPC-RAD23, maintaining the open DNA conformation and helping in the orientation of the endonuclease machinery in TFIIH. Once in place, the endonucleases XPF and XPG cleave the damaged DNA, at the 5' and 3' respectively, removing a stretch of 22-30 nts. Finally, DNA integrity is restored by the combined action of RFC, PCNA, and DNA polymerases $\delta/\epsilon/\kappa$ and break ligation by LIG1 or LIG3-XRCC1 [124, 126]. Polymerase and ligase choice depend on the proliferation status of the cells, with POL δ/κ and LIG1 working in replicating, and POL ϵ and XRCC1-LIG3 working in non-replicating cells [127, 128].

Double-strand break repair

Non-homologous end joining (NHEJ)

NHEJ is initiated through binding of the Ku heterodimer (Ku70 + Ku80) DSBs within seconds. This is achieved by the high binding affinity of Ku, its high cellular concentration, and the lack of sequence specificity [129, 130]. The ring-shaped heterodimer encircles the DNA, protects the DNA ends from being processed, holds them in close proximity, and serves as a recruitment platform for other NHEJ

factors [130, 131]. These factors include the DNA-dependent protein kinase catalytic subunit (DNA-PKcs), XRCC4, XRCC4-like factor (XPF), DNA ligase 4 (LIG4), Aprataxin-and-PNK-like factor (APLF), ARTEMIS, and others [132]. DNA-PKcs is activated upon interaction with DNA-bound Ku. The Ku complex is pushed inwardly on the DNA and DNA-PKcs phosphorylates proximal repair factors including itself [133, 134]. Depending on the source of the DSBs, DNA ends may need processing, as they might not be ligatable. AP sites, 3'-phosphoglycolate, absent 5'-phosphate or 3'-hydroxy groups, etc. are therefore processed by a battery of enzymes, including endonucleases (Artemis, APLF, WRN, etc.) and polymerases [135, 136]. Finally, the DNA break is sealed by the LIG4-XRCC4-XPF complex to restore the structural integrity of dsDNA. Both XRCC4 and XPF stimulate LIG4 activity and align DSB ends for efficient ligation, but also work as a scaffold for other factors beforehand [137, 138]. Since repair by NHEJ can include end-processing steps and does not rely on the sequence homology of a sister chromatid, it is inherently error-prone and can contribute to genome instability through chromosomal translocations and deletions [139]. An alternative, but less characterized NHEJ pathway is Ku-independent. Fittingly, it is termed alternative end-joining (aEJ) or microhomology-mediated end-joining (MMEJ), as it relies on the presence of small stretches of homology (5-25 nts) between the sequences flanking the DSB. Since overlapping DNA flaps are excised, aEJ always results in sequence deletions [140, 141].

Homologous recombination (HR)

HR allows the repair of DSBs in an error-free manner. Its high fidelity is based on the use of a homologous DNA template, typically the sister chromatid. Accordingly, HR is restricted to S and G2 phases of the cell cycle. In HR, DSBs are recognized by the MRN complex, which is formed by MRE11, RAD50, and NBS1. NBS1 appears to initiate binding of the complex to the DSBs and contains additional protein-protein interaction domains to drive repair progression [142]. Similar to Ku and DNA-PKcs in NHEJ, MRN is important for the recruitment and activation of ATM (Ataxia Telangiectasia Mutated) kinase. ATM mediates a signaling cascade on chromatin surrounding the break site, which, through a series of PTMs and protein recruitment, amplifies the damage signal. Commitment to the HR pathway is achieved through DNA end resection by the nucleases CtIP and MRN, generating short 3' overhangs. Long-range end-resection by BLM/DNA2 and EXO1 helicase/nucleases generate extensive tracks of ssDNA that are rapidly covered by the heterotrimer RPA (RPA1-2-3) [143, 144]. The binding of RPA prevents degradation of the ssDNA, the formation of secondary structures, and the spontaneous recombination between regions of microhomology [145]. Next, RPA is exchanged for the recombinase RAD51, which directs homology search and strand invasion of the homologous template, leading to the formation of a displacement loop (D-loop) structure (Figure 3). RAD51 loading is mediated by the BRCA1-PALB2-BRCA2 complex, with BRCA2 disrupting the RAD51 oligomers and enabling the formation of RAD51-ssDNA nucleofilaments as monomers. Other mediator proteins facilitating this process are RAD51 paralogs with distinct functions (RAD51B/C/D, XRCC2), and RAD54, all

stabilizing and remodeling the nucleofilament [146, 147]. After strand invasion, POL δ or translesion polymerases use the invading strand in the D-loop as a primer for strand elongation [148]. Most of the extended D-loops are disrupted and subsequently repaired by so-called synthesis-dependent strand annealing (SDSA; Figure 3). SDSA always results in a non-crossover. The extended D-loop can also undergo a second-end capture or invasion to form a double Holliday junction (dHJ). Dissolution of dHJ can lead to non-crossover products, as a result of the BLM-TOP3A-RMI (BTR) complex, which moves the two junctions towards each other before they are cleaved. Crossover products are formed when processed by the GEN1 resolvase or the MUS81-EME1/SLX1-SLX4 nuclease complex. Alternatively, non-error-free pathways, break-induced replication (BIR), and single-strand annealing (SSA) are employed [149, 150].

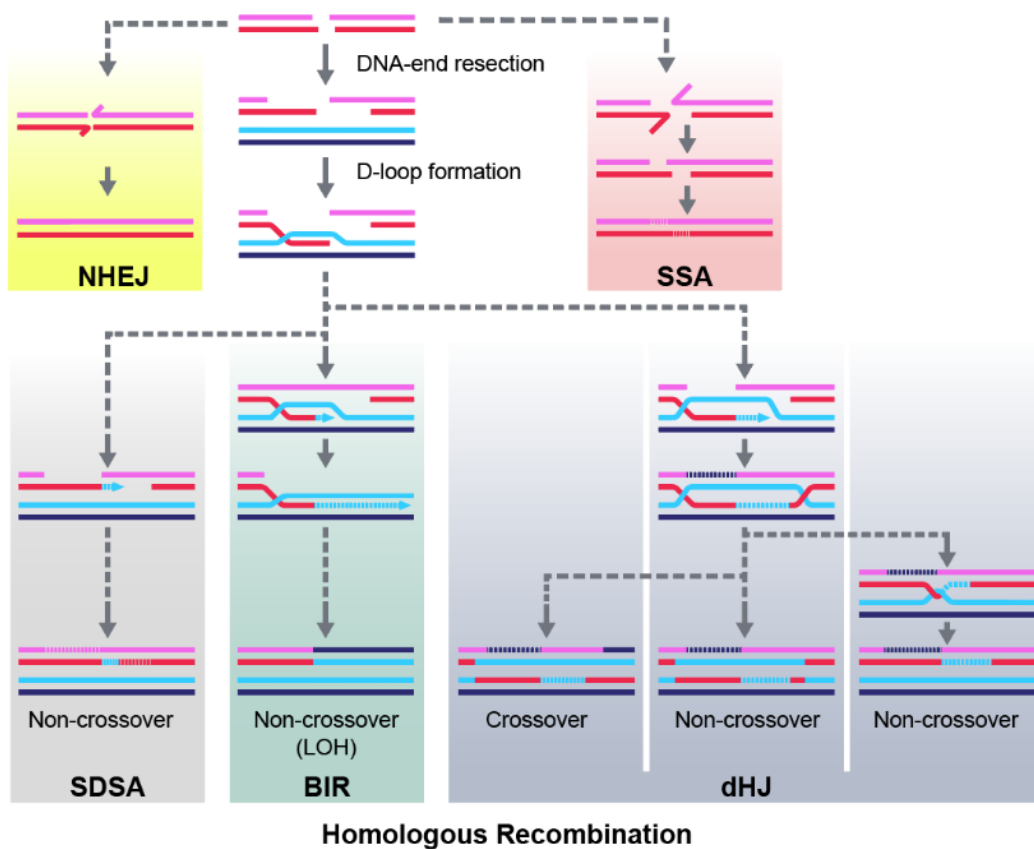


Figure 3: Double-strand break repair pathways. DSBs can be repaired by multiple pathways. NHEJ does not rely on homologous sequences and DSBs are repaired without the need for extensive end resection. SSA but also MMEJ (not shown) relies on short homologous repeats between two DSB ends to mediate repair independent of a donor molecule. For HR, the broken DNA strand performs homology search and strand invasion on the sister chromatid, which results in the generation of a D-loop. When DNA breaks have only one end, they are repaired by BIR (middle). Most of the D-loops in somatic cells are disrupted and repaired by SDSA (left) and results in a non-crossover. Alternatively, the D-loop can undergo a second-end capture and forms a double Holliday junction. This can result in either a crossover or a non-crossover outcome. Adapted from Heyer et al., 2010 [150].

Replication stress and recovery

Replication stress (RS) describes the slowing or stalling of the replication fork and is known as an early driver of tumorigenesis. A broad spectrum of endogenous or exogenous sources can induce RS, including special DNA structures (hairpins, G-quadruplexes, R-loops), DNA damage (AP sites, bulky lesions, NTP incorporation), nucleotide depletion (e.g. by hydroxyurea), as well as collisions between replication and transcription machinery [151]. For instance, when dNTP or histone pools become limiting, the MCM helicase complex as part of the replication machinery, continues DNA unwinding, while replication has ceased (helicase-polymerase uncoupling) [152] (Figure 4). As a result, stretches of ssDNA are exposed but are rapidly coated with the single-strand binding protein RPA, which recruits ATR interacting protein (ATRIP; Figure 4). ATRIP binds directly to RPA on ssDNA, and recruits, stabilizes, and activates Ataxia telangiectasia and Rad3 related (ATR) in the form of an ATRIP-ATR tetramer. Full kinase activation requires additional factors, including the 9-1-1 complex (RAD9-HUS1-RAD1) [153], topoisomerase 2 binding protein 1 (TOPBP1) [154], and Ewing tumor-associated antigen 1 (ETAA1) [155–158]. TOPBP1 and ETAA1 are allosteric activators of ATR, with TOPBP1 working during replication stress, and ETAA1 leading to S/G2 checkpoint activation during unperturbed cell cycle progression. At the same time, proliferating-cell-nuclear-antigen (PCNA), together with replication factor C (RFC) prevents DNA polymerase dissociation [158]. ATR safeguards stalled replication forks from breakage, provides time to resolve possible replication obstacles, and prevents replication catastrophe by preserving the RPA pool through checkpoint kinase 1 (CHK1)-mediated suppression of origin firing [159]. Stabilization of the replication fork is also achieved through fork reversal, adapting a “chicken foot” conformation, with the help of RAD51 [160]. Proteins TIM-TIPIN, CLASPIN, BRCA2, and FANCD2 also support fork stability [158]. However, when certain factors cannot fulfill their function, or the replication stress persists, the fork will eventually lose its integrity and collapse. When this happens, DSBs are formed through the action of nucleases [161]. Alternatively, the firing of adjacent dormant origins, the repriming of DNA replication in the proximity of the DNA lesion, or the initiation of replication tolerance pathways may take place in the case of persistent replication obstruction. The two damage tolerance pathways are translesion synthesis (TLS) or template switching (TS). In TLS, error-prone polymerases, which can even accommodate bulky lesions in their active site, replicate over the DNA lesion by allowing nucleotide misincorporations. In TS, a homologous DNA template is used to replicate over the lesions, restoring the original DNA sequence [162, 163]. However, in these cases, the encountered obstacle persists and must be resolved later on [164].

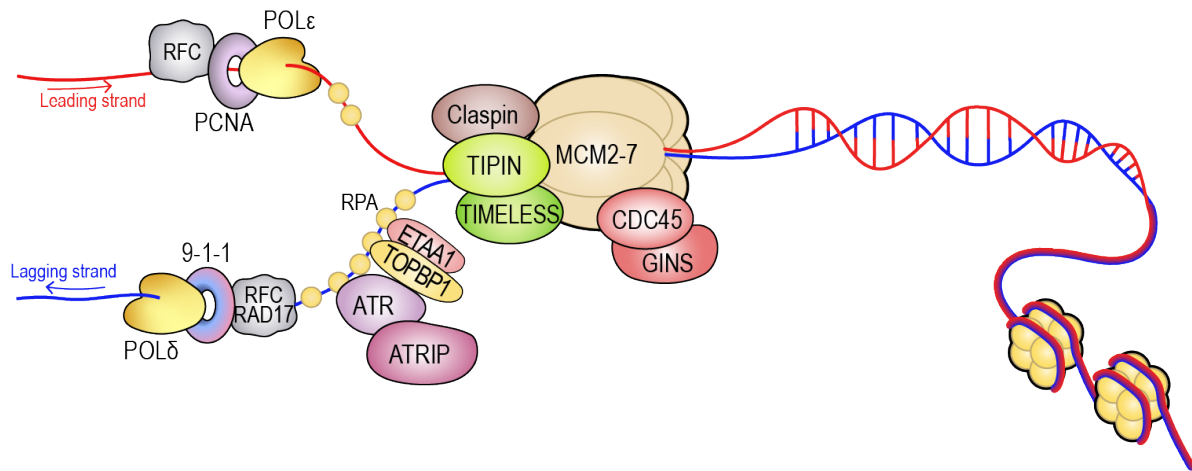


Figure 4: Schematic representation of a stalled replication fork. Under normal conditions, DNA replication is catalyzed by the replisome multi-subunit complex, formed by MCM2-7 and the replication factors CDC45 and the GINS complex. The Claspin-TIPIN-TIMELESS complex coordinates unwinding with DNA synthesis, carried out by POL δ and ϵ . PCNA tethers the polymerases to the DNA, while RFC controls PCNA loading and unloading. When replication stalls, due to DNA lesions or other sources, ssDNA is exposed and gets covered by RPA. In turn, the ATR-ATRIP tetramer is recruited, and proteins TOPBP1, ETAA1, and the 9-1-1 complex stimulate ATR activity. ATR phosphorylation prevents late origin firing via CHK1 activation and stabilizes the replication fork through the claspin-TIMELESS-TIPIN complex. This prevents replication fork processing through nucleases and provides time to resolve the obstacle for replication. Adapted from Saldivar et al. and Gaillard et al. [165, 166]

1.1.3 Posttranslational modifications in the DDR

DNA damage repair is a highly regulated process, assuring accurate and timely removal of DNA lesions. This finely orchestrated process is regulated through PTMs. Among the most prominent PTMs are phosphorylation, ubiquitination, sumoylation, acetylation, methylation, and poly(ADP-ribose)ation [167]. Phosphorylation and ubiquitination are discussed in more detail below.

Protein phosphorylation

Phosphorylation is the transfer of a charged γ -phosphate group from the high energy donor ATP to the serine (S), threonine (T), or tyrosine (Y) hydroxyl groups of proteins. It is estimated that more than 70% of all proteins are phosphorylated at some point. 518 protein kinases, 1.7% of the human genome, catalyze this reaction and about 140 phosphatases lead to their removal [168, 169]. Interestingly, S:T:Y phosphorylation occurs in a proportion of 86:12:2, with 20% of kinases but 60% of phosphatases acting on tyrosine [168, 170, 171]. While half of the tyrosine phosphatases also hydrolyze S/T phosphorylation, kinases do possess specificity towards S/T or Y residues [172, 173]. However, non-canonical phosphorylation events have been identified on histidine, aspartate, glutamate, lysine, arginine, and cysteine residues [174]. Phosphorylation changes a neutral hydroxy group to a di-anionic state. Along with larger hydrated shells, it features an even stronger formation of salt bridges and hydrogen bonds than those formed by the negatively charged amino acids glutamate or aspartate. Thus, phosphorylation often results in conformational changes that influence protein function or modulate protein-protein interaction through phosphorylation-specific binding domains. For instance, FHA (forkhead-associated) domains recognize phospho-threonine, SH2/3 (Src-homology-2/3) and PTB (phosphotyrosine-binding) bind phospho-tyrosine, and 14-3-3 proteins interact with phosphorylated serine or threonine [175–177].

Many kinases are involved in the promotion and regulation of the DNA damage response. The most prominent examples include ATM, ATR, and DNA-PKcs, with the former two being considered the main transducers or master regulators of the DDR response. All three kinases belong to the phosphatidylinositol 3-kinase-related kinases (PIKKs) family, share a similar structure, and specifically phosphorylate serine or threonine residues frequently followed by a glutamine (S/T-Q motif) [178]. Upon activation, these kinases phosphorylate hundreds of substrates regulating many cellular processes [179]. Some of the substrates can be phosphorylated by all three kinases (e.g. H2AX), while others are specifically targeted by one but not the others. Despite their similarities, these kinases also play different roles in the DDR. Since ATR was already discussed in the earlier section of “Replication fork stress and recovery”, ATM and DNA-PKcs will be discussed below.

As mentioned earlier (see NHEJ, 1.1.2), DNA-PKcs primarily functions in the NHEJ pathway, where it is recruited by the DNA-bound Ku heterodimer. It is the caspase-2-mediated cleavage of Ku80 that allows DNA-PKcs binding and formation of the DNA-PK complex [180]. This causes the inward translocation of Ku and the activation of the DNA-PKcs through conformational changes in its FAT and FATC domain [181]. DNA-PKcs is also likely to tether the broken DNA strands, thereby preventing nucleolytic degradation. In turn, DNA end-processing is mediated through autophosphorylation of its ABCDE clusters leading to conformational changes, and the phosphorylation of other NHEJ members, including Ku, XRCC4, XLF, and Artemis [182, 183]. DNA-PKcs also plays an active role in pathway choice between HR and NHEJ. For instance, BRCA1 prevents NHEJ by inhibiting DNA-PKcs autophosphorylation in S and G2 phase [184]. Additionally, it functions in HR repair, as it is phosphorylating both members of the p53-RPA complex, freeing RPA, and allowing it to protect ssDNA [185, 186]. DNA-PKcs also acts as a backup for ATR in preserving checkpoint activation [187]. More recently, DNA-PKcs has also been implicated in other cellular processes, including telomere maintenance and cell cycle progression [188, 189].

ATM is essential for HR repair and activated by the MRN complex (see HR, 1.1.2). MRN slides along dsDNA until it encounters a roadblock, such as Ku [142]. It then unwinds DNA ends and leads to the activation of ATM [190]. The C-terminal domain of MRN subunit NBS1 contains a motif that forms a direct contact point, in this process [142, 191]. ATM itself exists as a noncovalent homodimers/oligomer in its inactive state but undergoes monomerization and autoubiquitination when activated [190, 192]. Phosphorylation on position S1981 serves as a marker for ATM activation [193]. As a master regulator of the DNA damage response, ATM phosphorylates histone H2AX, which leads to further recruitment of MDC1 and eventually activation of the ubiquitination cascade. It also orchestrates the cell cycle checkpoint through its substrates, CHEK2 kinase that controls G2/M, and p53 that controls G1/S transition [194, 195].

Protein ubiquitination

One widespread PTM in eukaryotes is ubiquitination, the attachment of a 76 amino acid long protein to lysine residues of target proteins [196]. Initially discovered for its role in targeting proteins for degradation through the proteasome, it is now established that ubiquitination also regulates protein sorting, gene expression, cell signaling, and DNA repair [197–203]. Ubiquitination of proteins is mediated by three enzymes: In mammals, ubiquitin is activated by one of two ubiquitin-activating enzymes (E1) forming a thioester bond with the E1 in an ATP-dependent manner (Figure 5). Subsequently, it is passed on to one of ~40 ubiquitin-conjugating enzymes (E2). Finally, with the help of more than 600 ubiquitin ligases (E3), ubiquitin is specifically attached to target proteins via an isopeptide linkage between the ubiquitin C-terminus and the ϵ NH₂ group of lysine residues on target proteins [204, 205]. This process may be repeated until multiple lysine residues of the target protein are ubiquitinated or ubiquitin chains are formed, connected through specific isopeptide bonds (K6, K11, K27, K29, K33, K48, K63, N-terminal methionine) [206]. These various ubiquitin modifications adopt distinct conformations and result in specific outcomes in the cell. Although ubiquitination needs the concerted action of all enzymes of the ubiquitin cascade, it is mainly the E3 ligases that confer substrate specificity. There are three known families of E3 ligases, the RING (really interesting new gene), the HECT (homologous to the E6AP carboxyl terminus), and the RBR (RING-between-RING) ligases, with the RING ligases making up by far the largest one (~95%) [207, 208]. The biggest difference between these families lies in the mode of ubiquitin transfer. In the case of HECT and RBR ligases, ubiquitin is transferred from the E2 to a cysteine on the E3 ligase as an intermediate state, followed by the transfer to the substrate. In contrast, RING ligases are important for substrate recognition and the spatial arrangement of the E2 and the substrate, but they do not take part in the transfer itself. Instead, the ubiquitin is transferred from the E2 directly onto the substrate [207, 209]. Recently, experimental evidence has emerged that places the E2 conjugating enzymes as key mediators of ubiquitination. They were observed to control the switch from chain initiation to elongation, to regulate the processivity of chain formation, and to establish the topology of the chains. Therefore, they are not mere basic ubiquitination components but determine the consequences for ubiquitin-modified proteins [210–212].

The readers of ubiquitination are proteins with ubiquitin-binding domains (UBDs). More than 200 have been identified and the number is constantly growing [205]. UBDs display varying affinities towards mono- and differentially linked poly-Ub. UBDs come in a variety of structurally different types but can be broadly categorized into four subclasses, namely: the α -helix, the zinc finger, the pleckstrin homology, and the ubiquitin-conjugating-like domains [213–215]. Furthermore, ubiquitination is a reversible modification that can be cleaved by over 100 deubiquitinating enzymes (DUBs). DUBs can be separated according to their catalytic sites into two main groups, the cysteine peptidases, and the metalloproteases. Additionally, DUBs can be further divided into seven protein families according to their sequence and structure similarity: cysteine peptidases include the ubiquitin carboxyl-terminal hydrolases (UCH), the ubiquitin-specific proteases (USP), the ovarian tumor proteases (OTU), the

Machado-Joseph domain-containing proteases (MJD), the motif-interacting with ubiquitin-containing novel DUB family (MINDY), and the Zinc finger with UFM1-specific peptidase protein (ZUFSP). The metalloproteases only include the JAB1, MPN, MOV34 family (JAMM) [216–226]. DUBs can work as exo- or endo-peptidases and specifically cleave certain ubiquitin-linkages [220, 223].

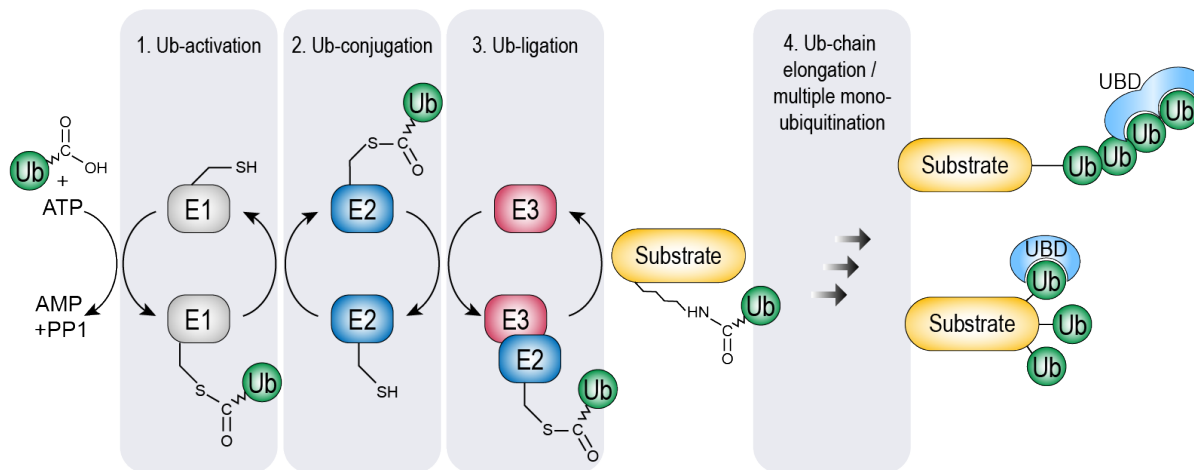


Figure 5: Schematic representation of the ubiquitin cascade. Ubiquitin is activated by a ubiquitin-activating enzyme (E1) in an ATP-dependent manner. It is passed on to a ubiquitin-conjugating enzyme (E2) and can specifically be attached to the substrate with the help of an E3 ligase. Ubiquitin chains are formed by repetitive attachment of ubiquitin. Proteins with ubiquitin-binding domains (UBDs) can specifically recognize mono-ubiquitin or poly-ubiquitin chains. The removal of ubiquitin is mediated through deubiquitination enzymes (DUBs; not shown). Adapted from Kliza and Husnjak, and Deribe et al. [227, 228].

Protein ubiquitination in the DNA damage response

Early in the DDR, the ligase RNF8 is sequestered to the DSBs via interaction with the ATM-phosphorylated TQXF motifs on MDC1 [229–231]. RNF8 promotes DDR via K63-linked polyubiquitin of surrounding substrates. Until recently, it has been believed that polyubiquitination of histone H1 leads to the recruitment of RNF168 [232]. However, now it seems more likely that the polycomb group-like protein L3MBTL2 is modified at K659 by RNF8, which then anchors RNF168 to these sites [233]. This triggers further signal amplification through H2A and H2AX ubiquitination, and to the recruitment of repair proteins such as BRCA1 and 53BP1. To prevent inappropriate activation of DSB response, the signaling cascade requires tight control, including both protein degradation and deubiquitination. For instance, RNF168 is stabilized by the action of USP34 in response to DNA damage [234]. In contrast, E3 ligases TRIP12 and UBR5 target RNF168 for degradation to keep chromatin ubiquitination in check [235]. A prominent example is also the regulation of damage tolerance pathways. As the replication forks stall, cells can continue DNA replication by either TLS or TS (see replication fork). Pathway choice is regulated depending on the ubiquitination status of the homotrimeric DNA clamp PCNA. Monoubiquitination of PCNA on position K164 leads to TLS, and is mediated by the E3 ligase RAD18 in combination with the E2 UBE2A/B. In contrast, poly-ubiquitination with K63-linked ubiquitin chains leads to TS, with the E3 ligases SHPRH and HLTF and the E2 UBE2V2-UBE2N heterodimer carrying out chain elongation [162, 163, 236–238].

Ubiquitination is most famous for its role in protein degradation through the proteasome, which is essential for protein turnover and maintenance of homeostasis in the cell. The 26S proteasome consists of a 19S regulatory and a 20S core particle. Proteins are primarily targeted to the proteasome by the attachment of K48 or K11-linked ubiquitin chains. These ubiquitin-labeled proteins are recognized by receptor proteins of the 19S regulatory particle, which further unfold them and guide them into the proteolytic chamber (20S) where they are digested [239, 240].

Interestingly, several studies have shown that there is a cross-talk between the ubiquitin-proteasome system and the DNA damage response. For instance, inhibition of the proteasome affects the formation of DNA foci and/or suppresses homologous recombination [241, 242], or suppresses DDB2-mediated lesion recognition in NER [243]. Furthermore, key components of the DDR, like BRCA1 and RAD52, have been shown to be degraded through the proteasome after DNA damage [244, 245]. Beyond this, recent studies have also proposed a role for 19S proteasomal subunits without the involvement of proteasomal degradation. The binding of the 19S subunit DSS1 to BRCA2, a protein involved in double-strand break (DSB) repair, is essential for BRCA2 function. BRCA2 binding has also been demonstrated for the 19S subunit RPN7, which is additionally suspected to be essential for long-term maintenance and stability of DNA foci [246]. Another interesting subunit in this context is the regulatory particle non-ATPase 10 (RPN10). RPN10 is one of the main ubiquitin receptors of the proteasome and exists in both proteasome-coupled and un-coupled forms. While its interaction with the core proteasome is mediated by its N-terminal von Willebrand factor A (VWA) domain, its capacity to interact with protein substrates is due to its two ubiquitin-binding motifs (UIMs) [247]. Ubiquitin-binding via the UIMs is inhibited by the mono-ubiquitination of RPN10. Under proteolytic stress conditions, RPN10 mono-ubiquitination is reduced and therefore poses a new mechanism for the regulation of proteasomal activity [248]. Like RPN7, RPN10 co-localizes with DNA repair foci [249]. Interestingly, it has been shown to get phosphorylated upon DNA damage by the kinases ATM and ATR [179, 250].

1.1.4 The HECT-type ubiquitin ligase E6AP/UBE3A

The E3 ligase E6AP/UBE3A is a multifaceted protein controlling diverse signaling pathways. Since its discovery, it has been extensively studied in two pathological contexts: in neurodevelopmental disorders and cancer development.

UBE3A was the first mammalian ubiquitin ligase ever studied, and hence the name HECT (Homologous to the E6AP Carboxyl Terminus) was coined [251]. E6AP possesses several well-characterized functional domains. The catalytic domain of this ligase is located at the C-terminus, spanning ~350 amino acids. At the N-terminus, it possesses a Zn²⁺-binding AZUL (Amino-terminal Zn-finger of UBE3A ligase) domain, which is involved in substrate recruitment and self-inhibitory regulation [252]. A domain necessary for interaction with the human papillomavirus protein E6 and a binding domain for the E3 ligase HERC2, are located in between. E6 enhances UBE3A catalytic activity by promoting a trimer complex formation, corresponding to UBE3A's fully active form. HERC2 association stimulates

UBE3A activity also in a none-viral context [253–256]. Besides its E3 ligase activity, UBE3A also acts as a transcriptional co-activator of steroid hormone receptors (estrogen, progesterone, and androgen receptor) [257–259]. Three LxxL motifs, important for receptor interaction, are located in the HECT domain or in between HECT and AZUL domain. The transactivating domain has been located outside the HECT domain. Both ligase and transactivation functionality have been implicated in cancer and neurodevelopmental disorders [257, 260, 261].

UBE3A was originally identified in the context of human papillomavirus (HPV) infection, as the protein that gets hijacked by the viral E6 and promotes degradation of the tumor suppressor p53 [262, 263]. Together with the degradation of the retinoblastoma protein (RB) through the viral E7 protein, it is a fundamental step in malignant transformation and HPV-driven carcinogenesis [264]. Since then, roles of UBE3A have also been uncovered for other viruses. In hepatitis C virus (HCV), UBE3A drives the development of hepatocellular carcinoma by targeting RB for degradation, and in encephalomyocarditis virus (EMCV) it facilitates EMCV survival during infection [265–267].

However, UBE3A has also been demonstrated to contribute to other cancers, beyond virus-related ones. In B-cell lymphoma and Burkitt's lymphoma (BL), UBE3A exerts oncogenic capacity by ubiquitination and degradation of the tumor suppressor PML. This is clinically relevant, as 60% of all BL patients display increased UBE3A expression levels [268, 269]. This role of UBE3A is not restricted to BL cancer. While UBE3A is essential for prostate gland development expressing its functions as transcriptional co-activator of the androgen receptor, overexpression of UBE3A is associated with degradation of both PML and the p27, and characteristic for late stage prostate cancer [270–274]. Simultaneously, the negative regulation of protein targets can also be mediated through its transactivator function, as in the case of the stress-induced chaperone and potential tumor suppressor clusterin [275]. In breast cancer, UBE3A expression might exert a tumor-suppressive function since it works as a co-activator of ER- α receptor, but also targets the receptor for degradation. Other breast cancer-related proteins such as ENO1 and AIB1 are also UBE3A substrates [276–283].

UBE3A is at least equally well-known for its involvement in neurodevelopmental disorders, which stem from genetic alterations (mutations, deletions, duplications) in the UBE3A locus. UBE3A dosage is critical for neuron development. Loss of expression results in Angelman syndrome (AS), while increased expression results in autism spectrum disorders (ASD) [284–286]. In neurons, the paternal allele of UBE3A is silenced. This is mediated, at least in part, through the paternal-specific expression of an antisense transcript [287]. Therefore, loss of the maternal allele leads to AS, characterized by impaired speech, seizures, and developmental delay. An increased copy number leads to ASD [288]. UBE3A has a broad effect on neuron morphology and function through direct or indirect regulation of key protein levels, such as ARC, SK2, and XIAP [289–294]. Interestingly, UBE3A has also been connected to proteasome function, which might exert broad-spectrum effects on homeostasis in neurons. It was reported that UBE3A interacts with and ubiquitinates the proteasome receptor RPN10. This might hamper the binding and degradation of ubiquitinated proteins targeted for degradation [295]. While this

might pose a mechanism for proteasome regulation under normal physiological conditions, certain UBE3A mutants have demonstrated excessively strong binding and blocking of RPN10 [296]. Additionally, it has been suggested that RPN10 provides a nuclear localization signal for UBE3A in an isoform-specific manner [297]. Lastly, also other proteasome subunits seem to be UBE3A substrates. This has been demonstrated in the context of an autism-linked mutant (T485A), which disrupts PKA-mediated phosphorylation and control of UBE3A activity. This hyperactive UBE3A mutant leads to ubiquitination and degradation of certain proteasome subunits, reduces proteasome activity, and ultimately results in increased Wnt signaling [298].

1.2 Mass spectrometry-based proteomics

Protein identification and characterization by mass spectrometry (MS) can be performed using two alternative strategies: Top-down or bottom-up. In the former, intact proteins are analyzed, theoretically allowing detection of all existing modifications simultaneously, as well as correlations between these modifications [299]. In the more commonly used bottom-up approach, complex mixtures of proteins are digested into peptides, separated by single-mode or multidimensional chromatography, and analyzed in a mass spectrometer [300]. A typical bottom-up workflow is depicted in and the separate steps are discussed in detail below (Figure 6). The essential part of any workflow is of course the mass spectrometer itself. To determine the m/z ratios of analytes, the mass spectrometer consists of three vital elements: The ion source, the mass analyzer, and the detector [301]. Their technical details are also discussed in the following paragraphs.

1.2.1 Sample preparation

Due to the complexity of the proteome, there is no standard method for sample preparation. Protocols differ depending on the sample type, analytical method, and experimental goal. Additionally, sample source, abundance, complexity, and physical properties have to be considered [302]. However, there are steps that most bottom-up sample preparations have in common. After proteins are isolated from the biological material, disulfide bridges are reduced and the resulting free cysteines are alkylated [303]. Subsequently, proteins are cleaved with a sequence-specific protease, typically trypsin, producing a complex mixture of peptides between ~ 500 and $3,500$ Da. Trypsin is advantageous as it is highly active and tolerant of many additives. It cuts C-terminally of lysine and arginine, leaving positive charges on the peptides and making them detectable by MS [304]. The use of other proteases (AspN, GluC, Chymotrypsin) has helped to increase protein sequence coverage and expand the number of measured peptidoforms, but trypsin remains the most popular [305, 306].

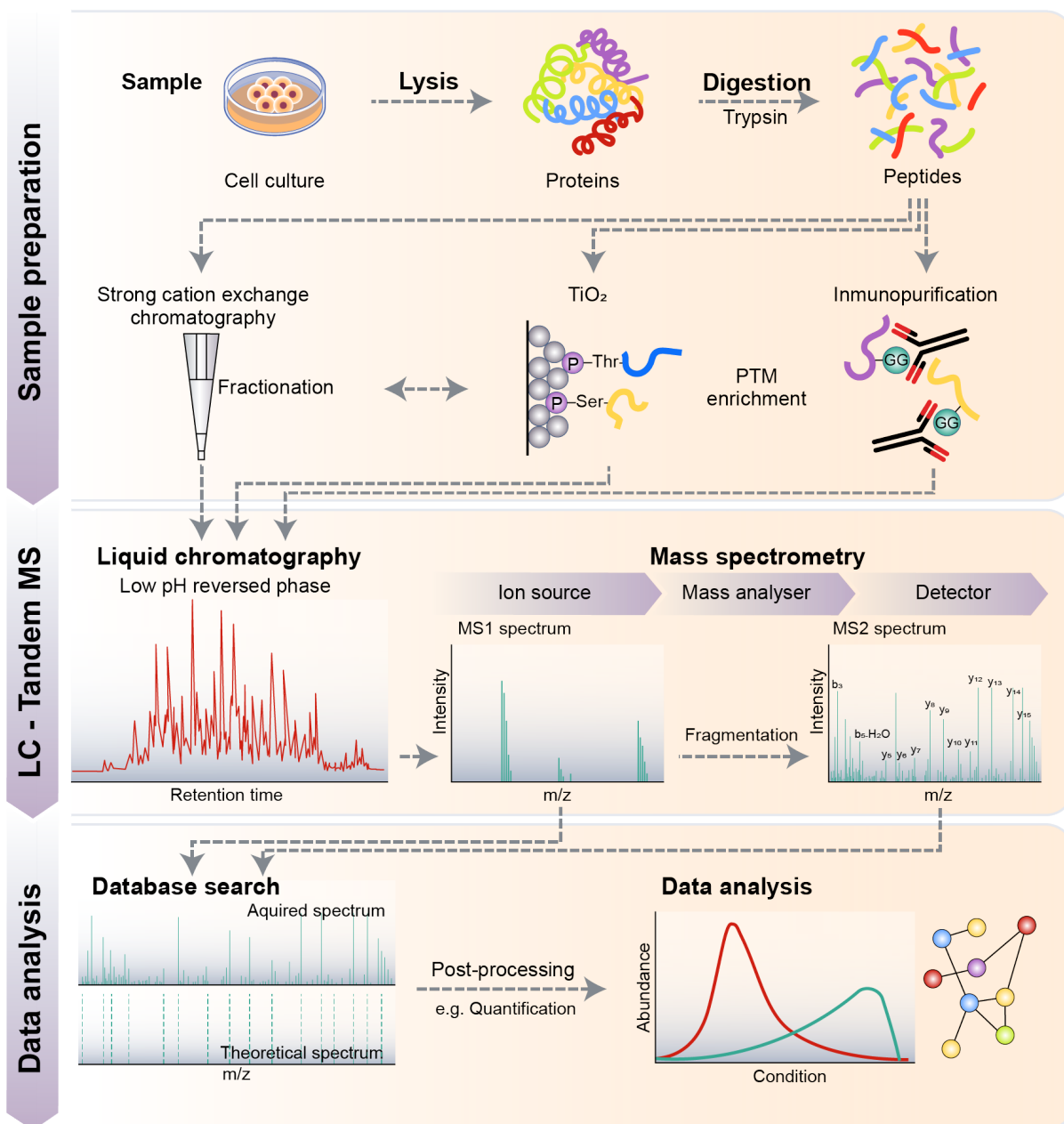


Figure 6: Workflow of a bottom-up mass spectrometric experiment. Proteins are isolated from biological samples and digested into peptides. These peptides can be enriched for specific PTMs (e.g. phosphorylation by TiO_2 , immunoprecipitation for diGlycyl remnant-containing peptides) and/or fractionated by various techniques. Peptides are further separated by low pH RP chromatography, which is directly coupled to the mass spectrometer. MS1 precursor and MS2 fragmentation spectra are recorded and subjected to peptide identification via database searching. Quantitative readouts, based on peptide intensities, can be used for downstream statistical analysis. Adapted from Mallick and Kuster, Altelaar, and Zecha [307–309].

1.2.2 Offline and online fractionation

Protein digestion of cell lysates gives rise to an incredibly complex mixture of peptides, which cannot be captured comprehensively by mass spectrometry. Therefore, off-line fractionation is commonly applied to reduce sample complexity to improve peptide identification. A wide-range of separation techniques based on physicochemical properties (polarity, hydrophobicity, charge, size) exist [310]. An appropriate separation technique shows good separation power and is highly orthogonal to the

subsequent online peptide separation step. The chosen number of fractions is always a compromise between measuring depth and the expenditure of measuring time [311].

However, even in highly fractionated samples, detection of PTM-modified peptides remains challenging due to the sub-stoichiometric nature of PTM-modified peptides. To overcome this problem, enrichment steps, based on specific interaction with the PTMs, are commonly performed when analyzing peptide modifications. Frequently used techniques include Fe-IMAC or TiO₂ based enrichment of phosphorylated peptides, and the use of a diGly remnant specific antibodies for the immunoprecipitation of ubiquitinated peptides [312–314].

To reduce sample complexity prior to MS even further, peptide mixtures are commonly separated by ion-pair reversed-phase high-performance chromatography (RP-HPLC) at low pH. High peak capacities and peptide resolution make this technique highly suitable for bottom-up approaches. Additionally, the mobile phase is electrospray ionization (ESI)-compatible, allowing direct (online) coupling to the mass spectrometer. In short, peptide separation is achieved through differential solvophobic interactions of nonpolar side chains with the non-polar stationary (usually octadecyl alkane chains, C₁₈) and mobile phase. Peptide retention and thereby resolution can be further increased by the addition of ion-pairing reagents (amphiphilic molecules) that mediate the interaction of polar peptide chains with the stationary phase. Consecutive elution of peptides is achieved by gradually increasing the concentration of organic solvents in the mobile phase. Hence, peptide retention increases with peptide hydrophobicity [310, 315].

1.2.3 Electrospray ionization

Separation and analysis based on the m/z ratio of a molecule require its ionization and transfer into the gas phase. For peptides, this is typically achieved by the “soft” ionization technique electrospray ionization (ESI), which allows vaporization of large peptides or even proteins without their destruction. Compatibility with LC, allowing an online LC-MS setup, makes ESI the most commonly used ionization technique by far [316, 317]. In ESI, the peptide solution exits the RP column through a thin capillary (emitter) to which an electric potential is applied. The electric field between the capillary and a counter electrode charges the emerging liquid and leads to the formation of the so-called Taylor cone. As the Coulomb forces become stronger, the liquid is dispersed into small, multiply charged droplets. While migrating through the electrostatic field towards the vacuum system of the mass spectrometer, the liquid evaporates, and the charge density on the droplets increases. Eventually, when the coulomb forces exceed the surface tension (Rayleigh limit) the charges repulse each other and the droplets explode into even smaller ones (Coulomb explosion). Final peptide ionization is hypothesized to occur in two ways: In the ion evaporation model, active ion emission from the surface of the droplet occurs due to field desorption, while the charged residue model proposes complete evaporation of the solvent, leaving behind the charge on the analyte. In all likelihood, both models account for analyte ionization [316–318].

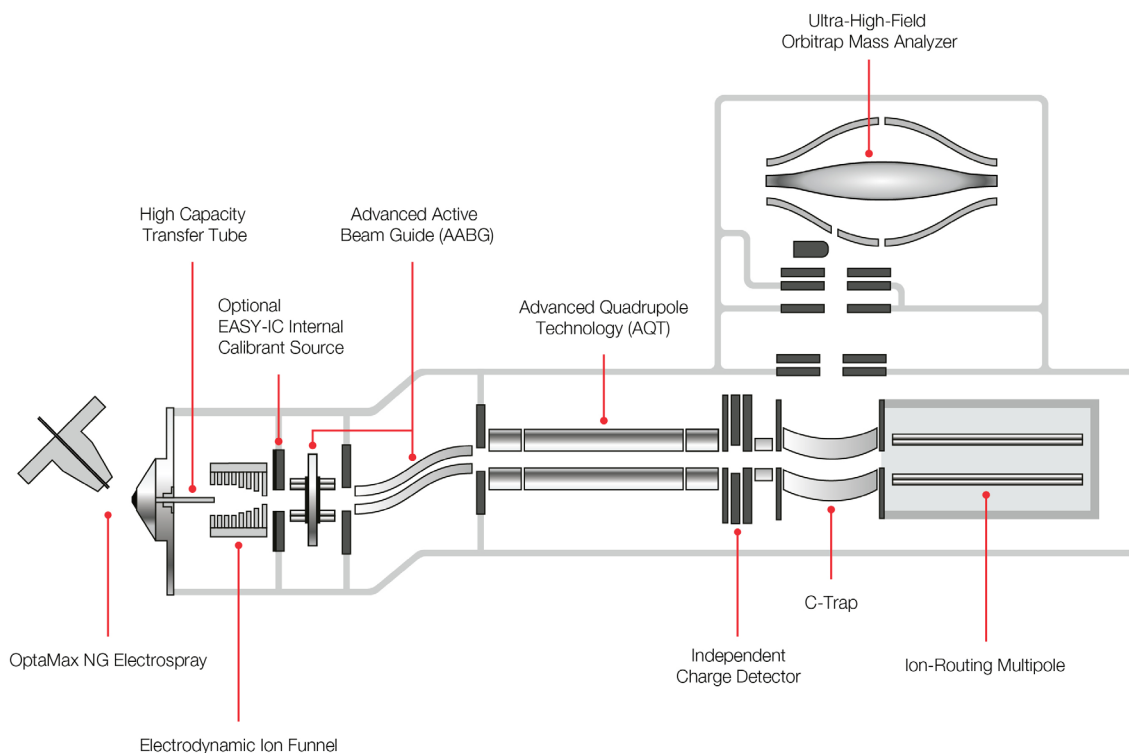


Figure 7: Schematic of the Orbitrap Exploris 480 mass spectrometer. Peptides are ionized and transferred into the gas phase by ESI. Ions are focused and propelled forward towards the quadrupole mass analyzer, which acts as a mass filter, via the ion optics. They are stored and focused in the C-trap and directed either to the ion-routing multipole for fragmentation, or the orbitrap for the acquisition of MS1 and MS2 spectra. (Schematic from Thermo Fisher Scientific, 2019 [319])

1.2.4 Mass-to-charge analysis

Mass analyzers determine the mass-to-charge ratio of an analyte. In combination with the detector, they determine the reliability and quality of the analysis. Common to all of them is the manipulation of analyte trajectories in an electromagnetic field through the application of direct (DC) and alternating (AC) currents. Subsequently, m/z ratios are inferred by measuring the response of the analytes and comparison to known m/z standards, resulting in a mass spectrum. Depending on the physics, analyzers belong to quadrupole, ion trap, Fourier transformation, time of flight, or magnetic sector analyzers. They all differ in resolution, mass accuracy, sensitivity, and dynamic range [320]. Modern mass spectrometers often combine at least two different mass analyzers, allowing flexible data acquisition. Two such hybrid mass spectrometers (Q Exactive and Exploris 480), incorporating both a quadrupole and an orbitrap mass analyzer, were used in this study [321].

Quadrupole – The movement of analyte ions depends on their mass, the charge, and of course on the force applied to them. Using this principle, ions can be stored, deflected, and separated, and it is applied in all parts of the mass spectrometer. For instance, the quadrupole in the Exploris can be used as a mass filter, permitting passage only to analyte ions of a certain m/z range (Figure 7). In short, the quadrupole consists of four rods, with superimposed DC and AC voltages applied to them. The AC, also called radiofrequency, confines the ions radially and keeps the ions on a corkscrew-like motion, while passing

through the quadrupole. As the smaller ions move faster than the bigger ones of the same charge, they describe bigger amplitudes. Therefore, small ions can be removed from the quadrupole by increasing the AC voltage (= lower filter). In turn, the upper filter depends on the DC voltage, which applies a negative charge to two of the rods. This attracts the positively charged ions. While small ions can be pushed back onto a stable trajectory by the AC, bigger ions with too much inertia cannot, and collide with the rods or escape between them. Consequently, the choice of the AC and DC currents determines the range of peptides (m/z window) that is allowed to pass through the quadrupole [301, 322].

Orbitrap – Orbitraps are mass analyzers of extraordinary accuracy and resolution, and are therefore used for spectra acquisition in the Exploris (Figure 7). Since they cannot store or collect ions, they are directly connected to an ion trap (here: C-trap). The Orbitrap essentially consists of three (two outer and one inner) electrodes. With voltage applied to these electrodes, analyte ions are trapped within an electric field, oscillating around the inner spindle-shaped electrode. The outer barrel-like electrodes are used for image current detection of the axial oscillations (ωz) along the spindle. These are independent of parameters like angle and energy but directly connected to the m/z value of the ions. The image current is Fourier-transformed into the frequency domain and subsequently deconvoluted into a mass spectrum. Since the resolving power of orbitraps depends on the recorded number of oscillations, very high mass resolution can be achieved, however, for the price of longer acquisition times [320, 322, 323].

1.2.5 Tandem mass spectrometry and data acquisition

Modern mass spectrometers allow measurement of peptides including their charge states and isotope patterns through their high accuracy and resolution. This allows conclusions about the charge state, the chemical composition, and therefore potentially the identity of the peptide. However, in complex mixtures, structurally different peptides with the same chemical composition cannot be distinguished. Thus, the peptide sequence is determined to narrow down potential peptide matches. To this end, a peptide precursor spectrum is recorded (MS1), a specific peptide is isolated, it is fragmented, and the resulting fragment peptides are recorded (MS2). In an ideal case, fragments only differ by one amino acid, allowing the determination of the peptide sequence. Altogether, this process is referred to as tandem MS (MS/MS) [324]. The record of a precursor spectrum, with the purpose of selecting peptides for fragmentation, is known as data-dependent acquisition (DDA) and does not require prior knowledge about the sample. Typically, the top N most intense precursor ions are selected for fragmentation. Alternative methods include targeted approaches like parallel reactive monitoring (PRM) or data-independent acquisition (DIA) [325, 326]. Fragmentation itself is commonly achieved by collision-induced dissociation (CID) or higher-energy c-trap/collision dissociation (HCD), in which peptide ions collide multiple times with inert neutral gas molecules (Ar, He, Ne). The kinetic energy is converted into internal vibrational energy which results in bond breakage. In both methods, fragmentation occurs predominantly at the peptide bond, which is advantageous for sequence determination. However, CID has a higher preference for low energy bonds, leading to neutral loss ions more frequently, and also

suffers from the loss of peptides in the low mass region. In the Exploris, ions of a certain m/z value are first accumulated, focused in a C-trap, and then accelerated towards the Ion-Routing Multipole for HCD [327–329]. Depending on the position of breakage, C-terminal fragments are referred to as x_n , y_n or z_n ions, N-terminal ones are called a_n , b_n or c_n ions (see Figure 7). HCD-induced fragmentation typically produces b and y ions [330, 331].

1.2.6 Peptide and protein identification

The acquired mass spectra build the bases for peptide and hence protein identification. The MS1 spectrum provides information about the peptide mass, while the MS2 allows the determination of the peptide sequence. Theoretically, this allows deduction of the complete peptide sequence (de-novo-sequencing) [332]. Yet, fragmentation spectra are often incomplete and/or contain fragments from co-isolated peptides. Additionally, bottom-up workflows produce tens of thousands of spectra rendering manual interpretation impossible [324]. Therefore, MS/MS-based peptide identification is typically performed via database searching. MS2 spectra are matched to theoretical ones, generated by *in silico* digestion of proteins from a selected proteome, genome, or transcriptome database, or compared to a spectral library [333]. Based on software and user-specific parameters, probabilities for the best matches are calculated and peptide identities are assigned. The accuracy of the assignments is evaluated by a target-decoy approach. Spectra matching to the decoy database are wrong by definition, allowing the calculation of a false discovery rate (FDR). Combining both information, and by setting stringent cut-offs, high-quality peptide identifications can be achieved [334, 335]. Ideally, an identified peptide matches a specific protein. However, proteins share parts of their primary sequence. Thus, the identification of a protein is only possible if a unique peptide is measured. This is referred to as the peptide inference problem [308].

1.2.7 Peptide and protein quantification

Mass spectrometry not only allows peptide and protein identification but also quantification. Since the signal intensity of a peptide is proportional to the peptide amount over a range of four magnitudes of order, peptide quantities can be compared between different sample runs, allowing relative quantification (label-free quantification (LFQ)) [336]. In this manner, only intensities of identical peptides can be compared, as different peptides produce different signals e.g. due to their ionizability. A drawback of LFQ is that samples are processed and measured separately, leading to relatively low reproducibility. Additionally, due to the stochastic nature of peak picking in DDA experiments, missing values between samples are common and make statistical analysis difficult. An improvement on LFQ is the stable metabolic labeling of amino acids in cell culture (SILAC). As the name implies, isotopically labeled amino acids are fed to cells which incorporate them into their proteins. This allows early mixing and simultaneous measurement of multiple samples. On the downside, SILAC is usually restricted to three sample conditions and generates more complex MS1 spectra (= less measuring depth) [337]. Another approach is based on the isobaric-tagging of peptides and is described in more detail below.

Absolute quantification of peptides can e.g. be achieved by spiking peptides, with incorporated stable isotopes and of known concentration, into the sample mix. Since the synthetic peptides and the naturally occurring ones are chemically identical but have a different weight, they can be distinguished in the MS and absolute concentrations can be inferred [338].

Peptide multiplexing – Precise and accurate quantification, high sample throughput, and deep coverage are challenges to most mass spectrometry (MS)-based experiments. Peptide multiplexing, using isobaric isotope labeling, addresses many of these challenges and has therefore become increasingly popular, especially for large-scale and proteoform / PTM studies. One such multiplexing technique, called tandem mass tag (TMT) labeling, allows multiplexing of up to 16 samples [339, 340]. TMT tags consist of a reactive group, a mass normalization spacer, and a reporter group (Figure 8A). Together, they have the same chemical structure and mass, but they are composed of unique combinations of heavy carbon and nitrogen isotopes. In the first step of a TMT experiment, the reactive N-hydroxysuccinimide (NHS) ester reacts with primary amino groups, such as N-termini of the peptides or the ϵ -amino groups of lysines. Subsequently, the labeled peptides are pooled and processed together, minimizing technical variation for the downstream workflow. In the mass spectrometer, peptides with identical sequences but different labels contribute to the same MS1 signal. Just after fragmentation, the sample-specific reporter groups with unique m/z ratios are released and can be used for relative quantification in the same MS2 scan (Figure 8B). Therefore, TMT usually leads to a low number of missing values and requires lower sample inputs in comparison to LFQ. Additionally, multiplexing allows deep peptide coverage in a reasonable time. These advantages are especially valuable for proteoform studies where quantification relies on one peptide [340, 341]. While TMT shows very high intra-batch reproducibility, it is lower for settings with multiple TMT batches. However, the identified peptides between inter-batch experiments can vary drastically, due to the nature of DDA. Moreover, TMT suffers from both reporter-ion and co-isolation interference, strongly decreasing quantification accuracy. Reporter-ion interference, which stems from isotope impurities of the tags, can be compensated computationally. Co-isolation interference refers to co-isolation of more than one peptide for fragmentation and therefore also to the interference of reporter quantification. To date, several methods have been used to alleviate these issues. These include software corrections, additional gas-phase manipulation, measuring the reporter ions in the third dimension (TMT-MS3), or quantifying of the peptide fragments complementary to the reporter ions (TMTc) [342–344].

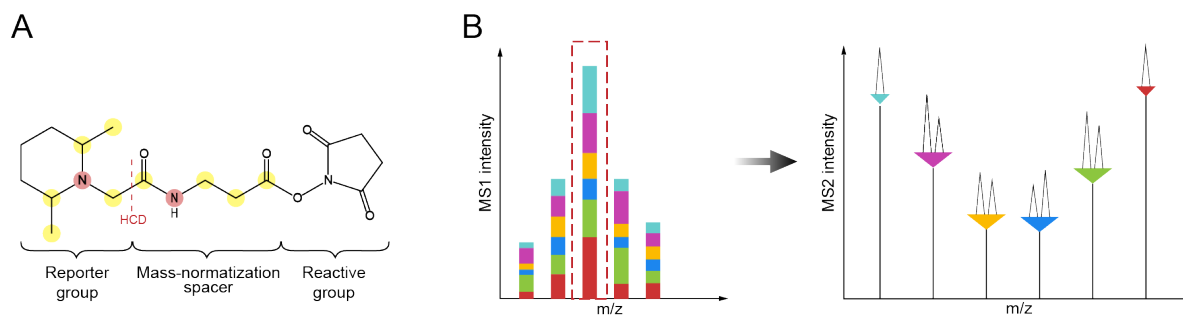


Figure 8: Isobaric labeling and data acquisition by TMT. Primary structure of TMT labels, consisting of a reporter, a mass normalizer, and a reactive group (NHS-ester). Dependent on the mass tag, heavy nitrogen (red) or carbon atoms (yellow) are incorporated into the label (A). Upon fragmentation between the reporter and normalizer group, label-specific reporter ions are released, allowing relative quantification (B). Adapted from Thermo Fisher Scientific [345].

1.3 Aim of the study

To counteract the deleterious outcomes of DNA damage, cells have developed dedicated DNA repair pathways and a general stress response to assure cell survival. These pathways are orchestrated by a broad network of proteins, regulated by PTMs. Although there is broad literature on the topic of DNA damage response, to this date, few systematic analyses have been undertaken, comparing the effects of different types of DNA damage.

Applying mass spectrometry-coupled proteomics, we set out to measure the effects of 11 different DNA damage-inducing agents on protein phosphorylation, ubiquitination, and the interaction of proteins with chromatin. To this end, we aim to establish a reproducible and efficient workflow for multiplexed deep-scale proteome and PTM analyses. The resulting screening data will be used to study distinct and common cellular responses to genotoxic stress, and to identify new players of the DNA damage response.

One such putative repair factor is the E3 ligase UBE3A. We aim to show that UBE3A plays an active role in the DDR using cell survival assays, DNA repair assays, and by characterizing its interaction and substrate landscape. Furthermore, we will investigate the role of DNA damage-dependent phosphorylation of UBE3A.

2 Results

2.1 A comprehensive analysis of the DNA damage response by mass spectrometry-based proteomics

To study both the distinct and common features of the cellular response to DNA damage, we selected a plethora of chemicals, chemotherapeutics, and radiations representing different forms of DNA damage. These included: DNA double-strand breaks (ETO, CPT, X-ray), DNA-protein crosslinks (formaldehyde = FA), oxidative damage (H_2O_2 , sodium arsenite = AsO_2), replication stress (gemcitabine = GEM, hydroxyurea = HU, aphidicolin = APH), helix-distorting lesions (UV), and alkylating damage (MMS). Since the DDR is largely regulated by PTMs, we decided to study both protein phosphorylation and ubiquitination by mass spectrometry-based proteomics. The chromatin-bound protein fractions were also examined to identify proteins that are removed from or recruited to DNA during the repair process. Additionally, we measured the changes in protein levels (Figure 9).

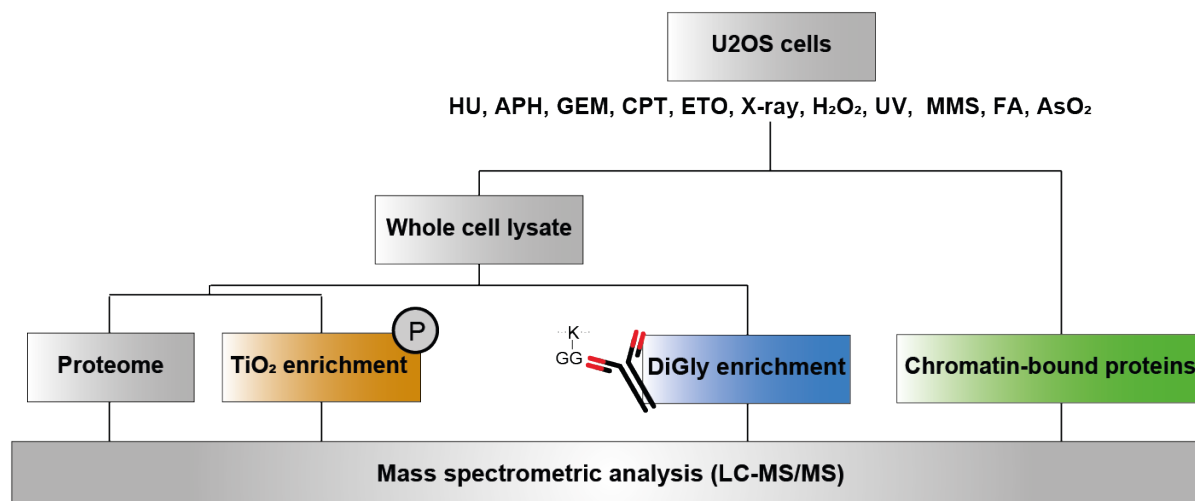
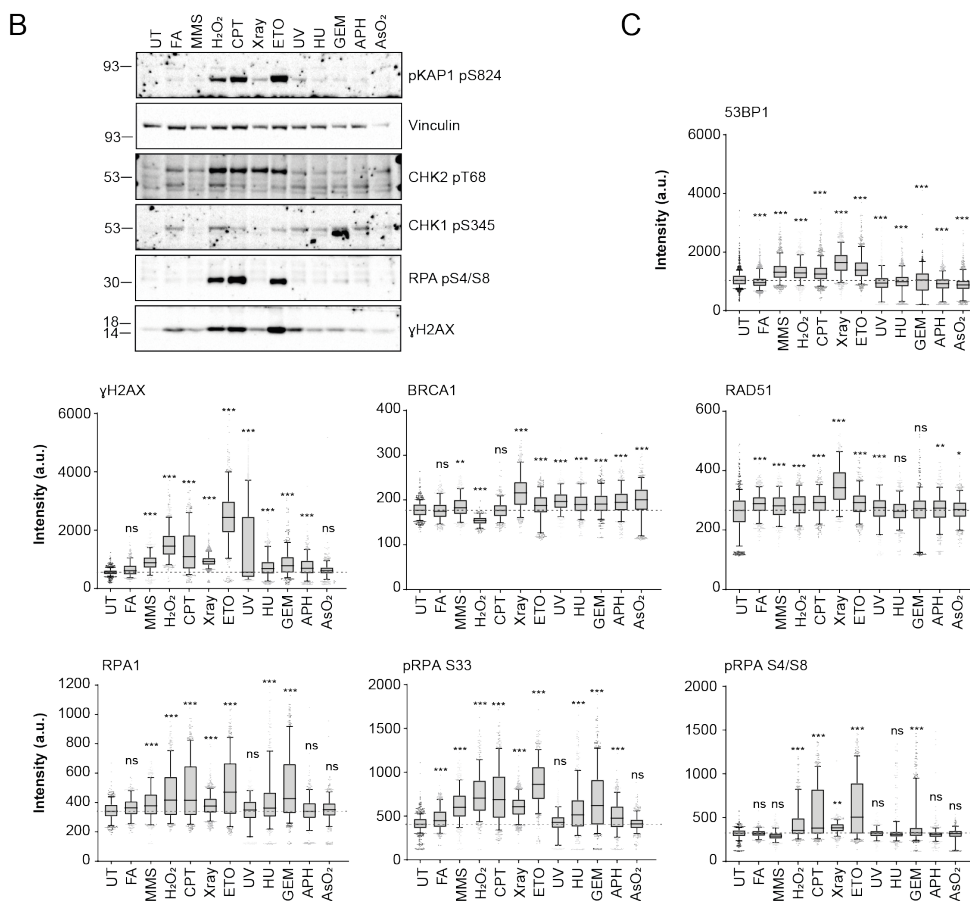
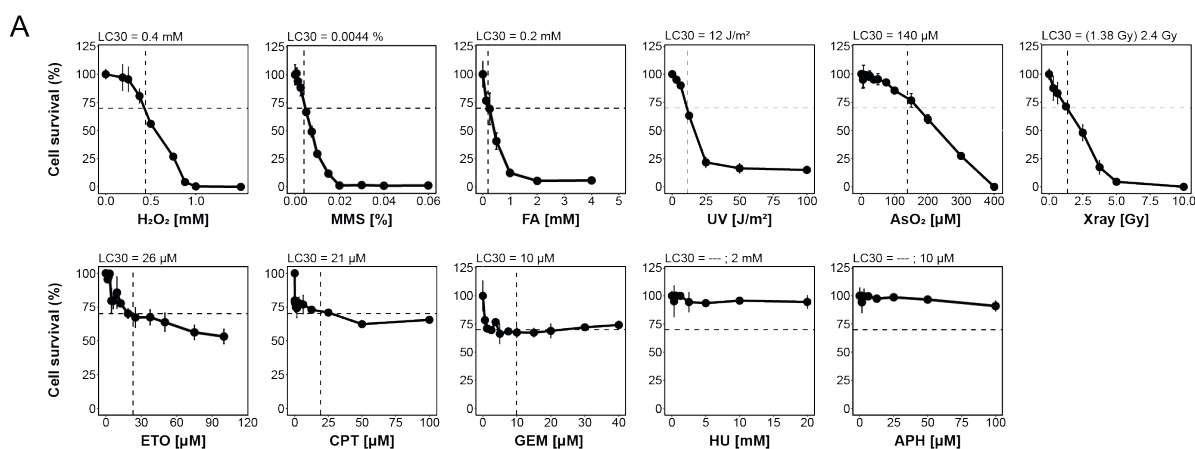


Figure 9: A comprehensive analysis of the DNA damage response. U2OS cells were treated with a variety of DNA damage-inducing agents. Whole-cell lysates were prepared and used for either complete proteome analysis, enrichment of phosphorylated peptides using TiO_2 beads, or for the enrichment of ubiquitinated peptides using diGly remnant-specific antibodies. Alternatively, proteins bound to chromatin were isolated. Finally, all samples were measured by quantitative mass spectrometry.

2.1.1 Selection and evaluation of screening conditions

In this study, we sought to investigate the acute early cellular response to DNA damage. Therefore, we decided on relatively short treatments, harvesting cells either 2 hours after DNA damage induction, or 1 hour in the case of UV irradiation. Treatment conditions were further based on their effect on cell viability. Equitoxic doses, reducing cell viability by 30% (LC_{30}), were determined in U2OS cells using CellTiter-Blue assays 48 hours post-treatment (Figure 10A). However, it should be noted that treatments, such as HU, APH, or GEM, only induce DNA damage in replicating cells. Therefore, direct comparison of toxicities between the treatments is difficult. As expected, toxicity increased with increasing doses for FA, H_2O_2 , UV, MMS, AsO_2 , and X-ray irradiation. For the topoisomerase inhibitors CPT, ETO, and the nucleoside analog GEM a plateau was observed, with toxicity only marginally

increasing beyond a saturation point. While for CPT and ETO the plateau probably represents complete inhibition of TOP1 and 2, respectively, it might correspond to the maximum amount of gemcitabine that is incorporated into the DNA within 2 hours. HU and APH did not elicit significant cell death upon 2-hour treatments even at high concentrations. Therefore, LC₃₀ values could not be determined. Instead, doses corresponding to complete inhibition of nucleotide reductase (2 mM HU) and DNA polymerase (10 μM APH), respectively, were chosen [159]. Finally, the toxicity of X-ray irradiation was not determined using the CellTiter-Blue assay, as X-ray irradiated cells are known for increased uptake and conversion of cell titer agents and consequently lead to incorrect viability readouts [346–348]. Alternatively, colony-forming assays were used to determine the LC values and an equivalent LC₃₀ was calculated (see methods 4.4.2).



Results

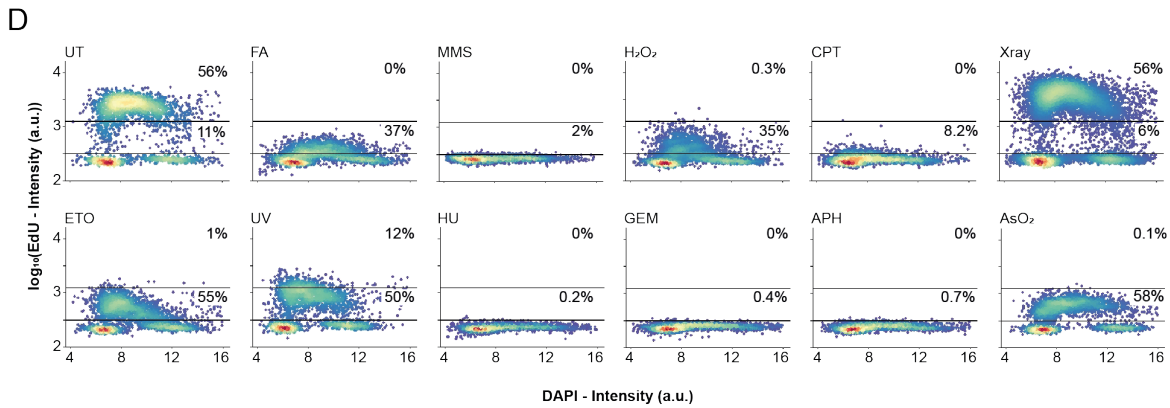


Figure 10: Determination and evaluation of treatment conditions. To determine LC₃₀ values of DNA damage-inducing agents, U2OS cells were treated for 2 hours with the indicated concentrations and left to recover for 48 hours. Cell viability was evaluated using the CellTiter-Blue viability assay. For X-ray treatment, colony-forming assays were used and an equivalent LC₃₀ was calculated (LC₃₀ colony-forming assay: 1.3 Gy; equivalent LC₃₀: 2.4 Gy). Titration curves are shown for one replicate. Reported LC₃₀ values were calculated from all replicates (n = 3-6). Error bars indicate SD (A). Western blot (B), immunofluorescence microscopy (*P-value < 0.01, **P-value < 0.001, ***P-value < 0.0001, compared to UT) (C), and cell cycle analyses (D) of U2OS cells upon treatment with the determined LC₃₀ for 2 hours (arbitrary units (a.u.)). For UV and X-ray treatments, DDR was assessed after 1 or 2 hours recovery time, respectively.

The effects of the determined doses were evaluated by Western blotting and immunofluorescence microscopy (IFM). Topoisomerase inhibitors ETO and CPT, followed by H₂O₂, elicited the strongest response for most of the tested DNA damage markers (Figure 10B-D), including the general DNA damage marker γ H2AX. Especially, checkpoint kinase CHK2 (pT68), RPA (pS4/S8), and KAP1 (pS824) phosphorylation was increased, indicating activation of the upstream kinases ATM and DNA-PK [349–352]. X-ray also induced CHK2 activation, but additionally displayed a strong increase in BRCA1 and RAD51 (Figure 10C), as well as 53BP1, marking repair by HR and NHEJ, respectively. The remaining treatments, except AsO₂, showed a clear accumulation of γ H2AX, and ssDNA markers (RPA1, RPA1 (pS33)), as well as activation of the ATR target CHK1 (pS345). AsO₂ treatment neither led to checkpoint activation nor the accumulation of γ H2AX under the experimental conditions (Figure 10B/C). Only an upregulation of BRCA1 by IFM could be observed (Figure 10C). Therefore, AsO₂ was assumed to induce a more general stress response beyond DNA damage, or at least apart from the activation of the kinases ATR and ATM. To distinguish the other treatments from AsO₂ in the chapters below, they will be referred to as “DDR conditions/treatments”.

Cell cycle progression was studied by EdU incorporation, reflective of origin firing and/or replication fork progression, and DAPI staining following damage induction. Due to the short time treatments, no major effects on the cell cycle phases or DAPI signal could be observed. However, in line with the checkpoint kinase activation, cell cycle progression was at least partially halted in most conditions, as EdU incorporation was greatly diminished (Figure 10D). Interestingly, we found marked differences in EdU incorporation among the treatments. Upon HU, APH, MMS, GEM, and CPT treatments replication was abolished completely. ETO, H₂O₂, AsO₂, and UV allowed some level of EdU incorporation, while cells displayed normal EdU incorporation upon X-ray treatment. In general, the degree of checkpoint activation was not directly correlated with the EdU signal or DNA replication. For instance, X-ray

induced strong CHK2 activation, but no effect on DNA replication could be observed. In contrast, AsO₂ displayed reduced DNA replication, but no checkpoint activation (Figure 10B/D).

2.1.2 Establishment of a reproducible and efficient workflow for multiplexed proteome and PTM analysis

Peptide multiplexing by TMT was chosen as the most appropriate technique for our screen, as it allows high sample throughput, with precise quantification, and deep coverage. To assure a high quality of mass spectrometric measurements, an efficient and robust workflow for the TMT analysis had to be established. For this purpose, our previously described SILAC workflow had to be adapted to TMT measurements and the most critical steps were optimized (Figure 11A) [353, 354].

Briefly, U2OS cells were lysed in modified RIPA buffer, and proteins were precipitated in acetone (Figure 11). Alternatively, chromatin-bound proteins were isolated beforehand, according to Mendez and Stillman, 2000 [355]. The proteins were re-solubilized in urea, digested to peptides using both LysC and trypsin, and purified using a C₁₈ RP column. The peptides originating from differentially treated cells were labeled with the TMT11-plex kit and mixed accordingly. Phosphopeptides were enriched using TiO₂ beads after sample labeling. For ubiquitination analysis by diGly remnant profiling, peptides were enriched before the labeling step, as the TMT label blocks antibody binding to the diGly remnant. In this context, it must be mentioned that proteins NEDD8 and ISG15 also results in a diGly remnant. However, the contribution of diGly sites derived from these ubiquitin-like modifications is very low (< 6%), and thus, diGly sites are also referred to as ubiquitination sites in this study [356]. To allow for downstream data normalization, a reference sample, mixed from all other samples, was included in each TMT batch. The samples were fractionated by micro SCX (strong cation exchange) chromatography and applied to an easy-nLC RP chromatography coupled to the Orbitrap Exploris mass spectrometer. Following the measurement, raw intensities were normalized and used for statistical analysis. Of these steps, protein digestion, peptide labeling, peptide fractionation, and data normalization were optimized and are described in more detail below.

The first step in all bottom-up proteomics experiments is the digestion of proteins to peptides amenable to mass spectrometric analysis. Incomplete protein digestion can lead to reduced sensitivity, accuracy, and reproducibility of the mass spectrometric measurement, as well as increased calculation times for the downstream analysis [357, 358]. As depicted in Figure 11B, our previous digestion protocol resulted in the identification of 35% and 70% of peptides and phosphopeptides with missed cleavages, respectively. While a lower cleavage efficiency of phosphopeptides is expected due to a higher prevalence of the negative charges close to the cleavage sites, for both cases higher cleavage efficiencies can be achieved [359, 360]. By increasing the protein concentration from 2 to 8 µg/µl, the enzyme to protein ratio from 1:150 to 1:75, as well as by stabilizing the pH with a buffer of higher buffering capacity (before: HEPES 2 mM, now: Tris 50 mM, pH 8), the digestion efficiency could be increased by ~2.5 fold. While higher digestion temperatures might further increase digestion efficiency, e.g. from

Results

25 °C (as used in this study) to 37 °C, raising the temperature was avoided to prevent peptide carbamylation, as this was shown to compromise peptide identification [358].

TMT labeling has many advantages for large-scale proteomics experiments, but it is quite costly. Rather than labeling peptides before PTM enrichment, TMT labeling can also be applied to the enriched peptides to save TMT reagent [361]. However, since this also means mixing the samples at a later stage, it reduces the reproducibility of the experiments. Therefore, we set out to improve the labeling efficiency. Starting with labeling conditions suggested by the manufacturer, a peptide concentration of 1 µg/µl in TEAB buffer (pH 8) was used [345]. Under these conditions, an 8-fold weight excess of TMT label to peptide had to be used to achieve near-complete peptide labeling ($\geq 97\%$, Figure 11C). The amount of TMT label could be drastically decreased by raising the peptide concentration to 5 µg/µl, as also recently reported by Zecha et al., 2019 [362]. However, only in combination with a pH of 8.5 and changing the buffering agent to HEPES, near-complete labeling, with little to no overlabeling, could be achieved, using a TMT-to-peptide ratio as low as 1:1. Additionally, ACN was added to the labeling buffer to a concentration of 30%, which greatly facilitated peptide resuspension and slightly increased peptide labeling. Under these conditions, near-complete labeling could even be achieved with a 1:2 TMT-to-peptide ratio, when the peptide concentration was raised to 10 µg/µl. In contrast, when low peptide concentrations had to be used, as was the case after diGly remnant enrichment, ratios had to be raised to 12:1 (Figure 11B).

Next, peptide fractionation was adjusted to the needs of TMT labeled peptides. In the first dimension, peptides were offline fractionated by micro SCX chromatography, followed by low pH RP chromatography on the easy-nLC system. In the case of phosphopeptide analysis, 12 fractions were collected from the SCX fractionation. To achieve deep coverage, equal distribution of the peptides between the fractions had to be assured. Therefore, total peptide intensity or the number of measured peptides per fraction were calculated, and the pH of the elution buffers was adjusted accordingly. Despite the narrow elution range of peptides at low pH, a relatively equal distribution of peptides could be achieved (Figure 11D) [363]. The percentage of peptides measured in only one fraction was about 60%, which is similar to the recently more popular high-pH reverse-phase chromatography when done in a microcolumn format [364, 365]. Similar to the SCX fractionation, the subsequent RP-gradient was adjusted to ensure equally distributed peptide elution (not shown). The elution conditions for proteome or diGly remnant analysis were optimized separately.

Lastly, after samples were measured in the Orbitrap Exploris mass spectrometer and processed by MaxQuant, the data were normalized to correct for both pipetting and measurement errors under the assumption of normal distribution. To remove the batch effects, a reference sample was included in all TMT experiments. Therefore, in the first step, each protein or peptide intensity was divided by the corresponding reference intensity, with the goal of removing the measurement differences between batches. In a second step, intensities in each sample were divided by the sample median. This so-called “median centering” corrects for sample loading errors. While this standard approach of data

normalization can perform well, it also depends on the correct preparation and measurement of the reference. Small changes to the reference sample can already alter the proteins or PTMs identified as differentially expressed [366–369]. Therefore, in the cases we found remaining batch effects, we used an additional normalization step. It was assumed that the average intensity of a protein or peptide overall 11 labels is the same for each batch [370]. In short, intensity averages for each protein or peptide were calculated per batch. Subsequently, each intensity was divided by said average, which can be referred to as internal reference or per-protein / per-peptide centering. Using this strategy, we could see a clear improvement in normalization, exemplified by clustering analysis of the diGly peptide data set (Figure 11E).

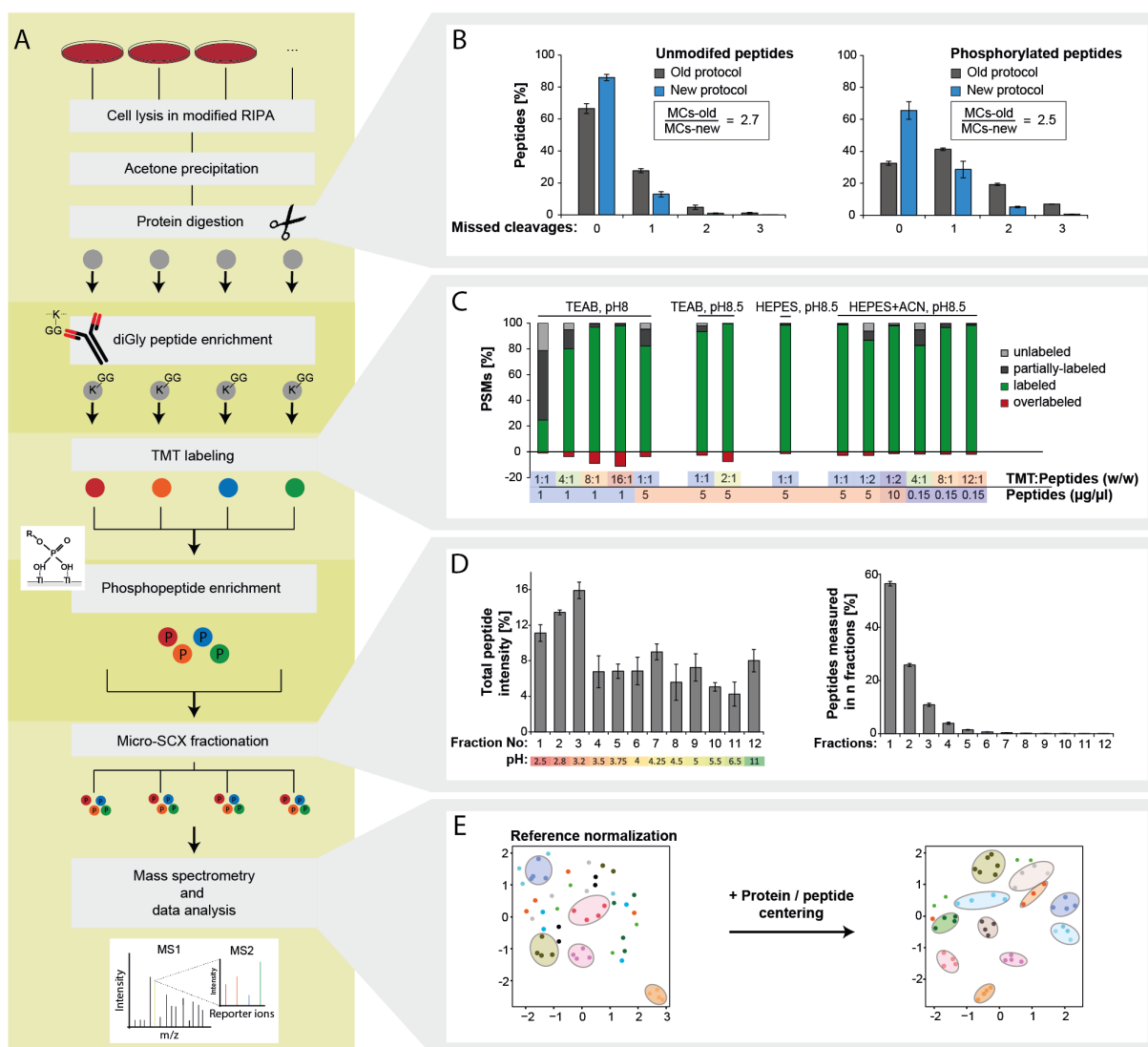


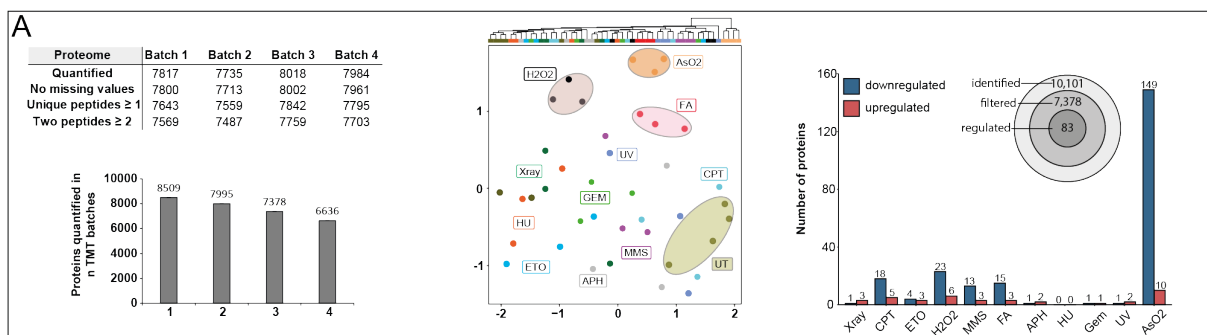
Figure 11: Establishment of an optimized TMT workflow. Cells were lysed in RIPA buffer, precipitated in acetone, and digested with both LysC and trypsin. Peptides were labeled with TMT, fractionated by SCX, and analyzed by LC-MS/MS (**light green**) (A). Alternatively, diGly remnant peptides were enriched using a specific antibody before TMT labeling, or phosphopeptides were enriched using TiO₂ beads after TMT labeling (**dark green**) (A). Protein digestion by trypsin and LysC was optimized by increasing protein concentration, enzyme to protein ratio, and by changing the buffer system (“New protocol”, n=4) (B). The amount of TMT label necessary for complete peptide labeling could be decreased by changing the buffering system, the pH, and the peptide concentration (n=1-2) (C). The pH of SCX elution buffers was adjusted to achieve equal peptide distribution among the fractions and allow higher peptide coverage. Barplots show peptide distribution (**left**) and peptide spillover into neighboring fractions (**right**, n=4) (D). Data normalization of TMT intensities was improved by internal reference or per protein/peptide centering when normalization by one reference sample alone performed poorly (n=4) (E). Error bars indicated SD.

2.1.3 Laying the foundation for a comprehensive DDR database

Using our newly established TMT workflow (Figure 11) in combination with the selected treatment conditions (Figure 10A), we carried out the DDR screen. We measured the changes in protein levels, protein phosphorylation, ubiquitination, and proteins bound to chromatin in 4 biological replicates. Since the number of treatments including the reference sample exceeded the labeling capacity (4x13 samples), the four replicates were equally distributed into 5 TMT11-plex batches. For technical reasons, one replicate of the phosphorylation and protein analysis was excluded. Figure 12 provides an overview of all screening data. Measuring depth is displayed by the number of quantified proteins and PTM peptides/sites for each replicate, and the overlaps between TMT experiments were depicted as bar plots (left). Pearson correlation, hierarchical clustering, and uniform manifold approximation (UMAP) were used to assess relations between the different treatment conditions and the reproducibility between replicates (Figure 12 middle and Appendix Figure 26). To determine significantly regulated proteins and sites, moderated *t*-test and fold-change cutoff were applied ($FDR \leq 0.05$; Fold-change $\geq 1.5x$ (PTM peptides), $1.25x$ (proteins); Figure 12 right). Venn diagrams show the number of proteins/sites that were identified in total, that were subjected to statistical testing, and that were regulated following at least one of the DDR treatments. An in-depth analysis of the datasets can be found in the chapters below.

Standing out from the analysis were samples treated with AsO₂. AsO₂ samples clustered apart from other treatments (Figure 12 middle) and displayed strong physiological changes reflected in a high number of significantly changed protein groups or PTM sites. Since these huge changes would dominate the comparisons between the different treatments (e.g. heatmap clustering analysis), the AsO₂ dataset was partially excluded from the downstream analysis.

Parts of the screening data are already available in a beta version of our **DNA Damage Response dataBase** (“**DDRBase**”) under “<https://hpc1.imb.uni-mainz.de/shiny/ddrbase/>“. The database currently features a search interface, making it possible to query for specific proteins, PTMs, and treatments in combination with user-defined cut-offs for fold-changes and FDRs. It includes all necessary details about the experimental setup, and all data can be downloaded. The database will continue to grow as a valuable resource as other screening data are added.



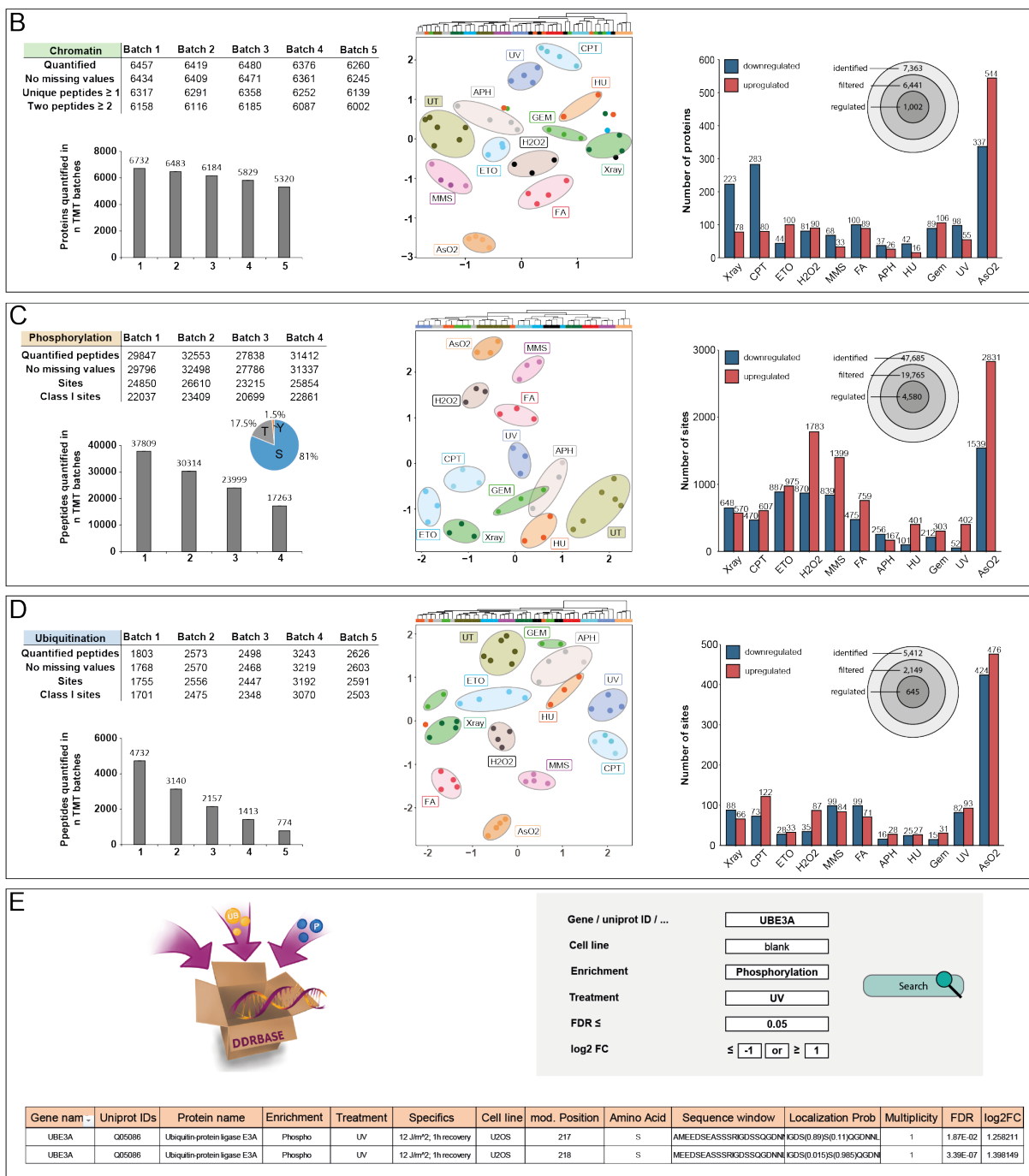


Figure 12: Overview of the DNA damage screen. Overview of quantified proteins from whole-cell lysates (A), proteins bound to chromatin (B), phospho- (C), and diGly peptides (D). Tables show the number of quantified proteins and peptides for each of the measured TMT experiments/batches before and after applying different quality filters. Protein groups were filtered for non-missing values across all labels within the TMT-11plex batch, and for a minimum of one unique and a total of two quantified peptides. PTM modified peptides were filtered for missing values. Additionally, site numbers and class I sites are reported (class I phosphorylation sites ≥ 0.75 localization probability; class I ubiquitination sites ≥ 0.9 localization probability). Bar plots display overlap of quantified proteins or peptides between the TMT experiments (A-D, left). UMAP and hierarchical cluster analysis of biological replicates (A-D, middle). The number of significantly regulated proteins or sites for each treatment is depicted in the bar plots (FDR ≤ 0.05 ; peptide fold-change ≥ 1.5 ; protein fold-change ≥ 1.25). Venn diagrams show the number of proteins/sites that were identified in total, that were subjected to statistical testing, and that were regulated in response to at least one of the DDR treatments (A-D, right). Search interface of the DNA Damage Response dataBase (“DDRBase”). The DDRBase encompasses the screening data of the presented study (E).

2.1.4 Analysis of the cellular proteome

In total, we identified 10,101 protein groups in the proteome analysis. After applying all quality filters (Figure 12A, left) 7,378 protein groups entered the statistical analysis (Figure 12A, right). As expected, protein levels remained largely unchanged following the 2-hour treatments with different DNA damaging agents (AsO₂ excluded). Few proteins changed significantly (83 proteins, Figure 13A), accounting for the relatively poor clustering of the treatment replicates (Figure 12A middle).

Network analysis of the 83 proteins using the STRING database, and GO annotation revealed that these proteins largely fall into 4 categories, namely: “nucleolus”, “extracellular matrix/Golgi”, “fatty acid biosynthetic process”, and “transcription regulation” (Figure 13B). Protein nodes outside the main network correspond to diverse cellular processes. Upregulated proteins connected in the network were involved in “transcription regulation”, with the tumor suppressor p53 as a central protein. Directly connected to p53 were the transcription factors (TFs) FOS, JUN, ATF3, EGR1, and protein RHOB. While p53 was significantly upregulated upon ETO treatment, the other TFs were mostly increased in response to H₂O₂. FOS and EGR1 also increased upon other treatments.

Most downregulated proteins were related to the “extracellular matrix”. This included proteoglycans (SDC1, SDC4), collagen (PCOLCE, COL1A1), enzymes like metalloproteinases (MMP2, MMP9; LOXL2, ADI1, MXRA8), proteins involved in cell adhesion (DSC2, GJA1) or cellular signaling (VGF, CLU, APP, SPARC, AXL). Interestingly, the downregulations were observed for chemical treatments with lesser specificity, namely H₂O₂, FA, MMS, and AsO₂. Only the desmosome component DSC2 was more consistently downregulated among treatments. The connected “Golgi” proteins were specifically decreased by H₂O₂. The proteins in the remaining two clusters were regulated by one specific treatment each. For instance, H₂O₂ displayed a pronounced effect on fatty acid metabolism. Six proteins including three fatty acid desaturases (FADS1/2/3), two stearoyl-CoA desaturases (SCD, SCD5), and the methylsterol monooxygenase (MSMO1) were reduced in their protein levels. By comparison, CPT treatment led to a strong reduction of 11 nucleolar proteins, which were simultaneously indicated in ribosome biogenesis. Importantly, we observed that CPT reduced the protein level of its direct target TOP1, which is known to be degraded within minutes of inhibition, and the SIRT1 regulator RPS19BP1, which participates in the suppression of p53 activity [371, 372].

A separate network analysis of AsO₂ regulated proteins can be found in the Appendix (Figure 27), displaying involvement of decreased proteins in “cell cycle”, “extracellular matrix organization”, “sulfur compound binding”, and “mitochondrial electron transport”.

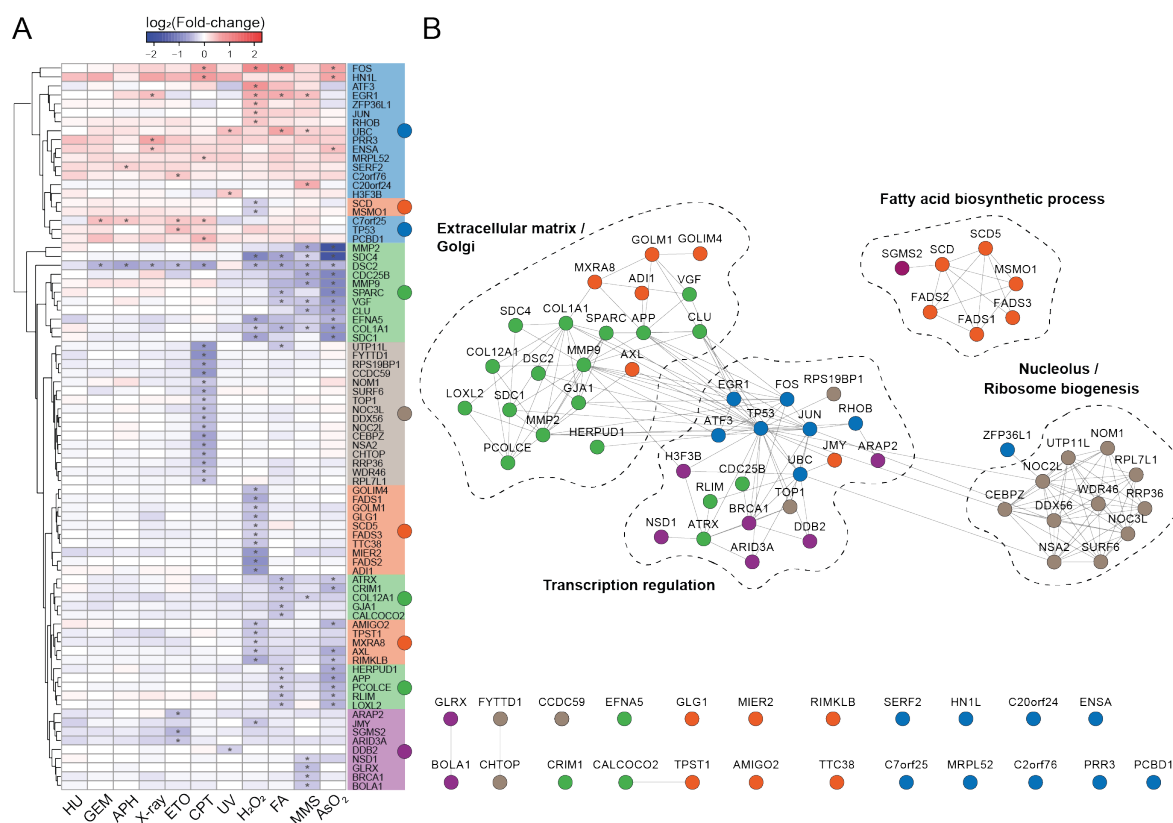


Figure 13: Heatmap and network analysis of protein groups differentially regulated upon DNA damage induction. Protein groups regulated in at least one of the DDR conditions were subjected to clustering analysis displayed in a heatmap. Related protein clusters are highlighted with the same colors. Significantly regulated protein groups are marked by an asterisk (*FDR \geq 0.05, fold-change \geq 1.25x) (A). Network analysis of the protein groups by STRING (confidence \geq 0.4). Nodes are colored according to the heatmap clusters. GO terms enriched for the network clusters are displayed. Proteins not connected to the main network are shown below (B).

2.1.5 Analysis of protein phosphorylation

Analysis of phosphorylation sites gained by unbiased approaches like TiO₂ enrichment coupled to quantitative mass spectrometry may lead to the discovery of new regulatory sites and allows the identification of differentially regulated kinase pathways. Using the established TMT workflow, we identified 47,685 phosphorylation sites (31,467 class I) within 6,678 (3,990) proteins using 100 μ g of peptide sample per condition. Importantly, 10,186 (3,282 class I = 10%) have not been previously reported in the PhosphoSitePlus database (date: 04/2021) [373]. After applying all quality filters, 23,999 phosphopeptides (19,765 sites) were subjected to statistical analysis (see methods). 4,984 peptides (4,580 sites) on 1,090 proteins were significantly regulated in at least one DDR condition (Figure 12C left, right). The number of phosphorylation sites per protein and the distribution of the residues (serine = 81%, threonine = 17.5%, tyrosine = 1.5%) were comparable to previously published data (Figure 12C left) [170]. Overall, the experiments clustered nicely according to their treatment conditions as shown by Pearson correlation, UMAP, or hierarchical clustering (Figure 12C middle, Appendix Figure 26). Roughly, HU, GEM, APH, and to some extent UV, displayed the greatest similarity. CPT, X-ray, and ETO also clustered closely to each other, as did FA, MMS, and H₂O₂. AsO₂ was most distinct from all other treatments but shared similarity with the FA, MMS, H₂O₂ cluster.

Results

To see if we can identify both known and novel responses to our treatment conditions, we studied and compared kinase activities using 3 different approaches. First, linear motif enrichment analysis was carried out using a stretch of 13-amino acids surrounding the differentially regulated phosphorylation sites. Overrepresentation of amino acids was displayed using IceLogo and enriched motifs were identified by sequence annotation in Perseus [374]. Treatments showing a similar overrepresentation of amino acids were displayed together (Figure 14A, Appendix Figure 28). While motif analysis also allows identification of binding motifs of proteins besides kinases (e.g. the 14-3-3 and WW domain motif), it cannot describe distinct kinase activities and is more informative for smaller, specific population subsets. A second, more powerful approach is the Kinase-Substrate Enrichment analysis (KSEA) which calculates Z-scores based on collective phosphorylation changes. Kinase-substrate relations are taken from the database PhosphoSitePlus or are predicted by the NetworKIN algorithm [375]. As a third strategy, PTM Signature Enrichment Analysis (PTM-SEA) was used. PTM-SEA applies single sample Gene Set Enrichment Analysis (GSEA) to the phosphorylation data, utilizing annotations from the PTMsigDB database [376]. Therefore, PTM-SEA can also be used to identify phosphorylation signatures other than kinase activation (not shown). Here, however, it was mainly used to confirm major findings from KSEA, as it lacks the kinase-substrate prediction of NetworKIN.

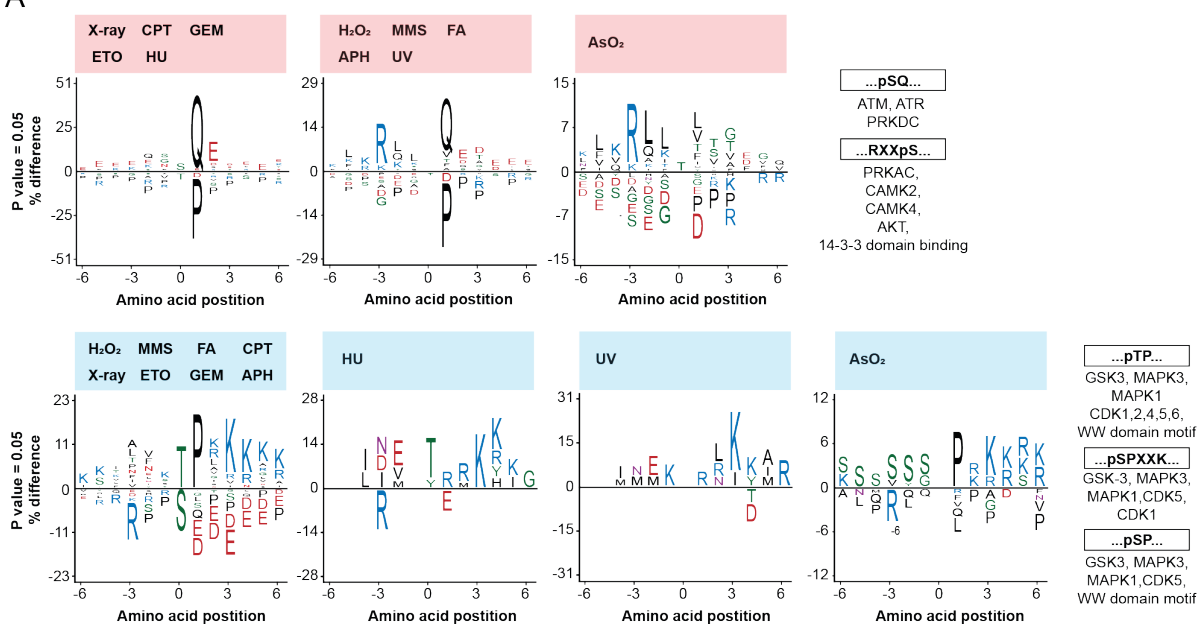
The three approaches reported different numbers of differentially regulated kinase activities: 81 by KSEA, 51 by PTM-SEA, and 15 by linear motif analysis (isoforms not distinguished), yet they agreed on the most significant changes (Figure 14A-C). 42 kinase activities were predicted by both KSEA and PTM-SEA (Figure 14D).

Kinases ATM, ATR, and DNA-PK were strongly activated upon all treatment conditions, except for AsO₂, leading to an overrepresentation of the indicative S/T-Q motif [377] (Figure 14A). KSEA and PTM-GSEA additionally reported activities of the downstream checkpoint kinases CHK1 and 2. Especially, KSEA could recapitulate the results from the Western blot analysis (Figure 10B). CHK2 activation was predicted for ETO, CPT, H₂O₂, X-ray, and FA. On the other hand, CHK1 seemed to be activated upon all treatments except for X-ray. Complementary to these findings, the strongest reduction in kinase activity was reported for the cyclin-dependent kinases CDK1 and 2 in all conditions. For most treatments, a similarly strong reduction could also be observed for the kinases CDC7, CDK6, AURKA/B, TTK, and NEK2. Interestingly, no such reduction was reported in the case of HU, UV, and AsO₂ treatment.

Beyond this, we observed that treatment conditions clustered similarly not only in UMAP and hierarchical clustering but also in all three kinase prediction analyses (Figure 12C middle, Figure 14). AsO₂, MMS, FA, H₂O₂, and to an extent UV, were predicted to activate mitogen-activated protein kinases (MAPKs). This pattern was also shared by the majority of kinases with predicted activation, including RPS6KA1/2/3, RPS6KB1/2, CAMK2B/D, AKT1, PRKCA/D, PRKD1, IKBKB, PRKACA, and RET. The only MAPK that showed consistent activation in all treatment conditions was MK2 (MAPKAPK2). Although slightly different kinase activities were reported by KSEA and PTM-SEA,

they generally agreed on this observation. In contrast, the motif analysis failed to predict MAPK activation, but rather reported its inhibition. Intriguingly, we found the complementary pattern of kinase activation for protein kinase CK2 (isoforms CSNK2A1 or CSNK2A2). CK2 activity was predicted for HU, GEM, APH, X-ray, ETO, and CPT but not for the treatments displaying pronounced MAPK activity. AsO₂ showed the most distinct kinase activity pattern. Besides the above-mentioned unresponsiveness of ATR, ATM, and DNA-PK, AsO₂ treatment uniquely displayed decreased activity of mTOR, pyruvate dehydrogenase kinases (PDK1, PDK2), and Casein kinase II subunit alpha (CSNK2A1) in both KSEA and PTM-SEA. KSEA additionally reported decreased activity of dual-specificity protein kinases (CLK2, CLK3), TBK1, PAK1/2, and CAMK2A/G.

A



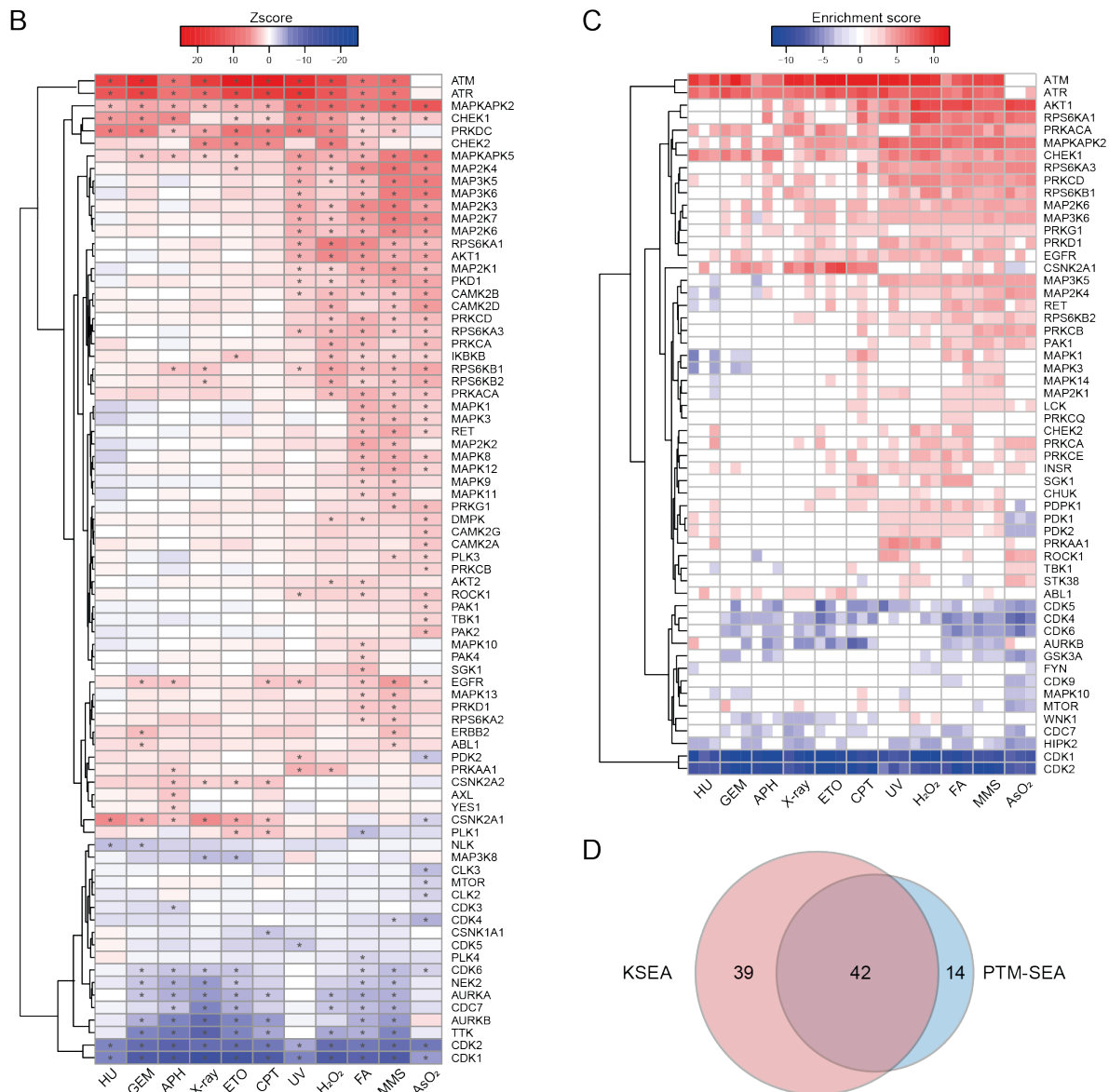


Figure 14: Phosphorylation site motif analysis and kinase prediction. Sequence motif analysis of treatment-specific phosphorylation sites by IceLogo. Sequence windows of significantly up- or downregulated phosphorylation sites were compared to all quantified phosphorylation sites. Overrepresentation of amino acids at positions relative to the phosphorylation site is displayed in percent. Treatments sharing similar motifs were analyzed together. Additionally, kinase-specific motifs were identified using sequence annotation in Perseus (A). Heatmaps displaying kinase predictions by KSEA (B) and PTM-SEA (C). For KSEA, kinases with an $FDR \leq 0.05$ are indicated with an asterisk (*). For PTM-SEA, only kinases with an $FDR \leq 0.1$ are displayed. Overlap of kinases predicted by the two methods (D).

For functional evaluation of the phosphorylation data, hierarchical cluster analysis was carried out on the phosphopeptides and displayed as a heatmap (Figure 15). Peptides solely regulated upon AsO_2 treatment were not considered, as these would have dominated the clustering due to very strong phosphorylation changes. Enrichment of GO and KEGG terms was performed for each cluster and the most significant terms were displayed. Kinase substrates predicted from KSEA were indicated for three kinase groups: MAPKs, PIKKs, and CDKs. In general, clusters consisted of either up or downregulated phosphopeptides. Only a small number of peptides showed upregulation in one, and downregulation upon another treatment condition. Overall, functional analysis agreed with the observations from the kinase prediction.

We identified several clusters with strongly upregulated peptides upon all treatment conditions, excluding AsO₂ (Figure 15, clusters #5-7). Of these peptides, 11% were annotated or predicted to be PIKKs substrates. Closer analysis showed that 65% carried the S/T-Q motif, compared to 8% for the complete heatmap, suggesting that many more peptides might be PIKK substrates. Functional analysis showed enrichment for “DNA repair” or directly related processes, like “DNA replication” and “checkpoint regulation”, highlighting the immediate regulation of these processes by PIKKs upon DNA damage. Proteins working in “chromosome organization” and “transcription by RNA polymerase II” were also enriched. Although clusters #5-7 shared the same enrichment terms, they differed in the extent of phosphorylation between the treatments. Sites in cluster #7 were relatively evenly regulated across DNA damage conditions, while sites in clusters #5 and #6 appeared to be more specific for DSB-inducing agents (ETO, CPT, H₂O₂, X-ray). In line with this, 3 out of 5 proteins in cluster #5 (CHK2, SMC1A, and SMC3) are known to have specific roles in DSB repair [378, 379]. In contrast, cluster #11 showed a complementary pattern encompassing phosphopeptides upregulated upon UV, HU, APH, and GEM treatment, which are less potent inducers of DSBs. For a more detailed look, we carried out network analysis for both, phosphopeptides that are more responsive to the DSB inducing agents (clusters #5-7; Appendix Figure 29B), and for the phosphopeptides rather upregulated upon UV, HU, APH, and GEM (cluster #11; Appendix Figure 29A). Additionally, we created a “core network” of the DDR response, which encompasses phosphopeptides differentially regulated in at least 7 out of the 10 DDR conditions. 7 was chosen as the optimal cut-off, based on enrichment analysis for the GO term “DNA repair” (Appendix Figure 29C/D). All three networks display a core of well-known DDR factors but also show tightly connected proteins that have not been identified as such. These proteins might be especially interesting for further studies. Among these, we also find many “RNA processing” and especially “RNA splicing” factors, illustrating that these processes are still understudied in the context of DNA damage.

Cluster #12 displayed upregulated phosphopeptides upon FA, MMS, H₂O₂, AsO₂, and UV treatment. This matches perfectly with the pattern observed for MAPK activation in the kinase prediction (Figure 14B/C). Accordingly, the number of predicted MAPK substrates was especially high in cluster #12, and the “MAPK cascade” was among the most enriched terms. Other enriched terms related to MAPK signaling were “Enzyme linked receptor protein signaling pathway” and “GTPase signal transduction”, containing several MAPKs, tyrosine receptor kinases, integrins, phosphatases, Rho GTPase, GAP (guanine activating protein), and GEF (guanine nucleotide exchange factor) proteins (not shown). Moreover, proteins involved in “cytoskeleton organization”, “intracellular transport”, and “focal adhesion” were increased in their phosphorylation. Interestingly, cluster #1 showed a complementary pattern to cluster #12, with downregulated phosphopeptides especially upon FA, MMS, H₂O₂, AsO₂, and UV treatment. Mainly “chromatin organization” including “histone acetylation/methylation”, “negative regulation of RNA metabolic processes”, and “negative regulation of macromolecule biosynthetic process” were enriched.

Results

The other cluster with strictly downregulated phosphopeptides, but more equally distributed among the treatments, showed a strong overlap with CDK substrates (cluster #2). These peptides corresponded to functions in “cell cycle”, “DNA replication” and “chromosome organization/separation”. We also found “DNA repair” to be enriched, highlighting that also protein dephosphorylation events are important in these processes. Lastly, the biggest cluster was enriched for proteins especially working in “RNA processing”, but also in “DNA repair”, “DNA replication”, and “damage checkpoint activation” similar to clusters #5-7. This cluster was also the most heterogeneous one when compared between the treatments, emphasizing the fact that there is no identical cellular reaction to different stimuli, but each treatment is met with an individual cellular response.

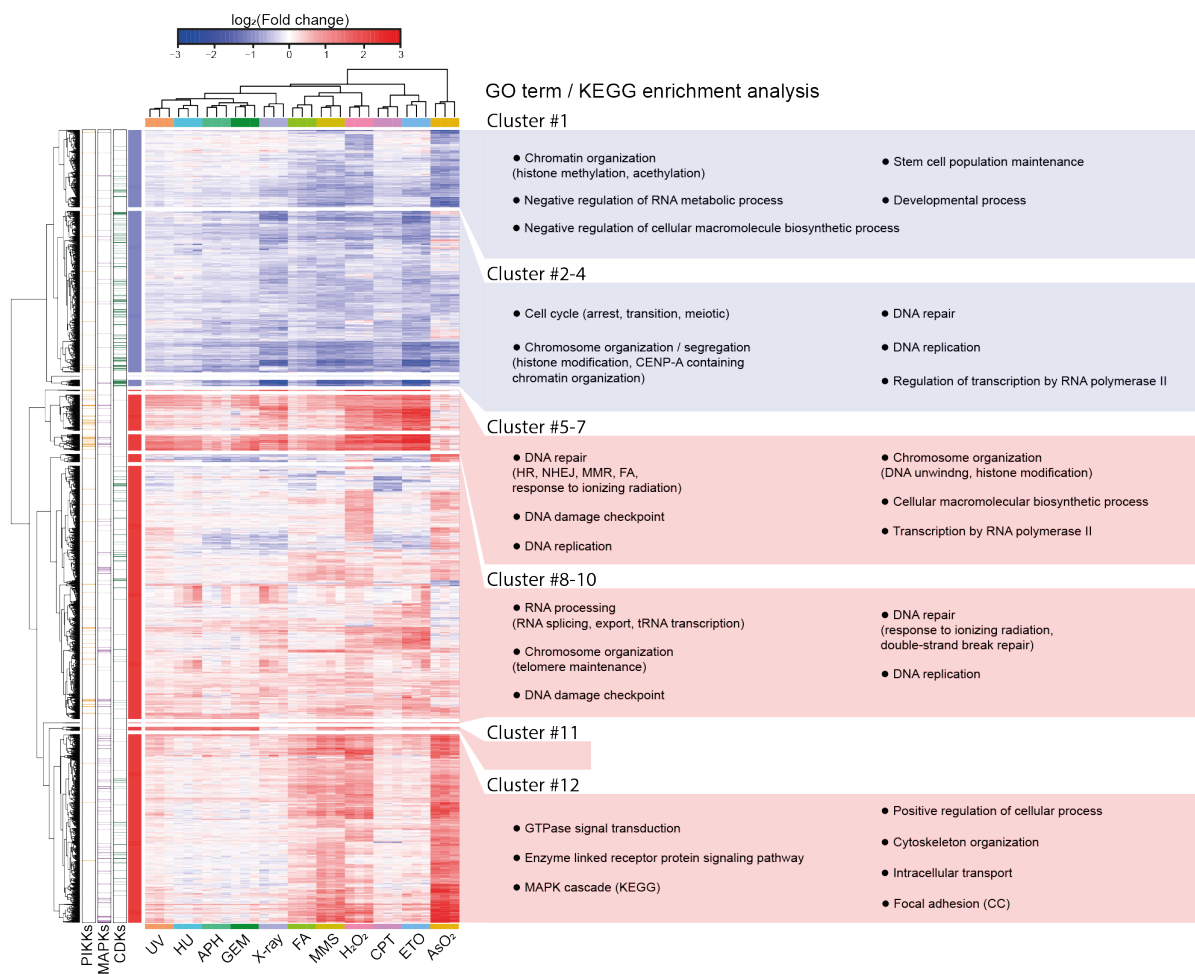


Figure 15: Hierarchical clustering analysis of phosphopeptides. Phosphopeptides regulated in at least one of the DDR conditions were analyzed by hierarchical clustering and displayed in a heatmap. For each cluster GO term and KEGG enrichment analysis were carried out and the highest scoring GO terms for the biological process (BP) are displayed (P-values < 0.001). When KEGG terms, GO terms for cellular compartment (CC), or for molecular function (MF) showed much higher enrichment, those were reported instead (indicated). When neighboring clusters shared the same terms, results were displayed together.

2.1.6 Analysis of protein ubiquitination

To study the ubiquitin landscape upon DNA damage induction, we applied the established TMT workflow as described above. Using less than 1 mg peptide sample per condition, we identified 5,412 (5,153 class I) diGly sites on 2,573 (2,494 class I) proteins. 808 (750 class I = 15%) sites have not been previously reported in the PhosphoSitePlus database (date: 04/2021). After applying all quality filters (Figure 12D left), 2,149 peptides were subjected to statistical analysis, and 652 peptides (645 sites) on 476 proteins were significantly regulated in at least one of the DDR conditions (Figure 12D right). ETO, HU, APH, and GEM led to low numbers of significant changes (~25 sites), while upon FA, UV, CPT, X-ray, and H₂O₂ ~150-200 sites were regulated. As for protein phosphorylation, AsO₂ treatment displayed very strong changes in ubiquitination with about 900 differentially regulated sites.

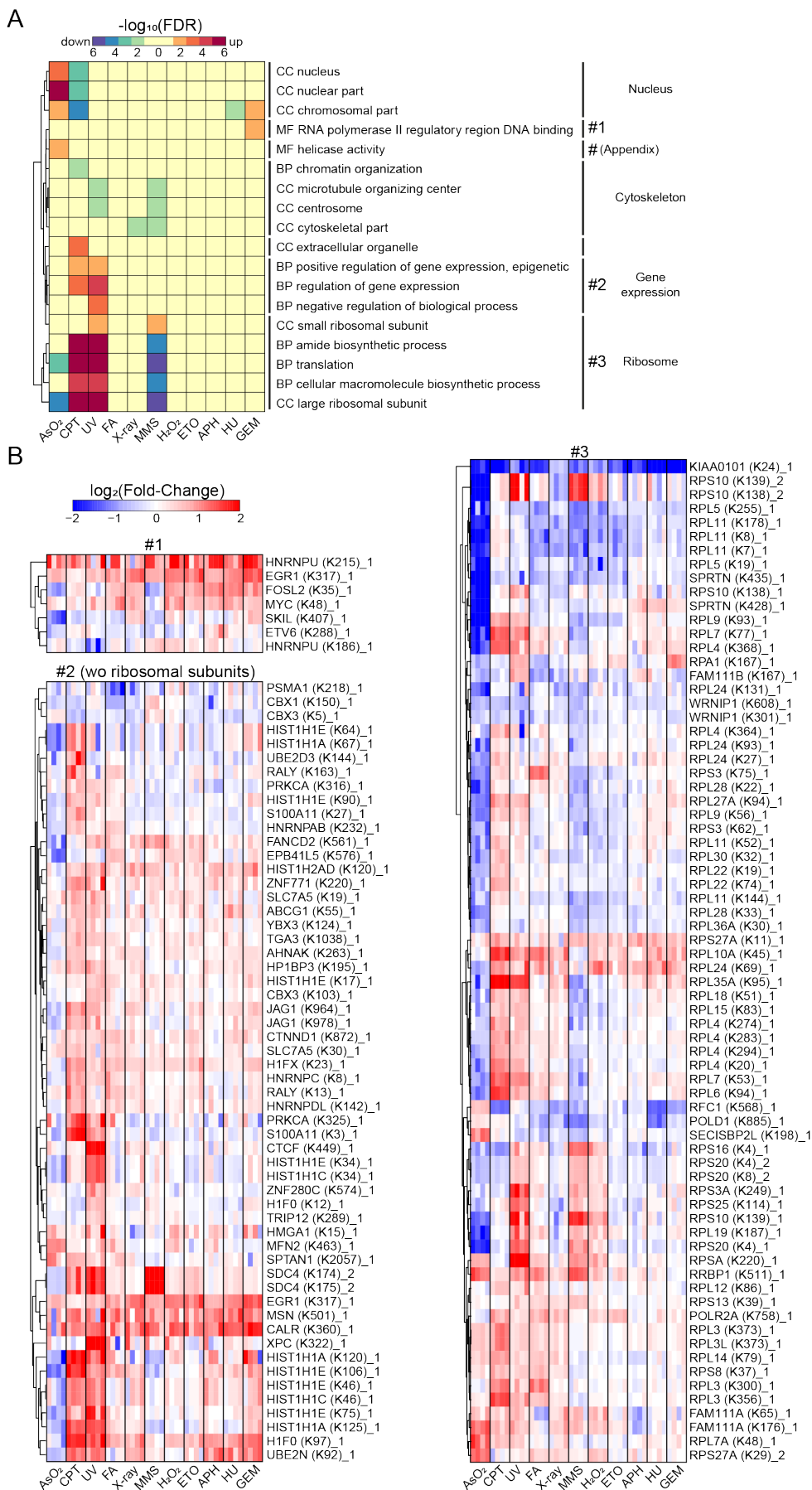
To identify significantly regulated processes, cellular compartments, or molecular functions, we carried out GO term enrichment analysis for proteins with either up- or downregulated ubiquitination sites (Figure 16A). Closely related terms corresponding to similar proteins were grouped. The analysis revealed, that proteins of the “nucleus”, the “cytoskeleton”, the “ribosome”, or proteins involved in “gene expression” were especially changed in their ubiquitination. Minor enrichment was detected for “helicase activity”, “RNA polymerase II regulatory region DNA binding”, and the “Extracellular organelle”. For a more detailed look at four of the clusters (“ribosome”, “gene expression”, “RNA polymerase II regulatory region DNA binding”, and “helicase activity”), the changes of the underlying ubiquitination sites were additionally displayed in a heatmap, and are discussed below (Figure 16B, Appendix Figure 30).

The most significant enrichment was found for proteins of the “ribosome” (Figure 16A #3). Overall, UV and CPT led to an increase in ribosome ubiquitination, while it was reduced upon AsO₂ and MMS treatments. However, closer analysis revealed that this was only true for the ubiquitination of large 60S ribosomal subunits (RPLs; Figure 16B #3). We found that both UV and MMS additionally led to strong ubiquitination of 40S ribosomal subunits (RPSs), which were rather decreased upon CPT and AsO₂ treatment. Excitingly, this included ubiquitination events on both RPS10 (K138/139) and RPS20 (K4/K8), which were reported to fulfill essential roles in ribosome-associated quality control (RQC) [380, 381]. RPL10 (K45) and RPL24A (K69) appeared to be the only ubiquitination sites increased upon all DDR treatments, except for MMS. Altogether, our data gives an overview of ribosomal ubiquitination, which might help to further elucidate the role of ubiquitination in RQC, especially in the context of the DDR. Beyond the ribosome, proteins corresponding to “gene expression” (Figure 16A/B #2) were ubiquitinated upon UV and CPT treatment. These included phosphatase PRKCA, calcium-binding protein S100A11, and many RNA-binding proteins (YBX3, HNRPNC, RALY). Yet, the most striking difference to other treatments was the increased ubiquitination of the linker histones HIST1H1A, C, and E. In contrast, histones H1F0, H1FX, and HIST1H2AD were also ubiquitinated in other conditions, suggesting treatment-specific histone ubiquitination. “RNA polymerase II regulatory region DNA binding” was enriched upon GEM treatment (Figure 16A #1). A closer look showed that

Results

the underlying proteins included several TFs (EGR1, FOSL2, MYC, SKIL, ETV6) and the RNA processing protein (HNRNU), which also increased upon other DDR treatments. Of note, the increase in ubiquitination could still be observed when normalized to the protein levels, even for EGR1 for which increased protein levels were detected beforehand (Figure 13). Lastly, “helicase activity” was specifically enriched upon AsO₂ treatment. This was due to strong ubiquitination of the MCM complex (MCM2-5, 7), which was not observed for any of the DDR conditions (Appendix Figure 30).

While the enrichment analysis identified overrepresented processes or compartments, it fails to reveal protein clusters that are not previously annotated under the same term. Therefore, hierarchical clustering can be used as an unbiased approach to look for prominent patterns (Figure 16C). Below, we describe three prominent clusters picked from the resulting heatmap. Cluster 1 (Figure 16C #1) showed proteins specifically ubiquitinated upon MMS. These included anti-oxidant enzymes peroxiredoxin PRDX1, 2, and 6, which work in the clearance of ROS (Figure 16C) [382, 383]. Proteins ADNP and ADNP2 have also been implicated in the protection against ROS, thus suggesting oxidative stress upon MMS treatment [384–387]. Curiously, we did not see a similar cellular response to H₂O₂. Additionally, E3 ubiquitin ligases TRIM56 and RNF114 displayed increased ubiquitination upon MMS. Cluster 2 (Figure 16C #2) was the only ETO-specific cluster we could identify. Fittingly, these included the etoposide targets topoisomerases TOP2A and B, and the E3 SUMO-protein ligase ZNF451, which licenses the reversal of the DNA-TOP2 crosslink (Figure 16C). While the role of TOP2 ubiquitination in the repair process has been described as necessary for crosslink removal, a possible role for ZNF451 ubiquitination remains to be investigated [388, 389]. Lastly, cluster 3 showed strong regulation of several ubiquitination sites on the polyadenosine RNA-binding protein ZC3H14 (Figure 16C #3). Decreased ubiquitination was especially observed upon UV, X-ray, and MMS treatments, while H₂O₂ led to increased ubiquitination. ZC3H14 has recently been reported to be phosphorylated by ATM and to regulate pathway choice of double-strand break repair in favor of NHEJ [390]. However, ubiquitination of ZC4H14 has not been described yet and might represent another regulatory mechanism for this protein.



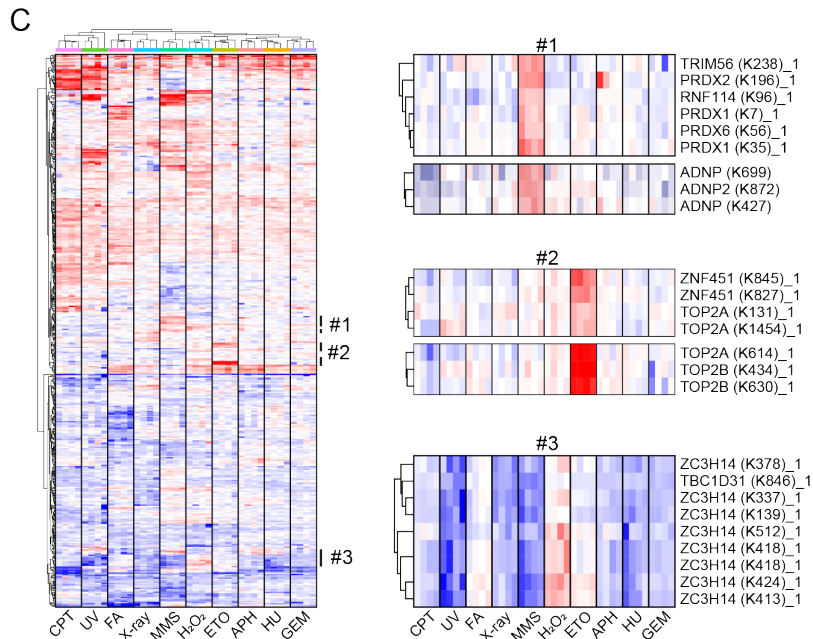


Figure 16: GO term enrichment and hierarchical clustering analysis of the diGly peptides. Proteins with either significantly up- or downregulated diGly peptides were subjected to GO term enrichment analysis ($FDR \leq 0.01$). FDR values of enriched terms are represented in the heatmap and closely related GO terms were grouped. Colors indicate if terms are based on up- or downregulated peptides (A). \log_2 fold-changes of diGly peptides corresponding to marked GO terms are displayed as heatmaps (B). DiGly peptides regulated in at least one of the DDR conditions were analyzed by hierarchical clustering and displayed in a heatmap. Three selected clusters are shown in detail. Clusters #1 and #2 each refers to two closely related clusters (C). For each peptide, the corresponding gene name, PTM localization, and multiplicity of the modification are indicated.

2.1.7 Analysis of the chromatin proteome

Chromatin fractions were isolated according to Mendez and Stillman, to quantify the removal from or recruitment to chromatin by mass spectrometry [355]. Using this protocol, chromatin-bound proteins, such as histones, could be strongly enriched, while other proteins, such as vinculin, were depleted. However, trace amounts of the non-chromatin bound proteins were also detected in the chromatin fractions (Figure 17A). Therefore, we expected to also measure proteins from other cellular compartments, albeit with lower intensities. As to not miss any interesting effects, we did not filter out such “contaminants”. In total, we identified 7,363 proteins from the isolated chromatin fractions (Figure 12A right). About 60% of these were annotated as nuclear proteins. 6,441 proteins were measured in at least two replicates, and for each of these proteins at least one unique and two matching peptides were quantified. Statistical analysis implicated about 1000 regulated proteins in at least one of the DDR conditions.

Similar to the ubiquitin analysis, we first sought to identify overrepresented signatures among the differentially regulated proteins. Therefore, we carried out Ensemble of Gene Set Enrichment Analyses (EGSEA), which integrates 12 prominent gene set testing algorithms to obtain biologically relevant results [391]. The significantly enriched GO and KEGG signatures were further grouped based on hierarchical clustering and named according to the most prominent feature (Figure 17B). Overall, significant changes were observed for the following signatures: “DNA replication”, “Ribosome

biogenesis”, “the Chaperonin complex”, “Transcription factors”, “the Proteasome”, “Tubulin”, “Protein localization”, “the Ribosome”, and “NER”.

Very strong enrichment was indicated for “DNA replication” (Figure 17B #1) upon all DDR treatments. Closer inspection of the underlying proteins revealed strong recruitment of the heterotrimer RPA (RPA1, 2, and 3) upon ETO, CPT, H₂O₂, GEM, MMS, and UV, but less so upon X-ray, FA, HU, and APH treatment. This corresponded with our observations from IFM analyses (Figure 10C), proving that our chromatin screen can provide biologically meaningful data. In contrast to RPA, proteins involved in DNA replication initiation, including the Pol α -DNA primase complex (PRIM1, PRIM2, POLA1, POLA2), a core component of the replicative helicase complex CMG (GINS4), the MCM helicase complex (MCM2-7), and especially the sliding clamp PCNA were removed from chromatin in most DDR conditions. Removal of the MCM complex was especially pronounced upon X-ray treatment. To a much lesser extent, this was also observed for the POL δ (POLD1, 2, 3) and the RNaseH2 complex (RNASEH2A, B, C). Together, this removal of the replication machinery reflects the previously observed cell cycle inhibition (Figure 10D). Surprisingly, AsO₂ seemed to lead to the recruitment of PCNA and the POL δ .

The indicated effect on “Ribosome biogenesis” (Figure 17C #2) was observed in response to CPT. A total of 28 proteins displayed strong dissociation from chromatin. Three of which (WDR46, NSA2, and UTP11L) were also among the proteins with decreased total protein levels (Figure 13). Together it further highlights the effect of CPT on the nucleolus. In contrast, ribosome subunits showed decreased chromatin association upon MMS, FA, X-ray, and AsO₂ treatments (#7).

Removal of the “TRiC chaperonin complex” from chromatin was observed upon most DDR treatments, with the exception of FA, MMS, and H₂O₂ (#3). As a chaperone complex, TRiC is involved in the folding and stabilization of proteins and is mainly located in the cytoplasm. However, it has recently been demonstrated that TRiC mediates HDAC1/2 complex assembly in the nucleus of mammalian cells [392]. Our data thus raise the interesting possibility that the TRiC complex also fulfills roles in the DNA damage response.

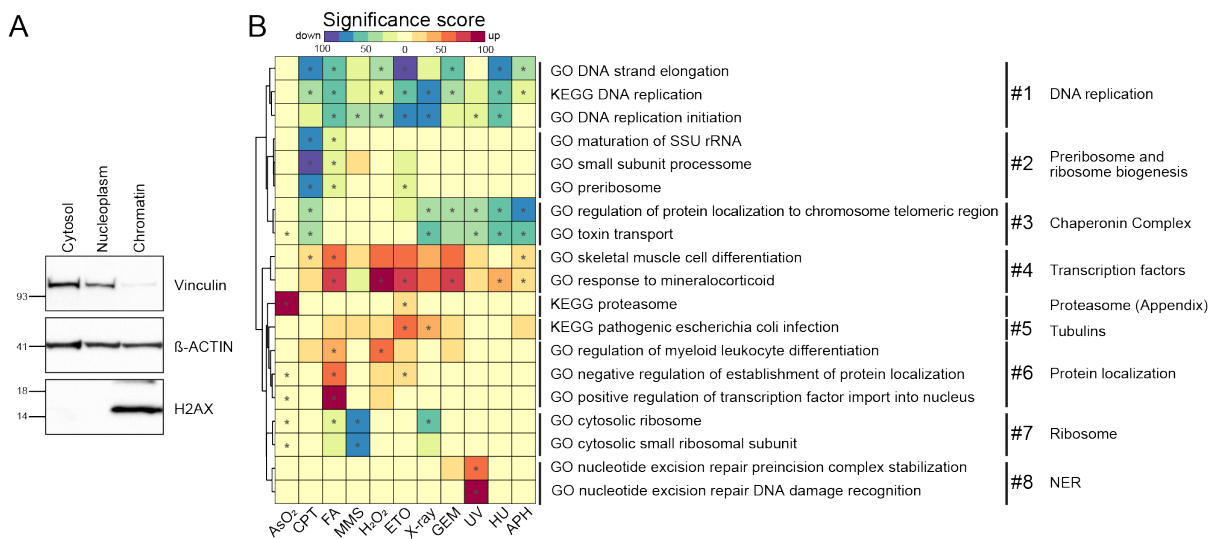
Among the signatures that showed protein recruitment upon all DDR treatments were “transcription factors” (#4). These included: MAFF, RB1, JUNB, FOSL1, FOS, and EGR1. The strongest increase was observed for the latter two, which had also displayed increased protein levels beforehand (Figure 13). Interestingly, we also found recruitment of the protein kinase SRC, for which nuclear functions have recently been described in both transcription and DDR [393, 394]. The remaining two clusters with generally increased chromatin association included “Tubulins” (#5) upon all treatments, except for CPT, and proteins involved in “Protein localization”, which were especially increased upon FA treatment (#6).

Proteins in cluster 8 (#8) were recruited to chromatin upon UV irradiation (Figure 17D). Fittingly, these proteins showed strong enrichment for the NER pathway, which is the main pathway for the removal of

Results

UV-induced lesions. Among these proteins were core components of the NER machinery including XPG (ERCC5), XPF (ERCC4), and ERCC1. Also, the E3 ligase CUL4A, which plays a role in lesion recognition in NER, and the COP9 signalosome which controls CLRs activity during this process, were recruited. All of these factors are additionally known to be involved in other repair pathways [395, 396]. However, our data suggest predominant recruitment to chromatin upon UV treatment, as we could not observe this effect for any other condition. Lastly, AsO₂ treatment led to a strong association of the “Proteasome” with chromatin. All 30 proteasome subunits were among the most significantly changing proteins in the entire chromatin dataset (Appendix Figure 31).

As for the ubiquitination data, we also carried out hierarchical clustering and selected 3 prominent clusters from the resulting heatmap for closer analysis. Cluster 1 contained proteins exclusively increased upon H₂O₂ treatment (Figure 17D #1). Curiously, except for the phosphatase SACM1L, all others (HSP9, CHCHD2, PRDX3, PMPCB, AARS) are annotated as mitochondrial proteins. Cluster 2 displayed the decreased chromatin association of 5 different phosphatidylinositol phosphate kinases (PIPKs; PIP4K2A/B/C, PIP5K1A/2A) upon CPT and UV treatment (#2). These kinases catalyze the phosphorylation of phosphatidylinositol to phosphoinositides, which function in cell signaling and membrane trafficking. PIPKs, or more precisely the specific phosphoinositides, also have various functions in the nucleus, regulating protein interactions and activity. They have been shown to be crucial for ATR recruitment to damage sites, to regulate p53 activity, or to be regulated themselves in a p38 dependent manner [397–400]. Therefore, it is tempting to speculate that the observed removal of the observed kinases from chromatin might either serve a purpose in the DNA damage response or is a reaction to cellular stress. Finally, the third cluster (#3) included the transcription elongation (P-TEFb) complex (CDK9, CCNT1, CCNT2), including its endogenous inhibitor HEXIM. Recruitment was observed upon CPT, FA, and UV treatment. As P-TEFb recruitment to promoters is usually associated with transcription elongation, it suggests similar transcription regulation upon the named treatments [401].



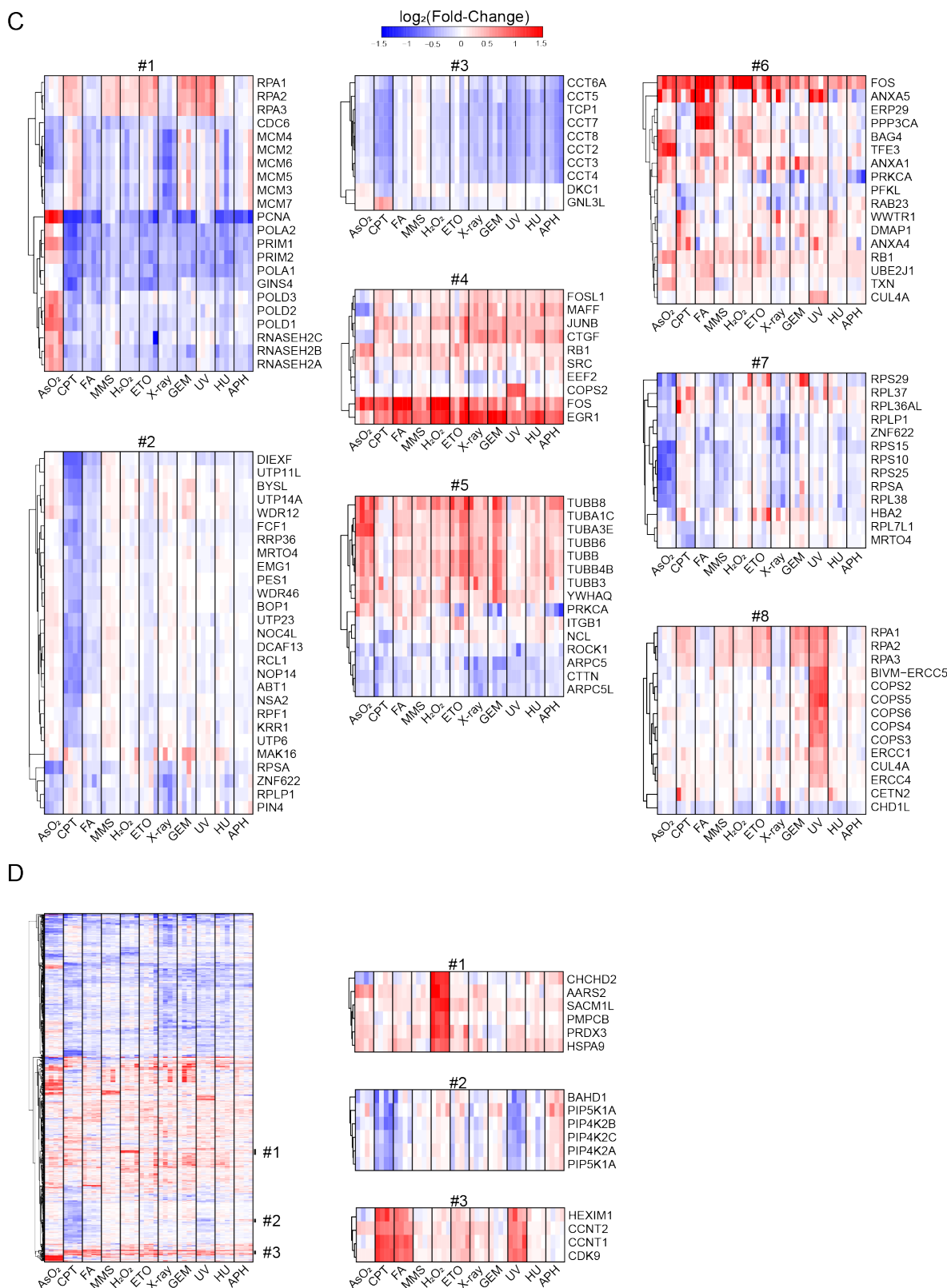


Figure 17: Analysis of chromatin-associated proteins. Cell fractionation was carried out according to Mendez and Stillman [355]. Cytosolic, nucleoplasmic, and chromatin fractions were analyzed by Western blotting (A). EGSEA analysis of chromatin-associated proteins. Significance scores of enriched GO and KEGG terms for different treatments are represented in a heatmap. Closely related terms were grouped. Significance scores with an FDR ≤ 0.001 are indicated by an asterisk (*). Only terms with a significance score of ≥ 50 in at least one of the treatments were included (B). Log₂ fold-changes of proteins corresponding to the marked GO terms are displayed as heatmaps (C). Proteins regulated in at least one of the DDR conditions were analyzed by hierarchical clustering and displayed in a heatmap. Three selected clusters are shown in detail (D).

2.1.8 Integration of screening data

Different DNA damage-inducing agents trigger a different DDR including changes in protein localization, posttranslational modification, protein-protein interaction, and the expression or degradation of proteins. While studying each of these changes in isolation can already provide significant insight into the DDR, it fails to encompass it in its entirety. Multiomics approaches try to close this gap by studying a process from different angles and by integrating the resulting datasets. This also applies to our DDR screen, as we do find significant overlaps between our datasets (Figure 18A).

To illustrate this point, we combined information from the phosphorylation, the ubiquitination, and the chromatin datasets upon UV treatment (Figure 18B). In total, 34 regulated proteins were shared among the datasets. Ten of the regulated chromatin proteins were also regulated in the phosphorylation, and 6 in the ubiquitination dataset. Eighteen proteins were both changed in their phosphorylation and ubiquitination. For easy visualization of this data, we carried out network analysis for the regulated chromatin proteins. Proteins clusters were marked according to enriched GO terms and the presence of differentially regulated phosphorylation and ubiquitination sites on these proteins were highlighted. We found that the chromatin dataset alone already recapitulated major parts of the known response to UV light (Figure 18C) [395]. Core factors of the NER repair machinery, parts of the cullin-RING E3 ligase complex together with the COP9 signalosome, replication fork stabilizing proteins, as well as several TFs showed increased association with chromatin (red nodes). In contrast, proteins involved in DNA replication, RNA processing, and RNA polymerase II transcription were rather removed (blue nodes). However, only by combining the chromatin with the PTM data, we can potentially provide molecular mechanisms underlying the observed changes in their localization, and/or known function. Well-known examples in the presented dataset include protein removal mediated by phosphorylation of EXO1 (fork stabilization, pS714), NELFE (RNA POLII elongation, e.g. pS49), and CHEK1 (full activation, pS317), or ubiquitin-mediated recruitment and/or activation of FANCD2 (K561) and RPA (Fork stabilization/restart; K167) [353, 402–406]. Additionally, by including proteins, changed both in their phosphorylation and ubiquitination, the network could be further expanded with proteins XPC, RAP80 (UIMC1), NUP153, DTL, ORC1, MATR3, or ZC3H11A [390, 407–412]. All of which, are either known repair factors or have reported roles in the DDR response. In the case of XPC, both ubiquitination and phosphorylation (pS892) regulate the recruitment and the subsequent function in DNA repair [413, 414]. Since the functional ubiquitination sites of XPC are still unknown, the sites identified in our dataset might close this gap (K330, K322). Additionally, it will be exciting to see if the PTMs we identified on other proteins like MATR3, ZC3H11A, or UIMC1 play a role in the UV-induced DDR.

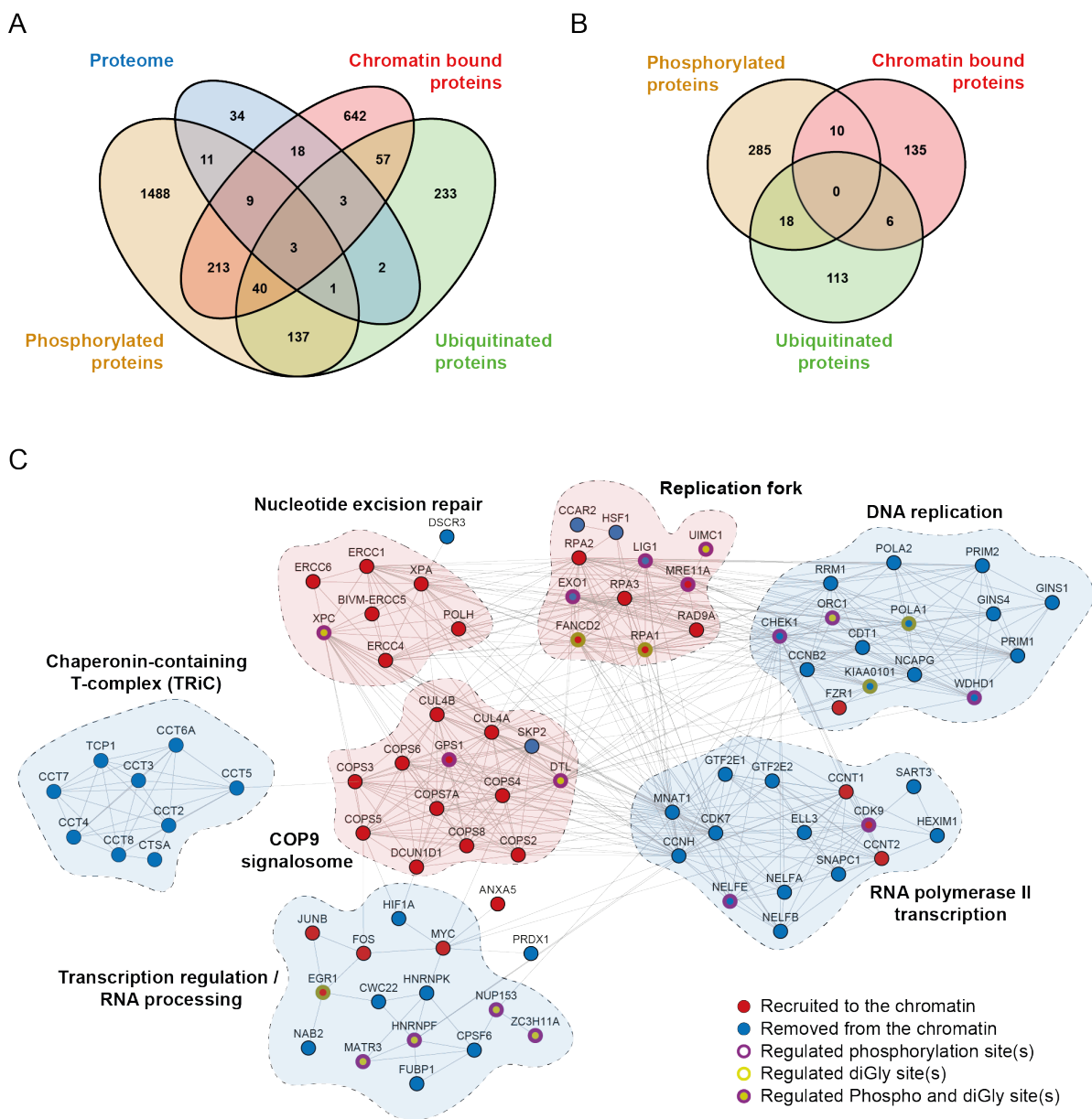


Figure 18: Integration of UV datasets. Overlap of proteins with differentially regulated protein levels, chromatin binding, phosphorylation, or ubiquitination upon any of the DDR treatments (**A**) or upon UV irradiation (**B**). Network of proteins recruited to (red) or removed from chromatin (blue) upon UV irradiation, and proteins with both regulated ubiquitination (yellow) and phosphorylation (violet). Clusters corresponding to certain protein complexes or biological processes are indicated. Proteins not connected to the main network are not shown (**C**).

2.2 UBE3A - a new player in the DNA damage response

2.2.1 Proteasome subunits and associated proteins are differentially phosphorylated upon treatment with DNA damage-inducing agents

Mounting evidence shows that the proteasome plays an integral role in the DDR response [241–249, 415]. For this reason, we decided to investigate proteasome subunits and associated proteins further.

Consulting our screening data, we found that proteasome subunits were primarily regulated in their phosphorylation. In total, 40 phosphorylation sites on 15 proteins were differentially regulated in at least one of the DNA damage-inducing conditions (Figure 19A). The vast majority of sites (37) were strictly increased and located to proteins of the 19S regulatory particle of the proteasome. Among these were four ubiquitin ligases HUWE1, RNF181, UBE3A, and UBR4, which were reported to associate with the proteasome and potentially regulate its activity [416]. We also identified two sites with known function. Phosphorylation of PSMD11 on S14 is carried out by kinase PKA and leads to increased levels of doubly-capped proteasomes, thus stimulating overall protein degradation rates [417]. On the contrary, T273 on PSMD1 is phosphorylated by p38 and leads to inhibition of proteasome activity [418]. Thus, no clear tendency towards activation or inhibition of the proteasome could be concluded.

Proteins UBE3A, the proteasome receptor RPN10 (PSMD4), and the Valosin-containing protein (VCP) showed increased phosphorylation on S/T-Q sites upon most treatments, suggesting a general response to DNA damage and modification by kinases ATM and ATR. Importantly, UBE3A and VCP were not phosphorylated upon AsO₂ treatment, which exhibited limited ATM and ATR activation (Figure 13). To add further confidence to the biological relevance of these sites, we additionally assigned functional scores to the phosphorylation sites based on the prediction from Ochoa et al. [419] (Figure 19B). Sites on UBE3A and VCP scored higher than 0.51 which is among the top 8% of all sites in the prediction. In comparison, the second non-S/T-Q phosphorylation site on S217 of UBE3A only reached a score of 0.19 (64%). Lastly, UBE3A also scored in the recently published KO screen from Olivieri et al., as a potential factor in the DNA damage response (Figure 18B) [414]. While both UBE3A and VCP represented interesting candidates for future research, UBE3A was selected for further investigation. Phosphorylation of VCP on S3, which was specifically observed upon treatment with either ETO or CPT, is being investigated for its role in topoisomerase extraction from chromatin in an ongoing study (Minneker, Heidelberg, Gothe, Piccinno; unpublished).

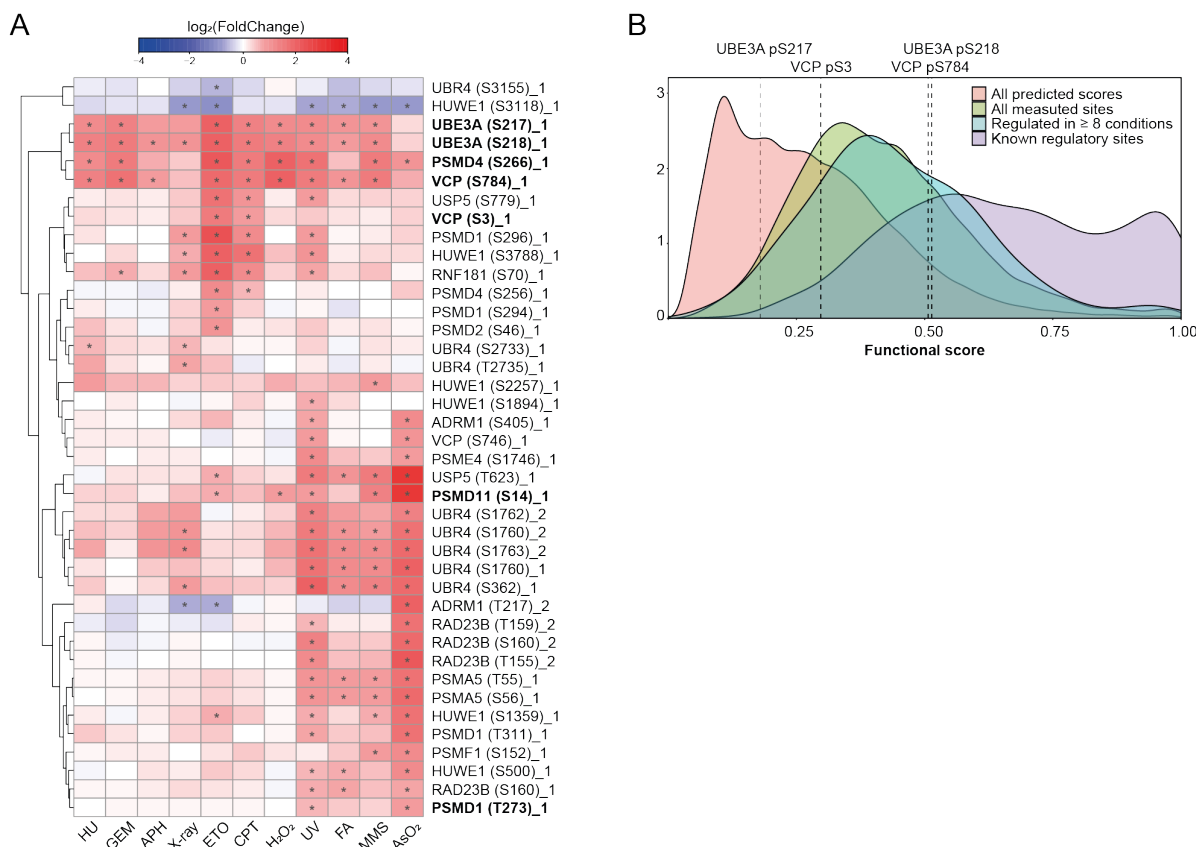


Figure 19: Regulated phosphopeptides on proteasome subunits and proteasome-associated proteins. For each peptide, the corresponding gene name, PTM localization, and multiplicity of the modification are indicated. Proteins/sites discussed in more detail above are highlighted (A). Density plot displaying functional scores of phosphorylation sites calculated by Ochao et al. [419]. Score distribution is shown for: All predicted sites, all measured sites in this study, all sites that were differentially regulated in at least 8 of the 11 conditions, and all measured sites that have a functional annotation in the PhosphoSitePlus database (B).

2.2.2 UBE3A is phosphorylated in an ATM/ATR-dependent manner

The two regulated phosphorylation sites on UBE3A (S217 and S218) were located next to each other, in the HERC2-binding domain (Figure 20A). We found that especially the S/T-Q motif was conserved in mammals, while this was less the case for the preceding S217 (Figure 20B). UBE3A phosphorylation on serine 218 was initially confirmed by consulting alternative mass spectrometry datasets, other than the TMT-based screen (Figure 20C/D). Inspection of the MS1 spectrogram of a SILAC experiment clearly showed the gradual increase of the S218 phosphorylation upon treatment with HU for 4 or 18 hours (Figure 20C). Interestingly, we could only confirm the increase of S218, but not the S217 phosphorylation (Figure 20D). Thus, we excluded S217 from further analysis. Further validation of the UBE3A phosphorylation on S218 was carried out by Western blotting using a pS/T-QG specific antibody. Indeed, gradual phosphorylation after both HU and ETO treatment, as well as the dependence of the phosphorylation on kinases ATR and ATM were observed (Figure 20D/E). Importantly, the pS/T-QG signal was lost upon UBE3A KD or mutation of serine 218 to alanine, showing that the antibody indeed specifically recognized phosphorylation on S218 (Figure 20E).

Results

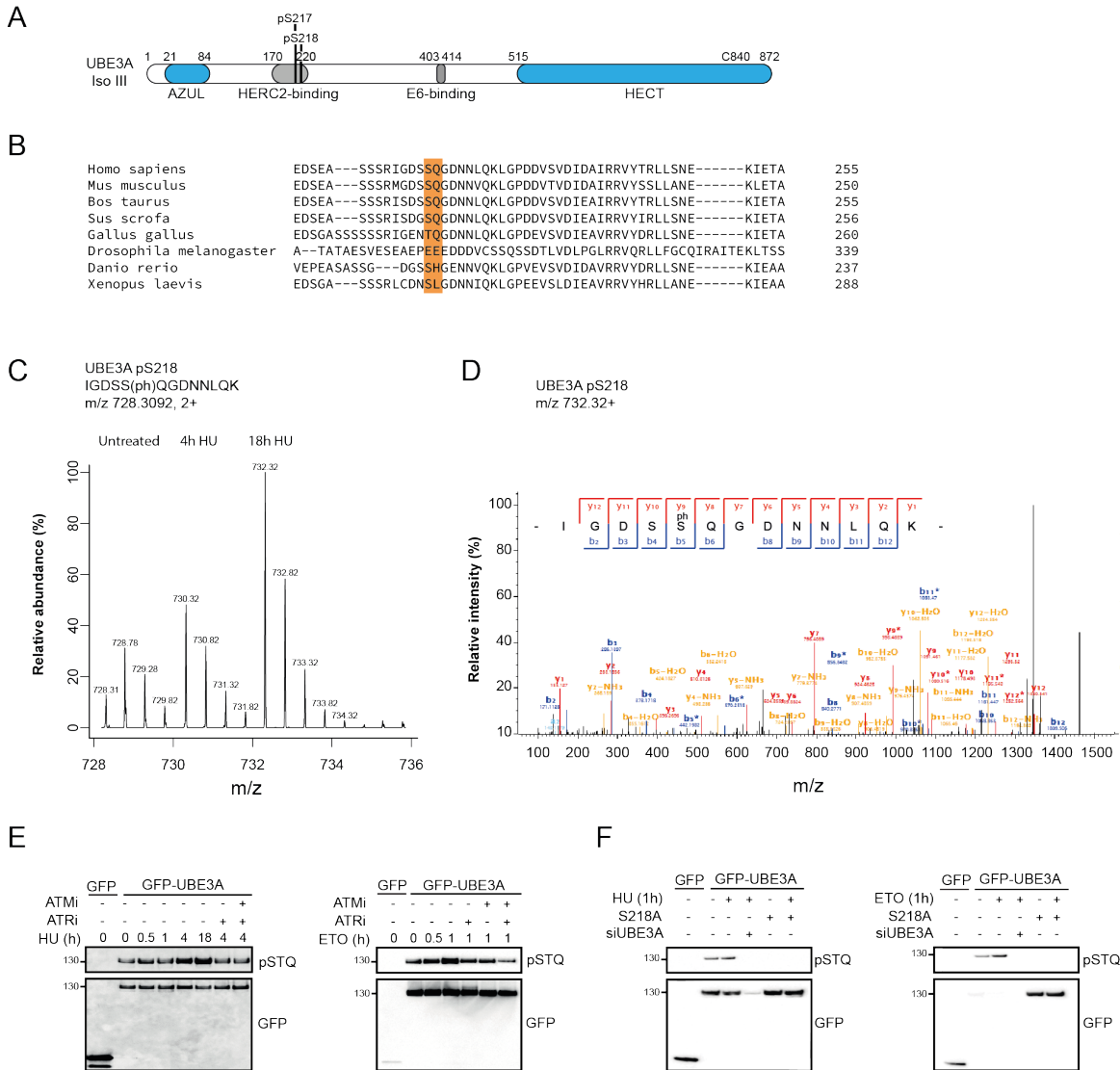


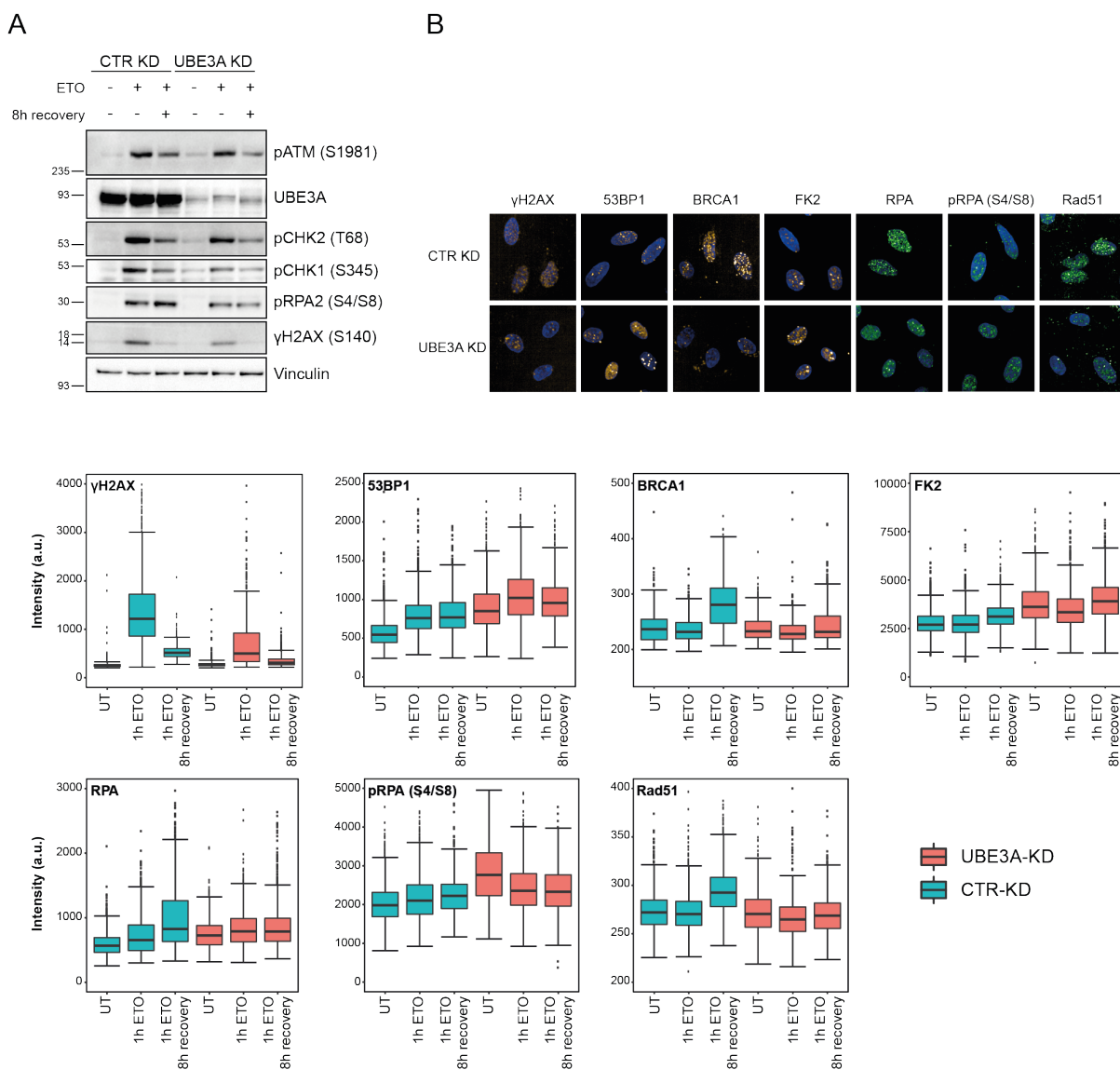
Figure 20: UBE3A is phosphorylated by ATR and ATM. Domains and regulated phosphorylation sites of UBE3A (A). Multiple sequence alignment of UBE3A from different species using Clustal Omega. The S/T-Q motif on position 218/219 (human isoform 2) is highlighted in orange (B). SILAC mass parent ion scan of the peptide IGDSSQGDNNLQK corresponding to S218 in UBE3A. The SILAC triplet showed the relative abundance and m/z of the phosphorylated peptide in mock-treated cells and cells treated with 4 hours and 18 hours HU (C). Mass spectrometric fragment ion scan of the peptide corresponding to phosphorylated serine 218 in UBE3A (D). The UBE3A S/T-Q phosphorylation site was validated after HU (2 mM) and ETO (10 μ M) treatment by Western blotting. Phosphorylation of S218 depended on the activity of the kinases ATM and ATR (E-F).

2.2.3 Depletion of UBE3A leads to genome instability and reduces DSB repair by homologous recombination

Before investigating the role of the UBE3A phosphorylation site, we first sought to confirm the potential function of UBE3A in the DNA damage response. Therefore, UBE3A was depleted using single siRNAs or an siRNA pool (Figure 21A). As all siRNAs showed similar effects for UBE3A KD, presented experiments were carried out using siRNA-I, unless otherwise indicated (Appendix Figure 33). Western blot analysis revealed an overall decrease in DNA damage signaling upon ETO treatment. Phosphorylation of the general DNA damage marker H2AX, checkpoint kinases CHK1 and 2, and the upstream kinase ATM was strongly reduced (Figure 21A). Analysis of DNA repair foci by immunofluorescence and high content microscopy confirmed this finding (Figure 21B). Beyond a

decrease in γ H2AX, we observed that UBE3A depletion reduced the signals for BRCA1 and the ssDNA binding proteins RPA and RAD51. This suggests an effect on HR repair, since BRCA1, RPA, and RAD51 fulfill important roles in this pathway. In contrast, the signal of the NHEJ promoting protein 53BP1 was increased. DSB repair reporter assays verified that UBE3A KD ablated HR repair response, without significantly affecting NHEJ (Figure 21C). This was still the case after correcting the HR efficiency for the partial G0/G1 arrest we observed upon UBE3A depletion (Figure 21C/D).

Notably, we did observe decreased cell viability upon UBE3A KD (not shown). Also, RPA, pS4/S8, 53BP1, and nuclear ubiquitin signal (FK2 antibody) were already increased even without DNA damage induction by ETO (Figure 21E). Supported by the results of the comet assay, which showed increased DNA fragmentation before and after ETO treatment, UBE3A depletion alone already leads to increased genomic instability, and cell death in U2OS cells.



Results

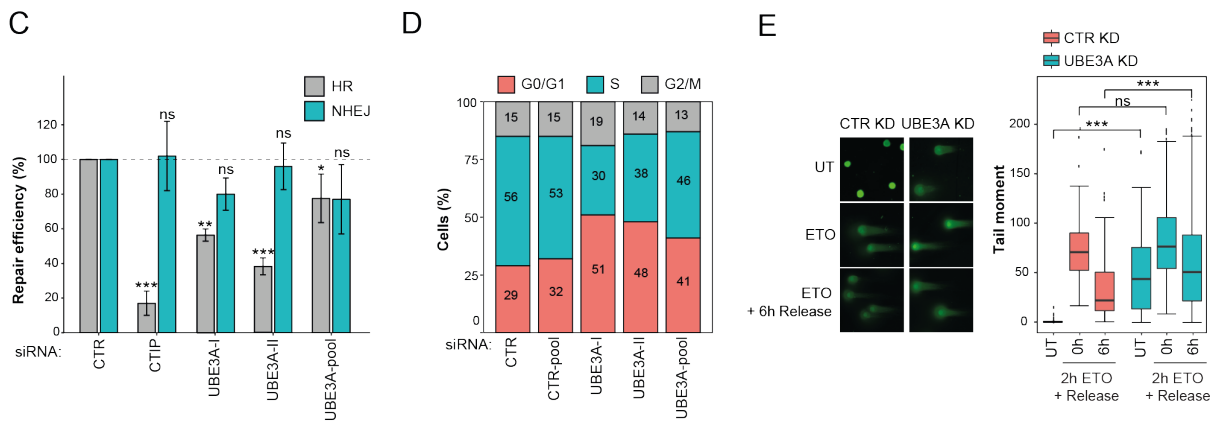


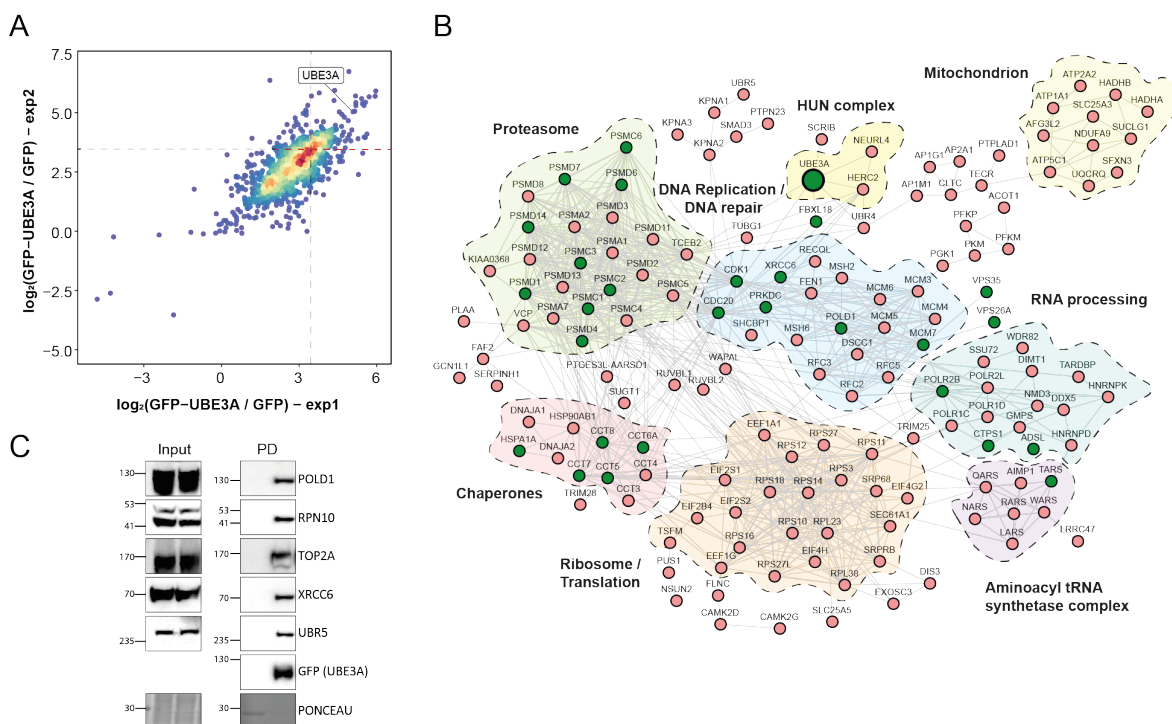
Figure 21: Depletion of UBE3A affects DNA damage signaling, DNA repair, cell cycle progression, and genome stability. In all assays, UBE3A depletion was achieved by siRNA knock-down (KD) in U2OS cells. If not indicated otherwise UBE3A siRNA-I was used. Western blot analysis after CTR (control) / UBE3A KD and ETO treatment (10 μ M) (A). IFM analyses of typical repair factors upon ETO treatment (10 μ M) (B). DSB repair efficiency was evaluated using the traffic light reporter assay [420]. HR was normalized to the fraction of cells in S/G2 phase (n=3) (C). Cell cycle analysis upon CTR and UBE3A KD was carried out after 72 hours by EdU incorporation and Hoechst staining (D). DSBs were measured by neutral comet assay (E). (*P-value < 0.02, **P-value < 0.001, ***P-value < 0.0001)

2.2.4 Proteasome subunits, and proteins involved in DNA replication and the DDR are putative UBE3A substrates

To learn more about the physiological role of UBE3A and its potential role in the DDR, we pulled-down GFP-tagged UBE3A to identify its interaction partners by SILAC-based quantitative MS. Network analysis of the interactors revealed a strong association of UBE3A with “proteasome” subunits, the “mitochondria”, the “ribosome”, and other parts of the translation machinery, including members of the “aminoacyl tRNA synthetase complex”. We also identified proteins HERC2 and NEURL4, which were recently reported to interact with UBE3A in the “HUN” complex (Figure 22A/B; [421]). Additionally, we found a strong connection to “DNA replication”, as the entire MCM complex (MCM 3-7), members of the replication factor C complex (RFC2, RFC3 RFC5), and the replicative polymerase catalytic subunit POLD1 were enriched. Together with the repair factors MSH2, MSH6, RECQL, FEN1, and XRCC6, UBE3A also displayed a clear connection to “DNA repair”. Of these proteins, we confirmed POLD1, RPN10, TOP2A, UBR5, and XRCC6 as interactors by Western blotting (Figure 22C). Overall, our data showed good agreement with a recently published large-scale effort to map and predict the UBE3A interactome by Martínez-Noël et al. (Appendix Figure 34B; [421]). Except for the mitochondrion, the same compartments and biological processes were associated with UBE3A.

As a complementary approach, we further employed ubiquitin remnant profiling in combination with proteome analysis to identify putative UBE3A substrates. We assumed substrates are less ubiquitinated after UBE3A depletion and/or potentially stabilized in their protein levels if UBE3A ubiquitination regulates their stability (Figure 22D-F). Most striking was the effect on proteasome subunits. Virtually, all the 22 detected proteasome subunits, including directly associated proteins (UBQLN1, TXNL1, UBLCP1, POMP, RAD23A) were significantly less ubiquitinated. In contrast, proteome analysis revealed negligible effects on their protein levels, indicating proteasome ubiquitination as a regulatory mechanism, rather than a signal for protein turnover. Importantly, all of these proteasome subunits localize to the 19S regulatory particle of the proteasome rather than the 20S catalytic subunit. We also

found many proteins involved in the DNA repair response to be less ubiquitinated, including several well-known repair factors (RPA, FANCI, DNA-PK, etc.; Figure 22F, Appendix Figure 34C). Interestingly, ubiquitination is known as a major regulatory mechanism for some of them [388, 403, 406, 422]. Other repair factors displayed decreased protein levels, in part explaining the effect on ubiquitination (e.g. TIM/TIMELESS, TOP2A, ERCC1, MDC1). In these cases, the observed changes might be explained by transcriptional regulation or indirect effects caused by UBE3A KD (cell cycle effects, etc.). Combination of the interactome and the ubiquitination datasets displayed a significant overlap, encompassing potential UBE3A substrates. Proteasome subunits were the biggest groups, followed by members of the TRiC chaperonin complex (CCT5, CCT6A, CCT7, CCT8) and proteins involved in DNA replication and repair (MCM7, PRKDC, POLD1, XRCC6, CDC20, CDK1). None of these proteins displayed a simultaneous upregulation of their protein levels. However, we noticed an increase of cell cycle inhibitory proteins such as p21 (CDKN1A) and a decrease in cell cycle promoting factors such as CDK2 and CCNB1, reflecting the effect on the cell cycle we observed beforehand (Figure 21D). In an independent second proteome analysis upon targeting of UBE3A with an siRNA pool, we also measured increased levels of the cell cycle inhibitory factor and reported UBE3A substrate p27 (CDKN1B; Figure 34A).



Results

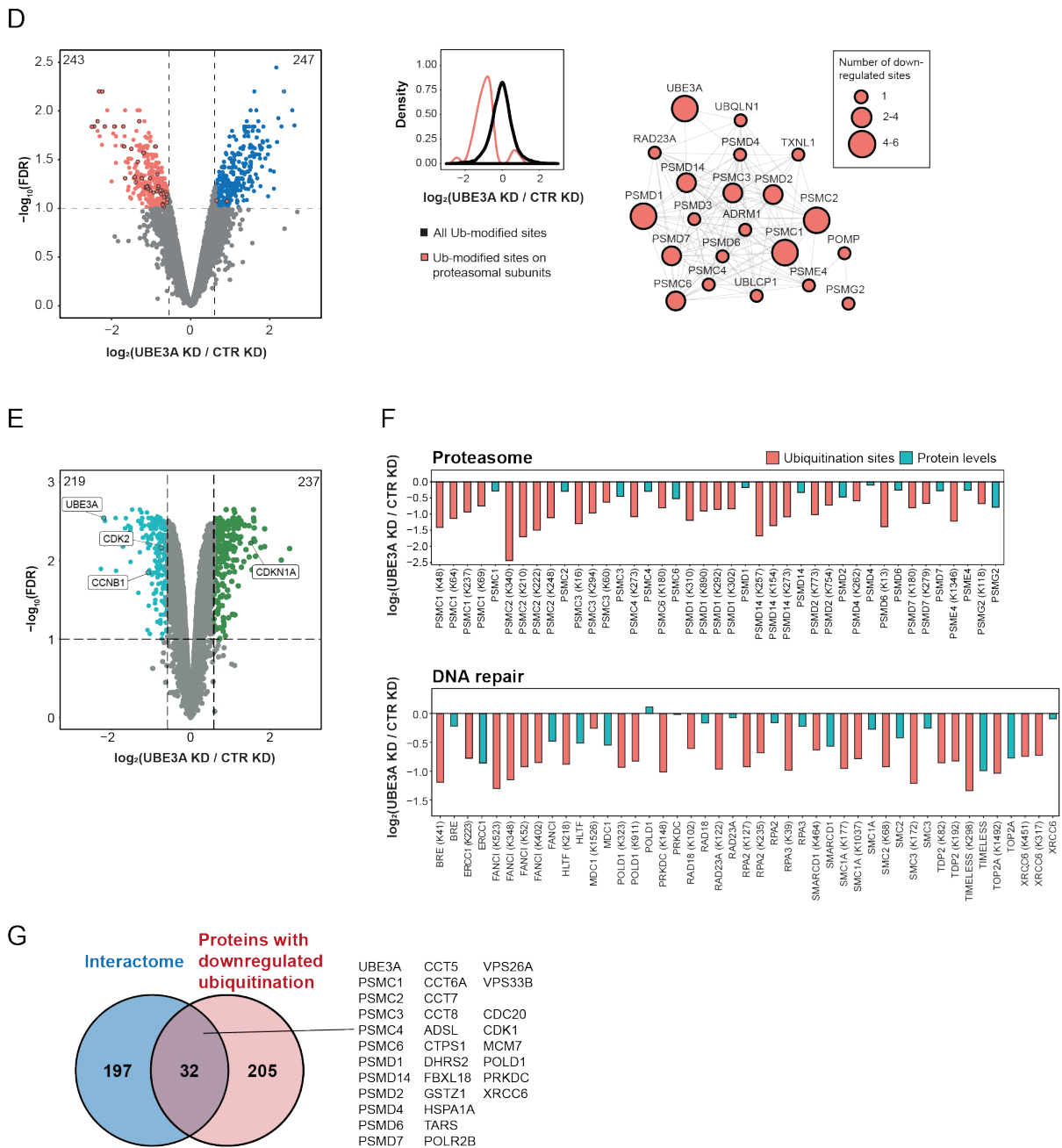


Figure 22: Identification of UBE3A interactors and substrates. SILAC labeled U2OS cells expressing GFP-UBE3A or GFP were used for interactome analysis (Ratio ≥ 11 (\pm top 10%)) (A). Interactors were analyzed using STRING database and visualized with Cytoscape (confidence ≥ 0.8). Clusters corresponding to certain protein complexes or biological processes are indicated. Proteins with decreased ubiquitination upon UBE3A KD are highlighted in green. Proteins not connected to the main network are not displayed (B). The interaction of several proteins was also confirmed by Western blotting (C). Ubiquitination after UBE3A KD was analyzed in SILAC labeled U2OS cells by diGly peptide enrichment coupled with MS (FDR ≤ 0.1 , 1.5x change, n=4). The volcano plot depicts significantly down- and upregulated ubiquitination sites after UBE3A KD. The density plot shows the shift in differentially regulated ubiquitination of proteasome subunits in comparison to all measured sites. These subunits are further depicted in a STRING network (D). Volcano plot depicts significantly down- and upregulated proteins of the same experiments (E). Proteins with decreased ubiquitination include proteasome subunits and DNA repair proteins. Both, changes in ubiquitination and protein levels are depicted in the bar plots (F). Overlap of UBE3A interactors with proteins displaying reduced ubiquitination upon UBE3A depletion (G).

2.2.5 POLD1 is a substrate of UBE3A

As we were studying UBE3A in the context of DNA repair, we were especially interested if UBE3A can target proteins for degradation upon DNA damage. We reasoned that the protein levels and/or ubiquitination of such proteins decreases upon DNA damage induction, but can be reversed in combination with proteasome inhibition. Additionally, UBE3A depletion should decrease ubiquitination and potentially rescue the protein levels of target proteins. To identify such proteins, we performed diGly remnant enrichment and proteome analysis upon replication stress induced by HU, with and without simultaneously blocking proteasomal degradation. The combination of these datasets allowed the identification of proteins that were ubiquitinated and targeted for proteasome degradation upon replication stress (Figure 23A/B). The only protein fulfilling these conditions was protein POLD1. Importantly, POLD1 was also among the high potential UBE3A substrates, which displayed both UBE3A interaction and reduced ubiquitination upon UBE3A KD (Figure 22G).

To confirm these results, POLD1 ubiquitination in response to HU was verified by isolating ubiquitinated proteins and Western blotting. Indeed, ubiquitinated POLD1 was pulled-down upon DNA damage induction and proteasome inhibition. Increased ubiquitination was not only observed for HU but also MMS treatment. However, other treatments could not reproduce this effect (APH, ETO, CPT, GEM, UV, H₂O₂, CIS, X-ray; Figure 23C). Inhibition of ATR neither significantly alleviated nor increased POLD1 ubiquitination (Figure 23F). Additionally, direct interaction of POLD1 with UBE3A was confirmed by recombinant expression of both proteins and *in vitro* pull-down experiments (Figure 23D). Using these recombinant proteins, we could further demonstrate the *in vitro* ubiquitination of POLD1 by UBE3A (Figure 23E). *In vivo*, UBE3A seemed to play a similar role, as UBE3A depletion abrogated polyubiquitination upon HU treatment (Figure 23F).

Since HU leads to replication fork stalling and reduced POLD1 levels could only be observed upon long-term treatments (Figure 23B, Appendix Figure 35A/B), we concluded that ubiquitination and subsequent degradation of POLD1 must be restricted to the fraction acting on the replication fork. This fraction was purified by isolation of Proteins On Nascent DNA (iPOND) [423]. Recruitment of pRPA (S4/S8) and removal of PCNA from stalled replication forks were used as controls. In untreated cells, POLD1 displayed a strong signal on nascent DNA, which was significantly less upon HU treatment and further decreased over time (Figure 23G; Appendix Figure 35B). A similar effect was also observed for the polymerase POLE1. In UBE3A depleted cells, POLD1 levels were lower compared to the CTR KD. This was expected since we observed a reduction in proliferating cells beforehand (Figure 21D, Figure 33). However, depletion of UBE3A could not prevent the removal of POLD1 from nascent DNA (Figure 23G). Localization of UBE3A to nascent DNA could not be tested due to technical issues.

Results

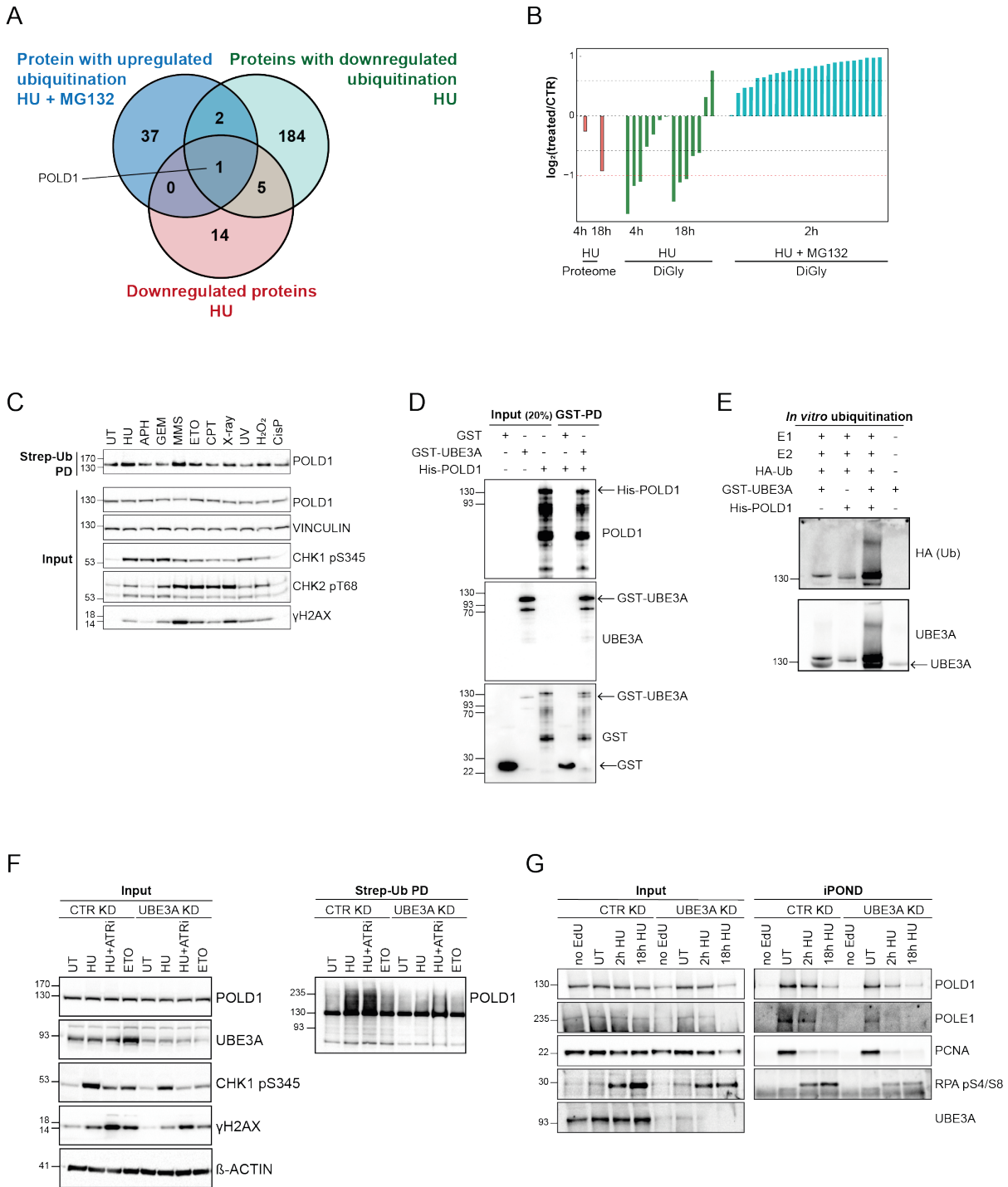


Figure 23: POLD1 is a UBE3A substrate and targeted for degradation upon HU treatment. U2OS cells were treated with HU (2 mM, 18 hours) or simultaneously with HU and MG132 (2 mM, 2 hours; 10 μ M MG132), and the changes in diGly remnant peptides and protein levels were measured by mass spectrometry. The Venn diagram depicts the overlap of proteins with significantly downregulated protein levels, diGly sites upon HU treatment (blue), and upregulated diGly sites upon both HU and MG132 (FDR \leq 0.1; 1.5x change, n=3) (A). Measured changes in POLD1 ubiquitination or protein levels are depicted in the barplot. Additionally, changes upon UBE3A KD are shown (B). Ubiquitinated proteins were isolated by strep pull-downs from a cell line stably expressing strep-ubiquitin (Strep-Ub). Western blot analysis showed increased POLD1 ubiquitination upon HU (2 mM) and MMS (0.02%) treatment for 2 hours. APH (10 μ M), GEM (10 μ M), ETO (10 μ M), CPT (10 μ M), Xray (10 Gy), UV (40 J/m²), H₂O₂ (500 μ M), and CisP (10 μ M) did not show an effect upon treatments for 2 hours (C). Recombinantly expressed His-POLD1 and GST-UBE3A showed direct interaction in an *in vitro* pull-down (D). The recombinant proteins were used in an *in vitro* ubiquitination assay by adding UBE1 (E1), UBE2D1 (E2), ubiquitin, and ATP. In the complete mix, POLD1 displayed increased ubiquitination (E). Protein ubiquitination was studied as described in (C). UBE3A KD abolished POLD1 ubiquitination upon HU treatment (F). iPOND upon EdU incorporation for 10 min followed by HU treatment for the indicated times. POLD1 was removed from nascent DNA upon HU treatment. UBE3A KD did not rescue this effect (G).

2.2.6 UBE3A localization and activity is regulated in response to DNA damage

We had chosen UBE3A for closer study because of its S-Q phosphorylation as a general response to DNA damage. Therefore, we investigated the functional relevance of this phosphorylation event.

Carrying out colony-forming assays, we found that cells were sensitized to HU or ETO treatment upon UBE3A depletion, corroborating our previous findings (Figure 24A, Figure 21). Using a doxycycline-inducible cell line, this effect could be rescued by restoring UBE3A expression with the exogenous wild-type (WT) UBE3A (UBE3A-GFP). Overexpression of UBE3A, especially when paired with the CTR KD, even displayed increased cell proliferation. In contrast, the expression of an S218A phosphomutant construct of UBE3A could not rescue the effect, indicating the functional importance of the S218 phosphorylation site in the DNA damage response. The re-expression of the UBE3A WT and phosphomutant was confirmed by Western blotting (Figure 24A).

To figure out the role of UBE3A phosphorylation, we examined its impact on protein localization, interaction, and activity. Protein localization of endogenous UBE3A was assessed by IFM. In line with previous reports about other cell types, UBE3A localized predominantly to the nucleus (Figure 24B, Appendix Figure 36A/B). Interestingly, UBE3A translocated further from the cytoplasm into the nucleus upon treatment with various DNA damage-inducing agents. This was abolished upon ATR inhibition. Accordingly, UBE3A translocation was not observed upon AsO₂ treatment either. Using the above-mentioned doxycycline-inducible cell lines, we could also show that the translocation was dependent on DNA damage-induced phosphorylation of UBE3A on S218. (Figure 24C).

Therefore, we also expected to see changes in the interaction landscape of UBE3A upon DNA damage-induction. As previously described, GFP-UBE3A was transiently expressed in U2OS cells, pulled-down and interacting proteins were analyzed by MS. Surprisingly, we found minimal changes in the interactome (Figure 24D). The few proteins that displayed decreased interaction upon ETO were not identified as interaction partners beforehand (Figure 22A/B) and were therefore regarded as contamination. In line with this observation, the interactome analysis using the S218A mutant also showed negligible changes (not shown). Of note, for the rescue and localization experiment UBE3A with a C-terminal GFP tag was used. However, we did not confirm the same behavior of the N-terminally tagged UBE3A construct that was used for the interaction analysis. Therefore, it is possible that changes in the interactome were masked by the N-terminal GFP-tag.

Lastly, we sought to examine whether S218A phosphorylation modulates UBE3A E3 ligase activity, using autoubiquitination as a proxy. Pull-down of ubiquitinated proteins followed by Western blotting revealed decreased ubiquitination of UBE3A upon both ETO and HU treatment (Figure 24E). Alternatively, we over-expressed and isolated GFP-tagged UBE3A from untreated and treated U2OS cells, and used the proteins for *in vitro* ubiquitination assays. As before, UBE3A displayed reduced ubiquitination upon both treatment conditions (Figure 24F). Together, these results imply decreased

Results

auto-ubiquitination activity of UBE3A upon DNA damage induction. Whether the activity change is due to the phosphorylation on S218 remains to be shown.

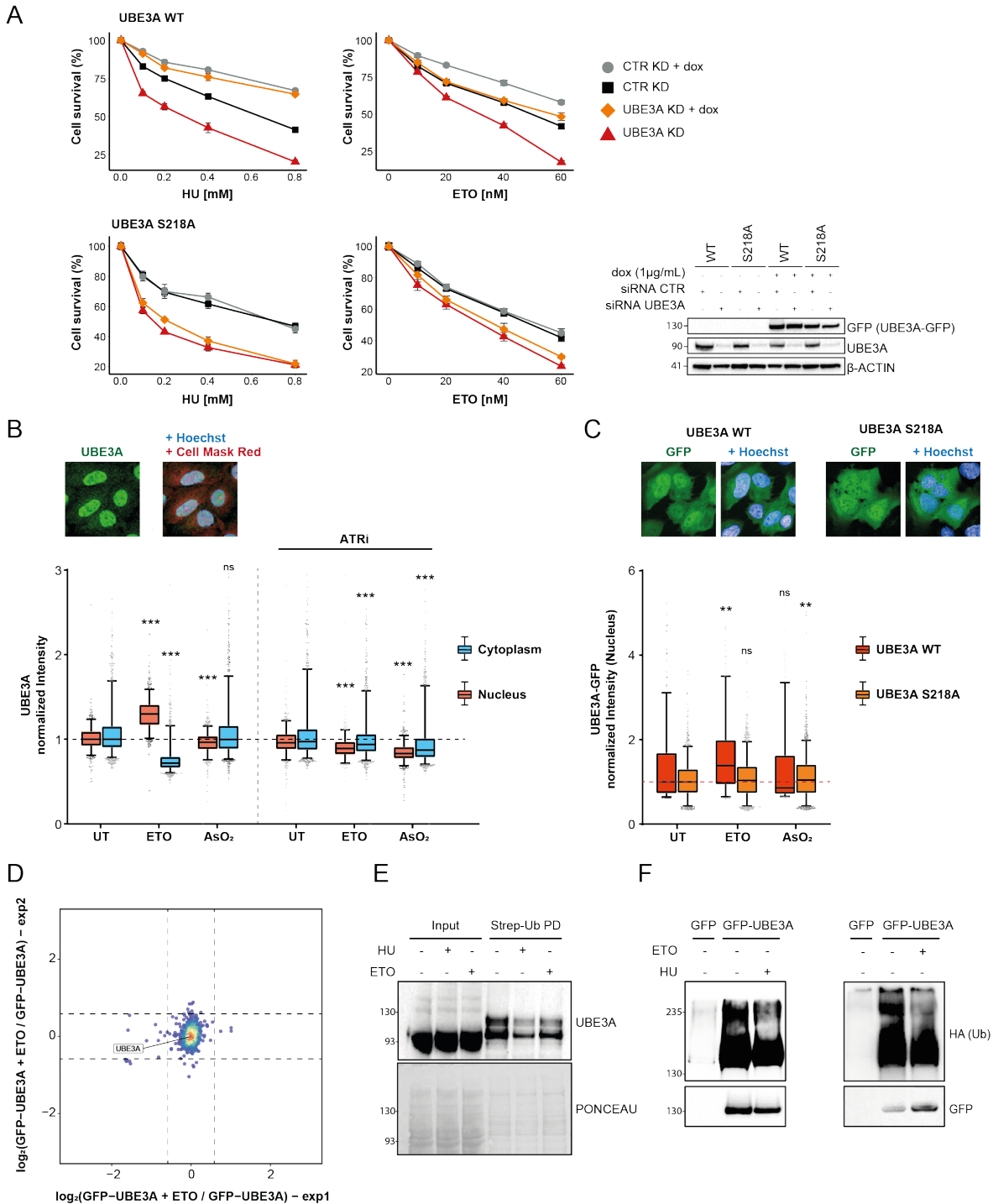


Figure 24: DNA damage affects UBE3A localization and ubiquitination activity. Colony-forming assays were carried out with dox-inducible cell lines expressing either UBE3A-GFP WT (**upper half**) or UBE3A-GFP S218A mutant (**lower half**). The cells were treated with the indicated concentration of ETO for 24 hours before they were allowed to recover for 10 days. KD of UBE3A and expression of UBE3A-GFP were verified by Western blotting (n=3) (**A**). Localization of endogenous UBE3A was determined by IFM. Cells were stained with CellMask red, and nuclei with Hoechst. Boxplots show UBE3A intensities upon ETO or AsO₂ treatment in the nucleus and cytoplasm (treatment conditions see Figure 10A). Cells were additionally treated with 5 μM ATR inhibitor (**right**). Intensities were normalized to the UT sample (*P-value < 0.01, **P-value < 0.001, ***P-value < 0.0001, compared to UT, n=3) (**B**). The experiment was repeated with the dox-inducible cells mentioned above (n=3) (**C**). Interactome analysis of UBE3A upon ETO treatment (1h, 10 μM). SILAC-labeled U2OS cells expressing GFP-UBE3A were used for interactome analysis (dashed lines indicate a ratio of 1.5) (**D**). Cells expressing Strep-tagged ubiquitin (Strep-Ub) were either treated with HU (2 mM, 4h) or ETO (10 μM, 1h). Total ubiquitin was pulled-down and UBE3A was detected by Western blotting (**E**). GFP-UBE3A was pulled-down from treated (see above) or untreated U2OS cells and subsequently used in an *in vitro* ubiquitination assay. Ubiquitination of UBE3A was detected by blotting for HA (HA-ubiquitin) (**F**).

2.2.7 Hydroxyurea inhibits the interaction of UBE3A with the proteasome and modifies proteasome activity

We also carried out interactome analysis of UBE3A upon HU treatment. Surprisingly, HU led to a very strong change in the interaction landscape, unlike ETO (Figure 25A, Figure 24B). Most strikingly, interaction with the proteasome seemed abolished. Western blot analysis after UBE3A pull-down and detection of the proteasome receptor RPN10 (PSMD4), a well-established interactor of UBE3A, confirmed this result (Figure 25B). We found this effect to be unique to HU, as it could not be reproduced with other DNA damage-inducing agents (Appendix Figure 37A). By making use of UBE3A and RPN10 S-to-A phosphorylation mutants, we could show that the phosphorylation events we observed in our screen (UBE3A S218; RPN10 S266) did not regulate this loss of interaction (Figure 25C; Appendix Figure 37B). We also excluded a recently reported phosphorylation site on RPN10 Y326, which was shown to regulate the interaction between RPN10 and UBE3A (not shown) [424]. Since we identified proteasome subunits as UBE3A substrates (Figure 22G), we wondered if the removal of UBE3A from the proteasome upon HU treatment leads to a decrease in proteasome ubiquitination. Consulting our diGly dataset upon 4-hour and 18-hour HU treatment, we could identify slightly up and down-regulated ubiquitination sites on several subunits but no obvious trend was visible (Figure 25C, Appendix Figure 37C). No significant changes were detected for sites on RPN10. However, Western blot analysis after isolating ubiquitinated proteins revealed significantly decreased (mono)ubiquitination of RPN10 upon both UBE3A KD and HU treatment (Figure 25D). This effect could not be reproduced with ETO.

As ubiquitination of the proteasome has been shown to regulate proteasome activity, we wondered if the interruption of UBE3A interaction with the proteasome by HU might display a similar effect. Therefore, we measured the enzymatic activity of the proteasome upon HU or other DNA damage-inducing agents. Again, HU was the only treatment showing a response, consistently increasing trypsin, chymotrypsin, and caspase-like activity (Figure 25E upper). This effect was more pronounced with increased concentration, but did not depend on the incubation time with HU before the measurement (Figure 25E lower).

Results

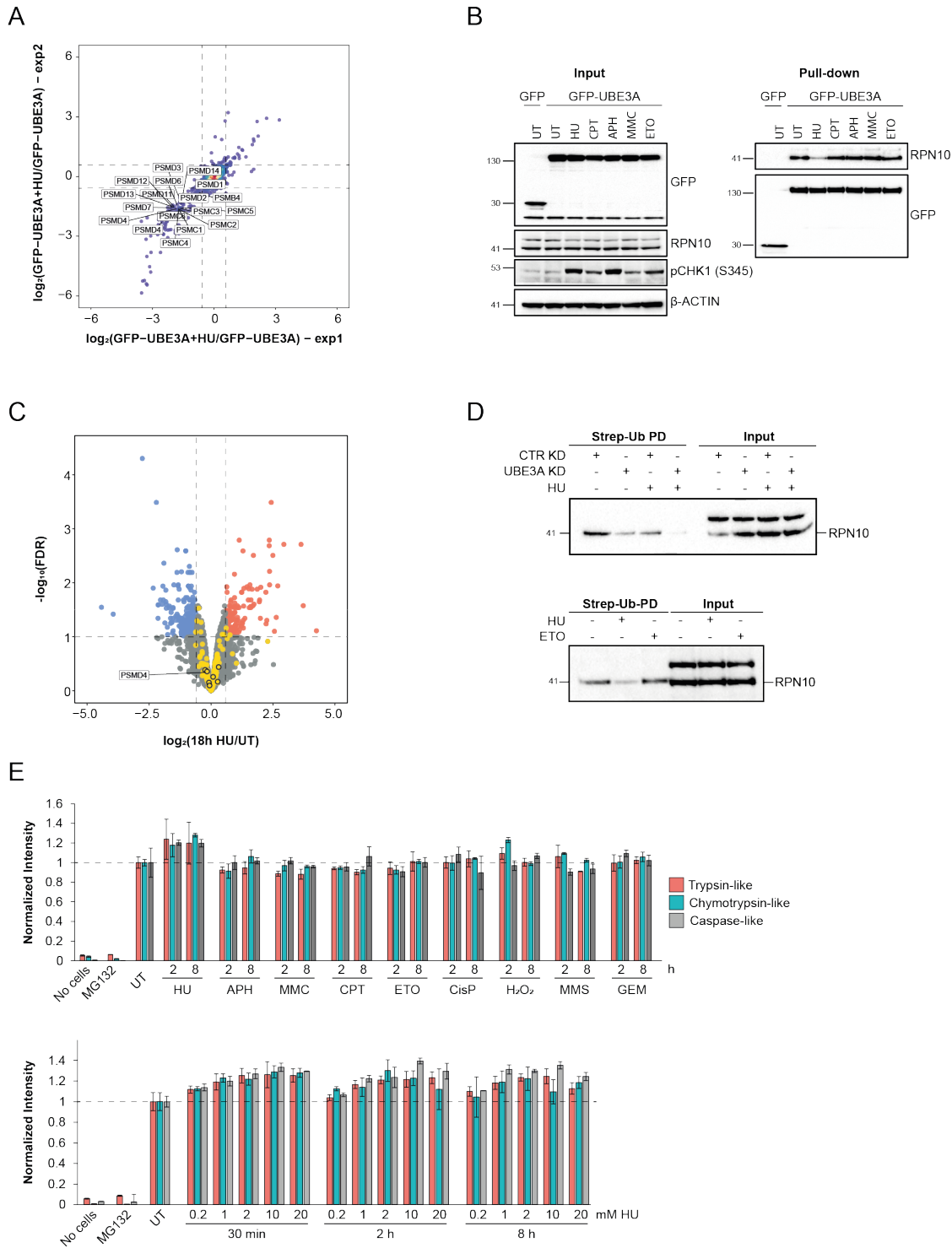


Figure 25: Hydroxyurea influences the interactome of UBE3A and affects proteasome activity. Interactome analysis of GFP-UBE3A upon HU treatment (2 mM, 4h) showed reduced interaction with proteasome subunits (dashed lines indicate 1.5-fold changes) (A). Interaction of GFP-UBE3A with RPN10 (PSMD4) was reduced upon 1-hour treatment with HU (2 mM) but not CPT (4 μ M), APH (5 μ g/ml), MMC (20 μ M), or ETO (10 μ M) (B). DiGly remnant enrichment analysis upon treatment with HU (2 mM) for 18 hours depicted in a volcano plot. Sites on proteasome subunits are indicated in gold. DiGly sites on RPN10 (PSMD4) are indicated by a black outline (FDR \leq 0.1, 1.5-fold change, n=3) (C). Cells expressing Strep-tagged ubiquitin (Strep-Ub) were either treated with HU (2 mM, 18h), ETO (5 μ M, 2h) or UBE3A was knocked-down. Ubiquitinated proteins were pulled-down and RPN10 was detected by Western blotting (D). Measurement of proteasome enzymatic activity (trypsin-, chymotrypsin-, and caspase-like) upon treatment with different DNA damage-inducing agents using the Cell-Based Proteasome-Glo Assays (upper half). Only HU consistently increased proteasome activity, in a concentration but time-independent manner (lower half; CisP (20 μ M), MMS (0.02%), GEM (10 μ M), other concentrations see (B), n= 3 (technical)) (E).

3 Discussion

In this study, the effects of 11 different DNA damage-inducing agents were assessed. For this purpose, a TMT-based mass spectrometry workflow was established to examine changes in the proteome, chromatin proteome, phosphoproteome, and ubiquitinome. An overview of the datasets was provided, known responses could be confirmed, and shared or treatment-specific effects were identified. Overlay of the datasets provided insights into molecular mechanisms by connecting PTMs to protein localization and function. Based on the screen, the E3 ligase UBE3A was identified as a putative new player in DNA replication and the DDR. Effects of UBE3A loss on DNA repair were assessed, DNA damage-dependent regulation of UBE3A was characterized, and potential new substrates of UBE3A, including POLD1, were identified. Additionally, HU was found to regulate proteasome activity potentially in a UBE3A-dependent manner.

3.1 A comprehensive analysis of the DNA damage response by mass spectrometry

Different types of DNA damage elicit distinct DNA damage responses. These are generally governed through a plethora of PTMs (phosphorylation, ubiquitination, acetylation, etc.), which in turn influence protein stability, localization, interaction, and activity. Since the advent of sensitive techniques that allow the proteome-wide analysis of these modifications, many have attempted to comprehensively study the response to DNA damage and large amounts of data have been published. However, the data are spread over different databases and are supplied in varying data formats, making access and comparisons inconvenient. As most studies are just looking at one or very few conditions, comparisons between the datasets are further hampered by differing experimental conditions (cell type, sample processing, data analysis, etc.) and by a low overlap between the datasets.

In the presented study, we tried to overcome several of these hurdles. For 11 different treatments, the changes in protein levels, phosphorylation, ubiquitination, and localization on chromatin were measured. Missing values in the proteomic measurements were largely avoided by employing peptide multiplexing. As the experiments were performed under the same conditions and in the same cell line, treatment outcomes are much more comparable. Side-by-side comparisons make it possible to extrapolate certain effects. For instance, if a phosphorylation site upon HU treatment seems to be increased but does not pass as statistically significant, other treatments like ETO, APH, or GEM, can be consulted. If these are significantly regulated, there is a high probability that prolonged incubation with HU would lead to the same effect. Moreover, the combination of the different datasets can lead to synergistic effects. As presented for the UV treatment, the PTM data can often provide information about the molecular mechanisms underlying the changes in protein localization. Simultaneous observation of different PTMs can strengthen the confidence in the relevance of the observed changes. Nonetheless, special care must be taken when interpreting the data, since different treatments also have

Discussion

different mechanisms of action. For instance, HU, APH, and GEM induced DNA damage largely depends on DNA replication, and thus mostly affect cells in S-phase. DNA repair is also a very dynamic process, and our dataset represents only a snapshot of the entire DDR response. Our database comprises 24,000 phosphopeptides, 2,200 diGly peptides, 8,500 protein, and 6,400 chromatin-associated proteins for each of the 11 treatment conditions, altogether ~450,000 data points. To our knowledge, there are currently no comparable proteomic studies of the DDR, especially regarding the number of treatment conditions and the measuring depth of the phosphoproteomes. For several other datasets, as in the case of FA, no proteomic screens are currently published. The data will be made available soon in a publicly accessible database featuring interactive visualization plots, which make it easy to look for protein-specific effects, compare between treatments, or simply explore. In the future, the database will continue to grow as a valuable resource for the DDR community, as further screens, including time-course experiments, other treatment conditions, and cell lines are added.

As the datasets were too extensive to analyze in detail, an overview of the most significant effects was presented and several interesting observations were compiled showing how the data can be used to extract unique effects, or such that are shared between treatments. For instance, we could confirm the DDR-dependent activation of PIKKs and other kinases, and displayed known treatment-specific responses such as the ubiquitination of TOP2A/B upon ETO, the degradation of TOP1 upon CPT, or the recruitment of NER repair factors to chromatin upon UV treatment [23, 389, 425]. The function of other changes such as the ubiquitination of ROS-responsive proteins upon MMS, or the differential ubiquitination of ZCH3H14, are still unknown and have already been briefly discussed. Several observations that were made across the different datasets are discussed below in more detail.

The smallest number of significant changes could be observed on the protein level. For instance, the upregulated proteins were mainly TFs, such as p53. This observation is in line with reports that the tumor suppressor p53 rapidly accumulates in response to DNA damage through ATM-dependent inhibition of the E3 ligase MDM2. In turn, p53 was shown to facilitate DNA repair and regulate cell survival, proliferation, and apoptosis [426, 427]. Closely connected to p53 were the proteins FOS, JUN, ATF3, and EGR1. These proteins share many regulatory roles with p53, either by direct interaction and regulation of p53 or by regulation of the same downstream targets. However, the increase of their protein level is due to quick protein expression, which is why their corresponding genes are referred to as immediate early genes [428–430]. Lastly, RhoB, which was shown to share pro-apoptotic functions, promote γ H2AX dephosphorylation, and DSB repair, was shown to be upregulated by CHEK2-dependent stabilization of its mRNA [431, 432]. Thus, we find that all three mechanisms can significantly increase protein levels in a relatively short time. Yet, the other datasets provided a more sensitive readout of TF activation, as we observed strong recruitment of proteins to chromatin in addition to increased phosphorylation (not shown) and ubiquitination of the TFs in response to most treatment conditions.

Among the downregulated protein groups, we found nucleolar proteins specifically decreased upon TOP1 inhibition by CPT. This observation was even more apparent within the chromatin proteome dataset, exhibiting removal of many more nucleolar proteins from chromatin. Similar observations were made by other groups as an immediate effect of nucleolar stress. This stress response was linked to inhibition of transcription and early rRNA processing, followed by subsequent disintegration of the nucleoli [371, 433, 434]. As the concept of a pluri-functional nucleolus that exerts non-canonical functions other than ribosomal biogenesis, is increasingly being recognized, it is tempting to speculate that CPT-induced toxicity is not only due to the direct induction of DNA damage but also mediated through the inhibition of nucleolar functions. These functions may include: maintenance, repair, and stabilization of the genome, and regulation of cellular senescence, cell-cycle control, telomere regulation, nuclear architecture, and response to stress [435]. While ETO has also been found to be a potent disruptor of nucleolar integrity, our data suggests CPT as a much more potent drug in this context.

Downregulation of extracellular matrix proteins was observed after H₂O₂, FA, MMS, and AsO₂. These treatments have arguably low target specificity, and can readily react with proteins, nucleic acids, or other molecules by oxidation, cross-linking, alkylation, or binding to sulfur ligands [436–441]. Thus, their toxicity might not only stem from DNA damage but also proteotoxic stress among others. At this point, further studies are necessary to determine whether the observed downregulation of extracellular matrix proteins was due to increased degradation or decreased expression. MAPK activation was predicted for the same treatments, including UV, and thus might be connected through the same unspecific mechanisms. MAPKs can be activated by an array of stimuli like extracellular mitogens, growth factors, cytokines, as well as stress signals like interleukins, irradiation, or chemotherapeutics. They regulate transcription, translation, apoptosis, and DNA repair [442]. Our data suggest that MAPK activation might happen at an intracellular level or through membrane receptors [443–445]. In fact, our phosphorylation data can be used to retrace major parts of the MAPK cascade from the activation of surface receptors to the regulation of effector proteins. For instance, stimulation of the epidermal growth factor receptor (EGFR) leads to activation of MAPKs via “GTPase signal transduction”. This signal is relayed through different members of the MAPK cascade (e.g. RAF, MEK, ERK) and downstream kinases such as RPS6 ribosomal protein kinases (S6Ks) are activated. In turn, MAPK activation can drive the expression of immediate early genes, providing one possible mechanism for the expression of the previously mentioned TFs (JUN, ATF2, EGR1, and FOS) [442, 446]. Although the actual interplays of the different kinases are probably much more intricate, it is a prime example of how the combination of different proteomic screens can help elucidate entire signaling pathways. Other kinases, with the same pattern, such as CAMKs and AKT1, can be activated through similar mechanisms, and show extensive cross-talk with MAPKs [447, 448]. The only MAPK that showed consistent activation in all treatment conditions was MK2. MK2 is activated by p38 (MAPK11-13) upon stress stimuli and is known as a master regulator of RNA-binding proteins (RBPs), influencing RNA stability. It has also been shown to play a role in cell cycle regulation and DNA repair. In this context, it can be activated by ATM/ATR

Discussion

through p38 or other kinases upon DNA damage [353, 449–451]. In the treatments arguably eliciting proteotoxic stress, p38 might be stimulated through several mechanisms, explaining the more pronounced activation. Complementary to the MAPK signaling, CK2 (CSNK2A1/2) activity was observed upon HU, GEM, APH, X-ray, ETO, and CPT treatment. This may signify, an important event in the DNA repair process, since CK2 has been shown to regulate apoptosis or to promote DNA repair through the phosphorylation of proteins like MDC1, RAD51, or XRCC1 [452]. Moreover, it is tempting to speculate whether CK2 activity is suppressed by the strong MAPK activation. This is in light of reports finding significant cross-talk between the MAPKs and the CK2, inhibiting or promoting each other's activity [453–455]. However, additional studies are required to draw conclusions about CK2 activation.

Regardless of the mechanistic details, the phosphorylation data can be roughly divided into two groups based on MAPK activation. As there is extensive crosstalk between ubiquitination and phosphorylation, and phosphorylation often governs protein localization, one might expect similar grouping patterns in the other datasets. Yet, such grouping is visibly absent in the ubiquitinome and the chromatin datasets, suggesting either minimal influence of the MAPK signaling or the effects are not yet visible at these early time points. As phosphorylation often precedes ubiquitination during the DDRs, the MAPK-associated pattern might thus manifest in the ubiquitinome and chromatin proteome datasets at later time points. Importantly, our current dataset identifies the strong, immediate responses to the different treatment conditions. One must also be aware of the limitations of the kinase activity prediction. Only ~2% of phosphorylation sites have an assigned regulatory kinase, while kinase-substrate predictions can also be false. This is further complicated by the fact that many phosphorylation sites are substrates of more than one kinase. Thus, kinase activity upon the different treatments is probably much more nuanced than it seems from the kinase prediction. Similarly, also functional interpretation is often difficult, as only ~3% of sites have a reported biological function [456].

Lastly, among all the treatment conditions AsO₂ held a special position. Arsenic compounds are well-known carcinogens, with chronic exposure inducing a variety of tumors. In lower concentrations, arsenic compounds do not induce DNA damage directly, but rather suppress DNA repair. They inhibit the activity of certain repair factors (PARP1, XPA, etc.) and reduce the expression of others (ATM, ATR, CHEK1, RAD23B, DDB2, FANCL, etc.) [457, 458]. However, acute exposure can also induce significant ROS generation mainly through the inhibition of the mitochondrial electron transport chain [437, 459]. In this study, AsO₂ treatment did not induce detectable activation of typical DDR kinases (ATR, ATM, DNA-PK, CHEK2, etc.), and thus was used as a reference condition representing cellular stress response, independent of the ATR/ATM-dependent DDR. As we did not directly assess DNA damage induction, e.g. by comet assay, it is likely that AsO₂ induced DNA damage under the chosen treatment conditions, but simultaneously suppressed PIKK activation. Although we did not show the full analysis for AsO₂ in favor of revealing DNA damage-specific effects, we still presented several interesting findings. Many of these findings can be traced back to the production of ROS and the

induction of proteotoxic stress. Recently, Guerra-Moreno et al. have found that yeast cells protect themselves against arsenite-induced proteotoxicity by reorganizing cellular proteostasis from an anabolic to a catabolic state [437]. Expression of components of the major degradation pathways (proteasome and autophagy) was increased, while components controlling protein synthesis, especially the ribosome itself, were down-regulated. In our study, we did not find any of these changes on the protein level, likely because of differences in the experimental setting. However, we did observe mTOR inhibition which signifies autophagy activation [460–462]. Ribosomal subunits showed decreased ubiquitination and were removed from the chromatin fraction, while an effect on nucleolar proteins, as in the case of CPT, was not detected. In turn, proteasome subunits were very strongly recruited to chromatin fraction. This might be connected to a recent report showing that proteasome subunits can undergo phase separation in the nucleus in response to hyperosmotic stress conditions [463]. AsO₂ also elicited broad activation of the MAPK pathway, possibly through induction of proteotoxic stress, activation via cell surface receptors, or other mechanisms [443, 464]. Lastly, our data indicated mitochondrial dysfunction, as we observed diminished protein levels of several NADH dehydrogenases, as well as strongly reduced activity of pyruvate dehydrogenase kinases PDK1 and PDK2 [465]. Thus, the mentioned mTOR inhibition could actually signify arsenite-induced mitophagy as previously described [466]. In conclusion, even the partially analyzed AsO₂ datasets could recapitulate major responses to AsO₂ induced stress in human cells, and thus serve as more than just a reference in our DDR screen.

3.1.1 TMT workflow and technical considerations

When setting up the TMT workflow several parameters had to be optimized, including protein digestion, TMT labeling, and peptide fractionation. Below, important findings are discussed and ideas for further improvement of the TMT workflow are described.

TMT-based workflows offer many advantages but can be quite costly. Hence, labeling parameters were optimized to minimize the amount of required TMT label. Under optimal conditions, the amount of TMT could be reduced by a factor of 16-fold, from a TMT:peptide ratio (w/w) of 8:1 down to 1:2. Assuming complete protein digestion, a 1:2 ratio is roughly equivalent to a 1.25:1 molar ratio of TMT-NHS-ester to primary amino groups [362]. Therefore, the labeling efficiency has virtually reached its limit. For samples where optimal labeling conditions could not be met, higher TMT amounts had to be used to achieve complete labeling. The determining factor in increasing labeling efficiency was increasing the peptide concentration, as found by Zecha et al. [362]. This can be explained by the competing reactions of the TMT reagent. Either it reacts with primary amines to form labeled peptides or undergoes hydrolysis. Higher concentrations of peptides will thus shift the reaction in favor of peptide labeling. Other factors, including an increased ACN concentration, adjustment of the pH from 8 to 8.5, and switching from TEAB to HEPES buffer were also found to improve labeling efficiency. The increased ACN concentration facilitated peptide resuspension and probably slowed TMT hydrolysis

Discussion

even further. While pH values up to 8.5 were found to increase the reactivity of primary amines exceeding the hydrolysis rate of NHS esters, and thus are favorable for TMT-labeling, it remains unclear why TEAB is less suitable than HEPES as a buffering agent [467, 468].

Despite steady advances in mass spectrometry, the in-depth analysis of digested proteomes still largely relies on off-line peptide fractionation. Here, peptide fractionation was carried out by SCX chromatography, based on our previously established in-house protocol. In the last few years, SCX is getting steadily replaced by techniques like high-pH RP chromatography. This is mainly due to charge clustering effects in SCX that are reflected in a poor resolution and spillover of peptides into other fractions [363, 469]. However, by carefully adjusting the buffer conditions, phosphopeptides could be equally distributed among the fractions, and the percentage of peptides measured in only one of the fractions was about 60%. This is on par with recently published high-pH RP chromatography protocols when also done in a microcolumn format [364, 365]. Additionally, SCX has a higher degree of orthogonality in combination with the low pH RP-HPLC, and might therefore lead to a higher number of identifications [469]. However, a side-by-side comparison is required to judge the performance of both methods. An important consideration when combining PTM enrichment with peptide fractionation is the order of the steps. In the established workflow, we are mixing the TMT labeled peptide samples, enrich for the desired PTMs, and subsequently fractionate. This simplifies the entire workflow substantially and increases reproducibility as samples are combined early on. It also makes it possible to use a microcolumn format, as the sample inputs are drastically decreased after PTM enrichment. On the other hand, starting with fractionation is beneficial, as the enrichment step might favor certain peptide species [470]. To this end, high-pH RP chromatography coupled to an HPLC system should be considered for future studies. Because it can separate higher peptide inputs and has a high resolution, it allows for extensive fractionation and fraction concatenation thus outperforming SCX setups [471].

As described, the steps in the TMT workflow common to both protein and PTM measurement were optimized. While we identified ~30,000 phosphopeptides in each of the replicates, the number of diGly sites (~2,600 sites) was comparably low to published benchmark studies [472, 473]. However, such comparison may not be appropriate, as these datasets were generated under deliberate proteasome inhibition, usually boosting diGly peptide identification 2- to 3-fold. Nonetheless, several measures can be undertaken to improve the current protocol. One identified source of peptide loss occurs between peptide enrichment and peptide labeling. After elution from the beads, diGly peptides were dried to allow dissolution in the TMT labeling buffer. Since peptide concentrations were very low, loss through adsorption to the test tube surface or incomplete dissolution may have been substantial. This might be avoided by TMT labeling while the peptides are still bound to the beads as the peptides can be directly fractionated after elution [472]. Additionally, it might significantly reduce the level of TMT contaminant side-products, as these can be washed away. Experimental accuracy might be improved, as already the washed beads can be mixed. Currently, this comes with the downside of a strongly increased TMT:peptide ratio, which makes on-bead labeling expensive. However, if it can be achieved to apply

the improved labeling protocol without eluting the peptides from the beads, on-bead labeling will greatly improve the TMT workflow for diGly peptides.

Overall, the current workflow based on TMT-MS2 is a powerful tool offering high throughput, reproducibility, and precision. However, accurate quantification is impaired by interference from co-isolated and co-fragmented peptides (see 1.2.7). Therefore, the extent of the resulting ratio compression should be assessed in the future to estimate the real FDR of the experiments. This can be done by a mixed species approach, in which peptides from yeast and human are mixed in fixed ratios and deviations from the expected ratios are calculated [361]. Popular methods to alleviate the effect of co-isolation are High Field Asymmetric-waveform Ion Mobility Spectrometry (FAIMS) or TMT-MS3. FAIMS separates peptides based on differences in mobility, which depends on the peptide mass, charge, size, and shape, while in TMT-MS3 peptides from the MS2 are fragmented in a third “purification” step [343, 474]. Both methods, especially in combination, greatly increase the accuracy of TMT. Yet, the need for specialized instrumentation limits their widespread application. To date, the most promising alternative is the use of complementary ions (see 1.2.7) [344, 475]. When peptides are fragmented in the MS2, the reporter groups leave balancer-peptide-conjugates with complementary isotope distributions behind. These conjugates have typically slightly different masses than the co-isolated peptides, and thus, can be used for quantification, drastically reducing the ratio distortion. While TMTc is applicable for most mass spectrometers, small isotope differences between the balancer-peptide-conjugates cannot be resolved, and therefore only half of the maximum plexing capacity can be used. The currently highest possible plexing capacity is thus 8-plex (“TMTProC”). In a recent publication from Johnson et al., TMTProC reduced ratio compression more than MS3 methods, while showing sensitivity levels slightly higher than TMT-MS2 [476]. In conclusion, TMTProC should be considered as an alternative method for experiments where quantification precision is more important than sample throughput and measuring depth. Lastly, it must be mentioned that DIA-based methods are quickly becoming an alternative also to multiplexed DDA methods. DIA typically provides higher peptide identification rates, a broader dynamic range, improved reproducibility, and accuracy. On the downside, it produces much more complex MS2 spectra, which need custom-made spectral libraries and elaborate data processing algorithms for spectral deconvolution [477]. However, these barriers are falling quickly and DIA is becoming more available as a mainstream method.

3.2 UBE3A – A putative new player in the DDR

3.2.1 UBE3A regulates cell cycle progression, genome stability, and possibly DNA replication and repair

Loss of UBE3A expression has broad consequences on neuron morphology and function, thus causing AS. 80% of all AS patients are suffering from microcephaly, which is characterized by a reduced brain volume and head circumference [478]. In contrast, UBE3A is overexpressed in certain types of cancer and promotes tumor growth. Hence, UBE3A expression is linked to the regulation of cell proliferation

Discussion

and cell survival [268–270, 274, 479, 480]. Although several studies try to explain these effects, the current understanding of the processes is far from complete. Therefore, based on our present work and the current literature, we discuss the potential underlying mechanisms and link UBE3A functions to so far unexplored processes, such as DNA replication and repair.

In our study, loss of UBE3A led to cell cycle arrest, genome instability, and reduced cell viability of U2OS cells. We observed that these effects came along with the upregulation of certain cell cycle regulatory proteins, such as p27, p21, and CDKs. Several groups have shown that UBE3A targets p27 for degradation by the proteasome, but also suppresses p27 expression on a transcriptional level [270, 479]. In turn, increased expression of p27 can induce cell cycle arrest and apoptosis. However, in a study by Raghu et al. depletion of p27 only led to a partial rescue of cell proliferation upon UBE3A loss, and thus p27 could not be the only affected protein [270]. The loss of UBE3A has also been reported to increase p53 levels, which potentially affects cell cycle progression and induces apoptosis as well. Yet, the significance of p53 alone in this context remains to be established [421, 481, 482]. Protein p21 might be regulated on the transcriptional level, by either UBE3A or by p53, but not as a direct UBE3A substrate at the protein level [479]. Additionally, we have identified several other cell cycle regulatory proteins as interactors or potential substrates (e.g. CDK1, CDK4, CDC20). Of these, CDK1 and CDK4 could be recently confirmed as substrates of UBE3A that are targeted for proteasome degradation [483]. Although increased levels of CDK1 and CDK4 do affect cell cycle progression, they are usually associated with increased, rather than decreased cell proliferation [484, 485]. Nonetheless, it further links UBE3A to cell cycle regulation. While the combined regulation of these proteins might already explain the observed effects on cell cycle and cell viability, our study indicates that even more processes might be involved.

A currently underexplored function of UBE3A that affects genome stability is in mitosis. Singhmar and Kumar have found UBE3A locates to the centrosome during mitosis when UBE3A levels are highest [478]. This is not very surprising, as all autosomal recessive primary microcephaly proteins can be found at the centrosome. There, UBE3A associates with ASPM, a centrosomal protein directly linked to microcephaly. Loss of UBE3A led to chromosome missegregation, abnormal cytokinesis, and apoptosis. Our results strengthen this connection as we identified SUGT1, which is involved in kinetochore assembly, as an interacting protein. This is supported by a study from Martínez-Noël et al. who additionally identified the centrosomal proteins CEP97 and CEP170 as UBE3A interactors [421]. How the lack of UBE3A leads to these mitotic defects is still unknown. Yet, the connection between loss of UBE3A, mitotic defects, AS, and microcephaly is evident.

Besides already acknowledged processes, our study indicates a strong link between UBE3A and the DNA replication machinery. Proteins of the replisome, including members of the MCM complex (MCM3-7), the RFC complex (RFC2,3, 5), DNA helicase RECQL, flap endonuclease 1 (FEN1), mismatch repair proteins (MSH2,6), the E3 ligase HERC2, and the catalytic subunit of POLD δ (POLD1, discussed in more detail below) were either identified as interactors and/or as potential UBE3A

substrates. For instance, MCM3-7 interacted with UBE3A and at least MCM7 showed decreased ubiquitination upon UBE3A KD. The MCM complex primes chromatin for DNA replication, unwinds the double-stranded DNA, recruits DNA polymerases, and initiates DNA synthesis [486]. As ubiquitination of MCM proteins has been identified as a major regulatory mechanism e.g. affecting MCM degradation, replication termination, and DNA repair, it is easy to imagine how deregulation would affect cell cycle progression and genome stability [487]. The same is true for the other proteins, as they also fulfill important tasks during DNA replication and the maintenance of genome integrity [108, 488–490]. Wang et al. have recently reported MCM2, MCM4, RECQL, and MSH2 as UBE3A substrates, confirming our results, but also adding POLA2, a component of the polymerase-primase complex Pol α , to this list [483]. Thus, UBE3A substrates work in every stage of DNA replication, from DNA unwinding, over priming, processive elongation, to post replicative mismatch repair. So far, the lack of functional studies for any of these proteins in the context of UBE3A makes them especially interesting for future research. In this regard, in the future we are planning to carry out DNA fiber assays, to analyze the potential effects on replication fork speed in the absence and upon overexpression of UBE3A. The use of p53/p27 deficient cell lines, will help to discern direct from indirect effects on the replication machinery. Co-localization of UBE3A with any of the replisome proteins will be determined by proximity ligation assay and/or super-resolution microscopy.

In our hands, loss of UBE3A led to a generally decreased DNA damage response. Western blot and IFM analysis showed that DNA damage signaling was negatively affected early in the signaling cascade, starting with reduced phosphorylation of ATM, CHEK1, CHEK2, RPA, and H2AX. MS data indicated a broad influence on the repair machinery by UBE3A KD. Decreased protein levels of factors like MDC1, acting early in the response, could explain these effects. MDC1 is involved in the recruitment and activation of ATM, and hence the expansion of checkpoint activation and γ H2AX signaling [491]. A similar effect could be contributed to the decrease in TIM levels. TIM interacts with PARP1 and leads to potentiation in DNA damage through PARylation and promotes HR [492]. Other well-known repair proteins (DNA-PKcs, FANCI, RAD18, RAD23, RPA, XRCC6, etc.) were also affected by the UBE3A KD and might also play a role. Regulation of UBE3A upon DNA damage induction is discussed below (see 3.2.3). Of course, when interpreting these results, the change in the cell cycle profile has to be kept in mind, especially since the protein levels of the ETO target TOP2 depend on the cell cycle phase. In that regard, we have observed ~40% decreased TOP2 levels upon UBE3A KD, and thus decreased damage induction is expected. To avoid this effect, future experiments could be performed in synchronized cells and X-ray treatment could be applied to assure equal DNA damage. As mentioned above, p53/p27 negative cells could alleviate cell cycle affects. Nonetheless, even when the effects were normalized to the percentage of cycling cells (not shown), we observed marked defects on HR markers such as BRCA1 and RAD51, as these were basically unresponsive to ETO treatment. This was confirmed by the cell cycle normalized TLR assay, which induces DSBs independent of ETO treatment.

Interestingly, the effect on HR can potentially be explained by the proteins discussed in the context of DNA replication, as many of them also play essential roles in DNA repair, particularly HR.

Lastly, it is worth mentioning that UBE3A also exists as part of several different protein complexes, including a complex with HERC2 and NEURL4 [421]. It was suggested that functions that are currently ascribed to HERC2 or NEURL4 could actually be carried out by or are dependent on UBE3A. These functions include DNA replication, DNA repair, or regulation of centrosome architecture [493–497]. The involvement of UBE3A in other processes indicated by our study or previous publications, such as transcriptional regulation [257, 498, 499], translation initiation [421, 500], protein folding [501, 502], and mitochondrial metabolism [503–505] might be also relevant but are beyond the scope of this manuscript.

3.2.2 POLD1 is a substrate of UBE3A

POLD1, together with POLD2, 3, 4, constitute the POL δ polymerase complex, which is the main polymerase for replicating the DNA lagging strand. The essential catalytic functions, namely 5'-3' DNA polymerase and 3'-5' exonuclease activity, are provided by the POLD1 subunit. The proofreading ability, conferred by the exonuclease activity, ensures replicative fidelity and serves to repair DNA lesions. In fact, POL δ has been shown to play a role in many DNA repair pathways, including base-excision, nucleotide excision, double-strand break and mismatch repair, e.g. by excision of lesions that cannot be repaired otherwise or by restarting strand synthesis [488].

Since we found direct interaction of POLD1 with and ubiquitination by UBE3A, POLD1 is a putative new UBE3A substrate. This would certainly fit well, as we could establish a strong connection to DNA replication, and several replisome components are directly ubiquitinated by UBE3A (see 3.2.1). Whether UBE3A regulates steady-state levels of POLD1 is currently unclear, as UBE3A depletion also affected cell cycle progression and hence POLD1 expression levels [506]. So far, we know that POLD1 is heavily ubiquitinated upon HU or MMS treatments and subsequently targeted for degradation by the proteasome. This ubiquitination is dependent on UBE3A, as UBE3A depletion abolished POLD1 (poly)ubiquitination. Other DNA damage-inducing agents or ATR inhibition did not influence POLD1 ubiquitination, thus excluding the involvement of the S218 phosphorylation site. Because of the obvious connection to replication stress and repair response, we hypothesized UBE3A might mitigate POLD1 ubiquitination, removal, and turnover on the stalled replication forks. Both timely recruitment and removal of proteins from the stalled forks are essential for fork rescue. Park et al. could recently show that ATAD5 unloads PCNA from stalled replication forks [507]. This allows the recruitment of RAD51 in an ATR-dependent manner, which mediates fork regression and hence fork stabilization and restart. In this context, PCNA is thought of as a physical barrier to fork regression that must be removed. These findings are in agreement with the data from Dungrawala et al. who also found ATR-independent removal of PCNA from HU stalled replication forks in their iPOND screens [508]. POL δ and POL ϵ removal seemed to follow the same laws, although it was not addressed whether the removal is an active

process or a passive dissociation after PCNA is gone. At least for damaged replication forks, active removal and turnover are described. For instance, POLD4 is degraded upon DNA damage by ligase RNF8, or by *CRL4^{Ctd2}* upon S-phase entry [509, 510]. This renders the POL δ complex less error-prone through increased proofreading ability and discrimination against mismatched primers and small lesions. In yeast, Def1 promotes Pol3 (POLD1 homolog) degradation upon DNA damage, whereas Pol31 and Pol32 stay behind in a complex with Rev1 to perform TLS [511]. So far, we found that POLD1 was removed from stalled replication forks, albeit slower than PCNA. Yet, depletion of UBE3A did not rescue the POLD1 removal. It is possible that the incomplete UBE3A KD in combination with the reduction in active replication forks upon UBE3A depletion still allowed POLD1 ubiquitination. However, since POLD1 ubiquitination was not detected upon APH, which also leads to replication fork stalling, and results from Dungrawala et al. support POLD1 removal upon this treatment, we must consider that POLD1 ubiquitination and POLD1 removal from stalled forks are separate processes. Thus, in future experiments it will be addressed if ubiquitinated POLD1 is identical with POLD1 on stalled replication forks.

3.2.3 DNA damage-dependent regulation of UBE3A

Two regulatory phosphorylation sites have been described for UBE3A. Protein kinase A (PKA) has been found to phosphorylate UBE3A on T485 outside its catalytic domain, which inhibits ubiquitination activity against itself and other substrates [512]. Mutations disrupting this phosphorylation site have been linked to autism pathogenesis, displaying excessive UBE3A activity and the resulting synaptic dysfunction [512]. Similarly, upon phosphorylation of Y636, located in the HECT-domain, by kinase c-Abl, UBE3A ubiquitination activity and possibly its stability is reduced [513]. Stress-induced c-Abl activity, and hence UBE3A inactivation, has been proposed as a mechanism for p53 protection from HPV-E6-UBE3A degradation in HPV-infected cells [514]. Additionally, UBE3A has been identified as a new player in Alzheimer's disease, since the accumulation of the A β peptide in the brain induces c-Abl activity followed by UBE3A depletion and increased levels of critical UBE3A substrates [515].

Here, we presented phosphorylation of UBE3A on S218 as a novel mechanism of UBE3A regulation in the context of DNA damage. Phosphorylation on S218 displayed an S/TQ motif indicative for PIKK kinases and was observed in response to a broad spectrum of DNA damage-inducing agents. Indeed, we could show that S218 was dependent on kinases ATM and ATR, as combined inhibition completely abrogated the phosphorylation. Yet, the participation of kinase DNA-PK cannot be ruled out. Colony-forming assays clearly showed that cells were sensitized to DNA damage upon UBE3A depletion, which was rescued by re-expression of UBE3A-GFP WT. Interestingly, this could not be achieved by expression of the UBE3A-GFP S218A mutant, highlighting the importance of UBE3A phosphorylation, and indicating a role in the DNA damage response.

Thus, we addressed UBE3A localization, interaction, stability, and activity of UBE3A upon DNA damage to investigate possible outcomes of S218 phosphorylation. The UBE3A gene encodes an E3

Discussion

ubiquitin ligase with three known protein isoforms in humans. Isoform 1 makes up the majority of cellular UBE3A, lacks the N-terminal extension of isoforms 2 and 3, and is mostly nuclear. Isoform 3 also localizes to the nucleus, while Isoform 2 is cytoplasmic [260, 297, 503]. Accordingly, the majority of endogenous UBE3A also localized to the nucleus in U2OS cells. Thus, it was surprising to find that phosphorylation on S218 led to further translocation of UBE3A into the nucleus, increasing the nuclear pool by ~20%. Currently, we can only speculate about the relevance of UBE3A translocation into the nucleus. As UBE3A is mostly known for its role in protein homeostasis, an increased nuclear pool could further elevate the capacity for protein turnover. This might include proteins that are directly involved in the DNA damage response, such as the repair factors discussed above. As a shown quality control ligase, UBE3A might also protect against potential proteotoxic stress [501, 516–518]. Of course, degradation or ligase-independent functions, such as its role as a transcriptional co-activator, could play a role as well. Another possibility is, that the cytosolic isoform 2 is recruited to the nucleus to fulfill isoform-specific tasks. This is especially exciting, as no isoform-specific substrates have been identified so far. However, since we could rescue UBE3A KD by overexpression of isoform 3, this option seems less likely. Nonetheless, it will be interesting to see if it translocates into the nucleus. Lastly, UBE3A might work as a shuttle into the nucleus for other factors that are needed in the nucleus.

Whatever the case, we expected this change in localization to be reflected in the interactome analysis upon ETO treatment, yet we did not observe any significant changes. However, it is possible that the N-terminal tagging of UBE3A (GFP-UBE3A) negatively affected the interactome analysis. Recent findings from the Elgersma group showed that the establishment of nuclear localization for the mouse isoforms is dependent on the interaction with RPN10 and retention in the nucleus by an unknown mechanism [297, 519]. Similar models were suggested for the human homologs (isoform 1 and 3). Fusion of an N-terminal HA tag to the nuclear mouse isoform 2 ablated the interaction with RPN10 and hence the translocation into the nucleus [519] This finding is further supported by Buel et al., who showed that UBE3A binds the C-terminal RAZUL domain of RPN10 by its N-terminal AZUL domain [424]. It is therefore plausible, that the N-terminal GFP tag on UBE3A led to the same outcome in our hands, and masked potential changes in interaction upon DNA damage-induction. However, it is curious how our interaction analysis could nicely recapitulate the known interaction landscape of UBE3A, including the interaction with the proteasome. Especially, binding to RPN10 could be confirmed repeatedly. Additionally, HU treatment diminished the interaction of UBE3A with RPN10, but did not alter UBE3A translocation into the nucleus. Therefore, we speculate UBE3A shuttles into the nucleus independent of RPN10, at least for the tested human isoform 3. Assuming the translocation does depend on the interaction with RPN10, it must be the pull-down conditions that lead to the discrepancy between the *in vivo* and *in vitro* situation. In future experiments, we will repeat the interactome analysis using IPs of endogenous UBE3A and PDs using C-terminal tags. Furthermore, we will apply proximity labeling (TurboID, APEX) to circumvent possible issues arising from the PD conditions [520, 521]. On a technical note, it seems that the localization of UBE3A cannot be addressed by chemical cell

fractionation. We (data are not shown) and others observed much higher cytoplasmic UBE3A levels upon fractionation, which is in clear conflict with IFM results [522]. Since proteins are fixed during IFM and therefore cannot change localization, UBE3A must leak from the nuclear fraction during standard fractionation protocols, thus leading to a false result.

We further found that UBE3A autoubiquitination activity is reduced upon DNA damage induction. Whether this reduction in activity also depends on phosphorylation of S218 still needs to be determined. In the case that it is neither dependent on the S218 site nor on ATM/ATR activity, the involvement of the aforementioned kinases c-Abl and PKA should be tested, as both can also be activated in response to DNA damage. A reduction in UBE3A autoubiquitination is usually associated with increased UBE3A stability. However, we could not observe an obvious increase in UBE3A levels, even upon long-term damage induction (e.g. 18h HU). Without conducting more experiments, a wide range of possible scenarios are conceivable, yet especially a scenario harmonizing the changes in UBE3A localization and activity is difficult at this point. Nonetheless, in the case that the decreased (auto)ubiquitination activity also extends towards UBE3A substrates, these might be stabilized. This could be beneficial for DDR proteins needed in lesion repair, or cell cycle regulators, like the UBE3A substrate p27. In an opposing scenario, decreased UBE3A activity might even increase protein turnover. Since ubiquitination of the proteasome by UBE3A can inhibit binding of ubiquitinated cargo by the proteasome, or even lead to turnover of proteasome subunits, decreased UBE3A activity might result in increased proteasome activity (discussed in more detail below, see 3.2.3). In future experiments, using S218 phosphomutants and mimetics, we will first address the relevance of UBE3A phosphorylation for the regulation of UBE3A activity. The effect on the stability and ubiquitination status of known UBE3A substrates will be evaluated and ubiquitination of potential substrates will be tested for UBE3A dependency.

3.2.4 Hydroxyurea and UBE3A regulate proteasome activity

Although UBE3A has been known to associate with the proteasome for many years, its physiological consequences are not well understood. Multiple labs have found that UBE3A has an inhibitory effect on the proteasome, while one study reported a stimulatory effect [295, 298, 482, 512]. Discrepancies between these studies could be due to the experimental approach or the cellular context. Jacobson et al. have shown that UBE3A inhibits the proteasome through ubiquitination, given the levels of polyubiquitinated proteins are low [295]. Under stress conditions, such as oxidative stress or starvation, when polyubiquitinated protein levels are raised, ubiquitination was blocked and proteasome activity increased. It was suggested, that the proteasome can sense the level of polyubiquitinated proteins and uses UBE3A, or other associated E3 ligases, to adjust its activity [295, 523]. Mechanistically, the ubiquitination of proteasome receptors might block the binding and therefore degradation of polyubiquitinated proteins. Similarly, AS-associated UBE3A mutants were shown to bind to the proteasome receptor RPN10 with high affinity, resulting in the inhibition of the catalytic activity of the proteasome [482]. Other, hyperactive UBE3A mutants, led to the ubiquitination and degradation of

Discussion

different proteasome subunits [512]. In *Drosophila melanogaster*, even overexpression of WT UBE3A could induce the degradation of RPN10 [296]. In summary, UBE3A and other ligases might regulate the proteasome by inhibiting proteasome catalytic activity, by inhibiting the binding of ubiquitinated substrates, or by promoting degradation of proteasome subunits.

In our study, DNA damage induction led to the decrease of UBE3A autoubiquitination and might therefore boost proteasome activity. However, unlike for ETO, treatment with HU showed strong changes in UBE3A interactions. Most striking was the strongly decreased interaction of UBE3A with RPN10 and the rest of the proteasome. Since the disrupted interaction with RPN10 was unique to HU treatment and could neither be reproduced by any other DNA damage-inducing agent nor rescued by mutation of any of the ATR/ATM-dependent phosphorylation sites, we conclude that the effect is independent of DNA damage induction. In line with this finding, we could show that HU, again unlike ETO, reduced ubiquitination of RPN10 to a similar extent as UBE3A KD, when analyzed by Western blot. Therefore, we assume it is mainly the diminished interaction with RPN10 and not the reduction in activity that decreases RPN10 ubiquitination. As RPN10 is known as a very promiscuous E3 substrate, an influence on the interaction with other E3 ligases should not be excluded [524]. Yet, unlike other ligases, UBE3A shows a tight interaction with RPN10, mediated through the former's AZUL and the latter's RAZUL domain [424].

In line with this observation, HU treatment increased the overall catalytic activity of the proteasome in a concentration-dependent but incubation time-independent manner. If HU concentration and proteasome activity are inversely correlated to the UBE3A-RPN10 interaction, still needs to be shown. The fact that we could not see generally reduced ubiquitination of the proteasome in the diGly experiment, as we observed for the UBE3A KD, can have multiple explanations. Since HU interrupted but not completely abolished the interaction, the effect of the UBE3A KD might have simply been stronger, or due to indirect effects of UBE3A loss. Additionally, it must be considered that the diGly experiment can neither provide information for all ubiquitination sites nor report changes in ubiquitin chain elongation. Our observations might be of special significance, as HU treatment is the only approved pharmacological therapy for sickle cell disease (SCD). SCD results from the missense mutation in the HBB (beta-globin) gene, leading to the expression of sickle hemoglobin in red blood cells. The alleviating effect of HU is mainly attributed to the inhibition of ribonucleotide reductase and the production of nitric oxide, which both increase the production of red blood cells containing high fetal hemoglobin levels [525, 526]. Recently, Warang et al. have reported that HU might also reduce proteotoxic stress by increasing proteasome activity. Red blood cells from SCD patients suffered from increased oxidative stress and showed accumulation of polyubiquitinated proteins. In contrast, cells from HU-treated patients displayed decreased levels of polyubiquitinated proteins and increased proteasomal activity. Since a previous publication had shown that HU inhibits the proteasome in HUVEC cells, they concluded that HU must increase proteasome activity in an indirect mechanism stronger than the inhibitory one [527]. However, our results in U2OS cells show that HU can increase

proteasome activity. This suggests a HU-dependent regulation of the proteasome in a cell type-specific way and makes a model in which HU regulates the proteasome in a more direct way possible. Additionally, our data provide a potential mechanism for how HU could modulate proteasome activity.

So far, we have not yet established a direct link between the UBE3A-dependent decrease of proteasome ubiquitination and the increased proteasome activity. Yet, based on the findings from Jacobson et al., it is certainly tempting to assume a direct causal connection. To further elucidate the effect of HU treatment on the proteasome, we have established the isolation of intact proteasomes, which allows us to analyze the composition of and interactions with the proteasome, and to study proteasome activity upon *in vitro* modification. When interpreting the results of the proteasome activity assay, it must be considered that protein degradation is a multistep process that encompasses substrate recognition, deubiquitination, unfolding, translocation, and hydrolysis [528]. Since the assay we applied in the presented study uses fluorogenic peptide probes, no conclusion about the substrate recognition, or unfolding could be made. Thus, we set up an assay based on a fluorescent reporter protein that allows *in vivo* monitoring of UBE3A, also accounting for substrate recognition and unfolding [529].

3.3 Concluding remarks

In this thesis, we have carried out a comprehensive analysis by mass spectrometry studying the acute DDR for 11 different DNA damage-inducing agents. By doing so, we have created one of the largest proteomic datasets on the DDR. To provide access to all relevant information and to facilitate data mining, a searchable database, “DDRBase”, was established. We demonstrated the identification of known and the discovery of many novel responses to the different DNA damage-inducing agents. Furthermore, our screen allowed us to distinguish the common from the treatment-specific effects and made it possible to link protein modification to protein localization. As discussed above, more comprehensive analyses, like enrichment analysis or kinase predication, further helped to integrate the datasets and revealed a more complete view of the cellular response to the different treatments. In the future, the database can be further expanded by adding other treatment conditions, cell lines, or time-resolved data. Additional PTM datasets such as, acetylation, sumoylation, and others, would allow studying crosstalk of PTMs in more detail. Ultimately, we hope that our screen and the related DDRBase will become a valuable resource for the DNA damage community that allows extraction of protein-specific information, easy comparison between different treatment conditions, and the identification of novel repair factors, as exemplified for UBE3A.

Previously, UBE3A had been implicated in DNA repair through interaction and substrate screens only. Here, we showed for the first time that UBE3A is modified and regulated as a direct result of DNA damage, which contributes to cell survival under genotoxic stress. Similarly, UBE3A had been implicated in the regulation of the DNA replication machinery via its ubiquitination activity on the MCM complex. As MCM is also involved in transcription, the identification of POLD1 as a putative new substrate now establishes a clear link of UBE3A to DNA replication. In the future, we plan to

Discussion

elucidate the exact function of UBE3A in the DDR and DNA replication as discussed above, and we hope that our research sparks further interest for these so far underappreciated roles of UBE3A.

4 Materials and Methods

4.1 Lists of all consumables, machines, and software

Table 1: Buffers/Solutions/Consumables

Cell culture	Composition / vendor
ATR inhibitor VE821	Selleckchem
Cell-Based Proteasome GLO assay	Promega
Dialyzed FBS (10,000 molecular weight cut-off)	Thermo Fisher Scientific
D-MEM for SILAC without lysine and arginine	Sigma Aldrich
Dulbecco's Modified Eagle Medium (D-MEM)	Gibco
Dulbecco's Phosphate-Buffered Saline (D-PBS)	Gibco
Fetal bovine serum (FBS)	Gibco
Human bone osteosarcoma epithelial cells (U2OS)	ATCC
Human embryonic kidney cells (HEK293/T)	ATCC
L-arginine (Arg0)	Cambridge Isotope Laboratories
L-lysine (Lys0)	Cambridge Isotope Laboratories
L-arginine-U-13C6 99% (Arg6)	Cambridge Isotope Laboratories
L-lysine-4,4,5,5,-D4 96–98% (Lys4)	Cambridge Isotope Laboratories
L-arginine-U-13C6-15N4 99% (Arg10)	Cambridge Isotope Laboratories
L-lysine-U-13C6-15N2 99% (Lys8)	Cambridge Isotope Laboratories
L-glutamine	Gibco
MG132	Sigma Aldrich
Penicillin/Streptomycin	Gibco
Polybrene	Sigma Aldrich
Puromycin	InvivoGen
Trypsin-EDTA (0.05%)	Gibco
DNA damage-inducing agents	
Aphidicolin	Santa Cruz Biotechnology
Camptothecin	Sigma Aldrich
Etoposide	Sigma Aldrich
Cisplatin	Sigma Aldrich
Formaldehyde	Sigma Aldrich
Gemcitabine	Sigma Aldrich
Hydroxyurea	Sigma Aldrich
Hydrogen peroxide	Sigma Aldrich
Methyl methanesulfonate	Sigma Aldrich
Mitomycin C	Sigma Aldrich
Sodium (meta)arsenite	Sigma Aldrich
Transfection	
Linear polyethylenimine transfection (PEI, HCl Max, 40000)	Polysciences, Inc.
Lipofectamine RNAiMAX	Life Technologies
Opti-MEM with GlutaMAX	Gibco
Colony formation, cell proliferation, and comet assays	
0.4% Crystal violet solution	Sigma Aldrich
CellTiter-Blue Cell Viability Assay	Promega
CometAssay 2 Well ES Unit w/ Starter Kit	Trevigen

Materials and Methods

SYBR gold Nucleic Acid Gel stain	Thermo Fisher Scientific
Cell lysis	
Complete protease inhibitor cocktail tablets	Roche Diagnostics
Modified RIPA buffer	50 mM Tris-HCl pH 7.5, 150 mM NaCl, 1 mM EDTA, 1% NP-40, 0.1% Sodium-deoxycholate
N-ethylmaleimide (NEM)	Sigma Aldrich
NuPAGE LDS Sample Buffer (4×) (LDS SB)	Thermo Fisher Scientific
Phosphatase inhibitors:	
1 mM sodium orthovanadate	Sigma Aldrich
5 mM β-glycerophosphate	Sigma Aldrich
5 mM sodium fluoride	Sigma Aldrich
QuickStart Bradford 1x Dye Protein Reagent	BioRad
RIPA buffer	50 mM Tris-HCl, pH 7.4, 1% Triton X-100, 0.5% Sodium Deoxycholate, 0.1% SDS • 150mM NaCl
Cell fractionation	
Fractionation buffer A	10 mM HEPES pH 7.5, 10 mM KCl, 1.5 mM MgCl ₂ , 0.34 M glucose, 10% glycerol, 1 mM DTT, 0.1% Triton-X100
Fractionation buffer B	3 mM EDTA, 0.2 mM EGTA, 1 mM DTT
Pull-downs	
GFP Trap agarose	Chromotek
Strep-Tactin Sepharose	IBA lifesciences
SDS-PAGE and Western blotting	
0.45 μm nitrocellulose	Sigma Aldrich
Blocking buffer	10% skimmed milk solution in PBS-T
Bovine serum albumin (BSA)	Sigma Aldrich
Dithiothreitol (DTT)	Sigma Aldrich
NuPAG MOPS SDS Running Buffer (20X)	Thermo Fisher Scientific
NuPAGE Bis-Tris gels 4-12%	Thermo Fisher Scientific
PBS-T	1x PBS, 0.1% Tween-20
Ponceau S	Sigma Aldrich
Ponceau S solution	0.1% (w/v) Ponceau S, 5% acetic acid
SuperSignal West Pico Chemiluminescent Substrate	Thermo Fisher Scientific
Transfer buffer	25 mM Tris, 192 mM Glycine, 20% (v/v) methanol, pH 8.3
Microscopy and flow cytometry	
4% paraformaldehyde (PFA) in PBS	Affymetrix
7-AAD Viability staining solution	eBioscience
Alexa Fluor 647 azide	Thermo Fisher Scientific
Blocking buffer	5% FBS in PBS-T
HCS CellMask Red stain	Thermo Fisher Scientific
Hoechst 33342	Thermo Fisher Scientific
Ubiquitination assay	
E6AP/S5a Ubiquitination Kit	Boston Biochem
iPOND	
Azide-PEG3-biotin conjugate	Sigma Aldrich
CL lysis buffer	50 mM HEPES pH 7.8, 150 mM NaCl, 0.5% NP-40, 0.25% Triton X-100, 10% glycerol
Copper (II) sulfate pentahydrate in PBS	Sigma Aldrich
Fixation solution	1% FA in PBS
Glycine buffer	125 mM in PBS
NeutraAvidin beads	Thermo Fisher Scientific

Permeabilization buffer	0.1% Trion-X100 in PBS
Sodium L-ascorbate	Sigma Aldrich
Washing buffer	10 mM Tris-HCl pH 8.0, 200 mM NaCl, 0.5 mM DTT
Production of recombinant proteins	
D-Tube Dialyzer tubes	Sigma Aldrich
Glutathione Agarose	Thermo Fisher Scientific
Lysis buffer protein purification	50 mM Tris-HCl PH8.0, 300 mM NaCl, 2 mM EDTA, 0.1% TritonX-100, 10% Glycerol, 1 mM DTT (add freshly prepared)
Ni-NTA beads	Qiagen
Rosetta2(DE3)pLysS	Novagen
DNA cloning	
Dh5 α	Thermo Fisher Scientific
Dimethyl sulfoxide (DMSO)	Sigma Aldrich
DpnI	NEB
Electro ligase	NEB
Gateway LR Clonase II Enzyme Mix	Invitrogen
High efficiency DH5 α E.coli	NEB
NucleoBond Xtra Midi	Macherey-Nagel
Plasmid Mini Kit	Qiagen
Q5 MasterMix	NEB
QIAquick PCR & Gel Cleanup Kit	Qiagen
Mass spectrometry	
In-gel digestion	
Buffer B	80% ACN, 0.5% acetic acid
Chloroacetamide (CAA)	Sigma Aldrich
Colloidal Blue Staining Kit	Life Technologies
Destaining solution	50% Ethanol, 50 mM ABC buffer pH 8.0
Digestion buffer	25 mM ABC buffer pH 8.0
Peptide extraction buffer	30% ACN, 3% TFA
Sequencing grade Trypsin (0.5 μ g/ μ l in 50 mM acetic acid)	Sigma Aldrich
In-solution digestion	
Denaturation buffer	6 M urea, 2 M thiourea in 10 mM HEPES-NaOH pH 8.0
Lysyl endopeptidase (Lys-C)	Wako Chemicals
SepPAK C18 cartridges	Waters
Stage tipping	
Buffer A	0.1% formic acid
Buffer B	80% ACN, 0.1% formic acid
C ₁₈ elution buffer	50% ACN, 0.1% formic acid
C ₁₈ Empore 47 mm extraction disks	CDS Analytical
Micro-SCX fractionation	
SCX elution buffers	40 mM acetic acid, 40 mM boric acid, 40 mM phosphoric acid. (Adjust pH to the indicated pH values with sodium hydroxide. Add 40% ACN before use)
SCX Empore Cation 47 mm extraction disks	CDS Analytical
SCX wash buffer	40% ACN, 0.1% TFA
Phosphopeptide enrichment	
Phospho binding buffer	50% ACN, 6% TFA
Phospho elution buffer 1	5% NH ₄ OH
Phospho elution buffer 2	10% NH ₄ OH, 25% ACN

Materials and Methods

Phospho wash buffer	50% ACN, 0.1% TFA
Titansphere TiO bulk material (TiO ₂) 10 µm	GL Sciences Inc
DiGly remnant enrichment	
DiGly immunoaffinity purification buffer (IAP, 10x)	500 mM MOPS pH 7.2, 100 mM Na ₃ PO ₄ , 500 mM NaCl
DiGly wash buffer 1	1x IAP buffer, 150 mM NaCl, 0.5% NP-40
PTMScan Ubiquitin Remnant Motif beads	Cell signaling
TMT	
hydroxylamine	Sigma Aldrich
TMT labeling buffer	150 mM HEPES pH 8.5, 30% ACN
TMT10plex Isobaric Label Reagent Set plus TMT11-131C Label Reagent	Thermo Fisher Scientific

Table 2: Antibodies

Antibodies	Product number	Manufacturer	Dilution	Origin
53BP1	MAB3802	Millipore	1:400	mouse
BRCA1	sc-6954	Santa Cruz Biotechnology	1:400	mouse
GFP	sc-9996	Santa Cruz	1:2000	mouse
gH2AX	A300-081A-M	Bethyl	1:1000	rabbit
IgG Alexa Fluor 488, 568	A11001, A11004	Life Technology	IF 1:1000	mouse
IgG Alexa Fluor 488, 568	A11008, A11011	Life Technology	IF 1:1000	rabbit
pCHEK1 (S345)	2344	Cell Signaling Technologies	1:1000	rabbit
pCHEK2 (T68)	2661	Cell Signaling Technologies	1:1000	rabbit
POLD1	sc-17776	Santa Cruz Biotechnology	1:400	mouse
POLE1	sc-390785	Santa Cruz Biotechnology	1:400	mouse
pRPA2 S4/S8	A300-245A	Bethyl	1:400	rabbit
pS/pT-QG	6966	Cell Signaling Technologies	1:1000	rabbit
pS-Q	9607	Cell Signaling Technologies	1:1000	rabbit
RPA1	ab176467	abcam	1:1000	mouse
RPAS33	A300-246A-M	Bethyl	1:1000	rabbit
RPN10	CPTC-PSMD4-3-s	DSHB	1:200	mouse
Secondary antibodies coupled to horseradish peroxidase		Jackson ImmunoResearch Laboratories	IF 1:5000	mouse, rabbit
UBE3A	7526	Cell Signaling Technologies	1:1000	rabbit
Vinculin	V9264	Sigma Aldrich	1:10000	mouse

Table 3: Plasmids

Plasmids	Source
pcDNA-DEST47	Life Technologies
pcDNA-DEST53	Life Technologies
pENTR221-UBE3A (isoform 3)	This study
pENTR221-UBE3A S218A (isoform 3)	This study
pOTB7-UBE3A-Isoform3	Harvard medical school
Lentivirus production	
pMD2.G	Addgene
psPAX2	Addgene
plix-402	Addgene
plix-Nterm-GFP	This study
plix-Cterm-GFP	This study

Protein production

pDEST-15	Thermo Fisher Scientific
pET-53-DEST	Millipore
pDEST-15-N-GST-UBE3A	This study
pET-53-DEST-N-His-POLD1	This study

TLR assay

pRRL sEF1a HA.NLS.Sce(opt).T2A.IFP	Addgene
pRRL SFFV d20GFP.T2A.mTAG BFP donor	Addgene

Table 4: Primers

Primers	Sequence 5'-3'
UBE3A S218A mutagenesis	Fwd – Phos-CCAGGGAGACAACAATTTGCAAAAATTAG Rev – Phos-GCGCTATCACCTATCCTTGAGGAAG
UBE3A siRNA1 insensitive mutation	Fwd – Phos-GTTCCGAGATAAAAAATGAACAAGAAAGGCCG Rev – Phos-AAGAATTGTTGGGGGCACCTTC
pENTR UBE3A	CPEC primer pair 1 – pOTB7-Ube3a-Isoform3 Fwd – CTTTGTACAAAAAAGCAGGCTGTATGGCCACAGCTTGTAAG Rev – CTTTGTACAAGAAAGCTGGGTACAGCATGCCAAATCCTTTGG CPEC primer pair 2 – pOTB7-Ube3a-Isoform3 Fwd – CTTATATGTGGAAGCCGGAATCTAGATTTCCAAGCACTAGAAGAAAC Rev – GTTCTTCTAGTCTTGAAATCTAGATTCGGCTCCACATATAAG CPEC primer pair 3 – pENTR221-ADRM1 Fwd – CCAAAGGATTTGGCATGCTGTACCCAGCTTCTTGACAAAG Rev – CTTTACAAGCTGTGGCCATACAGCCTGCTTTTTTGTACAAAG
plix-Cterm-GFP	CPEC primer pair 1 – plix402 Fwd – CATGGTGTCTAGCCAGCTCAATCGATGCTAGCCAATTC Rev – CTTGTACAAAGTGGTGATAATTAATTAACGCGTCCGGTCCACC CPEC primer pair 2 – pcDNA-Dest47 Fwd – GAATTGGCTAGCATCGATTGAGCTGGCTAGACACCATG Rev – GGTGGACCGGACGCGTTAATTAATTATCACCACTTTGTACAAG
plix-Nterm-GFP	CPEC primer pair 1 – plix402 Fwd – CTTCTCTTTGTAGCCATATACGGATAACCGGTAACC Rev – GCATGGATGAGCTCTACAAATAAACGCGTCCGGTCC CPEC primer pair 2 – pcDNA-Dest53 Fwd – GGTTACCGGTTATCCGTATATGGCTAGCAAAGGAGAAG Rev – GGACCGGACGCGTTTATTGTAGAGCTCATCCATGC

Table 5: siRNAs

siRNAs	Sequence 5'-3'
RBBP8 (CTIP)	GCUAAAACAGGAACGAAUC-TT
CTR	UGGUUUACAUGUUGUGUGA-TT
CTR pool	Dharmacon pool
UBE3A1	CAACUCCUGCUCUGAGAU-TT
UBE3A2	AGACAAAGAUGAAGAUGAA-TT
UBE3A3	CUGUUCUGAUUAGGGAGUUCUGG-TT
UBE3A pool	Dharmacon pool

Table 6: Software

Software
Adobe Illustrator CC2021
Clustal Omega (EMBL-EBI)
CometScore (TriTek Corp.)

Materials and Methods

Cytoscape version 3.8.2
EveryVECTOR
Harmony High-Content Imaging and Analysis Software (PerkinElmer)
IceLogo (University Ghent)
MaxQuant v1.5.2.8 / v1.6.14.0 (Cox lab)
Perseus 1.6.14.0 (Cox lab)
QuikChange Primer Design II tool (NEB)
R studio v1.2.1335 / R v3.6.1
Thermo Xcalibur 3.0.63 (Thermo Fisher Scientific)

Table 7: Machines

Machines	Vendor
AF7000	Leica
BD LSRFortessa SORP	BD Biosciences
Biometra TRIO Thermal Cyclers	Analytikjena
Biorupter NGS	Diagenode
ChemiDoc imaging system	BioRad
Easy-LC-1000	Thermo Fisher Scientific
Easy-LC-1200	Thermo Fisher Scientific
Faxitron	Faxitron Biooptics
GraphPad prism	Prism
NanoDrop 2000	Thermo Fisher Scientific
NuPage Novex Gel System	Thermo Fisher Scientific
Opera Phenix High Content Screening System	PerkinElmer
Orbitrap Exploris 480 mass spectrometer	Thermo Fisher Scientific
Plate reader infinite m200	Tecan
Q Exactive Plus	Thermo Fisher Scientific
Sonifier 450	Branson
Thermo Scientific 3311 Forma Steri-Cult CO ₂ Incubator	Eppendorf
Thermoshaker	Eppendorf
UV-C irradiator	Inhouse built
VacuFuge Plus	Eppendorf
Xcell II Blot-Modul	Thermo Fisher Scientific

4.2 Cell culture

4.2.1 Cell cultivation and passaging

Human osteosarcoma cells (U2OS) and human embryonic kidney cells (HEK293T) were obtained from ATCC, and cultured in D-MEM medium supplemented with 10% fetal bovine serum (FBS), 2 mM L-glutamine, and 100 U/ml Penicillin/Streptomycin. Additionally, puromycin was added to stable cell lines to a concentration of 1 µg/µl. For SILAC experiments, cells were cultured in medium containing either L-arginine and L-lysine, L-arginine [¹³C6] and L-Lysine [²H4], or L-arginine [¹³C6,¹⁵N4] and L-lysine [¹³C6,¹⁵N2]. To passage cells, cells were washed with PBS, detached with 0.05% trypsin, and resuspended in complete D-MEM medium. Afterward, cells were spun down at 220 x g and re-plated according to the desired confluence. All cells were grown at 37 °C in a humidified incubator at 5% CO₂.

4.2.2 Transfection of cells

For siRNA transfection of cells in a 6-well plate, cells were grown to a confluence of 80% in 2 ml complete D-MEM. Next, 4 µl of siRNA (10 µM) and 5 µl siRNAMax were each diluted in 100 µl Opti-MEM. The mixtures were combined, mixed by inversion, and incubated for 5 min at RT. Afterward, they were added to the cells for 6 hours before the medium was replaced with fresh D-MEM. Similarly, for DNA transfection, 2.5 µg of plasmid DNA were re-suspended in 150 µl Opti-MEM. Subsequently, 7.5 µl polyethylenimine (PEI) were added to the mix. It was vortexed and incubated for 15 min at RT. After addition to the cells, the medium was replaced after 8 to 12 hours [530]. The cells were used for experiments 48 to 72 hours after DNA or siRNA transfection, respectively. Transfection volumes in other culture dish sizes were scaled according to the surface area.

4.2.3 Stable cell line production by lentivirus transduction

For lentivirus production, HEK293T cells were co-transfected with an expression plasmid (pliX-GFP), along with the packaging plasmids psPAX2 and pMD2.G in a 4:3:2 w/w/w ratio. 72 hours post transfection, the supernatant was collected, filtered through a 0.45 µm filter, mixed with the same volume of fresh medium, and supplemented with polybrene to a concentration of 8 µg/µl. Subsequently, U2OS cells were transduced by exchanging the medium for the conditioned supernatant. The virus was removed 24 hours later, and cells incubated for a further 48 hours, after which stable cells were selected by the addition of 2 µg/µl puromycin for 5 days.

4.3 Methods for DNA modification and analysis

4.3.1 Gate-way cloning

GFP-expression vectors were created from Destination vectors and Entry / DONR vectors using the Gateway LR Clonase II Enzyme Mix according to manufacturer instructions. Vectors used in this work are listed in 4.1 (Table 3).

4.3.2 Site-directed mutagenesis

Primers used for site-directed mutagenesis were designed with the QuikChange Primer Design II tool. Mutagenesis was performed on the pENTR221 UBE3A using the PCR conditions indicated below. The resulting linear plasmids were treated with 20 U of DpnI for 1 hour at 37 °C and column purified using the QIAquick PCR & Gel Cleanup Kit. Ligation of the plasmids was performed using ElectroLigase according to manufacturer instructions.

PCR – MIX	
2x Q5 Master Mix	25 µl
Primer Mix	0.5 µM
100 ng Plasmid DNA	100 ng
H₂O	Fill up to 25 µl

Temperature	Time	Cycles
98°C	30 sec	1
98°C	10 sec	30
55 °C	30 sec	30
72°C	40 sec / kb	30
72°C	5 min	1
12°C	hold	

4.3.3 CPEC cloning

Circular polymerase extension cloning (CPEC) was modified from Quan and Tian [531]. Vector plix-Nterm-GFP was created from plix-402 and pcDNA-Dest53, plix-Cterm-GFP from plix-402 and pcDNA-Dest47, and pENTR223-UBE3A from pOTB7-UBE3A-Isoform3 and pENTR221-ADRM1. In short, primers were created in a way, that resulting vector fragments share overlapping regions at the ends. Melting temperatures of overlapping regions were typically around 70 °C. In a first round, PCR vector fragments were created with the designed primers. The DNA fragments were treated with 20 U of DpnI for 1 hour at 37 °C and gel purified using the QIAquick PCR & Gel Cleanup Kit. In a second PCR round, the purified fragments were hybridized and extended to form a complete plasmid. The resulting plasmids were directly transformed into competent DH5α bacteria. PCR conditions are listed below.

PCR1

PCR1 – MIX	
2x Q5 Master Mix	25 µl
Primer Mix	0.5 µM
100 ng Plasmid DNA	100 ng
H ₂ O	Fill up to 25 µl

Temperature	Time	Cycles
98°C	30 sec	1
98°C	10 sec	30
T _m + 3 °C	30 sec	30
72°C	40 sec / kb	30
72°C	5 min	1
12°C	hold	

PCR2

PCR2 – MIX	
2x Q5 Master Mix	25 µl
Backbone fragment	100 ng
Insert fragment	1.5 x molar amount Backbone fragment
DMSO	1 µl
H ₂ O	Fill up to 25 µl

Temperature	Time	Cycles
98°C	30 sec	1
98°C	10 sec	30
69°C	30 sec	30
72°C	~40 s/kb	30
72°C	5 min	1
12°C	hold	

4.4 Cell-based methods**4.4.1 Colony-forming assay**

Cells were transfected with the respective siRNAs. In the case of doxycyclin-inducible cell lines, doxycycline was added to a concentration of 1 µg/µl. The next day, 4,000 to 12,000 cells were re-seeded into 6-well plates. 72 hours after transfection, the cells were irradiated or treated with DNA damage-inducing agent for a period 24 hours, before the cells were washed twice with PBS and the medium was replaced. Surviving cell colonies were stained with crystal violet solution 10-14 days post treatment, and counted under the microscope. Each experiment was carried out with three technical and three biological replicates. LC₃₀ values were calculated by regression analysis in GraphPad prism. LC₃₀ values equivalent to the ones determined by CellTiter-Blue were determined by calculating scaling factors after carrying out both assays upon UV treatment.

4.4.2 Cell viability assay

2,500 cells per well were seeded onto 96-well plates in a volume of 100 µl. The next day, cells were treated with DNA damage-inducing agents for 2 hours, or irradiated, before the medium was replaced. 72 hours post treatment, cell viability was tested by adding 20 µl of CellTiter-Blue Cell Viability solution for 3 hours. Bioluminescence was measured on the Tecan Plate Reader with the following settings: excitation wavelength 560 nm, emission wavelength 590 nm, number of flashes 25, and integration time 20 µs. LC₃₀ values were calculated by regression analysis in GraphPad prism.

4.4.3 Immunofluorescence and confocal microscopy

For microscopy experiments, 20,000 cells were seeded into 96-well cell carrier plates. The next day, cells were treated according to the experimental setup, washed twice with PBS, and incubated with 50 μ l pre-extraction buffer for 40 min on ice (only for DNA damage foci). Subsequently, cells were fixed with 4% PFA solution for 20 min at RT, washed 3 times with PBS, and incubated in blocking buffer for 1 hour. Primary antibodies were diluted according to the manufacturer's instructions in blocking buffer and incubated with the cells overnight at 4 °C. Cells were washed 3 times with PBS-T, before the secondary antibody (1:1000 in blocking buffer) in combination with Hoechst (2 μ g/ μ l) and CellMask red (1:5000) was put on the cells for 1 hour at RT. Cells were washed 3 more times with PBS-T and finally stored in PBS until the measurement. Images were acquired on the Opera Phenix High Content Screening System using a 40X water objective lens. Per well about 30 fields with 5-10 z-planes separated by 0.5 μ m were obtained. Image analysis was performed in the Harmony High-Content Imaging and Analysis Software. Significance values were calculated in GraphPad (one-way ANOVA followed by Dunnett's test).

4.4.4 TLR assay

U2OS TLR cells were first treated with the indicated siRNAs, and co-transfected with the TLR expression plasmids 6 hours later. 72 hours post transfection, the cells were harvested, and the percentage of GFP⁺ (HR) and mCherry⁺ (mutagenic end joining) cells was measured on the BD LSRFortessa SORP flow cytometer (IFP: 640nm, 730/45; BFP: 405nm, 450/50; GFP: 488nm, 530/30; mCherry: 561nm, 610/20). A minimum of 200.000 cells was measured, and only IFP and BFP positive cells were scored. Analyses were conducted using the FlowJo software. Finally, the HR values were normalized to the percentage of cells in S or G2 phase, as described (see 4.4.5). Significance values were calculated in GraphPad (one-way ANOVA followed by Dunnett's test).

4.4.5 Cell-cycle profiling

Cells were grown to 80% confluence, and EdU was added to a concentration of 10 μ M for 1 hour. For the analysis by flow cytometry, the cells were harvested and washed with PBS, fixed for 10 min in 4% PFA, and the click reaction was carried out as described (see iPOND) using Alexa Fluor 647 Azide. Afterward, DNA was stained with either Hoechst (1 μ g/ml) or 7-Aminoactinomycin D (7-AAD, 1:100). Cells were analyzed on the BD LSRFortessa SORP cell analyzer (7-AAD: BL488nm, 610/20 nm; Alexa Fluor 647: RL635nm, 660/20; Hoechst 3342: 355nm, 450/50). For cell cycle analysis by microscopy, click reaction (see 4.5.8), Hoechst staining and subsequent measurement on the Opera Phenix High Content Screening System were carried out as described (see 4.4.3).

4.4.6 Neutral comet assay

Neutral comet assay was performed according to the manufacturer's protocol (Trevigen). Briefly, cells were embedded in low melting agarose at 37°C on Comet Slides. Overnight cell lysis at 4°C was

followed by equilibration in 1x Neutral Electrophoresis Buffer for 30 min at room temperature. Single-cell electrophoresis was performed at 4°C in 1x Neutral Electrophoresis buffer for 45 min with a constant 21V. After DNA precipitation with 1x DNA Precipitation Buffer, Comet Slides were dried with 70% EtOH at room temperature. To completely dry the samples, Comet Slides were transferred to 37°C for 15 min. DNA was stained with SYBR Gold solution for 30 min at room temperature. Images were taken with a Leica AF7000 microscope using a 20x air objective and a Fluorescein filter. Tailmoments of the comets were quantified using the CometScore software. At least 50 comets were quantified per condition. Significance values were calculated in GraphPad (one-way ANOVA followed by Tukey's test).

4.4.7 Proteasome activity assay

Trypsin-, Chymotrypsin-, and Caspase-like enzymatic proteasome activity were measured using the Cell-Based Proteasome GLO assay according to the manufacturer's instructions. In short, 3200 cells/well were seeded in 20 µl in a 384-well plate. The next day, 5 µl of DNA damage-inducing agents were added. As a background control, MG132 was added to a concentration of 30 µM. 30 min before the measurement, the plate was equilibrated to RT. 25 µl of substrate were added, and luminescence was measured every 2 min, with shaking (amplitude = 4, 100 sec) in between measurements on the Tecan Plate Reader. Differences between treatment conditions were assessed roughly 30 min after substrate addition when the luciferase activity reached a steady level.

4.5 Protein-specific methods

4.5.1 Cell lysis

Cells were washed twice with ice-cold PBS, placed on ice, and directly lysed in the plates by addition of modified RIPA buffer supplemented with the desired inhibitors (protease inhibitor, phosphatase inhibitors, 10 µM N-ethylmaleimide (NEM)) and collected by scraping. For samples prepared for Western blotting, NaCl was added to a concentration of 600 mM and sonicated. The lysates were cleared by centrifugation at 16,000 x g for 15 min at 4 °C, and protein concentrations were measured using the QuickStart Bradford Protein assay.

4.5.2 Cell fractionation

Cell fractionation was carried out according to Méndez and Stillman [355]. Cells were harvested by scraping in ice-cold PBS and spun down at 300 x g. For a 15 cm plate, pelleted cells were lysed in 500 µl fractionation buffer A, incubated for 15 min at 4 °C with rotation, and spun down at 1,300 x g for 5 min. The resulting nuclear pellet was washed once with 500 µl buffer A before it was resuspended in 500 µl fractionation buffer B and incubated for 30 min at 4 °C with rotation. The chromatin fraction was pelleted at 1,700 x g for 5 min and washed once with 500 µl buffer B. Finally, the chromatin fraction

was resuspended in RIPA buffer (600 mM NaCl), sonicated, and cleared by centrifugation at 16,000 x g at 4 °C for 15 min. All buffers were supplemented with protease inhibitor mix.

4.5.3 SDS-PAGE and Western blotting

LDS buffer containing protein samples were separated on a NuPAGE Bis-Tris gels with a 4-12% gradient at 150 V in MOPS SDS running buffer. Proteins were transferred onto a 0.45 µm nitrocellulose membrane in transfer buffer using the Xcell II Blot-Modul with 30 V for 115 min. All subsequent steps were carried out on a shaking platform and between the steps, the membrane was washed 3 times with PBS-T buffer. First, the protein transfer was checked by PONCEAU staining of the membrane. Next, the membrane was incubated in blocking buffer for 1 hour at RT, followed by incubation with primary antibody diluted in blocking buffer overnight at 4 °C. Lastly, the membrane was incubated with a secondary antibody coupled to horseradish peroxidase (1:5000 in blocking buffer) for 1 hour at RT. Signal detection was carried out in the ChemiDoc imaging system in combination with the SuperSignal West Pico Chemiluminescent Substrate.

4.5.4 Pull-down using GFP-Trap agarose / Strep-Tactin sepharose

Cell lysates were prepared as described above (see 4.6.2). 20 µl of pre-equilibrated GFP-trap or Strep-Tactin beads were added to 1 mg of lysate and incubated for 1 hour at 4 °C with rotation. The beads were washed 3 times with modified RIPA buffer supplemented with protease and phosphatase inhibitors, and excessive buffer was drained with a syringe. The dried beads were resuspended in 35 µl of 2x LDS buffer supplemented with 1 mM dithiothreitol (DTT) and incubated at 70 °C for 10 min before the supernatant was applied for SDS-PAGE. In the case of SILAC experiments, PDs were carried out separately and washed beads were mixed before eluting proteins in SDS buffer. For bait protein isolation, GFP-PDs were washed 3 times with 8M urea in PBS and twice in with RIPA buffer, before the proteins were eluted in SDS buffer.

4.5.5 Expression and purification of recombinant proteins

Vectors pDEST-15-N-GST-UBE3A or pET-53-DEST-N-His-POLD1 were transformed into Rosetta (DE3) cells, a colony was picked to inoculate a liquid culture overnight shaking at 37 °C in LB medium supplemented with the appropriate antibiotic. The next day, the culture was diluted 1:100 and grown at 37 °C in an antibiotic-containing LB medium while shaking until an optical density of ~0.5 was reached. Protein expression was induced with 0.4 mM IPTG, cells were shaken at 16 °C for 20 hours and pelleted for 15 min at 4000 g. The pellet was resuspended in lysis buffer and sonicated for 5 min on ice (5 mm tip, 20 cycles, output 5). The lysate was cleared at 18,500 g for 30 min, and the supernatant was incubated for 2 hours at 4 °C with pre-equilibrated glutathione agarose beads or Ni-NTA beads, respectively. Beads were washed three times with lysis buffer and proteins were eluted in elution buffer containing 10 mM reduced glutathione for His-POLD1 or 500 mM Imidazole for GST-UBE3A. Finally,

eluted proteins were dialyzed against 10% glycerol in PBS buffer and concentrated using D-Tube Dialyzer tubes.

4.5.6 Ubiquitination assay

For the UBE3A autoubiquitination assay, one 15 cm plate of U2OS cells was transfected with pcDNA-47-UBE3A-GFP. Two days later, cells were treated with the indicated chemotherapeutics, UBE3A-GFP was isolated as described (see 4.5.4). Dried beads were resuspended in 1x ubiquitination reaction mix from the E6AP/S5a Ubiquitination Kit. The mix was incubated for 4 hours at 37 °C while shaking at 400 rpm. Beads were washed 4-times with 8 M urea in PBS, and 2-times in modified RIPA. LDS buffer supplemented with 40 µM DTT was added to 2-fold concentration, and proteins were eluted for 10 min at 70 °C. For the POLD1 ubiquitination assay, the reaction mix was prepared as shown above including 1x His-UBE3A, and 1 µM His-POLD1.

4.5.7 GST Pull-down

50 ng GST-UBE3A were incubated with 20 µl of pre-equilibrated glutathione agarose beads in 500 µl modified RIPA lysis buffer supplemented with protease inhibitor and 1 mM DTT for 1 hour at 4 °C with rotation. Beads were washed 4 times with RIPA buffer, and 50 ng of His-POLD1 in 500 µl modified RIPA. After incubation for 1 hour at 4 °C with rotation, beads were washed 4 times with modified RIPA buffer, and proteins were eluted in 30 µl 2x LDS buffer supplemented with 1 mM DTT for 10 min at 70 °C.

4.5.8 iPOND

Per sample, three 15 cm dishes were grown to a confluence of 80%. EdU was added to the medium to a final concentration of 10 µM for 10 min. Afterward, cells were treated with the indicated chemotherapeutics. Cells were washed once with PBS and fixed with 10 ml fixation solution for 10 min at RT. PFA was removed and crosslinking was quenched with 10 ml glycine buffer. Cells were washed once with PBS, scraped in 10 ml 1% BSA in PBS, and spun down at 240 x g for 5 min (also for subsequent centrifugation steps). At this point, the cell pellet was snap-frozen and stored at -80 °C until the next day. Afterward, cells were resuspended in 1 ml permeabilization buffer and incubated for 10 min on ice, and then pelleted. The cell pellet was washed 2 times with 2 ml PBS. Click-reaction was carried out by resuspending the cells in 3480 µl H₂O, and sequential addition of 400 µl sodium L-ascorbate (100 mM), 40 µl azide-PEG3-biotin-conjugate (10 mM), and 80 µl copper sulfate (100 mM). The clique reaction was incubated for 30 min at RT. Cells were spun down, pelleted, and resuspended in 10 ml 1% BSA, 0.5% Tween-20 and incubated for 10 min at RT. Cells were washed 2 times in 2 ml PBS before they were lysed in 500 µl CL lysis buffer supplemented with inhibitors for 10 min with rotation at 4 °C. The lysate was spun down at 200 x g for 10 min, at 4 °C, and the pellet was incubated in 500 µl washing buffer for 10 min at 4 °C with rotation. The lysate was spun down at 200 x g for 10 min, the pellet was resuspended in 300 µl modified RIPA buffer (see, containing all inhibitors), and

sonicated using the Biorupter (20 cycles, output high, 30 sec sonication, 90 sec pause). Afterward, it was diluted with 300 μ l RIPA buffer and clarified at 16,100 x g for 45 min at 4 °C. Protein concentrations were measured by Bradford, equal amounts of lysate were mixed with 70 μ l of pre-equilibrated NeutraAvidin beads, and incubated for 1 hour at 4 °C with rotation. The beads were washed 5 times with modified RIPA buffer and excessive buffer was drained with a syringe. The dried beads were resuspended in 50 μ l of 2x LDS buffer supplemented with 1 mM DTT and incubated at 95 °C for 30 min before the supernatant was applied for SDS-PAGE.

4.6 Mass spectrometry-based proteomics

4.6.1 In-gel digestion

Cell lysates for in-gel digestion were mixed 1:4 with 4x LDS buffer containing 4 mM DTT. Samples were incubated for 10 min at 70 °C. After the samples had cooled down to RT, chloroacetamide (CAA) was added to a concentration of 5 mM and incubated for 40 min in the dark. Afterward, samples were separated on an SDS-PAGE (see 4.5.3) and stained using the Colloidal Blue Staining Kit. Each lane was cut into 6 to 10 pieces for separate processing. Each piece was further cut into 1 mm sized squares. The gel pieces were destained 4 times with 1 ml destaining solution for 20 min, and dehydrated by incubating 2 times with 1 ml 100% EtOH for 10 min, each with rotation. To digest the proteins, 50 μ l of trypsin solution (125 ng/ μ l trypsin in digestions buffer) were added to the pieces and it was incubated at 500 rpm for 2 min. The pieces were covered with digestions buffer and incubated overnight at 37 °C. The next day, the digest was stopped by adding 50 μ l of peptide extraction buffer. After 20 min incubation at 500 rpm, the supernatant was transferred to a fresh tube. Peptide extraction was further carried out by sequential incubation with extraction buffer, in-gel buffer B, and ACN using a volume big enough to cover the gel pieces (~100 μ l). Supernatants from the same gel piece were combined, concentrated by vacuum centrifugation at 45 °C to a volume of 100 μ l, and subjected to StageTip purification (see 4.6.7).

4.6.2 Cell lysis and in-solution digest

All steps were performed on ice. Cells were washed twice with ice-cold PBS and lysed in modified RIPA buffer supplemented with protease inhibitors and phosphatase inhibitors, and collected by scraping. For diGly-remnant enrichment, NEM was added to a concentration of 10 mM. After sonication, the lysates were cleared by centrifugation at 16,000 x g for 15 min. For lysates from SILAC labeled cells, protein concentrations were estimated using the QuickStart Bradford Protein assay and equal protein amounts from each label were combined. Proteins were precipitated in a fourfold excess of ice-cold acetone and incubated overnight at -20 °C, and the proteins were pelleted by centrifugation for 5 min at 1000 x g. Subsequently, the pellets were re-dissolved in denaturation buffer to a concentration of 2-8 μ g/ μ l. Cysteines were reduced with 2 mM DTT in the dark and alkylated with 10 mM CAA for 40 min respectively. For protein digestion, 1 μ g endoproteinase LysC was added to 75 μ g of protein for 6 hours. The mix was diluted 1:4 in water (old) / 50 mM Tris buffer (pH 8, new)

and sequencing grade-modified trypsin was added in a 1:150 (old) / 1:75 (new) ratio overnight. Protease digestion was stopped by the addition of TFA to 0.5% and the samples were incubated for 30 min at 4 °C. Formed precipitates were removed by centrifugation for 10 min at 4000 x g. To purify and concentrate the peptides, reversed-phase Sep-Pak C₁₈ cartridges were prepared by washing them once with ACN and three times with 0.1% TFA. After peptide samples were loaded, the columns were washed three times with water, dried, and stored at 4 °C.

4.6.3 TMT labeling

Peptides were eluted from SepPak columns in 2 ml 50% ACN, fully dried in a vacuum concentrator at RT, and resuspended in labeling buffer. Concentrations were determined with the Nanodrop at 280 nm and adjusted to 5 µg/µl. For each labeling reaction, 100 µg of peptides were mixed with an equal amount of TMT label (20 µg/µl) and incubated for 1 hour at 25 °C and 500 rpm in a thermoshaker. Labeling reactions were quenched by the addition of 5% hydroxylamine to an end concentration of 0.4% and incubated for 20 min at 25 °C and 1000 rpm. For samples with peptide concentrations lower than 0.2 µg/µl (diGly-remnant profiling), a TMT:peptide ratio of 16:11 (w/w) was used. Subsequently, the peptide samples were diluted in 0.1% TFA, reducing the ACN concentration below 3% [532]. At this point, peptide labeling was assessed as described previously by Zecha et al. [362]. To adjust for differences in labeled peptides between the labels, 5% of the samples were pooled, purified on C₁₈ STAGE tips, measured on the mass spectrometer, and adjustment factors were calculated. The remaining samples were pooled accordingly and purified on Sep-PAK columns as described above (4.6.2).

4.6.4 Phosphopeptide enrichment

TMT labeled peptides were eluted from Sep-PAK columns in 2 ml 50% ACN and acidified to a concentration 6% TFA. 1 mg of peptides were mixed with 2 mg of TiO₂ spheres and incubated for 1 hour at RT with rotation. Spheres were washed twice with 1 ml binding buffer and twice 1ml wash buffer. They were loaded onto a StageTip made with 1 layer of a C₈ 47 mm extraction disk and dried by centrifugation at 500 x g. Phosphorylated peptides were eluted with 100 µl of elution buffer 1, followed by 100 µl of elution buffer 2 by centrifugation at 400 x g. The eluted peptides were vacuum concentrated at 45 °C for 20 min to remove NH₄OH. pH was adjusted to < pH 2 with TFA and peptides were fractionated by Micro-SCX.

4.6.5 DiGly-remnant enrichment

TMT labeled peptides were eluted from Sep-PAK columns in 2 ml 50% ACN, vacuum dried, and resuspended in immunoprecipitation buffer. Precipitates were removed by centrifugation at 16.000 x g. PTMScan Ubiquitin Remnant Motif beads were equilibrated by washing three times in immunoprecipitation buffer. 1 mg of peptides were mixed with 1/7th of diGly beads and incubated for 4 hours at 4 °C with rotation. Beads were washed twice with diGly wash buffer 1, three times with immunoprecipitation buffer, and twice with water, using 1 ml each. Enriched peptides were eluted by

three consecutive incubations with 100 μ l 0.15% TFA at 1000 rpm. Finally, eluted peptides were dried to completion by vacuum centrifugation at RT and stored at -80 °C.

4.6.6 Micro-tip based strong cation exchange chromatography (Micro-SCX)

Micro-SCX tips were built by cutting out six disks from 47 mm cation exchange extraction disks with a 17-gauge Hamilton syringe and placed into a 200 μ l pipette tip [533–535]. SCX-tips were equilibrated with 50 μ l of methanol, SCX elution buffer pH 2.5, SCX elution buffer pH 11, and 100 μ l of SCX wash buffer by centrifuging at 500 x g. Acidified peptides samples (< pH 2) were loaded onto the SCX-tips at 400 x g. Subsequently, peptides were fractionated by eluting with 100 μ l of SCX elution buffers at 700 x g from lowest to highest pH. Eluates were vacuum centrifuged to remove ACN for 20 min at 45 °C and subsequently desalted by C₁₈ StageTipping (see 4.6.7).

pH of SCX-buffers:

(Chromatin-) proteome: 3.2 / 3.6 / 3.9 / 4.25 / 4.8 / 5.5 / 7 / 11

Phosphopeptides: 2.5 / 2.8 / 3.2 / 3.5 / 3.75 / 4 / 4.25 / 4.5 / 5 / 5.5 / 6.5 / 11

DiGly-remnant peptides: 3.5 / 4.5 / 5.5 / 6.5 / 8 / 11

4.6.7 Desalting and concentration of peptides

Peptide purification was carried out using self-made and extremely economical stop-and-go-extraction tips (StageTips) [533]. In short, StageTips were built by cutting out 2 disks from a C₁₈ 47 mm extraction disks with a 17-gauge Hamilton syringe and placed into a 200 μ l pipette tip. StageTips were equilibrated with each 25 μ l of methanol, followed by 25 μ l stage tip buffer B and 2 x 25 μ l stage tip buffer A by centrifuging at 500 x g. The samples were loaded on the tip and washed with 50 μ l Buffer A in the same fashion. Dried StageTips were stored at 4 °C. The peptides were eluted with 50 μ l elution buffer into 96-well sample plates by applying pressure with a syringe and vacuum concentrated to a volume of 2 μ l. Finally, 3 μ l of 0.1% FA was added.

4.6.8 MS analysis

Peptide fractions were analyzed on quadrupole Orbitrap mass spectrometers equipped with a UHPLC system. Peptide samples were loaded onto C₁₈ reversed-phase columns and eluted with a linear ACN gradient containing 0.1% formic acid. The mass spectrometer was operated in DDA mode, automatically switching between MS1 and MS2 acquisition. Survey full-scan MS spectra were acquired in the Orbitrap. The n most intense ions were sequentially isolated and fragmented by HCD. Peptides with unassigned charge states, as well as with charge states less than +2 were excluded from fragmentation. Fragment spectra were acquired in the Orbitrap mass analyzer [321, 328, 536]. LC and mass spectrometer settings are listed below. Data of the initial screen was solely acquired on the Exploris mass spectrometer setup.

LC parameter							
LC system	Analytical column (Reprosil Pur, Dr. Maisch)	Flow rate (nL/min)	Solvent A	Solvent B	Gradient (B in A)	Effective gradient length (min)	Total length of method (min)
EASY-nLC 1000	25 cm x 75 μ m, 1.9 μ m C18 resin	250	0.1 % FA in 3 % ACN	0.1 % FA, 90 % ACN	2-65%	Interactome: 88 min Proteome: 158 min DiGly: 108 min	Interactome: 105 min Proteome: 175 min DiGly: 125 min
EASY-nLC 1200	55 cm x 75 μ m, 1.9 μ m C18 resin	250	0.1 % FA in 3 % ACN	0.1 % FA, 90 % ACN	3-42 %	Proteome: 103 min Phospho: 103 min DiGly: 103 min	Proteome: 120 min Phospho: 120 min DiGly: 120 min

MS settings														
Mass spectrometer	MS1 resolution	MS1 AGC	MS1 maxIT (ms)	MS1 mass range (m/z)	MS2 resolution	TurboTMT	Advanced peak determination	MS2 AGC	MS2 maxIT (ms)	TopN / Cycle time	Isolation window (m/z)	Fixed first mass (m/z)	NCE	Dynamic exclusion (s)
Q Exactive Plus	70k	3.E+06	20	350-1,650	35k	---	---	1.E+05	120	Top10	2.6	---	25	Interactome: 20s Proteome: 25s
Exploris	60k	300%	Proteome: 28 ms Phospho: 28 ms DiGly: 40 ms	350-1,650	15k	on	off	100%	Proteome: 40 ms Phospho: 40 ms DiGly: 110 ms	Top15	0.8	100	33	25

4.6.9 MS peptide identification

Raw data files were analyzed using MaxQuant (version 1.5.2.8) [537]. Parent ion and MS2 spectra were searched against a database containing 92,578 human protein sequences obtained from the UniProtKB released in December 2016 using the Andromeda search engine [538]. Spectra were searched with a mass tolerance of 6 ppm in MS mode, 20 p.p.m. in HCD MS2 mode, strict trypsin specificity, and allowing up to two miscleavages. Cysteine carbamidomethylation was searched as a fixed modification, whereas cysteine modification with NEM, protein N-terminal acetylation, methionine oxidation, and phosphorylation of serine, threonine, and tyrosine were searched as variable modifications. Site localization probabilities were determined by MaxQuant using the PTM scoring algorithm as described previously. The dataset was filtered based on posterior error probability to arrive at a false discovery rate below 1% estimated using a target-decoy approach [539]. The match between runs and the re-quantify features were switched on.

TMT samples

Raw files from TMT samples were analyzed with the same settings as shown above with the following exceptions: Maxquant version 1.6.14 was used. Spectra were searched against a database containing 96,788 human protein sequences obtained from the UniProtKB released in February 2020. Up to three miscleavages were allowed, and spectra were filtered for precursor ion fractions (PIF) > 0.75.

4.6.10 Data processing and visualization

Proteins/Peptides identified from the reversed database, identified by site, or identified as potential contaminants were excluded, as were proteins with no unique or less than two identified peptides. The cut-off criterion for the localization probability of each phosphosite was ≥ 0.75 , or 0.9 in the case of diGly sites (= class I sites). For the TMT experiments, multiply modified peptides were analyzed separately. Furthermore, protein and peptide intensities were normalized to correct for loading mistakes and batch effects. Isotope corrected intensities were first divided by the corresponding reference intensity separately for each batch (reference normalization). In a second step, intensities in each sample were divided by the sample mean/median (mean/median centering). Last, intensity averages for each protein or peptide were calculated per batch. Subsequently, each intensity was divided by said average (per-protein/peptide centering). Statistical analysis and data visualization was performed using the R

Materials and Methods

software environment (v3.6.1). Moderated *t*-tests corrected for multiple hypothesis testing (Benjamini Hochberg) were calculated using the limma package, allowing peptides/proteins measured in at least two replicates (“FDR”) [540]. Unsupervised hierarchical clustering and corresponding heatmaps were created using the pheatmap or the gplots package. The umap package was used for UMAP clustering [541]. GOterm enrichment analysis was carried out using Gorilla [542]. Sequence motif analysis was performed in IceLogo, and overrepresented motifs were identified by sequence annotation followed by a Fisher’s exact test in Perseus (v1.6.14.0) [374, 543]. Protein interaction networks were analyzed using the STRING database and visualized with Cytoscape (v3.8.2) [544]. Enrichment analysis for protein clusters was also carried out using “stringApp” in cytoscape. Kinase activities were predicted using the KSEA algorithm (KSEAapp) with updated known kinase-substrate relations (PhosphoSitePlus, 04/2021) and a prediction NetworKIN cutoff of 5 [375, 545]. Kinase prediction using PTM-SEA, and enrichment analysis by EGSEA were performed as implemented in ProteoViz [366, 376, 391].

5 Abbreviations

•O ₂	Hydroxyl radical
5'-dRP	5'-deoxyribose phosphate
53BP1	TP53-binding protein 1
5mC	5-methylcytosine
6-4PPs	6'-4' photoproducts
8-oxoG	7,8 dihydro-8-oxoguanine
A (DNA)	Adenine
A (Proteins)	Alanine
ABC	Ammonium bicarbonate
AC	Alternating voltage
ACN	Acetonitril
ADR	Alylation damage repair
aEJ	Alternative end-joining
AID	Activation-Induced Cytidine Deaminase
alt-NHEJ	Alternative NHEJ
APE1	DNA-(apurinic or apyrimidinic site)endonucleases 1
APE2	DNA-(apurinic or apyrimidinic site)endonucleases 2
APEX	Ascorbic acid peroxidase
APH	Aphidicolin
AP-site	Abasic site
AS	Angelman syndrome
ASD	Autism spectrum disorders
AsO ₂	Sodium(meta)arsenite
AspN	Endoproteinase AspN
ATM	Ataxia telangiectasia mutated
ATP	Adenosine triphosphate
ATR	Ataxia telangiectasia and Rad3 related
ATRIP	ATR interacting protein
AZUL	Amino-terminal Zn-finger of UBE3A ligase
BER	Base excision repair
BIR	Break-induced replication
BL	B-cell lymphoma and Burkitt's lymphoma
Bp	Base pairs
BP	Biological process
BRCA1	Breast cancer type 1 susceptibility protein
BRCA2	Breast cancer type 2 susceptibility protein
C	Cytosine
C ₁₈	Octadodecyl alkane chains
CAA	Chloroacetamide
CC	Cellular compartment
CDKs	Cyclin-dependent kinases
CETN2	Centrin-2
CHEK1	Checkpoint kinase 1 (gene)
CHEK2	Checkpoint kinase 2 (gene)
CHK1	Checkpoint kinase 1 (protein)
CHK2	Checkpoint kinase 2 (protein)
CID	Collision-induced dissociation
CisP	Cisplatin
CK2	Casein kinase 2
CPDs	Cyclopurimidine dimers

Abbreviations

CPT	Camptothecin
CRL	Cullin-RING E3 ligases
CSA	Cockayne syndrome A protein
CSB	Cockayne syndrome B protein
CSNK2A1	Casein kinase II subunit alpha
CTR	Control
DAM	DNA adenine methylase
DC	Direct current
DDA	Data-dependent acquisition
DDR	DNA damage response
DDR base	DNA Damage Response dataBase
DDR conditions / treatments	Treatments eliciting ATM/ATR activation; all treatments expect AsO ₂
Degron	Degradation signal
dHJ	Double HJ
DIA	Data-independent acquisition
DiGly	Lys- ϵ -Gly-Gly
D-loop	Displacement loop
DNA	Deoxyribonucleic acid
DNA-PK	DNA-dependent protein kinase
DNA-PKcs	DNA-dependent protein kinase catalytic subunit
DNS	Desoxyribonukleinsäure
dNTP	Deoxynucleotide
dNTPs	Deoxyribonucleotide triphosphates
DSB	Double strand break
DSBR	Double strand break repair
DTT	Dithiothreitol
DUB	Deubiquitinating enzyme
DVIs	Dewar valence isomeres
E1	Ubiquitin-activating enzyme
E2	Ubiquitin-conjugating enzyme
E3	Ubiquitin-ligating enzyme
EASI-tags	Easily abstractable sulfoxide-based isobaric-tag
EdU	5-Ethynyl-2'-deoxyuridine
EGFR	Epidermal growth factor receptor
EGSEA	Ensemble Gene Set Enrichment Analysis
ELM	Eukaryotic Linear Motif
EMCV	Encephalomyocarditis virus
ESI	Electrospray ionization
ETAA1	Ewing's tumor-associated antigen 1
ETO	Etoposide
EXO1	Exonuclease 1
FA	Formaldehyd
FAIMS	High-Field Asymmetric-waveform Ion Mobility Spectrometry
FDR	False discovery rate
FEN1	Flap endonuclease 1
G	Guanine
GEM	Gemcitabine
GG-NER	Global genome NER
GluC	Endoproteinase GluC
GO	Gene enrichment
GSEA	Gene Set Enrichment Analysis

Gy	Gray
H ₂ O ₂	Hydrogen peroxide
HA	Human influenza hemagglutinin
HBB	Beta-globin
HCD	Higher-energy c-trap/collision dissociation
HCV	Hepatitis C virus
HECT	Homologous to the E6AP carboxyl terminus
HEPES	4-(2-hydroxyethyl)-1-piperazineethanesulfonic acid
HJ	Holliday junction
HPV	Human papillomavirus
HR	Homologous recombination
HU	Hydroxyurea
HUVEC	Human umbilical vein endothelial cells
ICL	Inter-strand crosslink
IDLs	Insertion-deletion loops
IFM	Immunofluorescence microscopy
IMB	Institute of Molecular Biology
IP	Immunoprecipitation
iPOND	Isolation of proteins on nascent DNA
IR	Ionizing radiation
JAMM	JAB1, MPN, MOV34 family
KD	Knock-down
KDa	1,000 Dalton
KEGG	Kyoto Encyclopedia of Genes and Genomes
KO	Knock-out
LC ₃₀	Lethal concentration - killing 30% of cells
LC-MS/MS	Liquid chromatography and tandem mass spectrometry
LET	Linear energy transfer
LFQ	Label-free quantification
LIG1	DNA ligase 1
LIG3	DNA ligase 3
LysC	Endoproteinase LysC
m/z	Mass to charge
m ⁶ a	N6-methyladenine
MAPK	Mitogen-activated protein kinases
MCM	Minichromosome maintenance
MDC1	Mediator of DNA damage checkpoint protein 1
MF	Molecular function
Micro-SCX	Micro-tip based strong cation exchange chromatography
MINDY	Motif-interacting with ubiquitin-containing novel DUB family
MJD	Machado-Josephin domain-containing proteases
MMC	Mitomycin C
MMEJ	Microhomology-mediated end-joining
MMR	Mismatch repair
MMS	Methyl methanesulfonate
MNNG	N-methyl-N-nitro-N-nitrosoguanidine
MNU	N-methyl-N-nitrosourea
mRNA	Messenger RNA

Abbreviations

MS	Mass spectrometry
MS/MS	Tandem MS
MS1	First stage of mass analysis / precursor spectrum
MS2	Second stage of mass analysis / fragment spectrum
Multiplicity	Number of PTMs on a detected peptide
N	Number of biological replicates
NADPH	Nicotinamide adenine dinucleotide phosphate
NEM	N-ethylmaleimide
NER	Nucleotide excision repair
NHEJ	Non-homologous end joining
NHS	N-hydroxysuccinimide
NLS	Nuclear localization signal
NMPs	Nucleotide monophosphates
O ⁶ -mG	O ⁶ -methyl-guanine
OTU	Ovarian tumor proteases
PARP	Poly (ADP-ribose) polymerase (PARP)
PBS	Phosphate buffered saline
PCNA	Proliferating cell nuclear antigen
PCR	Polymerase chain reaction
PEI	Polyethylenimine
PEP	Posterior error probability
PIF	Filtered for precursor ion fractions
PIKKs	phosphatidylinositol 3-kinase-related kinases
PIPKs	Phosphatidylinositol phosphate (PIP) kinases
PKA	Protein kinase A
PML	Promyelocytic leukaemia
PNKP	Polynucleotide kinase 3'-phosphatase
POLD1	DNA polymerase delta catalytic subunit
POL δ	DNA polymerase δ
POL ϵ	DNA polymerase ϵ
PRDX	Peroxiredoxin
PRR	Postreplication repair
PSM	Peptide spectral match
P-TEFb	Positive transcription elongation factor b
PTM	Posttranslational modification
PTMs	Post-translational modification
PTM-SEA	PTM Signature Enrichment Analysis
RAZUL	hRpn10 AZUL-binding domain
RB	Retinoblastoma protein
RBP	RNA-binding proteins
RBR	RING-Between-RING
RER	Ribonucleotide excision repair
RFC	Replication factor C
RFWD3	RING finger and WD repeat domain-containing protein 3
RING	Really interesting new gene
RIPA	Radioimmunoprecipitation assay buffer
RLIM	RING finger LIM domain-binding protein
RNA	Ribonucleic acid
RNAPII	RNA polymerase II

ROS	Reactive oxygen species
RP	Reversed-phase
RPA	Replication protein A
RP-HPLC	Reversed-phase high-performance chromatography
RPLs	60S ribosomal subunits
Rpm	Rotations per minute
RPN10	26S proteasome regulatory subunit RPN10
RPSs	40S ribosomal subunits
RQC	Ribosome-associated quality control
RS	Replication stress
RT	Room temperature (~22-23°C)
S	Serine
S/TQ motif	Serine or threonine residues followed by glutamine
S6Ks	RPS6 ribosomal protein kinases
SAM	S-adenosylmethionine
SCD	Sickle cell disease
SCX	Strong cation exchange
SDS-PAGE	Sodium dodecyl sulfate polyacrylamide gel electrophoresis
SH2/3	Src-homology-2/3
SILAC	Stable isotope labeling with amino acids in cell culture
siRNA	Short interfering RNA
SSA	Single-strand annealing
SSB	Single-strand DNA break
SSBR	Single-strand DNA break repair
ssDNA	Single stranded DNA
StageTips	Self-made and extremely economical stop-and-go-extraction tips
Strep-Ub	Strep-tagged ubiquitin
SUMO	Small ubiquitin-related modifier
T (DNA)	Thymidine
T (Protein)	Tyrosine
TC-NER	Transcription-coupled NER
TDP1	Tyrosyl DNA phosphodiesterase 1
TDP2	Tyrosyl DNA phosphodiesterase 2
TEAB	Triethylammonium bicarbonate
TFs	Transcription factors
TiO ₂	Titanium dioxide
TLS	Translesion synthesis
TMT	Tandem mass tag
TMTc	TMTcomplementary
TMT-MS3	TMT-Measuring the reporter ions in the third dimension
TOP1	Topoisomerase 1
TOP1cc	Topoisomerase 1 cleavage complex
TOP2	Topoisomerase 2
TOP2cc	Topoisomerase 2 cleavage complex
TOPBP1	Topoisomerase 2 binding protein 1
TRIC	T-complex protein Ring Complex
TS	Template switching
U	Uridine
U2OS	Human Bone Osteosarcoma Epithelial Cells

Abbreviations

UBA	Ubiquitin associated domain
UBC	Ubiquitin conjugating enzyme
UBDs	Ubiquitin-binding domains
UBE3A (E6AP)	HECT-type ubiquitin transferase E3A
UCH	Ubiquitin carboxyl-terminal hydrolases
UIM	Ubiquitin interacting motif
UMAP	Uniform manifold approximation
USP	Ubiquitin-specific proteases
USP	Ubiquitin-specific protease
UV	Ultraviolet
VCP	Valosin-containing protein
VIM	VCP-interacting motif
VWA	Von Willebrand factor A
WB	Western blot
WCL	Whole cell lysate
WT	Wild type
XP	Xeroderma pigmentosum
XPA	Xeroderma pigmentosum group A-complementing protein
XPC	Xeroderma pigmentosum group C
Y	Tyrosine
ZUFSP	Zinc finger with UFM1-specific peptidase protein
ϵ -NH ₂	Epsilon-amino group
ω z	Axial oscillations

6 Appendix

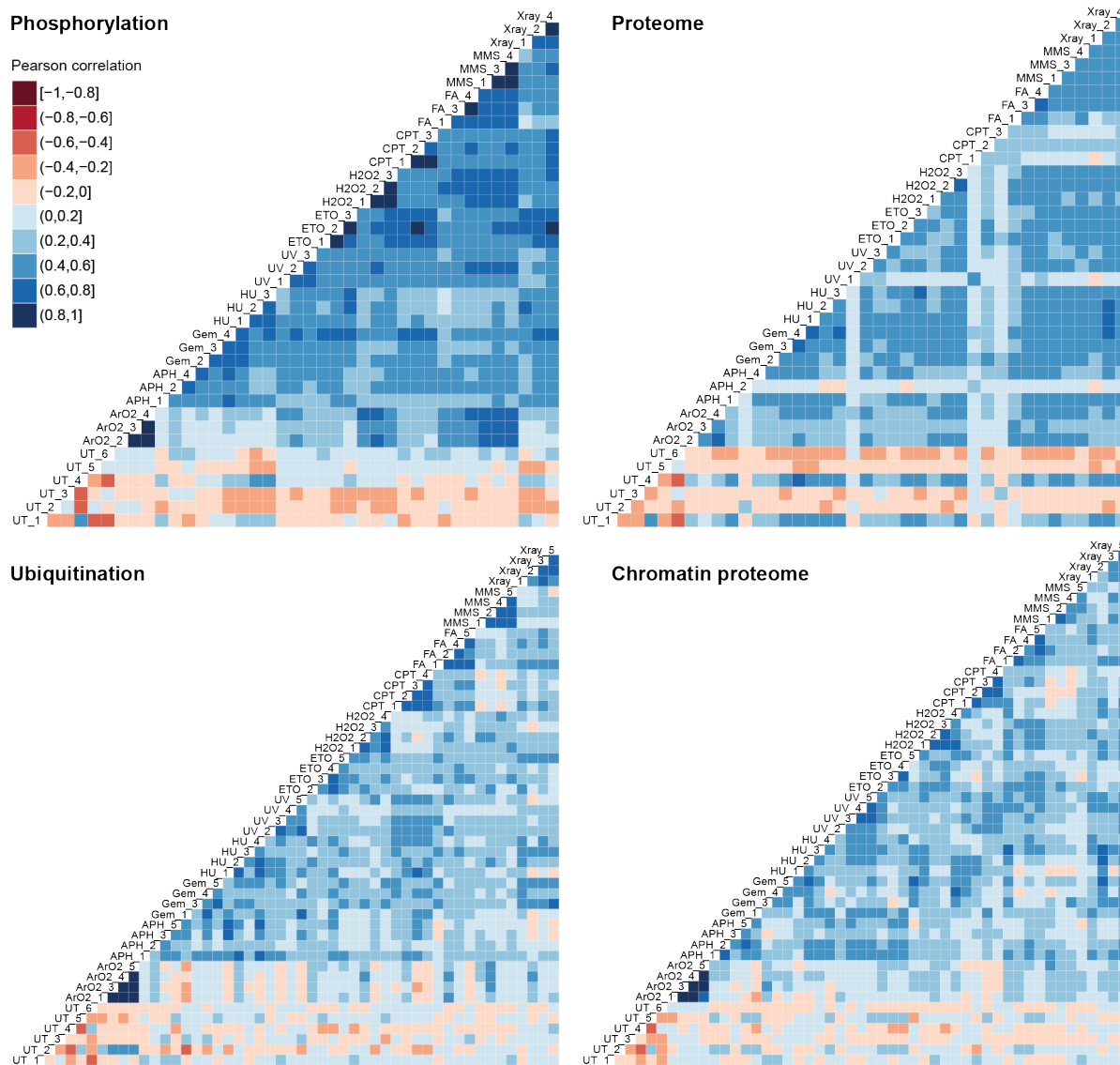


Figure 26: Correlation of phosphoproteome, proteome, ubiquitinome, and chromatin proteome experiments. For each measured protein/peptide intensity, a ratio was calculated against the corresponding untreated intensity mean. Pearson correlations were calculated from the \log_2 transformed ratios.

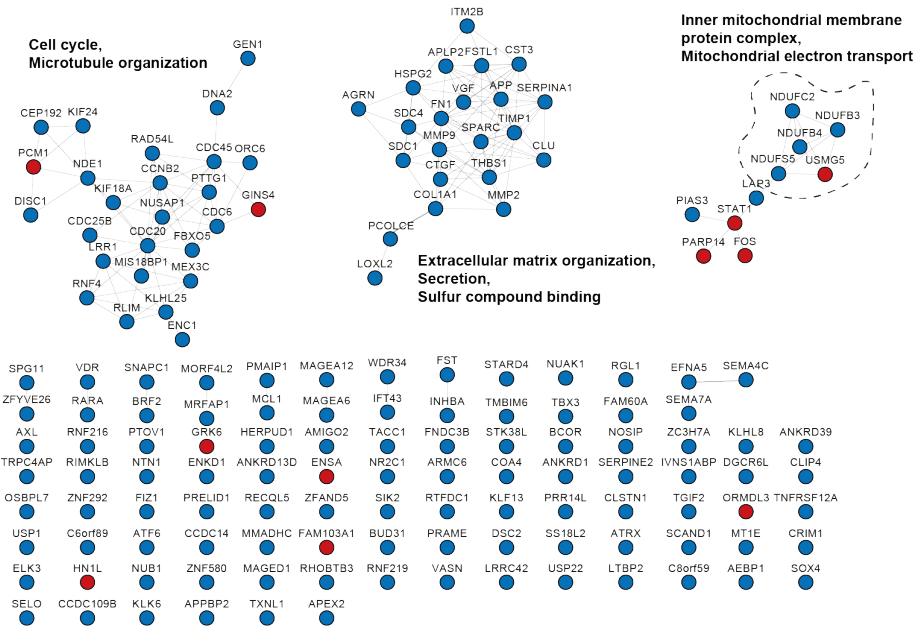


Figure 27: Network analysis of proteins up- (red) or downregulated (blue) upon AsO₂ treatment. Network analysis was carried out using the STRING database (confidence ≥ 0.7). GO terms enriched for the network clusters are displayed. Proteins not connected to the main networks are shown below.

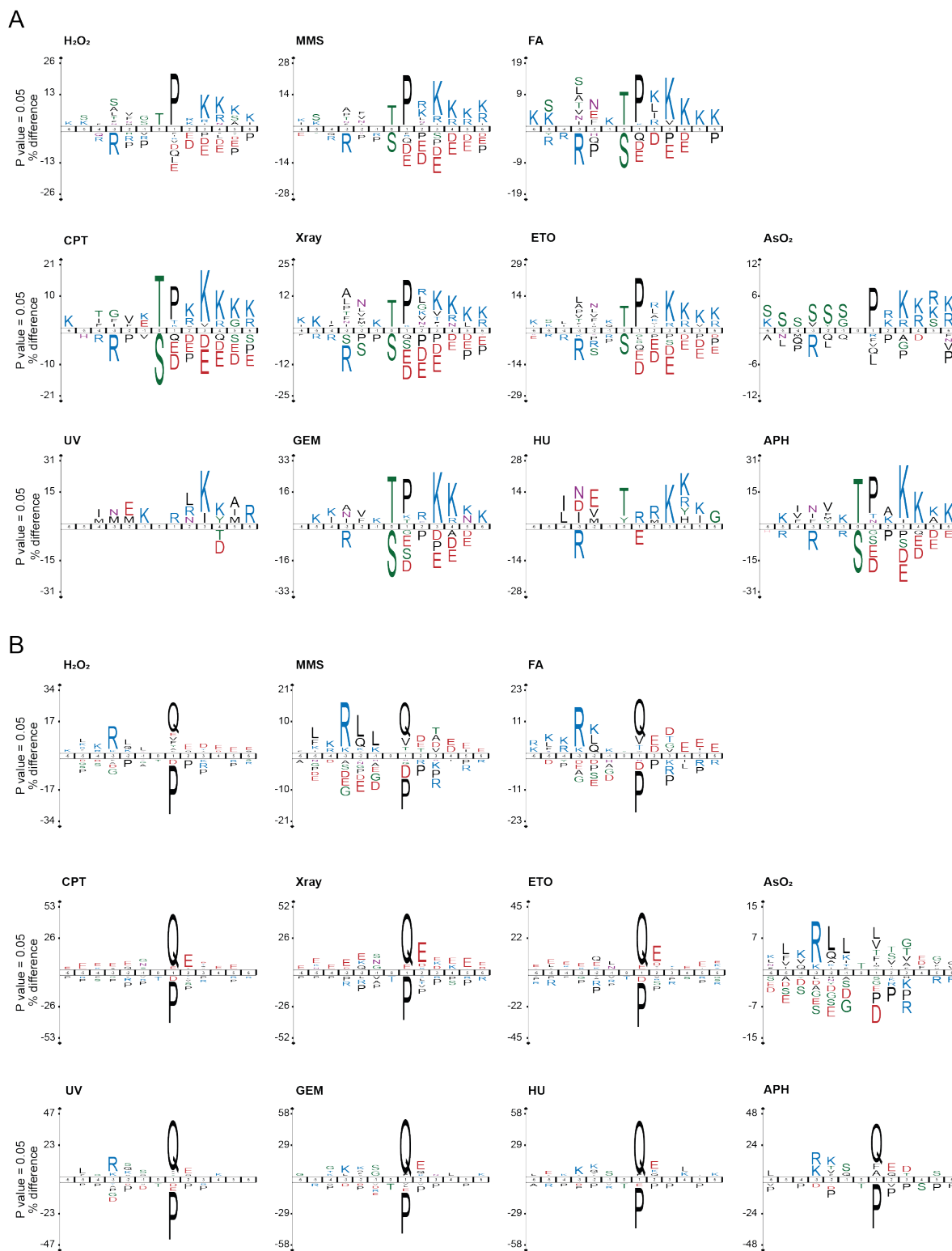
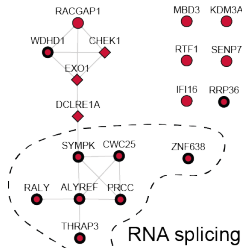
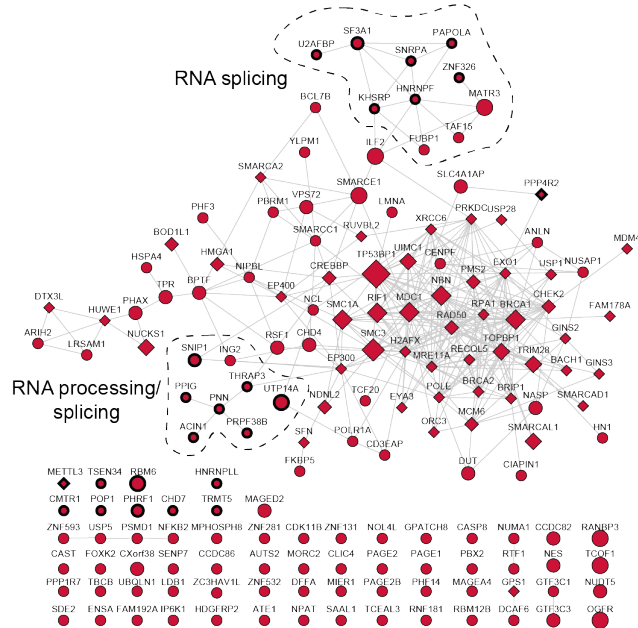


Figure 28: Sequence motif analysis of treatment-specific phosphorylation sites by IceLogo. Sequence windows of significantly down- (A) or up-regulated (B) phosphorylation sites were compared to all quantified phosphorylation sites. Overrepresentation of amino acids at positions relative to the phosphorylation site is displayed in percent.

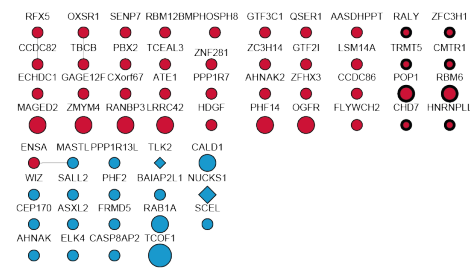
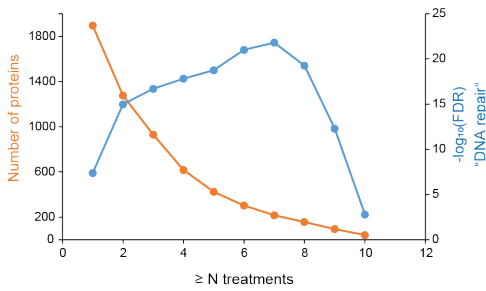
A



B



C



D

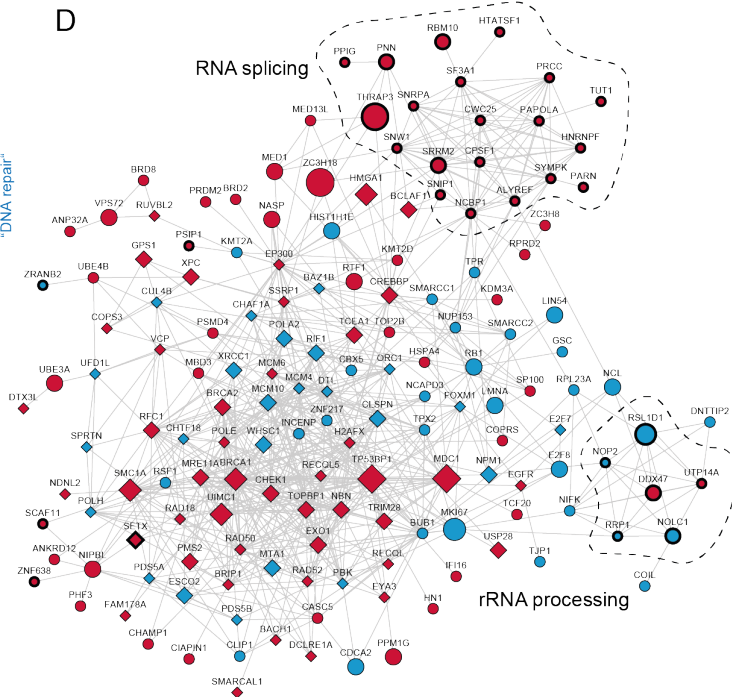


Figure 29: Network analysis of phosphorylated proteins in the DNA damage response. The network displays proteins with upregulated phosphorylation sites, especially upon HU, APH, GEM, and UV treatments. This information was extracted from **Figure 15** cluster #11 (A). Proteins with upregulated phosphorylation sites especially upon DSB inducing treatments (ETO, CPT, X-ray, H₂O₂; extracted from **Figure 15** cluster #5-6) (B). Enrichment analysis of the GO term “DNA repair” for proteins with differentially regulated phosphorylation sites in n treatment conditions. The plot shows the number of proteins that are regulated in n treatment conditions, and the corresponding FDR from the enrichment analysis (C). Network of proteins with regulated phosphorylation in at least 7 of the DNA damage conditions (D). Clusters other than proteins annotated for “DNA repair” are highlighted.

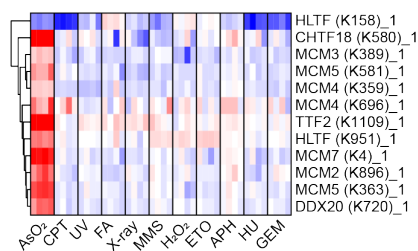


Figure 30: Ubiquitination sites of proteins corresponding to “MF helicase activity” (see Figure 16A).

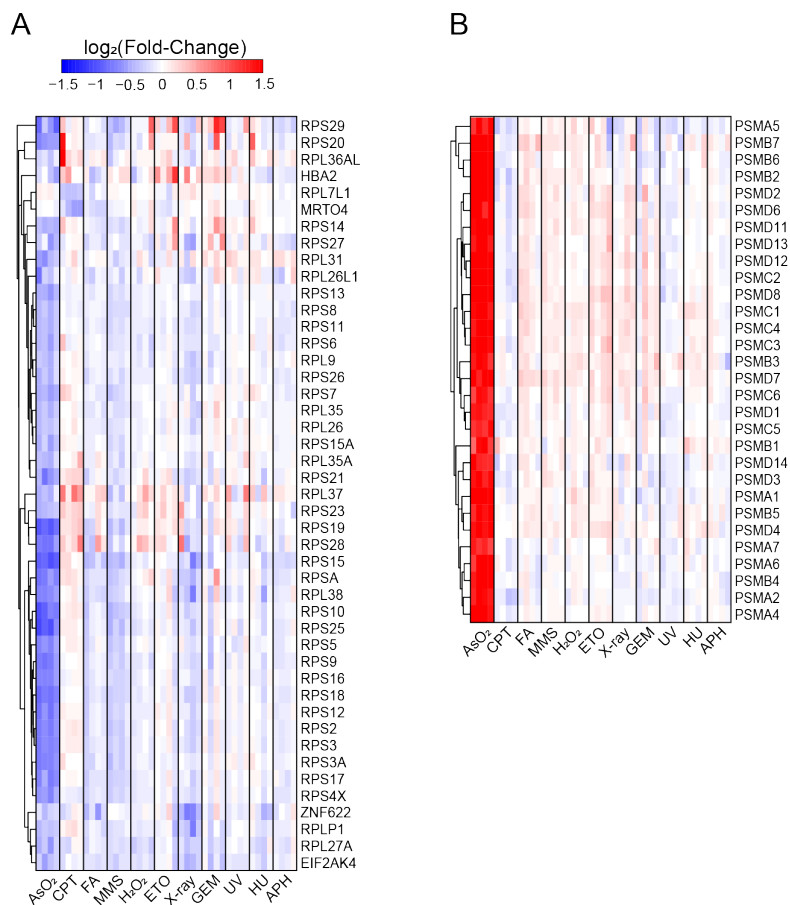


Figure 31: Proteins recruited to or removed from chromatin corresponding to the enriched GO terms “Ribosome” (A) or “MF helicase activity” (see Figure 16A) (B).

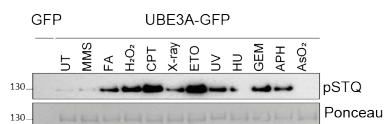


Figure 32: S/Q-specific phosphorylation of UBE3A upon DNA damage induction. UBE3A-GFP was overexpressed in U2OS cells and treated with the indicated agents (treatment conditions see Figure 10A). UBE3A was pulled-down, washed with urea, and S/T-Q specific phosphorylation was detected by Western blotting.

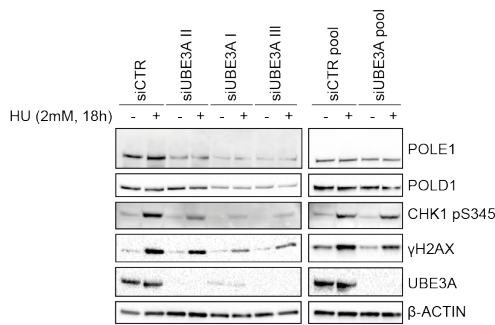


Figure 33: DNA damage signaling upon UBE3A depletion using different siRNAs analyzed by Western blotting.

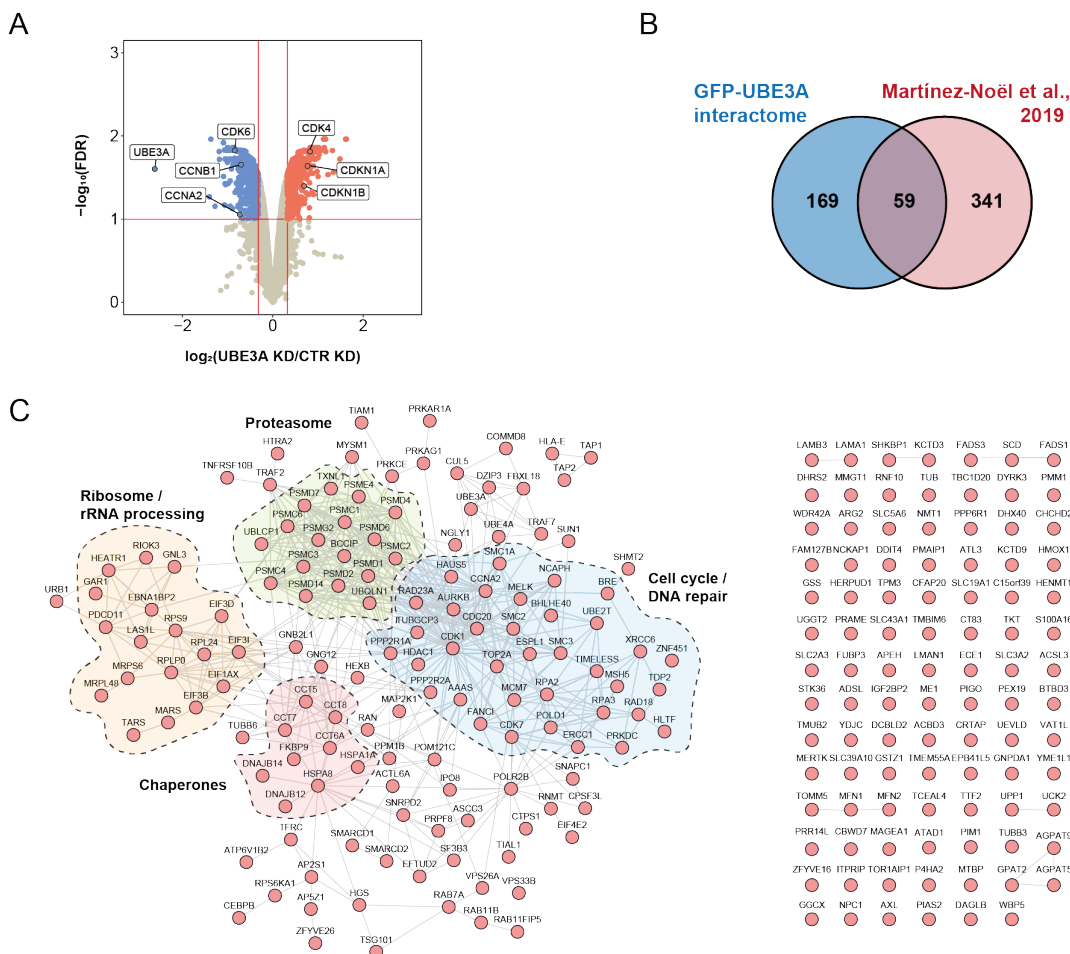


Figure 34: Proteome analysis upon UBE3A depletion using an siRNA pool. CDKs (CDK4/6) cyclins (CCNB1, CCNA2), and cyclin-dependent kinase inhibitors (CDKN1A (p21), CDKN1B (p27)) are highlighted ($FDR \leq 0.01$, 1.5-fold change, $n=4$) (A). Overlap of UBE3A interactors determined by GFP-UBE3A PD and interactors predicted by Martinez-Noël et al, 2019 [421] (B). Network of proteins with decreased diGly sites upon UBE3A KD. Enriched GO terms of the indicated clusters are indicated ($FDR \leq 0.01$, 1.5-fold change, $n=4$) (C).

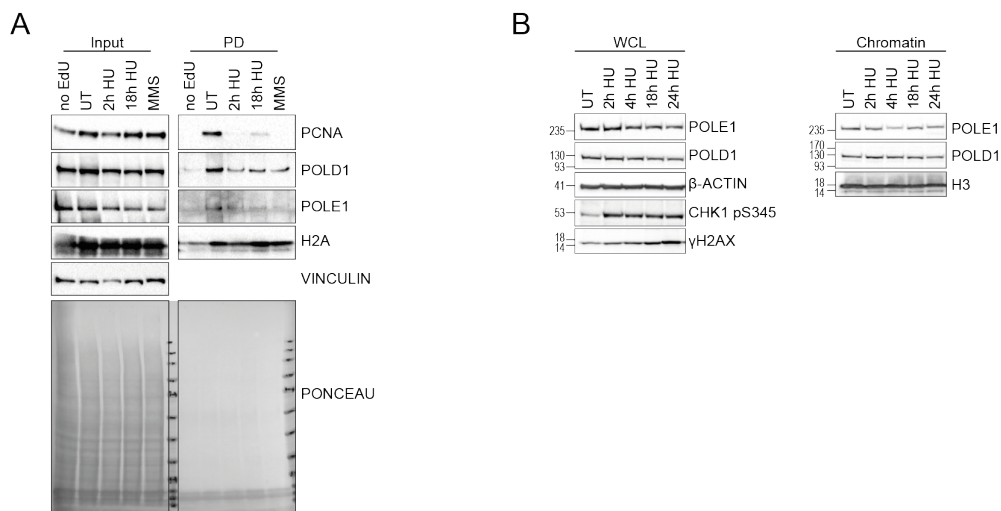


Figure 35: iPOND upon HU (2 mM) and MMS (0.02%) treatment for 2 hours (A). WCL and isolated chromatin fraction upon 2, 4, 18, and 24 hour HU treatments. POLD1 and POLE1 levels decreased over time (B).

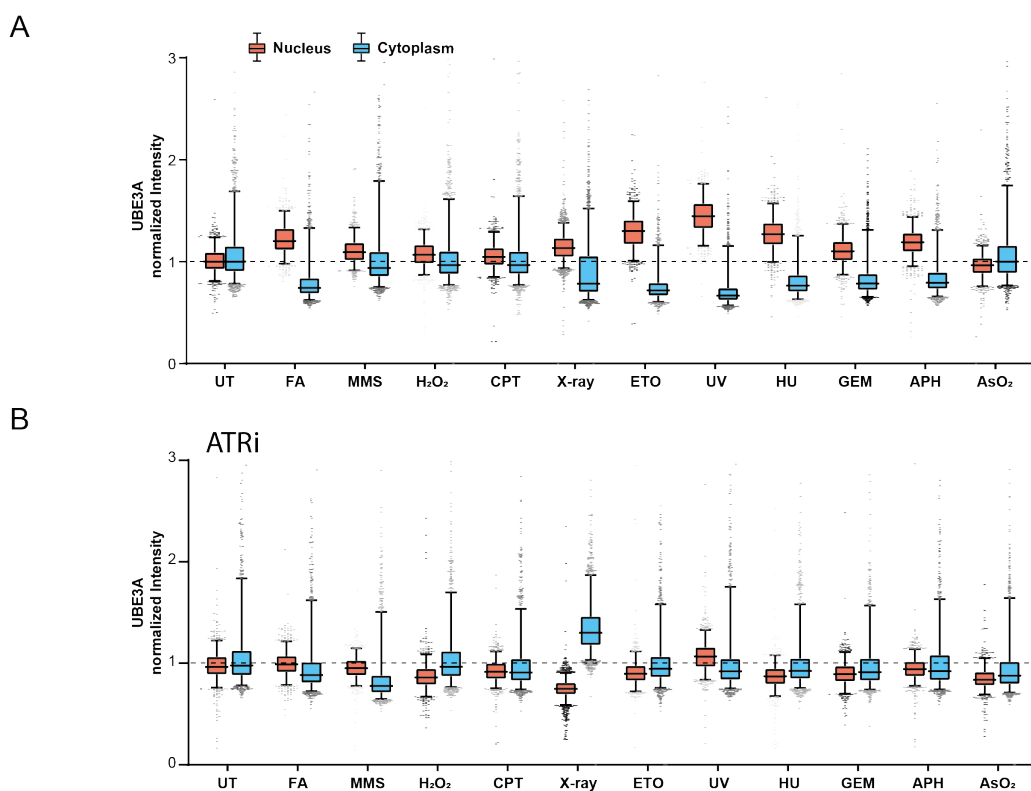
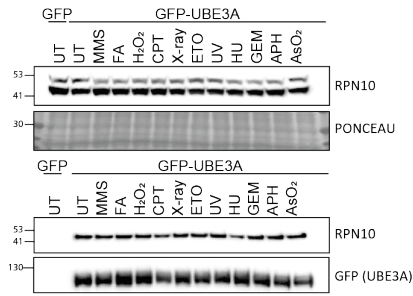
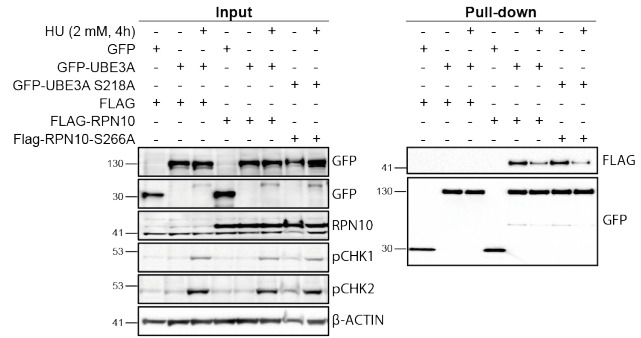


Figure 36: Localization of endogenous UBE3A upon DNA damage induction. Boxplots show UBE3A intensities upon ETO or AsO₂ treatment in the nucleus and cytoplasm determined by IFM (treatment conditions see Figure 10A) (A). Cells were additionally treated with 5 μM ATR inhibitor (B). Intensities were normalized to the UT sample (n=3).

A



B



C

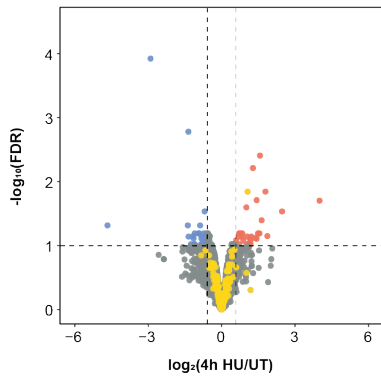


Figure 37: Interaction of GFP-UBE3A with RPN10 upon treatment with different DNA damage-inducing agents for 2 hours (for concentrations see Figure 10A) (A). Mutation of serines in UBE3A (S218A) and RPN10 (S266A), did not rescue interaction upon HU treatment (B). DiGlyc remnant enrichment analysis upon treatment with 2 mM HU for 4 hours depicted in a volcano plot. Sites on proteasome subunits are indicated in gold (FDR \leq 0.1, 1.5-fold change, n=3) (C).

7 References

1. Tasaki E, Mitaka Y, Nozaki T, Kobayashi K, Matsuura K, Iuchi Y. High expression of the breast cancer susceptibility gene BRCA1 in long-lived termite kings. *Aging (Albany NY)*. 2018;10:2668–83. doi:10.18632/aging.101578.
2. Lindahl T, Barnes DE. Repair of endogenous DNA damage. *Cold Spring Harb Symp Quant Biol*. 2000;65:127–33. doi:10.1101/sqb.2000.65.127.
3. Bont R de, van Larebeke N. Endogenous DNA damage in humans: a review of quantitative data. *Mutagenesis*. 2004;19:169–85. doi:10.1093/mutage/geh025.
4. Kunkel TA. DNA replication fidelity. *J Biol Chem*. 2004;279:16895–8. doi:10.1074/jbc.R400006200.
5. Kunkel TA. Balancing eukaryotic replication asymmetry with replication fidelity. *Curr Opin Chem Biol*. 2011;15:620–6. doi:10.1016/j.cbpa.2011.07.025.
6. Kunkel TA. Evolving views of DNA replication (in)fidelity. *Cold Spring Harb Symp Quant Biol*. 2009;74:91–101. doi:10.1101/sqb.2009.74.027.
7. Kunkel TA, Erie DA. DNA mismatch repair. *Annu Rev Biochem*. 2005;74:681–710. doi:10.1146/annurev.biochem.74.082803.133243.
8. Nick McElhinny SA, Kumar D, Clark AB, Watt DL, Watts BE, Lundström E-B, et al. Genome instability due to ribonucleotide incorporation into DNA. *Nat Chem Biol*. 2010;6:774–81. doi:10.1038/nchembio.424.
9. Williams JS, Lujan SA, Kunkel TA. Processing ribonucleotides incorporated during eukaryotic DNA replication. *Nat Rev Mol Cell Biol*. 2016;17:350–63. doi:10.1038/nrm.2016.37.
10. Sparks JL, Chon H, Cerritelli SM, Kunkel TA, Johansson E, Crouch RJ, Burgers PM. RNase H2-initiated ribonucleotide excision repair. *Mol Cell*. 2012;47:980–6. doi:10.1016/j.molcel.2012.06.035.
11. Viguera E, Canceill D, Ehrlich SD. Replication slippage involves DNA polymerase pausing and dissociation. *EMBO J*. 2001;20:2587–95. doi:10.1093/emboj/20.10.2587.
12. Pommier Y, Barcelo JM, Rao VA, Sordet O, Jobson AG, Thibaut L, et al. Repair of topoisomerase I-mediated DNA damage. *Prog Nucleic Acid Res Mol Biol*. 2006;81:179–229. doi:10.1016/S0079-6603(06)81005-6.
13. Wang JC. Cellular roles of DNA topoisomerases: a molecular perspective. *Nat Rev Mol Cell Biol*. 2002;3:430–40. doi:10.1038/nrm831.
14. Pommier Y, Sun Y, Huang S-YN, Nitiss JL. Roles of eukaryotic topoisomerases in transcription, replication and genomic stability. *Nat Rev Mol Cell Biol*. 2016;17:703–21. doi:10.1038/nrm.2016.111.
15. Staker BL, Hjerrild K, Feese MD, Behnke CA, Burgin AB, Stewart L. The mechanism of topoisomerase I poisoning by a camptothecin analog. *Proc Natl Acad Sci U S A*. 2002;99:15387–92. doi:10.1073/pnas.242259599.
16. Sordet O, Redon CE, Guirouilh-Barbat J, Smith S, Solier S, Douarre C, et al. Ataxia telangiectasia mutated activation by transcription- and topoisomerase I-induced DNA double-strand breaks. *EMBO Rep*. 2009;10:887–93. doi:10.1038/embor.2009.97.
17. Strumberg D, Pilon AA, Smith M, Hickey R, Malkas L, Pommier Y. Conversion of topoisomerase I cleavage complexes on the leading strand of ribosomal DNA into 5'-phosphorylated DNA double-strand breaks by replication runoff. *Mol Cell Biol*. 2000;20:3977–87. doi:10.1128/mcb.20.11.3977-3987.2000.
18. Pourquier P, Ueng LM, Fertala J, Wang D, Park HJ, Essigmann JM, et al. Induction of reversible complexes between eukaryotic DNA topoisomerase I and DNA-containing oxidative base damages. 7, 8-dihydro-8-oxoguanine and 5-hydroxycytosine. *J Biol Chem*. 1999;274:8516–23. doi:10.1074/jbc.274.13.8516.
19. Pourquier P, Pilon AA, Kohlhagen G, Mazumder A, Sharma A, Pommier Y. Trapping of mammalian topoisomerase I and recombinations induced by damaged DNA containing nicks or gaps. Importance of DNA end phosphorylation and camptothecin effects. *J Biol Chem*. 1997;272:26441–7. doi:10.1074/jbc.272.42.26441.

20. Pourquier P, Ueng LM, Kohlhagen G, Mazumder A, Gupta M, Kohn KW, Pommier Y. Effects of uracil incorporation, DNA mismatches, and abasic sites on cleavage and religation activities of mammalian topoisomerase I. *J Biol Chem.* 1997;272:7792–6. doi:10.1074/jbc.272.12.7792.
21. Leshner D-TT, Pommier Y, Stewart L, Redinbo MR. 8-Oxoguanine rearranges the active site of human topoisomerase I. *Proc Natl Acad Sci U S A.* 2002;99:12102–7. doi:10.1073/pnas.192282699.
22. Lin C-P, Ban Y, Lyu YL, Desai SD, Liu LF. A ubiquitin-proteasome pathway for the repair of topoisomerase I-DNA covalent complexes. *J Biol Chem.* 2008;283:21074–83. doi:10.1074/jbc.M803493200.
23. Lin C-P, Ban Y, Lyu YL, Liu LF. Proteasome-dependent processing of topoisomerase I-DNA adducts into DNA double strand breaks at arrested replication forks. *J Biol Chem.* 2009;284:28084–92. doi:10.1074/jbc.M109.030601.
24. Riccio AA, Schellenberg MJ, Williams RS. Molecular mechanisms of topoisomerase 2 DNA-protein crosslink resolution. *Cell Mol Life Sci.* 2020;77:81–91. doi:10.1007/s00018-019-03367-z.
25. Nakamura J, La DK, Swenberg JA. 5'-nicked apurinic/apyrimidinic sites are resistant to beta-elimination by beta-polymerase and are persistent in human cultured cells after oxidative stress. *J Biol Chem.* 2000;275:5323–8. doi:10.1074/jbc.275.8.5323.
26. Lindahl T, Nyberg B. Rate of depurination of native deoxyribonucleic acid. *Biochemistry.* 1972;11:3610–8. doi:10.1021/bi00769a018.
27. He Y-F, Li B-Z, Li Z, Liu P, Wang Y, Tang Q, et al. Tet-mediated formation of 5-carboxylcytosine and its excision by TDG in mammalian DNA. *Science.* 2011;333:1303–7. doi:10.1126/science.1210944.
28. Kohli RM, Zhang Y. TET enzymes, TDG and the dynamics of DNA demethylation. *Nature.* 2013;502:472–9. doi:10.1038/nature12750.
29. Loeb LA, Preston BD. Mutagenesis by apurinic/apyrimidinic sites. *Annu Rev Genet.* 1986;20:201–30. doi:10.1146/annurev.ge.20.120186.001221.
30. Gao R, Schellenberg MJ, Huang S-YN, Abdelmalak M, Marchand C, Nitiss KC, et al. Proteolytic degradation of topoisomerase II (Top2) enables the processing of Top2·DNA and Top2·RNA covalent complexes by tyrosyl-DNA-phosphodiesterase 2 (TDP2). *J Biol Chem.* 2014;289:17960–9. doi:10.1074/jbc.M114.565374.
31. Yonekura S-I, Nakamura N, Yonei S, Zhang-Akiyama Q-M. Generation, biological consequences and repair mechanisms of cytosine deamination in DNA. *J Radiat Res.* 2009;50:19–26. doi:10.1269/jrr.08080.
32. Lindahl T. Instability and decay of the primary structure of DNA. *Nature.* 1993;362:709–15. doi:10.1038/362709a0.
33. Chen H, Shaw BR. Kinetics of bisulfite-induced cytosine deamination in single-stranded DNA. *Biochemistry.* 1993;32:3535–9. doi:10.1021/bi00065a003.
34. Moyer R, Briley D, Johnsen A, Stewart U, Shaw BR. Echinomycin, a bis-intercalating agent, induces C→T mutations via cytosine deamination. *Mutation Research/Fundamental and Molecular Mechanisms of Mutagenesis.* 1993;288:291–300. doi:10.1016/0027-5107(93)90097-y.
35. Pfeifer GP, You Y-H, Besaratinia A. Mutations induced by ultraviolet light. *Mutation Research/Fundamental and Molecular Mechanisms of Mutagenesis.* 2005;571:19–31. doi:10.1016/j.mrfmmm.2004.06.057.
36. d'Ischia M, Napolitano A, Manini P, Panzella L. Secondary targets of nitrite-derived reactive nitrogen species: nitrosation/nitration pathways, antioxidant defense mechanisms and toxicological implications. *Chem Res Toxicol.* 2011;24:2071–92. doi:10.1021/tx2003118.
37. Rivière J, Klarskov K, Wagner JR. Oxidation of 5-hydroxypyrimidine nucleosides to 5-hydroxyhydantoin and its alpha-hydroxy-ketone isomer. *Chem Res Toxicol.* 2005;18:1332–8. doi:10.1021/tx050121i.
38. Lindahl T. DNA Glycosylases, Endonucleases for Apurinic/Apyrimidinic Sites, and Base Excision-Repair. In: : Elsevier; 1979. p. 135–192. doi:10.1016/s0079-6603(08)60800-4.
39. Cooper DN, Youssoufian H. The CpG dinucleotide and human genetic disease. *Hum Genet.* 1988;78:151–5. doi:10.1007/BF00278187.
40. Chandra V, Bortnick A, Murre C. AID targeting: old mysteries and new challenges. *Trends Immunol.* 2015;36:527–35. doi:10.1016/j.it.2015.07.003.

41. Muramatsu M, Kinoshita K, Fagarasan S, Yamada S, Shinkai Y, Honjo T. Class Switch Recombination and Hypermutation Require Activation-Induced Cytidine Deaminase (AID), a Potential RNA Editing Enzyme. *Cell*. 2000;102:553–63. doi:10.1016/s0092-8674(00)00078-7.
42. Wiebauer K, Jiricny J. Mismatch-specific thymine DNA glycosylase and DNA polymerase beta mediate the correction of G.T mispairs in nuclear extracts from human cells. *Proc Natl Acad Sci U S A*. 1990;87:5842–5. doi:10.1073/pnas.87.15.5842.
43. Waters TR, Swann PF. Kinetics of the action of thymine DNA glycosylase. *J Biol Chem*. 1998;273:20007–14. doi:10.1074/jbc.273.32.20007.
44. COMMONER B, TOWNSEND J, PAKE GE. Free radicals in biological materials. *Nature*. 1954;174:689–91. doi:10.1038/174689a0.
45. Dahlgren C, Karlsson A. Respiratory burst in human neutrophils. *J Immunol Methods*. 1999;232:3–14. doi:10.1016/s0022-1759(99)00146-5.
46. Perry JJP, Shin DS, Getzoff ED, Tainer JA. The structural biochemistry of the superoxide dismutases. *Biochim Biophys Acta*. 2010;1804:245–62. doi:10.1016/j.bbapap.2009.11.004.
47. Meitzler JL, Antony S, Wu Y, Juhasz A, Liu H, Jiang G, et al. NADPH oxidases: a perspective on reactive oxygen species production in tumor biology. *Antioxid Redox Signal*. 2014;20:2873–89. doi:10.1089/ars.2013.5603.
48. Fransen M, Nordgren M, Wang B, Apanasets O. Role of peroxisomes in ROS/RNS-metabolism: implications for human disease. *Biochim Biophys Acta*. 2012;1822:1363–73. doi:10.1016/j.bbadis.2011.12.001.
49. Ziech D, Franco R, Pappa A, Panayiotidis MI. Reactive oxygen species (ROS)--induced genetic and epigenetic alterations in human carcinogenesis. *Mutation Research/Fundamental and Molecular Mechanisms of Mutagenesis*. 2011;711:167–73. doi:10.1016/j.mrfmmm.2011.02.015.
50. Zhang F, Paramasivam M, Cai Q, Dai X, Wang P, Lin K, et al. Arsenite binds to the RING finger domains of RNF20-RNF40 histone E3 ubiquitin ligase and inhibits DNA double-strand break repair. *J Am Chem Soc*. 2014;136:12884–7. doi:10.1021/ja507863d.
51. Croteau DL, Bohr VA. Repair of oxidative damage to nuclear and mitochondrial DNA in mammalian cells. *J Biol Chem*. 1997;272:25409–12. doi:10.1074/jbc.272.41.25409.
52. Dizdaroglu M. Chemical determination of free radical-induced damage to DNA. *Free Radic Biol Med*. 1991;10:225–42. doi:10.1016/0891-5849(91)90080-m.
53. Cadet J, Douki T, Ravanat J-L. Oxidatively generated base damage to cellular DNA. *Free Radic Biol Med*. 2010;49:9–21. doi:10.1016/j.freeradbiomed.2010.03.025.
54. Kasai H, Nishimura S. Hydroxylation of deoxyguanosine at the C-8 position by ascorbic acid and other reducing agents. *Nucleic Acids Res*. 1984;12:2137–45. doi:10.1093/nar/12.4.2137.
55. Cheng KC, Cahill DS, Kasai H, Nishimura S, Loeb LA. 8-Hydroxyguanine, an abundant form of oxidative DNA damage, causes G---T and A---C substitutions. *J Biol Chem*. 1992;267:166–72.
56. Cadet J, Delatour T, Douki T, Gasparutto D, Pouget J-P, Ravanat J-L, Sauvaigo S. Hydroxyl radicals and DNA base damage. *Mutation Research/Fundamental and Molecular Mechanisms of Mutagenesis*. 1999;424:9–21. doi:10.1016/s0027-5107(99)00004-4.
57. Ishii K, Zhen LX, Wang DH, Funamori Y, Ogawa K, Taketa K. Prevention of mammary tumorigenesis in acatalasemic mice by vitamin E supplementation. *Jpn J Cancer Res*. 1996;87:680–4. doi:10.1111/j.1349-7006.1996.tb00277.x.
58. Li Y, Huang TT, Carlson EJ, Melov S, Ursell PC, Olson JL, et al. Dilated cardiomyopathy and neonatal lethality in mutant mice lacking manganese superoxide dismutase. *Nat Genet*. 1995;11:376–81. doi:10.1038/ng1295-376.
59. MatÉs JM, Pérez-Gómez C, Castro IN de. Antioxidant enzymes and human diseases. *Clinical Biochemistry*. 1999;32:595–603. doi:10.1016/s0009-9120(99)00075-2.
60. Matés JM, Sánchez-Jiménez F. Antioxidant enzymes and their implications in pathophysiologic processes. *Front Biosci*. 1999;4:D339-45. doi:10.2741/mates.
61. Dizdaroglu M, Jaruga P. Mechanisms of free radical-induced damage to DNA. *Free Radic Res*. 2012;46:382–419. doi:10.3109/10715762.2011.653969.
62. Giloni L, Takeshita M, Johnson F, Iden C, Grollman AP. Bleomycin-induced strand-scission of DNA. Mechanism of deoxyribose cleavage. *J Biol Chem*. 1981;256:8608–15.
63. Demple B, Harrison L. Repair of oxidative damage to DNA: enzymology and biology. *Annu Rev Biochem*. 1994;63:915–48. doi:10.1146/annurev.bi.63.070194.004411.

64. Henner WD, Grunberg SM, Haseltine WA. Sites and structure of gamma radiation-induced DNA strand breaks. *J Biol Chem.* 1982;257:11750–4.
65. Desouky O, Ding N, Zhou G. Targeted and non-targeted effects of ionizing radiation. *Journal of Radiation Research and Applied Sciences.* 2015;8:247–54. doi:10.1016/j.jrras.2015.03.003.
66. Friedberg EC. DNA repair and mutagenesis. 2nd ed. Washington, DC: ASM Press; 2006.
67. Henner WD, Rodriguez LO, Hecht SM, Haseltine WA. gamma Ray induced deoxyribonucleic acid strand breaks. 3' Glycolate termini. *J Biol Chem.* 1983;258:711–3.
68. Price A. The repair of ionising radiation-induced damage to DNA. *Semin Cancer Biol.* 1993;4:61–71.
69. Jilani A, Ramotar D, Slack C, Ong C, Yang XM, Scherer SW, Lasko DD. Molecular cloning of the human gene, PNKP, encoding a polynucleotide kinase 3'-phosphatase and evidence for its role in repair of DNA strand breaks caused by oxidative damage. *J Biol Chem.* 1999;274:24176–86. doi:10.1074/jbc.274.34.24176.
70. Zhou T, Lee JW, Tatavarthi H, Lupski JR, Valerie K, Povirk LF. Deficiency in 3'-phosphoglycolate processing in human cells with a hereditary mutation in tyrosyl-DNA phosphodiesterase (TDP1). *Nucleic Acids Res.* 2005;33:289–97. doi:10.1093/nar/gki170.
71. El-Khamisy SF, Hartsuiker E, Caldecott KW. TDP1 facilitates repair of ionizing radiation-induced DNA single-strand breaks. *DNA Repair (Amst).* 2007;6:1485–95. doi:10.1016/j.dnarep.2007.04.015.
72. Hutchinson F. Chemical Changes Induced in DNA by Ionizing Radiation. In: *Progress in Nucleic Acid Research and Molecular Biology Volume 32*: Elsevier; 1985. p. 115–154. doi:10.1016/s0079-6603(08)60347-5.
73. Iliakis G. The role of DNA double strand breaks in ionizing radiation-induced killing of eukaryotic cells. *Bioessays.* 1991;13:641–8. doi:10.1002/bies.950131204.
74. Petkau A. Role of superoxide dismutase in modification of radiation injury. *Br J Cancer Suppl.* 1987;8:87–95.
75. Vignard J, Mirey G, Salles B. Ionizing-radiation induced DNA double-strand breaks: a direct and indirect lighting up. *Radiother Oncol.* 2013;108:362–9. doi:10.1016/j.radonc.2013.06.013.
76. Wardman P. The importance of radiation chemistry to radiation and free radical biology (The 2008 Silvanus Thompson Memorial Lecture). *Br J Radiol.* 2009;82:89–104. doi:10.1259/bjr/60186130.
77. Diffey BL. Sources and measurement of ultraviolet radiation. *Methods.* 2002;28:4–13. doi:10.1016/s1046-2023(02)00204-9.
78. Davies RJ. Royal Irish Academy Medal Lecture. Ultraviolet radiation damage in DNA. *Biochem Soc Trans.* 1995;23:407–18. doi:10.1042/bst0230407.
79. Taylor JS, Cohrs MP. DNA, light, and Dewar pyrimidinones: the structure and biological significance to TpT3. *J Am Chem Soc.* 1987;109:2834–5. doi:10.1021/ja00243a052.
80. Varghese AJ. Photochemistry of nucleic acids and their constituents. *Photophysiology.* 1972:207–74.
81. Mitchell DL, Jen J, Cleaver JE. Relative induction of cyclobutane dimers and cytosine photohydrates in DNA irradiated in vitro and in vivo with ultraviolet-C and ultraviolet-B light. *Photochem Photobiol.* 1991;54:741–6. doi:10.1111/j.1751-1097.1991.tb02084.x.
82. Dumaz N, Drougard C, Sarasin A, Daya-Grosjean L. Specific UV-induced mutation spectrum in the p53 gene of skin tumors from DNA-repair-deficient xeroderma pigmentosum patients. *Proc Natl Acad Sci U S A.* 1993;90:10529–33. doi:10.1073/pnas.90.22.10529.
83. Gentil A, Le Page F, Margot A, Lawrence CW, Borden A, Sarasin A. Mutagenicity of a unique thymine-thymine dimer or thymine-thymine pyrimidine pyrimidone (6-4) photoproduct in mammalian cells. *Nucleic Acids Res.* 1996;24:1837–40. doi:10.1093/nar/24.10.1837.
84. Sancar A. DNA Excision Repair. *Annu Rev Biochem.* 1996;65:43–81. doi:10.1146/annurev.bi.65.070196.000355.
85. Besaratinia A, Yoon J, Schroeder C, Bradforth SE, Cockburn M, Pfeifer GP. Wavelength dependence of ultraviolet radiation-induced DNA damage as determined by laser irradiation suggests that cyclobutane pyrimidine dimers are the principal DNA lesions produced by terrestrial sunlight. *FASEB J.* 2011;25:3079–91. doi:10.1096/fj.11-187336.
86. Ravanat J-L, Douki T, Cadet J. Direct and indirect effects of UV radiation on DNA and its components. *Journal of Photochemistry and Photobiology B: Biology.* 2001;63:88–102. doi:10.1016/s1011-1344(01)00206-8.

87. Bäumlér W, Regensburger J, Knak A, Felgenträger A, Maisch T. UVA and endogenous photosensitizers – the detection of singlet oxygen by its luminescence. *Photochem. Photobiol. Sci.* 2012;11:107–17. doi:10.1039/C1PP05142C.
88. Holliday R, Ho T. Gene silencing and endogenous DNA methylation in mammalian cells. *Mutation Research/Fundamental and Molecular Mechanisms of Mutagenesis.* 1998;400:361–8. doi:10.1016/s0027-5107(98)00034-7.
89. Rydberg B, Lindahl T. Nonenzymatic methylation of DNA by the intracellular methyl group donor S-adenosyl-L-methionine is a potentially mutagenic reaction. *EMBO J.* 1982;1:211–6.
90. Loveless A. Possible relevance of O-6 alkylation of deoxyguanosine to the mutagenicity and carcinogenicity of nitrosamines and nitrosamides. *Nature.* 1969;223:206–7. doi:10.1038/223206a0.
91. Loechler EL. A violation of the Swain-Scott principle, and not SN1 versus SN2 reaction mechanisms, explains why carcinogenic alkylating agents can form different proportions of adducts at oxygen versus nitrogen in DNA. *Chem Res Toxicol.* 1994;7:277–80. doi:10.1021/tx00039a001.
92. Loechler EL, Green CL, Essigmann JM. In vivo mutagenesis by O6-methylguanine built into a unique site in a viral genome. *Proc Natl Acad Sci U S A.* 1984;81:6271–5. doi:10.1073/pnas.81.20.6271.
93. Singer B. O-alkyl pyrimidines in mutagenesis and carcinogenesis: occurrence and significance. *Cancer Res.* 1986;46:4879–85.
94. O'Connor TR, Boiteux S, Laval J. Ring-opened 7-methylguanine residues in DNA are a block to in vitro DNA synthesis. *Nucleic Acids Res.* 1988;16:5879–94. doi:10.1093/nar/16.13.5879.
95. Tudek B, Boiteux S, Laval J. Biological properties of imidazole ring-opened N7-methylguanine in M13mp18 phage DNA. *Nucleic Acids Res.* 1992;20:3079–84. doi:10.1093/nar/20.12.3079.
96. Beranek DT. Distribution of methyl and ethyl adducts following alkylation with monofunctional alkylating agents. *Mutation Research/Fundamental and Molecular Mechanisms of Mutagenesis.* 1990;231:11–30. doi:10.1016/0027-5107(90)90173-2.
97. Wyatt MD, Pittman DL. Methylating agents and DNA repair responses: Methylated bases and sources of strand breaks. *Chem Res Toxicol.* 2006;19:1580–94. doi:10.1021/tx060164e.
98. Lawley PD. Effects of Some Chemical Mutagens and Carcinogens on Nucleic Acids. In: Elsevier; 1966. p. 89–131. doi:10.1016/s0079-6603(08)60232-9.
99. Kelland L. The resurgence of platinum-based cancer chemotherapy. *Nat Rev Cancer.* 2007;7:573–84. doi:10.1038/nrc2167.
100. DeVita VT, Chu E. A history of cancer chemotherapy. *Cancer Res.* 2008;68:8643–53. doi:10.1158/0008-5472.CAN-07-6611.
101. Dasari S, Tchounwou PB. Cisplatin in cancer therapy: molecular mechanisms of action. *Eur J Pharmacol.* 2014;740:364–78. doi:10.1016/j.ejphar.2014.07.025.
102. Chatterjee N, Walker GC. Mechanisms of DNA damage, repair, and mutagenesis. *Environ Mol Mutagen.* 2017;58:235–63. doi:10.1002/em.22087.
103. Li G-M. Mechanisms and functions of DNA mismatch repair. *Cell Res.* 2008;18:85–98. doi:10.1038/cr.2007.115.
104. Genschel J, Littman SJ, Drummond JT, Modrich P. Isolation of MutSbeta from human cells and comparison of the mismatch repair specificities of MutSbeta and MutSalpha. *J Biol Chem.* 1998;273:19895–901. doi:10.1074/jbc.273.31.19895.
105. Habraken Y, Sung P, Prakash L, Prakash S. Binding of insertion/deletion DNA mismatches by the heterodimer of yeast mismatch repair proteins MSH2 and MSH3. *Curr Biol.* 1996;6:1185–7. doi:10.1016/s0960-9822(02)70686-6.
106. Palombo F, Iaccarino I, Nakajima E, Ikejima M, Shimada T, Jiricny J. hMutSβ, a heterodimer of hMSH2 and hMSH3, binds to insertion/deletion loops in DNA. *Curr Biol.* 1996;6:1181–4. doi:10.1016/s0960-9822(02)70685-4.
107. Putnam CD. MutS sliding clamps on an uncertain track to DNA mismatch repair. *Proc Natl Acad Sci U S A.* 2020;117:20351–3. doi:10.1073/pnas.2013560117.
108. Pećina-Šlaus N, Kafka A, Salamon I, Bukovac A. Mismatch Repair Pathway, Genome Stability and Cancer. *Front Mol Biosci.* 2020;7:122. doi:10.3389/fmolb.2020.00122.
109. Chatterjee N, Lin Y, Santillan BA, Yotnda P, Wilson JH. Environmental stress induces trinucleotide repeat mutagenesis in human cells. *Proc Natl Acad Sci U S A.* 2015;112:3764–9. doi:10.1073/pnas.1421917112.

110. Jiricny J. The multifaceted mismatch-repair system. *Nat Rev Mol Cell Biol.* 2006;7:335–46. doi:10.1038/nrm1907.
111. Jiricny J. Postreplicative mismatch repair. *Cold Spring Harb Perspect Biol.* 2013;5:a012633. doi:10.1101/cshperspect.a012633.
112. Dianov GL, Hübscher U. Mammalian base excision repair: the forgotten archangel. *Nucleic Acids Res.* 2013;41:3483–90. doi:10.1093/nar/gkt076.
113. Huffman JL, Sundheim O, Tainer JA. DNA base damage recognition and removal: new twists and grooves. *Mutation Research/Fundamental and Molecular Mechanisms of Mutagenesis.* 2005;577:55–76. doi:10.1016/j.mrfmmm.2005.03.012.
114. Odell ID, Wallace SS, Pederson DS. Rules of engagement for base excision repair in chromatin. *J Cell Physiol.* 2013;228:258–66. doi:10.1002/jcp.24134.
115. Krokan HE, Bjørås M. Base excision repair. *Cold Spring Harb Perspect Biol.* 2013;5:a012583. doi:10.1101/cshperspect.a012583.
116. Akbari M, Peña-Díaz J, Andersen S, Liabakk N-B, Otterlei M, Krokan HE. Extracts of proliferating and non-proliferating human cells display different base excision pathways and repair fidelity. *DNA Repair (Amst).* 2009;8:834–43. doi:10.1016/j.dnarep.2009.04.002.
117. Svilar D, Goellner EM, Almeida KH, Sobol RW. Base excision repair and lesion-dependent subpathways for repair of oxidative DNA damage. *Antioxid Redox Signal.* 2011;14:2491–507. doi:10.1089/ars.2010.3466.
118. Caldecott KW. Single-strand break repair and genetic disease. *Nat Rev Genet.* 2008;9:619–31. doi:10.1038/nrg2380.
119. Amé J-C, Spenlehauer C, Murcia G de. The PARP superfamily. *Bioessays.* 2004;26:882–93. doi:10.1002/bies.20085.
120. Gong F, Kwon Y, Smerdon MJ. Nucleotide excision repair in chromatin and the right of entry. *DNA Repair (Amst).* 2005;4:884–96. doi:10.1016/j.dnarep.2005.04.007.
121. Masutani C, Sugawara K, Yanagisawa J, Sonoyama T, Ui M, Enomoto T, et al. Purification and cloning of a nucleotide excision repair complex involving the xeroderma pigmentosum group C protein and a human homologue of yeast RAD23. *EMBO J.* 1994;13:1831–43.
122. Nishi R, Okuda Y, Watanabe E, Mori T, Iwai S, Masutani C, et al. Centrin 2 stimulates nucleotide excision repair by interacting with xeroderma pigmentosum group C protein. *Mol Cell Biol.* 2005;25:5664–74. doi:10.1128/MCB.25.13.5664-5674.2005.
123. Lans H, Marteijs JA, Schumacher B, Hoeijmakers JHJ, Jansen G, Vermeulen W. Involvement of global genome repair, transcription coupled repair, and chromatin remodeling in UV DNA damage response changes during development. *PLoS Genet.* 2010;6:e1000941. doi:10.1371/journal.pgen.1000941.
124. Volker M, Moné MJ, Karmakar P, van Hoffen A, Schul W, Vermeulen W, et al. Sequential Assembly of the Nucleotide Excision Repair Factors In Vivo. *Mol Cell.* 2001;8:213–24. doi:10.1016/s1097-2765(01)00281-7.
125. Gregersen LH, Svejstrup JQ. The Cellular Response to Transcription-Blocking DNA Damage. *Trends Biochem Sci.* 2018;43:327–41. doi:10.1016/j.tibs.2018.02.010.
126. Nospikel T. DNA repair in mammalian cells : Nucleotide excision repair: variations on versatility. *Cell Mol Life Sci.* 2009;66:994–1009. doi:10.1007/s00018-009-8737-y.
127. Ogi T, Lehmann AR. The Y-family DNA polymerase kappa (pol kappa) functions in mammalian nucleotide-excision repair. *Nat Cell Biol.* 2006;8:640–2. doi:10.1038/ncb1417.
128. Moser J, Kool H, Giakzidis I, Caldecott K, Mullenders LHF, Fousteri MI. Sealing of chromosomal DNA nicks during nucleotide excision repair requires XRCC1 and DNA ligase III alpha in a cell-cycle-specific manner. *Mol Cell.* 2007;27:311–23. doi:10.1016/j.molcel.2007.06.014.
129. Burma S, Chen BPC, Chen DJ. Role of non-homologous end joining (NHEJ) in maintaining genomic integrity. *DNA Repair (Amst).* 2006;5:1042–8. doi:10.1016/j.dnarep.2006.05.026.
130. Davis AJ, Chen DJ. DNA double strand break repair via non-homologous end-joining. *Transl Cancer Res.* 2013;2:130–43. doi:10.3978/j.issn.2218-676X.2013.04.02.
131. Walker JR, Corpina RA, Goldberg J. Structure of the Ku heterodimer bound to DNA and its implications for double-strand break repair. *Nature.* 2001;412:607–14. doi:10.1038/35088000.
132. Mari P-O, Florea BI, Persengiev SP, Verkaik NS, Brüggewirth HT, Modesti M, et al. Dynamic assembly of end-joining complexes requires interaction between Ku70/80 and XRCC4. *Proc Natl Acad Sci U S A.* 2006;103:18597–602. doi:10.1073/pnas.0609061103.

133. Hartley KO, Gell D, Smith GC, Zhang H, Divecha N, Connelly MA, et al. DNA-dependent protein kinase catalytic subunit: A relative of phosphatidylinositol 3-kinase and the ataxia telangiectasia gene product. *Cell*. 1995;82:849–56. doi:10.1016/0092-8674(95)90482-4.
134. Cary RB, Peterson SR, Wang J, Bear DG, Bradbury EM, Chen DJ. DNA looping by Ku and the DNA-dependent protein kinase. *Proc Natl Acad Sci U S A*. 1997;94:4267–72. doi:10.1073/pnas.94.9.4267.
135. Povirk LF. Processing of damaged DNA ends for double-strand break repair in mammalian cells. *ISRN Mol Biol* 2012. doi:10.5402/2012/345805.
136. Singh DK, Ghosh AK, Croteau DL, Bohr VA. RecQ helicases in DNA double strand break repair and telomere maintenance. *Mutation Research/Fundamental and Molecular Mechanisms of Mutagenesis*. 2012;736:15–24. doi:10.1016/j.mrfmmm.2011.06.002.
137. Grawunder U, Wilm M, Wu X, Kulesza P, Wilson TE, Mann M, Lieber MR. Activity of DNA ligase IV stimulated by complex formation with XRCC4 protein in mammalian cells. *Nature*. 1997;388:492–5. doi:10.1038/41358.
138. Lu H, Pannicke U, Schwarz K, Lieber MR. Length-dependent binding of human XLF to DNA and stimulation of XRCC4.DNA ligase IV activity. *J Biol Chem*. 2007;282:11155–62. doi:10.1074/jbc.M609904200.
139. Moynahan ME, Jasin M. Mitotic homologous recombination maintains genomic stability and suppresses tumorigenesis. *Nat Rev Mol Cell Biol*. 2010;11:196–207. doi:10.1038/nrm2851.
140. McVey M, Radut D, Sekelsky JJ. End-joining repair of double-strand breaks in *Drosophila melanogaster* is largely DNA ligase IV independent. *Genetics*. 2004;168:2067–76. doi:10.1534/genetics.104.033902.
141. Seol J-H, Shim EY, Lee SE. Microhomology-mediated end joining: Good, bad and ugly. *Mutat Res*. 2018;809:81–7. doi:10.1016/j.mrfmmm.2017.07.002.
142. Myler LR, Gallardo IF, Soniat MM, Deshpande RA, Gonzalez XB, Kim Y, et al. Single-Molecule Imaging Reveals How Mre11-Rad50-Nbs1 Initiates DNA Break Repair. *Mol Cell*. 2017;67:891–898.e4. doi:10.1016/j.molcel.2017.08.002.
143. Mimitou EP, Symington LS. DNA end resection--unraveling the tail. *DNA Repair (Amst)*. 2011;10:344–8. doi:10.1016/j.dnarep.2010.12.004.
144. Liu S, Kong D. End resection: a key step in homologous recombination and DNA double-strand break repair. *GENOME INSTAB. DIS*. 2020. doi:10.1007/s42764-020-00028-5.
145. Chen H, Lisby M, Symington LS. RPA coordinates DNA end resection and prevents formation of DNA hairpins. *Mol Cell*. 2013;50:589–600. doi:10.1016/j.molcel.2013.04.032.
146. Sullivan MR, Bernstein KA. RAD-ical New Insights into RAD51 Regulation. *Genes (Basel)* 2018. doi:10.3390/genes9120629.
147. Mazin AV, Mazina OM, Bugreev DV, Rossi MJ. Rad54, the motor of homologous recombination. *DNA Repair (Amst)*. 2010;9:286–302. doi:10.1016/j.dnarep.2009.12.006.
148. Sebesta M, Burkovics P, Juhasz S, Zhang S, Szabo JE, Lee MYWT, et al. Role of PCNA and TLS polymerases in D-loop extension during homologous recombination in humans. *DNA Repair (Amst)*. 2013;12:691–8. doi:10.1016/j.dnarep.2013.05.001.
149. Wright WD, Shah SS, Heyer W-D. Homologous recombination and the repair of DNA double-strand breaks. *J Biol Chem*. 2018;293:10524–35. doi:10.1074/jbc.TM118.000372.
150. Heyer W-D, Ehmsen KT, Liu J. Regulation of homologous recombination in eukaryotes. *Annu Rev Genet*. 2010;44:113–39. doi:10.1146/annurev-genet-051710-150955.
151. Zeman MK, Cimprich KA. Causes and consequences of replication stress. *Nat Cell Biol*. 2014;16:2–9. doi:10.1038/ncb2897.
152. Tourrière H, Pasero P. Maintenance of fork integrity at damaged DNA and natural pause sites. *DNA Repair (Amst)*. 2007;6:900–13. doi:10.1016/j.dnarep.2007.02.004.
153. Zou L, Cortez D, Elledge SJ. Regulation of ATR substrate selection by Rad17-dependent loading of Rad9 complexes onto chromatin. *Genes Dev*. 2002;16:198–208. doi:10.1101/gad.950302.
154. Kumagai A, Lee J, Yoo HY, Dunphy WG. TopBP1 activates the ATR-ATRIP complex. *Cell*. 2006;124:943–55. doi:10.1016/j.cell.2005.12.041.
155. Haahr P, Hoffmann S, Tollenaere MAX, Ho T, Toledo LI, Mann M, et al. Activation of the ATR kinase by the RPA-binding protein ETAA1. *Nat Cell Biol*. 2016;18:1196–207. doi:10.1038/ncb3422.

156. Feng S, Zhao Y, Xu Y, Ning S, Huo W, Hou M, et al. Ewing Tumor-associated Antigen 1 Interacts with Replication Protein A to Promote Restart of Stalled Replication Forks. *J Biol Chem.* 2016;291:21956–62. doi:10.1074/jbc.C116.747758.
157. Lee Y-C, Zhou Q, Chen J, Yuan J. RPA-Binding Protein ETAA1 Is an ATR Activator Involved in DNA Replication Stress Response. *Curr Biol.* 2016;26:3257–68. doi:10.1016/j.cub.2016.10.030.
158. Bass TE, Luzwick JW, Kavanaugh G, Carroll C, Dugrawala H, Glick GG, et al. ETAA1 acts at stalled replication forks to maintain genome integrity. *Nat Cell Biol.* 2016;18:1185–95. doi:10.1038/ncb3415.
159. Toledo LI, Altmeyer M, Rask M-B, Lukas C, Larsen DH, Povlsen LK, et al. ATR prohibits replication catastrophe by preventing global exhaustion of RPA. *Cell.* 2013;155:1088–103. doi:10.1016/j.cell.2013.10.043.
160. Zellweger R, Dalcher D, Mutreja K, Berti M, Schmid JA, Herrador R, et al. Rad51-mediated replication fork reversal is a global response to genotoxic treatments in human cells. *J Cell Biol.* 2015;208:563–79. doi:10.1083/jcb.201406099.
161. Pasero P, Vindigni A. Nucleases Acting at Stalled Forks: How to Reboot the Replication Program with a Few Shortcuts. *Annu Rev Genet.* 2017;51:477–99. doi:10.1146/annurev-genet-120116-024745.
162. Ulrich HD. Timing and spacing of ubiquitin-dependent DNA damage bypass. *FEBS Lett.* 2011;585:2861–7. doi:10.1016/j.febslet.2011.05.028.
163. Jackson SP, Durocher D. Regulation of DNA damage responses by ubiquitin and SUMO. *Mol Cell.* 2013;49:795–807. doi:10.1016/j.molcel.2013.01.017.
164. Bi X. Mechanism of DNA damage tolerance. *World J Biol Chem.* 2015;6:48–56. doi:10.4331/wjbc.v6.i3.48.
165. Saldivar JC, Cortez D, Cimprich KA. The essential kinase ATR: ensuring faithful duplication of a challenging genome. *Nat Rev Mol Cell Biol.* 2017;18:622–36. doi:10.1038/nrm.2017.67.
166. Gaillard H, García-Muse T, Aguilera A. Replication stress and cancer. *Nat Rev Cancer.* 2015;15:276–89. doi:10.1038/nrc3916.
167. Dantuma NP, van Attikum H. Spatiotemporal regulation of posttranslational modifications in the DNA damage response. *EMBO J.* 2016;35:6–23. doi:10.15252/embj.201592595.
168. Manning G, Whyte DB, Martinez R, Hunter T, Sudarsanam S. The protein kinase complement of the human genome. *Science.* 2002;298:1912–34. doi:10.1126/science.1075762.
169. Olsen JV, Vermeulen M, Santamaria A, Kumar C, Miller ML, Jensen LJ, et al. Quantitative phosphoproteomics reveals widespread full phosphorylation site occupancy during mitosis. *Sci Signal.* 2010;3:ra3. doi:10.1126/scisignal.2000475.
170. Olsen JV, Blagoev B, Gnäd F, Macek B, Kumar C, Mortensen P, Mann M. Global, in vivo, and site-specific phosphorylation dynamics in signaling networks. *Cell.* 2006;127:635–48. doi:10.1016/j.cell.2006.09.026.
171. Alonso A, Sasin J, Bottini N, Friedberg I, Friedberg I, Osterman A, et al. Protein tyrosine phosphatases in the human genome. *Cell.* 2004;117:699–711. doi:10.1016/j.cell.2004.05.018.
172. Fabbro D. 25 years of small molecular weight kinase inhibitors: potentials and limitations. *Mol Pharmacol.* 2015;87:766–75. doi:10.1124/mol.114.095489.
173. Tebbutt N, Pedersen MW, Johns TG. Targeting the ERBB family in cancer: couples therapy. *Nat Rev Cancer.* 2013;13:663–73. doi:10.1038/nrc3559.
174. Pao W, Miller VA, Politi KA, Riely GJ, Somwar R, Zakowski MF, et al. Acquired resistance of lung adenocarcinomas to gefitinib or erlotinib is associated with a second mutation in the EGFR kinase domain. *PLoS Med.* 2005;2:e73. doi:10.1371/journal.pmed.0020073.
175. Mandell DJ, Chorny I, Groban ES, Wong SE, Levine E, Rapp CS, Jacobson MP. Strengths of hydrogen bonds involving phosphorylated amino acid side chains. *J Am Chem Soc.* 2007;129:820–7. doi:10.1021/ja063019w.
176. Yaffe MB. Phosphotyrosine-binding domains in signal transduction. *Nat Rev Mol Cell Biol.* 2002;3:177–86. doi:10.1038/nrm759.
177. Reinhardt HC, Yaffe MB. Phospho-Ser/Thr-binding domains: navigating the cell cycle and DNA damage response. *Nat Rev Mol Cell Biol.* 2013;14:563–80. doi:10.1038/nrm3640.
178. Shiloh Y. ATM and related protein kinases: safeguarding genome integrity. *Nat Rev Cancer.* 2003;3:155–68. doi:10.1038/nrc1011.

179. Matsuoka S, Ballif BA, Smogorzewska A, McDonald ER, Hurov KE, Luo J, et al. ATM and ATR substrate analysis reveals extensive protein networks responsive to DNA damage. *Science*. 2007;316:1160–6. doi:10.1126/science.1140321.
180. Yan Q, Zhu H, Lan L, Yi J, Yang J. Cleavage of Ku80 by caspase-2 promotes non-homologous end joining-mediated DNA repair. *DNA Repair (Amst)*. 2017;60:18–28. doi:10.1016/j.dnarep.2017.10.001.
181. Spagnolo L, Rivera-Calzada A, Pearl LH, Llorca O. Three-dimensional structure of the human DNA-PKcs/Ku70/Ku80 complex assembled on DNA and its implications for DNA DSB repair. *Mol Cell*. 2006;22:511–9. doi:10.1016/j.molcel.2006.04.013.
182. Cui X, Yu Y, Gupta S, Cho Y-M, Lees-Miller SP, Meek K. Autophosphorylation of DNA-dependent protein kinase regulates DNA end processing and may also alter double-strand break repair pathway choice. *Mol Cell Biol*. 2005;25:10842–52. doi:10.1128/MCB.25.24.10842-10852.2005.
183. Drouet J, Frit P, Delteil C, Villartay J-P de, Salles B, Calsou P. Interplay between Ku, Artemis, and the DNA-dependent protein kinase catalytic subunit at DNA ends. *J Biol Chem*. 2006;281:27784–93. doi:10.1074/jbc.M603047200.
184. Davis AJ, Chi L, So S, Lee K-J, Mori E, Fattah K, et al. BRCA1 modulates the autophosphorylation status of DNA-PKcs in S phase of the cell cycle. *Nucleic Acids Res*. 2014;42:11487–501. doi:10.1093/nar/gku824.
185. Shao RG, Cao CX, Zhang H, Kohn KW, Wold MS, Pommier Y. Replication-mediated DNA damage by camptothecin induces phosphorylation of RPA by DNA-dependent protein kinase and dissociates RPA:DNA-PK complexes. *EMBO J*. 1999;18:1397–406. doi:10.1093/emboj/18.5.1397.
186. Bochkareva E, Kaustov L, Ayed A, Yi G-S, Lu Y, Pineda-Lucena A, et al. Single-stranded DNA mimicry in the p53 transactivation domain interaction with replication protein A. *Proc Natl Acad Sci U S A*. 2005;102:15412–7. doi:10.1073/pnas.0504614102.
187. Brunner A, Suryo Rahmanto A, Johansson H, Franco M, Viiliäinen J, Gazi M, et al. PTEN and DNA-PK determine sensitivity and recovery in response to WEE1 inhibition in human breast cancer. *Elife* 2020. doi:10.7554/eLife.57894.
188. Ruis BL, Fattah KR, Hendrickson EA. The catalytic subunit of DNA-dependent protein kinase regulates proliferation, telomere length, and genomic stability in human somatic cells. *Mol Cell Biol*. 2008;28:6182–95. doi:10.1128/MCB.00355-08.
189. Jette N, Lees-Miller SP. The DNA-dependent protein kinase: A multifunctional protein kinase with roles in DNA double strand break repair and mitosis. *Prog Biophys Mol Biol*. 2015;117:194–205. doi:10.1016/j.pbiomolbio.2014.12.003.
190. Lee J-H, Paull TT. ATM activation by DNA double-strand breaks through the Mre11-Rad50-Nbs1 complex. *Science*. 2005;308:551–4. doi:10.1126/science.1108297.
191. Uziel T, Lerenthal Y, Moyal L, Andegeko Y, Mittelman L, Shiloh Y. Requirement of the MRN complex for ATM activation by DNA damage. *EMBO J*. 2003;22:5612–21. doi:10.1093/emboj/cdg541.
192. Bakkenist CJ, Kastan MB. DNA damage activates ATM through intermolecular autophosphorylation and dimer dissociation. *Nature*. 2003;421:499–506. doi:10.1038/nature01368.
193. Burma S, Chen BP, Murphy M, Kurimasa A, Chen DJ. ATM phosphorylates histone H2AX in response to DNA double-strand breaks. *J Biol Chem*. 2001;276:42462–7. doi:10.1074/jbc.C100466200.
194. Khanna KK, Keating KE, Kozlov S, Scott S, Gatei M, Hobson K, et al. ATM associates with and phosphorylates p53: mapping the region of interaction. *Nat Genet*. 1998;20:398–400. doi:10.1038/3882.
195. Banin S, Moyal L, Shieh S, Taya Y, Anderson CW, Chessa L, et al. Enhanced phosphorylation of p53 by ATM in response to DNA damage. *Science*. 1998;281:1674–7. doi:10.1126/science.281.5383.1674.
196. Ciechanover A, Hod Y, Hershko A. A heat-stable polypeptide component of an ATP-dependent proteolytic system from reticulocytes. *Biochemical and Biophysical Research Communications*. 1978;81:1100–5. doi:10.1016/0006-291x(78)91249-4.
197. Lecker SH, Goldberg AL, Mitch WE. Protein degradation by the ubiquitin-proteasome pathway in normal and disease states. *J Am Soc Nephrol*. 2006;17:1807–19. doi:10.1681/ASN.2006010083.

198. Hammond-Martel I, Yu H, Affar EB. Roles of ubiquitin signaling in transcription regulation. *Cell Signal.* 2012;24:410–21. doi:10.1016/j.cellsig.2011.10.009.
199. Piper RC, Dikic I, Lukacs GL. Ubiquitin-dependent sorting in endocytosis. *Cold Spring Harb Perspect Biol* 2014. doi:10.1101/cshperspect.a016808.
200. Brinkmann K, Schell M, Hoppe T, Kashkar H. Regulation of the DNA damage response by ubiquitin conjugation. *Front Genet.* 2015;6:98. doi:10.3389/fgene.2015.00098.
201. Hu H, Sun S-C. Ubiquitin signaling in immune responses. *Cell Res.* 2016;26:457–83. doi:10.1038/cr.2016.40.
202. Grumati P, Dikic I. Ubiquitin signaling and autophagy. *J Biol Chem.* 2018;293:5404–13. doi:10.1074/jbc.TM117.000117.
203. Wu Y, Kang J, Zhang L, Liang Z, Tang X, Yan Y, et al. Ubiquitination regulation of inflammatory responses through NF- κ B pathway. *Am J Transl Res.* 2018;10:881–91.
204. Pickart CM, Eddins MJ. Ubiquitin: structures, functions, mechanisms. *Biochim Biophys Acta.* 2004;1695:55–72. doi:10.1016/j.bbamcr.2004.09.019.
205. Husnjak K, Dikic I. Ubiquitin-binding proteins: decoders of ubiquitin-mediated cellular functions. *Annu Rev Biochem.* 2012;81:291–322. doi:10.1146/annurev-biochem-051810-094654.
206. Peng J, Schwartz D, Elias JE, Thoreen CC, Cheng D, Marsischky G, et al. A proteomics approach to understanding protein ubiquitination. *Nat Biotechnol.* 2003;21:921–6. doi:10.1038/nbt849.
207. Zheng N, Shabek N. Ubiquitin Ligases: Structure, Function, and Regulation. *Annu Rev Biochem.* 2017;86:129–57. doi:10.1146/annurev-biochem-060815-014922.
208. Li W, Bengtson MH, Ulbrich A, Matsuda A, Reddy VA, Orth A, et al. Genome-wide and functional annotation of human E3 ubiquitin ligases identifies MULAN, a mitochondrial E3 that regulates the organelle's dynamics and signaling. *PLoS ONE.* 2008;3:e1487. doi:10.1371/journal.pone.0001487.
209. Stewart MD, Ritterhoff T, Klevit RE, Brzovic PS. E2 enzymes: more than just middle men. *Cell Res.* 2016;26:423–40. doi:10.1038/cr.2016.35.
210. Eddins MJ, Carlile CM, Gomez KM, Pickart CM, Wolberger C. Mms2-Ubc13 covalently bound to ubiquitin reveals the structural basis of linkage-specific polyubiquitin chain formation. *Nat Struct Mol Biol.* 2006;13:915–20. doi:10.1038/nsmb1148.
211. Li W, Tu D, Li L, Wollert T, Ghirlando R, Brunger AT, Ye Y. Mechanistic insights into active site-associated polyubiquitination by the ubiquitin-conjugating enzyme Ube2g2. *Proc Natl Acad Sci U S A.* 2009;106:3722–7. doi:10.1073/pnas.0808564106.
212. Wickliffe KE, Lorenz S, Wemmer DE, Kuriyan J, Rape M. The mechanism of linkage-specific ubiquitin chain elongation by a single-subunit E2. *Cell.* 2011;144:769–81. doi:10.1016/j.cell.2011.01.035.
213. Dikic I, Wakatsuki S, Walters KJ. Ubiquitin-binding domains - from structures to functions. *Nat Rev Mol Cell Biol.* 2009;10:659–71. doi:10.1038/nrm2767.
214. Clague MJ, Coulson JM, Urbé S. Cellular functions of the DUBs. *J Cell Sci.* 2012;125:277–86. doi:10.1242/jcs.090985.
215. Mattern M, Sutherland J, Kadimisetty K, Barrio R, Rodriguez MS. Using Ubiquitin Binders to Decipher the Ubiquitin Code. *Trends Biochem Sci.* 2019;44:599–615. doi:10.1016/j.tibs.2019.01.011.
216. Makarova KS, Aravind L, Koonin EV. A novel superfamily of predicted cysteine proteases from eukaryotes, viruses and *Chlamydia pneumoniae*. *Trends Biochem Sci.* 2000;25:50–2. doi:10.1016/s0968-0004(99)01530-3.
217. Ambroggio XI, Rees DC, Deshaies RJ. JAMM: a metalloprotease-like zinc site in the proteasome and signalosome. *PLoS Biol.* 2004;2:E2. doi:10.1371/journal.pbio.0020002.
218. Balakirev MY, Tcherniuk SO, Jaquinod M, Chroboczek J. Otubains: a new family of cysteine proteases in the ubiquitin pathway. *EMBO Rep.* 2003;4:517–22. doi:10.1038/sj.embor.embor824.
219. Amerik AY, Hochstrasser M. Mechanism and function of deubiquitinating enzymes. *Biochim Biophys Acta.* 2004;1695:189–207. doi:10.1016/j.bbamcr.2004.10.003.
220. Komander D, Rape M. The ubiquitin code. *Annu Rev Biochem.* 2012;81:203–29. doi:10.1146/annurev-biochem-060310-170328.
221. Abdul Rehman SA, Kristariyanto YA, Choi S-Y, Nkosi PJ, Weidlich S, Labib K, et al. MINDY-1 Is a Member of an Evolutionarily Conserved and Structurally Distinct New Family of Deubiquitinating Enzymes. *Mol Cell.* 2016;63:146–55. doi:10.1016/j.molcel.2016.05.009.

222. Mevissen TET, Hospenthal MK, Geurink PP, Elliott PR, Akutsu M, Arnaudo N, et al. OTU deubiquitinases reveal mechanisms of linkage specificity and enable ubiquitin chain restriction analysis. *Cell*. 2013;154:169–84. doi:10.1016/j.cell.2013.05.046.
223. Mevissen TET, Komander D. Mechanisms of Deubiquitinase Specificity and Regulation. *Annu Rev Biochem*. 2017;86:159–92. doi:10.1146/annurev-biochem-061516-044916.
224. Haahr P, Borgermann N, Guo X, Typas D, Achuthankutty D, Hoffmann S, et al. ZUFSP Deubiquitylates K63-Linked Polyubiquitin Chains to Promote Genome Stability. *Mol Cell*. 2018;70:165-174.e6. doi:10.1016/j.molcel.2018.02.024.
225. Harrigan JA, Jacq X, Martin NM, Jackson SP. Deubiquitylating enzymes and drug discovery: emerging opportunities. *Nat Rev Drug Discov*. 2018;17:57–78. doi:10.1038/nrd.2017.152.
226. Kwasna D, Abdul Rehman SA, Natarajan J, Matthews S, Madden R, Cesare V de, et al. Discovery and Characterization of ZUFSP/ZUP1, a Distinct Deubiquitinase Class Important for Genome Stability. *Mol Cell*. 2018;70:150-164.e6. doi:10.1016/j.molcel.2018.02.023.
227. Kliza K, Husnjak K. Resolving the Complexity of Ubiquitin Networks. *Front Mol Biosci*. 2020;7:21. doi:10.3389/fmolb.2020.00021.
228. Deribe YL, Pawson T, Dikic I. Post-translational modifications in signal integration. *Nat Struct Mol Biol*. 2010;17:666–72. doi:10.1038/nsmb.1842.
229. Huen MSY, Grant R, Manke I, Minn K, Yu X, Yaffe MB, Chen J. RNF8 transduces the DNA-damage signal via histone ubiquitylation and checkpoint protein assembly. *Cell*. 2007;131:901–14. doi:10.1016/j.cell.2007.09.041.
230. Mailand N, Bekker-Jensen S, Fastrup H, Melander F, Bartek J, Lukas C, Lukas J. RNF8 ubiquitylates histones at DNA double-strand breaks and promotes assembly of repair proteins. *Cell*. 2007;131:887–900. doi:10.1016/j.cell.2007.09.040.
231. Kolas NK, Chapman JR, Nakada S, Ylanko J, Chahwan R, Sweeney FD, et al. Orchestration of the DNA-damage response by the RNF8 ubiquitin ligase. *Science*. 2007;318:1637–40. doi:10.1126/science.1150034.
232. Thorslund T, Ripplinger A, Hoffmann S, Wild T, Uckelmann M, Villumsen B, et al. Histone H1 couples initiation and amplification of ubiquitin signalling after DNA damage. *Nature*. 2015;527:389–93. doi:10.1038/nature15401.
233. Newshean S, Aziz K, Aziz A, Deng M, Qin B, Luo K, et al. L3MBTL2 orchestrates ubiquitin signalling by dictating the sequential recruitment of RNF8 and RNF168 after DNA damage. *Nat Cell Biol*. 2018;20:455–64. doi:10.1038/s41556-018-0071-x.
234. Sy SMH, Jiang J, O WS, Deng Y, Huen MSY. The ubiquitin specific protease USP34 promotes ubiquitin signaling at DNA double-strand breaks. *Nucleic Acids Res*. 2013;41:8572–80. doi:10.1093/nar/gkt622.
235. Gudjonsson T, Altmeyer M, Savic V, Toledo L, Dinant C, Grøfte M, et al. TRIP12 and UBR5 suppress spreading of chromatin ubiquitylation at damaged chromosomes. *Cell*. 2012;150:697–709. doi:10.1016/j.cell.2012.06.039.
236. Hofmann RM, Pickart CM. Noncanonical MMS2-Encoded Ubiquitin-Conjugating Enzyme Functions in Assembly of Novel Polyubiquitin Chains for DNA Repair. *Cell*. 1999;96:645–53. doi:10.1016/s0092-8674(00)80575-9.
237. Hoegge C, Pfander B, Moldovan G-L, Pyrowolakis G, Jentsch S. RAD6-dependent DNA repair is linked to modification of PCNA by ubiquitin and SUMO. *Nature*. 2002;419:135–41. doi:10.1038/nature00991.
238. Parker JL, Ulrich HD. Mechanistic analysis of PCNA poly-ubiquitylation by the ubiquitin protein ligases Rad18 and Rad5. *EMBO J*. 2009;28:3657–66. doi:10.1038/emboj.2009.303.
239. Peth A, Nathan JA, Goldberg AL. The ATP costs and time required to degrade ubiquitinated proteins by the 26 S proteasome. *J Biol Chem*. 2013;288:29215–22. doi:10.1074/jbc.M113.482570.
240. Ravid T, Hochstrasser M. Diversity of degradation signals in the ubiquitin-proteasome system. *Nat Rev Mol Cell Biol*. 2008;9:679–90. doi:10.1038/nrm2468.
241. Jacquemont C, Taniguchi T. Proteasome function is required for DNA damage response and fanconi anemia pathway activation. *Cancer Res*. 2007;67:7395–405. doi:10.1158/0008-5472.CAN-07-1015.
242. Murakawa Y, Sonoda E, Barber LJ, Zeng W, Yokomori K, Kimura H, et al. Inhibitors of the proteasome suppress homologous DNA recombination in mammalian cells. *Cancer Res*. 2007;67:8536–43. doi:10.1158/0008-5472.CAN-07-1166.

243. Sakai W, Yuasa-Sunagawa M, Kusakabe M, Kishimoto A, Matsui T, Kaneko Y, et al. Functional impacts of the ubiquitin-proteasome system on DNA damage recognition in global genome nucleotide excision repair. *Sci Rep.* 2020;10:19704. doi:10.1038/s41598-020-76898-2.
244. Gudmundsdottir K, Lord CJ, Witt E, Tutt ANJ, Ashworth A. DSS1 is required for RAD51 focus formation and genomic stability in mammalian cells. *EMBO Rep.* 2004;5:989–93. doi:10.1038/sj.embor.7400255.
245. Krogan NJ, Lam MHY, Fillingham J, Keogh M-C, Gebbia M, Li J, et al. Proteasome involvement in the repair of DNA double-strand breaks. *Mol Cell.* 2004;16:1027–34. doi:10.1016/j.molcel.2004.11.033.
246. Tsolou A, Nelson G, Trachana V, Chondrogianni N, Saretzki G, Zglinicki T von, Gonos ES. The 19S proteasome subunit Rpn7 stabilizes DNA damage foci upon genotoxic insult. *IUBMB Life.* 2012;64:432–42. doi:10.1002/iub.1018.
247. Riedinger C, Boehringer J, Trempe J-F, Lowe ED, Brown NR, Gehring K, et al. Structure of Rpn10 and its interactions with polyubiquitin chains and the proteasome subunit Rpn12. *J Biol Chem.* 2010;285:33992–4003. doi:10.1074/jbc.M110.134510.
248. Isasa M, Katz EJ, Kim W, Yugo V, González S, Kirkpatrick DS, et al. Monoubiquitination of RPN10 regulates substrate recruitment to the proteasome. *Mol Cell.* 2010;38:733–45. doi:10.1016/j.molcel.2010.05.001.
249. Galanty Y, Belotserkovskaya R, Coates J, Jackson SP. RNF4, a SUMO-targeted ubiquitin E3 ligase, promotes DNA double-strand break repair. *Genes Dev.* 2012;26:1179–95. doi:10.1101/gad.188284.112.
250. Beli P, Lukashchuk N, Wagner SA, Weinert BT, Olsen JV, Baskcomb L, et al. Proteomic investigations reveal a role for RNA processing factor THRAP3 in the DNA damage response. *Mol Cell.* 2012;46:212–25. doi:10.1016/j.molcel.2012.01.026.
251. Beaudenon S, Huijbregtse JM. HPV E6, E6AP and cervical cancer. *BMC Biochem.* 2008;9 Suppl 1:S4. doi:10.1186/1471-2091-9-S1-S4.
252. White MK, Pagano JS, Khalili K. Viruses and human cancers: a long road of discovery of molecular paradigms. *Clin Microbiol Rev.* 2014;27:463–81. doi:10.1128/CMR.00124-13.
253. Rotin D, Kumar S. Physiological functions of the HECT family of ubiquitin ligases. *Nat Rev Mol Cell Biol.* 2009;10:398–409. doi:10.1038/nrm2690.
254. Harlalka GV, Baple EL, Cross H, Kühnle S, Cubillos-Rojas M, Matentzoglou K, et al. Mutation of HERC2 causes developmental delay with Angelman-like features. *J Med Genet.* 2013;50:65–73. doi:10.1136/jmedgenet-2012-101367.
255. Kühnle S, Kogel U, Glockzin S, Marquardt A, Ciechanover A, Matentzoglou K, Scheffner M. Physical and functional interaction of the HECT ubiquitin-protein ligases E6AP and HERC2. *J Biol Chem.* 2011;286:19410–6. doi:10.1074/jbc.M110.205211.
256. Ronchi VP, Klein JM, Edwards DJ, Haas AL. The active form of E6-associated protein (E6AP)/UBE3A ubiquitin ligase is an oligomer. *J Biol Chem.* 2014;289:1033–48. doi:10.1074/jbc.M113.517805.
257. Nawaz Z, Lonard DM, Smith CL, Lev-Lehman E, Tsai SY, Tsai MJ, O'Malley BW. The Angelman syndrome-associated protein, E6-AP, is a coactivator for the nuclear hormone receptor superfamily. *Mol Cell Biol.* 1999;19:1182–9.
258. Khan OY, Fu G, Ismail A, Srinivasan S, Cao X, Tu Y, et al. Multifunction steroid receptor coactivator, E6-associated protein, is involved in development of the prostate gland. *Mol Endocrinol.* 2006;20:544–59. doi:10.1210/me.2005-0110.
259. Ramamoorthy S, Nawaz Z. E6-associated protein (E6-AP) is a dual function coactivator of steroid hormone receptors. *Nucl Recept Signal.* 2008;6:e006. doi:10.1621/nrs.06006.
260. Hatakeyama S, Jensen JP, Weissman AM. Subcellular localization and ubiquitin-conjugating enzyme (E2) interactions of mammalian HECT family ubiquitin protein ligases. *J Biol Chem.* 1997;272:15085–92. doi:10.1074/jbc.272.24.15085.
261. Heery DM, Kalkhoven E, Hoare S, Parker MG. A signature motif in transcriptional co-activators mediates binding to nuclear receptors. *Nature.* 1997;387:733–6. doi:10.1038/42750.
262. Scheffner M, Huijbregtse JM, Vierstra RD, Howley PM. The HPV-16 E6 and E6-AP complex functions as a ubiquitin-protein ligase in the ubiquitination of p53. *Cell.* 1993;75:495–505. doi:10.1016/0092-8674(93)90384-3.

263. Scheffner M, Werness BA, Huibregtse JM, Levine AJ, Howley PM. The E6 oncoprotein encoded by human papillomavirus types 16 and 18 promotes the degradation of p53. *Cell*. 1990;63:1129–36. doi:10.1016/0092-8674(90)90409-8.
264. Scheffner M, Münger K, Huibregtse JM, Howley PM. Targeted degradation of the retinoblastoma protein by human papillomavirus E7-E6 fusion proteins. *EMBO J*. 1992;11:2425–31. doi:10.1002/j.1460-2075.1992.tb05307.x.
265. Munakata T, Liang Y, Kim S, McGivern DR, Huibregtse J, Nomoto A, Lemon SM. Hepatitis C virus induces E6AP-dependent degradation of the retinoblastoma protein. *PLoS Pathog*. 2007;3:1335–47. doi:10.1371/journal.ppat.0030139.
266. Oliveria Andrade LJ de, D'Oliveira A, Melo RC, Souza EC de, Costa Silva CA, Paraná R. Association between hepatitis C and hepatocellular carcinoma. *J Glob Infect Dis*. 2009;1:33–7. doi:10.4103/0974-777X.52979.
267. Carocci M, Bakkali-Kassimi L. The encephalomyocarditis virus. *Virulence*. 2012;3:351–67. doi:10.4161/viru.20573.
268. Wolyniec K, Shortt J, Stanchina E de, Levav-Cohen Y, Alsheich-Bartok O, Louria-Hayon I, et al. E6AP ubiquitin ligase regulates PML-induced senescence in Myc-driven lymphomagenesis. *Blood*. 2012;120:822–32. doi:10.1182/blood-2011-10-387647.
269. Louria-Hayon I, Alsheich-Bartok O, Levav-Cohen Y, Silberman I, Berger M, Grossman T, et al. E6AP promotes the degradation of the PML tumor suppressor. *Cell Death Differ*. 2009;16:1156–66. doi:10.1038/cdd.2009.31.
270. Raghu D, Paul PJ, Gulati T, Deb S, Khoo C, Russo A, et al. E6AP promotes prostate cancer by reducing p27 expression. *Oncotarget*. 2017;8:42939–48. doi:10.18632/oncotarget.17224.
271. Paul PJ, Raghu D, Chan A-L, Gulati T, Lambeth L, Takano E, et al. Restoration of tumor suppression in prostate cancer by targeting the E3 ligase E6AP. *Oncogene*. 2016;35:6235–45. doi:10.1038/onc.2016.159.
272. Buczek ME, Miles AK, Green W, Johnson C, Boocock DJ, Pockley AG, et al. Cytoplasmic PML promotes TGF- β -associated epithelial-mesenchymal transition and invasion in prostate cancer. *Oncogene*. 2016;35:3465–75. doi:10.1038/onc.2015.409.
273. Gurrieri C, Nafa K, Merghoub T, Bernardi R, Capodiecì P, Biondi A, et al. Mutations of the PML tumor suppressor gene in acute promyelocytic leukemia. *Blood*. 2004;103:2358–62. doi:10.1182/blood-2003-07-2200.
274. Birch SE, Kench JG, Takano E, Chan P, Chan A-L, Chiam K, et al. Expression of E6AP and PML predicts for prostate cancer progression and cancer-specific death. *Ann Oncol*. 2014;25:2392–7. doi:10.1093/annonc/mdu454.
275. Gulati T, Huang C, Caramia F, Raghu D, Paul PJ, Goode RJA, et al. Proteotranscriptomic Measurements of E6-Associated Protein (E6AP) Targets in DU145 Prostate Cancer Cells. *Mol Cell Proteomics*. 2018;17:1170–83. doi:10.1074/mcp.RA117.000504.
276. Anzick SL, Kononen J, Walker RL, Azorsa DO, Tanner MM, Guan XY, et al. AIB1, a steroid receptor coactivator amplified in breast and ovarian cancer. *Science*. 1997;277:965–8. doi:10.1126/science.277.5328.965.
277. Torres-Arzayus MI, Font de Mora J, Yuan J, Vazquez F, Bronson R, Rue M, et al. High tumor incidence and activation of the PI3K/AKT pathway in transgenic mice define AIB1 as an oncogene. *Cancer Cell*. 2004;6:263–74. doi:10.1016/j.ccr.2004.06.027.
278. Tilli MT, Reiter R, Oh AS, Henke RT, McDonnell K, Gallicano GI, et al. Overexpression of an N-terminally truncated isoform of the nuclear receptor coactivator amplified in breast cancer 1 leads to altered proliferation of mammary epithelial cells in transgenic mice. *Mol Endocrinol*. 2005;19:644–56. doi:10.1210/me.2004-0106.
279. Alkner S, Jensen M-B, Rasmussen BB, Bendahl P-O, Fernö M, Rydén L, Mouridsen H. Prognostic and predictive importance of the estrogen receptor coactivator AIB1 in a randomized trial comparing adjuvant letrozole and tamoxifen therapy in postmenopausal breast cancer: the Danish cohort of BIG 1-98. *Breast Cancer Res Treat*. 2017;166:481–90. doi:10.1007/s10549-017-4416-0.
280. Lee K, Lee A, Song BJ, Kang CS. Expression of AIB1 protein as a prognostic factor in breast cancer. *World J Surg Oncol*. 2011;9:139. doi:10.1186/1477-7819-9-139.
281. Ory V, Tassi E, Cavalli LR, Sharif GM, Saenz F, Baker T, et al. The nuclear coactivator amplified in breast cancer 1 maintains tumor-initiating cells during development of ductal carcinoma in situ. *Oncogene*. 2014;33:3033–42. doi:10.1038/onc.2013.263.

282. Mani A, Oh AS, Bowden ET, Lahusen T, Lorick KL, Weissman AM, et al. E6AP mediates regulated proteasomal degradation of the nuclear receptor coactivator amplified in breast cancer 1 in immortalized cells. *Cancer Res.* 2006;66:8680–6. doi:10.1158/0008-5472.CAN-06-0557.
283. Mishra M, Sharma A, Thacker G, Trivedi AK. Nano-LC based proteomic approach identifies that E6AP interacts with ENO1 and targets it for degradation in breast cancer cells. *IUBMB Life.* 2019;71:1896–905. doi:10.1002/iub.2132.
284. Rougeulle C, Glatt H, Lalonde M. The Angelman syndrome candidate gene, UBE3A/E6-AP, is imprinted in brain. *Nat Genet.* 1997;17:14–5. doi:10.1038/ng0997-14.
285. Vu TH, Hoffman AR. Imprinting of the Angelman syndrome gene, UBE3A, is restricted to brain. *Nat Genet.* 1997;17:12–3. doi:10.1038/ng0997-12.
286. Bai J-L, Qu Y-J, Zou L-P, Yang X-Y, Liu L-J, Song F. A novel missense mutation of the ubiquitin protein ligase E3A gene in a patient with Angelman syndrome. *Chin Med J (Engl).* 2011;124:84–8.
287. Chamberlain SJ, Brannan CI. The Prader-Willi syndrome imprinting center activates the paternally expressed murine Ube3a antisense transcript but represses paternal Ube3a. *Genomics.* 2001;73:316–22. doi:10.1006/geno.2001.6543.
288. Borgatti R, Piccinelli P, Passoni D, Dalprà L, Miozzo M, Micheli R, et al. Relationship between clinical and genetic features in “inverted duplicated chromosome 15” patients. *Pediatric Neurology.* 2001;24:111–6. doi:10.1016/S0887-8994(00)00244-7.
289. Khatri N, Gilbert JP, Huo Y, Sharaflari R, Nee M, Qiao H, Man H-Y. The Autism Protein Ube3A/E6AP Remodels Neuronal Dendritic Arborization via Caspase-Dependent Microtubule Destabilization. *J Neurosci.* 2018;38:363–78. doi:10.1523/JNEUROSCI.1511-17.2017.
290. Lisman J, Yasuda R, Raghavachari S. Mechanisms of CaMKII action in long-term potentiation. *Nat Rev Neurosci.* 2012;13:169–82. doi:10.1038/nrn3192.
291. Yashiro K, Riday TT, Condon KH, Roberts AC, Bernardo DR, Prakash R, et al. Ube3a is required for experience-dependent maturation of the neocortex. *Nat Neurosci.* 2009;12:777–83. doi:10.1038/nn.2327.
292. Sato M, Stryker MP. Genomic imprinting of experience-dependent cortical plasticity by the ubiquitin ligase gene Ube3a. *Proc Natl Acad Sci U S A.* 2010;107:5611–6. doi:10.1073/pnas.1001281107.
293. Greer PL, Hanayama R, Bloodgood BL, Mardinly AR, Lipton DM, Flavell SW, et al. The Angelman Syndrome protein Ube3A regulates synapse development by ubiquitinating Arc. *Cell.* 2010;140:704–16. doi:10.1016/j.cell.2010.01.026.
294. Kühnle S, Mothes B, Matentzoglou K, Scheffner M. Role of the ubiquitin ligase E6AP/UBE3A in controlling levels of the synaptic protein Arc. *Proc Natl Acad Sci U S A.* 2013;110:8888–93. doi:10.1073/pnas.1302792110.
295. Jacobson AD, MacFadden A, Wu Z, Peng J, Liu C-W. Autoregulation of the 26S proteasome by in situ ubiquitination. *Mol Biol Cell.* 2014;25:1824–35. doi:10.1091/mbc.E13-10-0585.
296. Lee SY, Ramirez J, Franco M, Lectez B, Gonzalez M, Barrio R, Mayor U. Ube3a, the E3 ubiquitin ligase causing Angelman syndrome and linked to autism, regulates protein homeostasis through the proteasomal shuttle Rpn10. *Cell Mol Life Sci.* 2014;71:2747–58. doi:10.1007/s00018-013-1526-7.
297. Avagliano Trezza R, Sonzogni M, Bossuyt SNV, Zampeta FI, Punt AM, van den Berg M, et al. Loss of nuclear UBE3A causes electrophysiological and behavioral deficits in mice and is associated with Angelman syndrome. *Nat Neurosci.* 2019;22:1235–47. doi:10.1038/s41593-019-0425-0.
298. Yi JJ, Berrios J, Newbern JM, Snider WD, Philpot BD, Hahn KM, Zylka MJ. An Autism-Linked Mutation Disables Phosphorylation Control of UBE3A. *Cell.* 2015;162:795–807. doi:10.1016/j.cell.2015.06.045.
299. Tipton JD, Tran JC, Catherman AD, Ahlf DR, Durbin KR, Kelleher NL. Analysis of intact protein isoforms by mass spectrometry. *J Biol Chem.* 2011;286:25451–8. doi:10.1074/jbc.R111.239442.
300. Duncan MW, Aebersold R, Caprioli RM. The pros and cons of peptide-centric proteomics. *Nat Biotechnol.* 2010;28:659–64. doi:10.1038/nbt0710-659.
301. Savaryn JP, Toby TK, Kelleher NL. A researcher's guide to mass spectrometry-based proteomics. *Proteomics.* 2016;16:2435–43. doi:10.1002/pmic.201600113.
302. Shehadul Islam M, Aryasomayajula A, Selvaganapathy P. A Review on Macroscale and Microscale Cell Lysis Methods. *Micromachines.* 2017;8:83. doi:10.3390/mi8030083.

303. Sechi S, Chait BT. Modification of cysteine residues by alkylation. A tool in peptide mapping and protein identification. *Anal Chem.* 1998;70:5150–8. doi:10.1021/ac9806005.
304. Olsen JV, Ong S-E, Mann M. Trypsin cleaves exclusively C-terminal to arginine and lysine residues. *Mol Cell Proteomics.* 2004;3:608–14. doi:10.1074/mcp.T400003-MCP200.
305. Giansanti P, Aye TT, van den Toorn H, Peng M, van Breukelen B, Heck AJR. An Augmented Multiple-Protease-Based Human Phosphopeptide Atlas. *Cell Rep.* 2015;11:1834–43. doi:10.1016/j.celrep.2015.05.029.
306. Bekker-Jensen DB, Kelstrup CD, Bath TS, Larsen SC, Haldrup C, Bramsen JB, et al. An Optimized Shotgun Strategy for the Rapid Generation of Comprehensive Human Proteomes. *Cell Syst.* 2017;4:587–599.e4. doi:10.1016/j.cels.2017.05.009.
307. Altelaar AFM, Munoz J, Heck AJR. Next-generation proteomics: towards an integrative view of proteome dynamics. *Nat Rev Genet.* 2013;14:35–48. doi:10.1038/nrg3356.
308. Mallick P, Kuster B. Proteomics: a pragmatic perspective. *Nat Biotechnol.* 2010;28:695–709. doi:10.1038/nbt.1658.
309. Zecha J. Studying peptidofrom-resolved proteome turnover; 2019.
310. Manadas B, Mendes VM, English J, Dunn MJ. Peptide fractionation in proteomics approaches. *Expert Rev Proteomics.* 2010;7:655–63. doi:10.1586/epr.10.46.
311. Ducret A, van Oostveen I, Eng JK, Yates JR, Aebersold R. High throughput protein characterization by automated reverse-phase chromatography/electrospray tandem mass spectrometry. *Protein Sci.* 1998;7:706–19. doi:10.1002/pro.5560070320.
312. Doll S, Burlingame AL. Mass spectrometry-based detection and assignment of protein posttranslational modifications. *ACS Chem Biol.* 2015;10:63–71. doi:10.1021/cb500904b.
313. Ruprecht B, Koch H, Medard G, Mundt M, Kuster B, Lemeer S. Comprehensive and reproducible phosphopeptide enrichment using iron immobilized metal ion affinity chromatography (Fe-IMAC) columns. *Mol Cell Proteomics.* 2015;14:205–15. doi:10.1074/mcp.M114.043109.
314. Wagner SA, Beli P, Weinert BT, Nielsen ML, Cox J, Mann M, Choudhary C. A proteome-wide, quantitative survey of in vivo ubiquitylation sites reveals widespread regulatory roles. *Mol Cell Proteomics.* 2011;10:M111.013284. doi:10.1074/mcp.M111.013284.
315. Zhou F, Sikorski TW, Ficarro SB, Webber JT, Marto JA. Online nanoflow reversed phase-strong anion exchange-reversed phase liquid chromatography-tandem mass spectrometry platform for efficient and in-depth proteome sequence analysis of complex organisms. *Anal Chem.* 2011;83:6996–7005. doi:10.1021/ac200639v.
316. Kebarle P, Verkerk UH. Electrospray: from ions in solution to ions in the gas phase, what we know now. *Mass Spectrom Rev.* 2009;28:898–917. doi:10.1002/mas.20247.
317. Kebarle P. A brief overview of the present status of the mechanisms involved in electrospray mass spectrometry. *J. Mass Spectrom.* 2000;35:804–17. doi:10.1002/1096-9888(200007)35:7<804::AID-JMS22>3.0.CO;2-Q.
318. Iribarne JV. On the evaporation of small ions from charged droplets. *J. Chem. Phys.* 1976;64:2287. doi:10.1063/1.432536.
319. Thermo Fisher Scientific Inc. Orbitrap Exploris 480 Quadrupole mass spectrometer.
320. Makarov. Electrostatic axially harmonic orbital trapping: a high-performance technique of mass analysis. *Anal Chem.* 2000;72:1156–62. doi:10.1021/ac991131p.
321. Bekker-Jensen DB, Martínez-Val A, Steigerwald S, Rütger P, Fort KL, Arrey TN, et al. A Compact Quadrupole-Orbitrap Mass Spectrometer with FAIMS Interface Improves Proteome Coverage in Short LC Gradients. *Mol Cell Proteomics.* 2020;19:716–29. doi:10.1074/mcp.TIR119.001906.
322. Mirzaei H, Carrasco M, editors. *Modern Proteomics - Sample Preparation, Analysis and Practical Applications.* Cham, s.l.: Springer International Publishing; 2016.
323. Hu Q, Noll RJ, Li H, Makarov A, Hardman M, Graham Cooks R. The Orbitrap: a new mass spectrometer. *J. Mass Spectrom.* 2005;40:430–43. doi:10.1002/jms.856.
324. Steen H, Mann M. The ABC's (and XYZ's) of peptide sequencing. *Nat Rev Mol Cell Biol.* 2004;5:699–711. doi:10.1038/nrm1468.
325. Peterson AC, Russell JD, Bailey DJ, Westphall MS, Coon JJ. Parallel reaction monitoring for high resolution and high mass accuracy quantitative, targeted proteomics. *Mol Cell Proteomics.* 2012;11:1475–88. doi:10.1074/mcp.O112.020131.

326. Ludwig C, Gillet L, Rosenberger G, Amon S, Collins BC, Aebersold R. Data-independent acquisition-based SWATH-MS for quantitative proteomics: a tutorial. *Mol Syst Biol.* 2018;14:e8126. doi:10.15252/msb.20178126.
327. Martin DB, Eng JK, Nesvizhskii AI, Gemmill A, Aebersold R. Investigation of neutral loss during collision-induced dissociation of peptide ions. *Anal Chem.* 2005;77:4870–82. doi:10.1021/ac050701k.
328. Olsen JV, Macek B, Lange O, Makarov A, Horning S, Mann M. Higher-energy C-trap dissociation for peptide modification analysis. *Nat Methods.* 2007;4:709–12. doi:10.1038/nmeth1060.
329. Olsen JV, Schwartz JC, Griep-Raming J, Nielsen ML, Damoc E, Denisov E, et al. A dual pressure linear ion trap Orbitrap instrument with very high sequencing speed. *Mol Cell Proteomics.* 2009;8:2759–69. doi:10.1074/mcp.M900375-MCP200.
330. Roepstorff P, Fohlman J. Proposal for a common nomenclature for sequence ions in mass spectra of peptides. *Biomed Mass Spectrom.* 1984;11:601. doi:10.1002/bms.1200111109.
331. Hunt DF, Yates JR, Shabanowitz J, Winston S, Hauer CR. Protein sequencing by tandem mass spectrometry. *Proc Natl Acad Sci U S A.* 1986;83:6233–7. doi:10.1073/pnas.83.17.6233.
332. Muth T, Hartkopf F, Vaudel M, Renard BY. A Potential Golden Age to Come-Current Tools, Recent Use Cases, and Future Avenues for De Novo Sequencing in Proteomics. *Proteomics.* 2018;18:e1700150. doi:10.1002/pmic.201700150.
333. Frewen BE, Merrihew GE, Wu CC, Noble WS, MacCoss MJ. Analysis of peptide MS/MS spectra from large-scale proteomics experiments using spectrum libraries. *Anal Chem.* 2006;78:5678–84. doi:10.1021/ac060279n.
334. Perkins DN, Pappin DJC, Creasy DM, Cottrell JS. Probability-based protein identification by searching sequence databases using mass spectrometry data. *Electrophoresis.* 1999;20:3551–67. doi:10.1002/(SICI)1522-2683(19991201)20:18<3551::AID-ELPS3551>3.0.CO;2-2.
335. Tyanova S, Temu T, Cox J. The MaxQuant computational platform for mass spectrometry-based shotgun proteomics. *Nat Protoc.* 2016;11:2301–19. doi:10.1038/nprot.2016.136.
336. Cox J, Hein MY, Luber CA, Paron I, Nagaraj N, Mann M. Accurate proteome-wide label-free quantification by delayed normalization and maximal peptide ratio extraction, termed MaxLFQ. *Mol Cell Proteomics.* 2014;13:2513–26. doi:10.1074/mcp.M113.031591.
337. Ong S-E, Blagoev B, Kratchmarova I, Kristensen DB, Steen H, Pandey A, Mann M. Stable isotope labeling by amino acids in cell culture, SILAC, as a simple and accurate approach to expression proteomics. *Mol Cell Proteomics.* 2002;1:376–86. doi:10.1074/mcp.M200025-MCP200.
338. Kirkpatrick DS, Gerber SA, Gygi SP. The absolute quantification strategy: a general procedure for the quantification of proteins and post-translational modifications. *Methods.* 2005;35:265–73. doi:10.1016/j.ymeth.2004.08.018.
339. Thompson A, Wölmer N, Koncarevic S, Selzer S, Böhm G, Legner H, et al. TMTpro: Design, Synthesis, and Initial Evaluation of a Proline-Based Isobaric 16-Plex Tandem Mass Tag Reagent Set. *Anal Chem.* 2019;91:15941–50. doi:10.1021/acs.analchem.9b04474.
340. Thompson A, Schäfer J, Kuhn K, Kienle S, Schwarz J, Schmidt G, et al. Tandem mass tags: a novel quantification strategy for comparative analysis of complex protein mixtures by MS/MS. *Anal Chem.* 2003;75:1895–904. doi:10.1021/ac0262560.
341. Mertins P, Tang LC, Krug K, Clark DJ, Gritsenko MA, Chen L, et al. Reproducible workflow for multiplexed deep-scale proteome and phosphoproteome analysis of tumor tissues by liquid chromatography-mass spectrometry. *Nat Protoc.* 2018;13:1632–61. doi:10.1038/s41596-018-0006-9.
342. Virreira Winter S, Meier F, Wichmann C, Cox J, Mann M, Meissner F. EASI-tag enables accurate multiplexed and interference-free MS2-based proteome quantification. *Nat Methods.* 2018;15:527–30. doi:10.1038/s41592-018-0037-8.
343. Ting L, Rad R, Gygi SP, Haas W. MS3 eliminates ratio distortion in isobaric multiplexed quantitative proteomics. *Nat Methods.* 2011;8:937–40. doi:10.1038/nmeth.1714.
344. Wühr M, Haas W, McAlister GC, Peshkin L, Rad R, Kirschner MW, Gygi SP. Accurate multiplexed proteomics at the MS2 level using the complement reporter ion cluster. *Anal Chem.* 2012;84:9214–21. doi:10.1021/ac301962s.
345. Thermo Fisher Scientific Inc. TMT10plex Mass Tag Labeling Kits and Reagents. 2017. https://assets.thermofisher.com/TFS-Assets/LSG/manuals/MAN0016969_2162457_TMT10plex_UG.pdf.

346. Blockhuys S, Vanhoecke B, Paelinck L, Bracke M, Wagter C de. Development of in vitro models for investigating spatially fractionated irradiation: physics and biological results. *Phys Med Biol*. 2009;54:1565–78. doi:10.1088/0031-9155/54/6/011.
347. Blockhuys S, Vanhoecke B, Smet J, Paepe B de, van Coster R, Bracke M, Wagter C de. Unraveling the mechanisms behind the enhanced MTT conversion by irradiated breast cancer cells. *Radiat Res*. 2013;179:433–43. doi:10.1667/RR3070.1.
348. Hodzic J, Dingjan I, Maas MJ, van der Meulen-Muileman IH, Menezes RX de, Heukelom S, et al. A cell-based high-throughput screening assay for radiation susceptibility using automated cell counting. *Radiat Oncol*. 2015;10:55. doi:10.1186/s13014-015-0355-2.
349. Ashley AK, Shrivastav M, Nie J, Amerin C, Troksa K, Glanzer JG, et al. DNA-PK phosphorylation of RPA32 Ser4/Ser8 regulates replication stress checkpoint activation, fork restart, homologous recombination and mitotic catastrophe. *DNA Repair (Amst)*. 2014;21:131–9. doi:10.1016/j.dnarep.2014.04.008.
350. White D, Rafalska-Metcalf IU, Ivanov AV, Corsinotti A, Peng H, Lee S-C, et al. The ATM substrate KAP1 controls DNA repair in heterochromatin: regulation by HP1 proteins and serine 473/824 phosphorylation. *Mol Cancer Res*. 2012;10:401–14. doi:10.1158/1541-7786.MCR-11-0134.
351. Lu H, Saha J, Beckmann PJ, Hendrickson EA, Davis AJ. DNA-PKcs promotes chromatin decondensation to facilitate initiation of the DNA damage response. *Nucleic Acids Res*. 2019;47:9467–79. doi:10.1093/nar/gkz694.
352. García-Santisteban I, Llopis A, Krenning L, Vallejo-Rodríguez J, van den Broek B, Zubiaga AM, Medema RH. Sustained CHK2 activity, but not ATM activity, is critical to maintain a G1 arrest after DNA damage in untransformed cells. *BMC Biol*. 2021;19:35. doi:10.1186/s12915-021-00965-x.
353. Borisova ME, Voigt A, Tollenaere MAX, Sahu SK, Juretschke T, Kreim N, et al. p38-MK2 signaling axis regulates RNA metabolism after UV-light-induced DNA damage. *Nat Commun*. 2018;9:1017. doi:10.1038/s41467-018-03417-3.
354. Heidelberger JB, Voigt A, Borisova ME, Petrosino G, Ruf S, Wagner SA, Beli P. Proteomic profiling of VCP substrates links VCP to K6-linked ubiquitylation and c-Myc function. *EMBO Rep* 2018. doi:10.15252/embr.201744754.
355. Méndez J, Stillman B. Chromatin association of human origin recognition complex, cdc6, and minichromosome maintenance proteins during the cell cycle: assembly of prereplication complexes in late mitosis. *Mol Cell Biol*. 2000;20:8602–12. doi:10.1128/MCB.20.22.8602-8612.2000.
356. Kim W, Bennett EJ, Huttlin EL, Guo A, Li J, Possemato A, et al. Systematic and quantitative assessment of the ubiquitin-modified proteome. *Mol Cell*. 2011;44:325–40. doi:10.1016/j.molcel.2011.08.025.
357. Glatter T, Ludwig C, Ahrné E, Aebersold R, Heck AJR, Schmidt A. Large-scale quantitative assessment of different in-solution protein digestion protocols reveals superior cleavage efficiency of tandem Lys-C/trypsin proteolysis over trypsin digestion. *J Proteome Res*. 2012;11:5145–56. doi:10.1021/pr300273g.
358. Betancourt LH, Sanchez A, Pla I, Kuras M, Zhou Q, Andersson R, Marko-Varga G. Quantitative Assessment of Urea In-Solution Lys-C/Trypsin Digestions Reveals Superior Performance at Room Temperature over Traditional Proteolysis at 37 °C. *J Proteome Res*. 2018;17:2556–61. doi:10.1021/acs.jproteome.8b00228.
359. Gershon PD. Cleaved and missed sites for trypsin, lys-C, and lys-N can be predicted with high confidence on the basis of sequence context. *J Proteome Res*. 2014;13:702–9. doi:10.1021/pr400802z.
360. Šlechtová T, Gilar M, Kalíková K, Tesařová E. Insight into Trypsin Miscleavage: Comparison of Kinetic Constants of Problematic Peptide Sequences. *Anal Chem*. 2015;87:7636–43. doi:10.1021/acs.analchem.5b00866.
361. Hogrebe A, Stechow L von, Bekker-Jensen DB, Weinert BT, Kelstrup CD, Olsen JV. Benchmarking common quantification strategies for large-scale phosphoproteomics. *Nat Commun*. 2018;9:1045. doi:10.1038/s41467-018-03309-6.
362. Zecha J, Satpathy S, Kanashova T, Avanesian SC, Kane MH, Clauser KR, et al. TMT Labeling for the Masses: A Robust and Cost-efficient, In-solution Labeling Approach. *Mol Cell Proteomics*. 2019;18:1468–78. doi:10.1074/mcp.TIR119.001385.

363. Yang F, Shen Y, Camp DG, Smith RD. High-pH reversed-phase chromatography with fraction concatenation for 2D proteomic analysis. *Expert Rev Proteomics*. 2012;9:129–34. doi:10.1586/epr.12.15.
364. Ruprecht B, Zecha J, Zolg DP, Kuster B. High pH Reversed-Phase Micro-Columns for Simple, Sensitive, and Efficient Fractionation of Proteome and (TMT labeled) Phosphoproteome Digests. *Methods Mol Biol*. 2017;1550:83–98. doi:10.1007/978-1-4939-6747-6_8.
365. Kim H, Dan K, Shin H, Lee J, Wang JI, Han D. An efficient method for high-pH peptide fractionation based on C18 StageTips for in-depth proteome profiling. *Anal. Methods*. 2019;11:4693–8. doi:10.1039/C9AY01269A.
366. Storey AJ, Naceanceno KS, Lan RS, Washam CL, Orr LM, Mackintosh SG, et al. ProteoViz: a tool for the analysis and interactive visualization of phosphoproteomics data. *Mol Omics*. 2020;16:316–26. doi:10.1039/c9mo00149b.
367. Zhang H, Liu T, Zhang Z, Payne SH, Zhang B, McDermott JE, et al. Integrated Proteogenomic Characterization of Human High-Grade Serous Ovarian Cancer. *Cell*. 2016;166:755–65. doi:10.1016/j.cell.2016.05.069.
368. Rauniyar N, Yates JR. Isobaric labeling-based relative quantification in shotgun proteomics. *J Proteome Res*. 2014;13:5293–309. doi:10.1021/pr500880b.
369. Herbrich SM, Cole RN, West KP, Schulze K, Yager JD, Groopman JD, et al. Statistical inference from multiple iTRAQ experiments without using common reference standards. *J Proteome Res*. 2013;12:594–604. doi:10.1021/pr300624g.
370. Plubell DL, Wilmarth PA, Zhao Y, Fenton AM, Minnier J, Reddy AP, et al. Extended Multiplexing of Tandem Mass Tags (TMT) Labeling Reveals Age and High Fat Diet Specific Proteome Changes in Mouse Epididymal Adipose Tissue. *Mol Cell Proteomics*. 2017;16:873–90. doi:10.1074/mcp.M116.065524.
371. Cohen AA, Geva-Zatorsky N, Eden E, Frenkel-Morgenstern M, Issaeva I, Sigal A, et al. Dynamic proteomics of individual cancer cells in response to a drug. *Science*. 2008;322:1511–6. doi:10.1126/science.1160165.
372. Kim E-J, Kho J-H, Kang M-R, Um S-J. Active regulator of SIRT1 cooperates with SIRT1 and facilitates suppression of p53 activity. *Mol Cell*. 2007;28:277–90. doi:10.1016/j.molcel.2007.08.030.
373. Hornbeck PV, Kornhauser JM, Tkachev S, Zhang B, Skrzypek E, Murray B, et al. PhosphoSitePlus: a comprehensive resource for investigating the structure and function of experimentally determined post-translational modifications in man and mouse. *Nucleic Acids Res*. 2012;40:D261–70. doi:10.1093/nar/gkr1122.
374. Colaert N, Helsens K, Martens L, Vandekerckhove J, Gevaert K. Improved visualization of protein consensus sequences by iceLogo. *Nat Methods*. 2009;6:786–7. doi:10.1038/nmeth1109-786.
375. Wiredja DD, Koyutürk M, Chance MR. The KSEA App: a web-based tool for kinase activity inference from quantitative phosphoproteomics. *Bioinformatics*. 2017;33:3489–91. doi:10.1093/bioinformatics/btx415.
376. Krug K, Mertins P, Zhang B, Hornbeck P, Raju R, Ahmad R, et al. A Curated Resource for Phosphosite-specific Signature Analysis. *Mol Cell Proteomics*. 2019;18:576–93. doi:10.1074/mcp.TIR118.000943.
377. Kim ST, Lim DS, Canman CE, Kastan MB. Substrate specificities and identification of putative substrates of ATM kinase family members. *J Biol Chem*. 1999;274:37538–43. doi:10.1074/jbc.274.53.37538.
378. Schär P, Fäsi M, Jessberger R. SMC1 coordinates DNA double-strand break repair pathways. *Nucleic Acids Res*. 2004;32:3921–9. doi:10.1093/nar/gkh716.
379. Litwin I, Pilarczyk E, Wysocki R. The Emerging Role of Cohesin in the DNA Damage Response. *Genes (Basel)* 2018. doi:10.3390/genes9120581.
380. Hildebrandt A, Brüggemann M, Rücklé C, Boerner S, Heidelberger JB, Busch A, et al. The RNA-binding ubiquitin ligase MKRN1 functions in ribosome-associated quality control of poly(A) translation. *Genome Biol*. 2019;20:216. doi:10.1186/s13059-019-1814-0.
381. Garshott DM, Sundaramoorthy E, Leonard M, Bennett EJ. Distinct regulatory ribosomal ubiquitylation events are reversible and hierarchically organized. *Elife* 2020. doi:10.7554/eLife.54023.

382. Perkins A, Nelson KJ, Parsonage D, Poole LB, Karplus PA. Peroxiredoxins: guardians against oxidative stress and modulators of peroxide signaling. *Trends Biochem Sci.* 2015;40:435–45. doi:10.1016/j.tibs.2015.05.001.
383. Tao R-R, Wang H, Hong L-J, Huang J-Y, Lu Y-M, Liao M-H, et al. Nitrosative stress induces peroxiredoxin 1 ubiquitination during ischemic insult via E6AP activation in endothelial cells both in vitro and in vivo. *Antioxid Redox Signal.* 2014;21:1–16. doi:10.1089/ars.2013.5381.
384. Steingart RA, Gozes I. Recombinant activity-dependent neuroprotective protein protects cells against oxidative stress. *Mol Cell Endocrinol.* 2006;252:148–53. doi:10.1016/j.mce.2006.03.029.
385. Kushnir M, Dresner E, Mandel S, Gozes I. Silencing of the ADNP-family member, ADNP2, results in changes in cellular viability under oxidative stress. *J Neurochem.* 2008;105:537–45. doi:10.1111/j.1471-4159.2007.05173.x.
386. Jiang Y, Zhang X-Y, Sun L, Zhang G-L, Duerksen-Hughes P, Zhu X-Q, Yang J. Methyl methanesulfonate induces apoptosis in p53-deficient H1299 and Hep3B cells through a caspase 2- and mitochondria-associated pathway. *Environ Toxicol Pharmacol.* 2012;34:694–704. doi:10.1016/j.etap.2012.09.019.
387. Kitanovic A, Walther T, Loret MO, Holzwarth J, Kitanovic I, Bonowski F, et al. Metabolic response to MMS-mediated DNA damage in *Saccharomyces cerevisiae* is dependent on the glucose concentration in the medium. *FEMS Yeast Res.* 2009;9:535–51. doi:10.1111/j.1567-1364.2009.00505.x.
388. Schellenberg MJ, Appel CD, Riccio AA, Butler LR, Krahn JM, Liebermann JA, et al. Ubiquitin stimulated reversal of topoisomerase 2 DNA-protein crosslinks by TDP2. *Nucleic Acids Res.* 2020;48:6310–25. doi:10.1093/nar/gkaa318.
389. Swan RL, Poh LLK, Cowell IG, Austin CA. Small Molecule Inhibitors Confirm Ubiquitin-Dependent Removal of TOP2-DNA Covalent Complexes. *Mol Pharmacol.* 2020;98:222–33. doi:10.1124/mol.119.118893.
390. Baldascini M. Characterisation of three zinc finger proteins ZC3H8, ZC3H11A and ZC3H14, identified as new partners of ATM, the central regulator of biological response to DNA double strand breaks. ARAN - Access to Research at NUI Galway. 2019.
391. Alhamdoosh M, Law CW, Tian L, Sheridan JM, Ng M, Ritchie ME. Easy and efficient ensemble gene set testing with EGSEA. *F1000Res.* 2017;6:2010. doi:10.12688/f1000research.12544.1.
392. Banks CAS, Miah S, Adams MK, Eubanks CG, Thornton JL, Florens L, Washburn MP. Differential HDAC1/2 network analysis reveals a role for prefoldin/CCT in HDAC1/2 complex assembly. *Sci Rep.* 2018;8:13712. doi:10.1038/s41598-018-32009-w.
393. Fukumoto Y, Morii M, Miura T, Kubota S, Ishibashi K, Honda T, et al. Src family kinases promote silencing of ATR-Chk1 signaling in termination of DNA damage checkpoint. *J Biol Chem.* 2014;289:12313–29. doi:10.1074/jbc.M113.533752.
394. Bagnato G, Leopizzi M, Urciuoli E, Peruzzi B. Nuclear Functions of the Tyrosine Kinase Src. *Int J Mol Sci* 2020. doi:10.3390/ijms21082675.
395. Schärer OD. Nucleotide excision repair in eukaryotes. *Cold Spring Harb Perspect Biol.* 2013;5:a012609. doi:10.1101/cshperspect.a012609.
396. Trego KS, Groesser T, Davalos AR, Parplys AC, Zhao W, Nelson MR, et al. Non-catalytic Roles for XPG with BRCA1 and BRCA2 in Homologous Recombination and Genome Stability. *Mol Cell.* 2016;61:535–46. doi:10.1016/j.molcel.2015.12.026.
397. Bulley SJ, Clarke JH, Droubi A, Giudici M-L, Irvine RF. Exploring phosphatidylinositol 5-phosphate 4-kinase function. *Adv Biol Regul.* 2015;57:193–202. doi:10.1016/j.jbior.2014.09.007.
398. Wang Y-H, Hariharan A, Bastianello G, Toyama Y, Shivashankar GV, Foiani M, Sheetz MP. DNA damage causes rapid accumulation of phosphoinositides for ATR signaling. *Nat Commun.* 2017;8:2118. doi:10.1038/s41467-017-01805-9.
399. Choi S, Chen M, Cryns VL, Anderson RA. A nuclear phosphoinositide kinase complex regulates p53. *Nat Cell Biol.* 2019;21:462–75. doi:10.1038/s41556-019-0297-2.
400. Fiume R, Faenza I, Sheth B, Poli A, Vidalle MC, Mazzetti C, et al. Nuclear Phosphoinositides: Their Regulation and Roles in Nuclear Functions. *Int J Mol Sci* 2019. doi:10.3390/ijms20122991.
401. Wang Y, Qiu T. Positive transcription elongation factor b and its regulators in development. *All Life.* 2020;13:23–33. doi:10.1080/21553769.2019.1663277.

402. Kais Z, Rondinelli B, Holmes A, O'Leary C, Kozono D, D'Andrea AD, Ceccaldi R. FANCD2 Maintains Fork Stability in BRCA1/2-Deficient Tumors and Promotes Alternative End-Joining DNA Repair. *Cell Rep.* 2016;15:2488–99. doi:10.1016/j.celrep.2016.05.031.
403. Elia AEH, Wang DC, Willis NA, Boardman AP, Hajdu I, Adeyemi RO, et al. RFWD3-Dependent Ubiquitination of RPA Regulates Repair at Stalled Replication Forks. *Mol Cell.* 2015;60:280–93. doi:10.1016/j.molcel.2015.09.011.
404. Smits VAJ, Reaper PM, Jackson SP. Rapid PIKK-dependent release of Chk1 from chromatin promotes the DNA-damage checkpoint response. *Curr Biol.* 2006;16:150–9. doi:10.1016/j.cub.2005.11.066.
405. Lombardi PM, Matunis MJ, Wolberger C. RAP80, ubiquitin and SUMO in the DNA damage response. *J Mol Med (Berl).* 2017;95:799–807. doi:10.1007/s00109-017-1561-1.
406. Rennie ML, Lemonidis K, Arkinson C, Chaugule VK, Clarke M, Streetley J, et al. Differential functions of FANCI and FANCD2 ubiquitination stabilize ID2 complex on DNA. *EMBO Rep.* 2020;21:e50133. doi:10.15252/embr.202050133.
407. Sugawara K, Ng JM, Masutani C, Iwai S, van der Spek PJ, Eker AP, et al. Xeroderma Pigmentosum Group C Protein Complex Is the Initiator of Global Genome Nucleotide Excision Repair. *Mol Cell.* 1998;2:223–32. doi:10.1016/s1097-2765(00)80132-x.
408. Yan J, Yang X-P, Kim Y-S, Jetten AM. RAP80 responds to DNA damage induced by both ionizing radiation and UV irradiation and is phosphorylated at Ser 205. *Cancer Res.* 2008;68:4269–76. doi:10.1158/0008-5472.CAN-07-5950.
409. Mackay DR, Howa AC, Werner TL, Ullman KS. Nup153 and Nup50 promote recruitment of 53BP1 to DNA repair foci by antagonizing BRCA1-dependent events. *J Cell Sci.* 2017;130:3347–59. doi:10.1242/jcs.203513.
410. Sansam CL, Shepard JL, Lai K, Ianari A, Danielian PS, Amsterdam A, et al. DTL/CDT2 is essential for both CDT1 regulation and the early G2/M checkpoint. *Genes Dev.* 2006;20:3117–29. doi:10.1101/gad.1482106.
411. Salton M, Lerenthal Y, Wang S-Y, Chen DJ, Shiloh Y. Involvement of Matrin 3 and SFPQ/NONO in the DNA damage response. *Cell Cycle.* 2010;9:1568–76. doi:10.4161/cc.9.8.11298.
412. Saha T, Ghosh S, Vassilev A, DePamphilis ML. Ubiquitylation, phosphorylation and Orc2 modulate the subcellular location of Orc1 and prevent it from inducing apoptosis. *J Cell Sci.* 2006;119:1371–82. doi:10.1242/jcs.02851.
413. Shah P, Zhao B, Qiang L, He Y-Y. Phosphorylation of xeroderma pigmentosum group C regulates ultraviolet-induced DNA damage repair. *Nucleic Acids Res.* 2018;46:5050–60. doi:10.1093/nar/gky239.
414. Olivieri M, Cho T, Álvarez-Quilón A, Li K, Schellenberg MJ, Zimmermann M, et al. A Genetic Map of the Response to DNA Damage in Human Cells. *Cell.* 2020;182:481-496.e21. doi:10.1016/j.cell.2020.05.040.
415. Gudmundsdottir K, Lord CJ, Ashworth A. The proteasome is involved in determining differential utilization of double-strand break repair pathways. *Oncogene.* 2007;26:7601–6. doi:10.1038/sj.onc.1210579.
416. Besche HC, Sha Z, Kukushkin NV, Peth A, Hock E-M, Kim W, et al. Autoubiquitination of the 26S proteasome on Rpn13 regulates breakdown of ubiquitin conjugates. *EMBO J.* 2014;33:1159–76. doi:10.1002/embj.201386906.
417. Lokireddy S, Kukushkin NV, Goldberg AL. cAMP-induced phosphorylation of 26S proteasomes on Rpn6/PSMD11 enhances their activity and the degradation of misfolded proteins. *Proc Natl Acad Sci U S A.* 2015;112:E7176-85. doi:10.1073/pnas.1522332112.
418. Lee S-H, Park Y, Yoon SK, Yoon J-B. Osmotic stress inhibits proteasome by p38 MAPK-dependent phosphorylation. *J Biol Chem.* 2010;285:41280–9. doi:10.1074/jbc.M110.182188.
419. Ochoa D, Jarnuczak AF, Viéitez C, Gehre M, Soucheray M, Mateus A, et al. The functional landscape of the human phosphoproteome. *Nat Biotechnol.* 2020;38:365–73. doi:10.1038/s41587-019-0344-3.
420. Certo MT, Ryu BY, Annis JE, Garibov M, Jarjour J, Rawlings DJ, Scharenberg AM. Tracking genome engineering outcome at individual DNA breakpoints. *Nat Methods.* 2011;8:671–6. doi:10.1038/nmeth.1648.

421. Martínez-Noël G, Luck K, Kühnle S, Desbuleux A, Szajner P, Galligan JT, et al. Network Analysis of UBE3A/E6AP-Associated Proteins Provides Connections to Several Distinct Cellular Processes. *J Mol Biol.* 2018;430:1024–50. doi:10.1016/j.jmb.2018.01.021.
422. Ho S-R, Mahanic CS, Lee Y-J, Lin W-C. RNF144A, an E3 ubiquitin ligase for DNA-PKcs, promotes apoptosis during DNA damage. *Proc Natl Acad Sci U S A.* 2014;111:E2646-55. doi:10.1073/pnas.1323107111.
423. Dungrawala H, Cortez D. Purification of proteins on newly synthesized DNA using iPOND. *Methods Mol Biol.* 2015;1228:123–31. doi:10.1007/978-1-4939-1680-1_10.
424. Buel GR, Chen X, Chari R, O'Neill MJ, Ebelle DL, Jenkins C, et al. Structure of E3 ligase E6AP with a proteasome-binding site provided by substrate receptor hRpn10. *Nat Commun.* 2020;11:1291. doi:10.1038/s41467-020-15073-7.
425. Martejijn JA, Lans H, Vermeulen W, Hoeijmakers JHJ. Understanding nucleotide excision repair and its roles in cancer and ageing. *Nat Rev Mol Cell Biol.* 2014;15:465–81. doi:10.1038/nrm3822.
426. Cheng Q, Chen J. Mechanism of p53 stabilization by ATM after DNA damage. *Cell Cycle.* 2010;9:472–8. doi:10.4161/cc.9.3.10556.
427. Williams AB, Schumacher B. p53 in the DNA-Damage-Repair Process. *Cold Spring Harb Perspect Med* 2016. doi:10.1101/cshperspect.a026070.
428. Murai J, Zhang H, Pongor L, Tang S-W, Jo U, Moribe F, et al. Chromatin Remodeling and Immediate Early Gene Activation by SLFN11 in Response to Replication Stress. *Cell Rep.* 2020;30:4137-4151.e6. doi:10.1016/j.celrep.2020.02.117.
429. Bahrami S, Drabløs F. Gene regulation in the immediate-early response process. *Adv Biol Regul.* 2016;62:37–49. doi:10.1016/j.jbior.2016.05.001.
430. Tanaka Y, Nakamura A, Morioka MS, Inoue S, Tamamori-Adachi M, Yamada K, et al. Systems analysis of ATF3 in stress response and cancer reveals opposing effects on pro-apoptotic genes in p53 pathway. *PLoS ONE.* 2011;6:e26848. doi:10.1371/journal.pone.0026848.
431. Vega FM, Ridley AJ. The RhoB small GTPase in physiology and disease. *Small GTPases.* 2018;9:384–93. doi:10.1080/21541248.2016.1253528.
432. Mamouni K, Cristini A, Guirouilh-Barbat J, Monferran S, Lemarié A, Faye J-C, et al. RhoB promotes γ H2AX dephosphorylation and DNA double-strand break repair. *Mol Cell Biol.* 2014;34:3144–55. doi:10.1128/MCB.01525-13.
433. Burger K, Mühl B, Harasim T, Rohrmoser M, Malamoussi A, Orban M, et al. Chemotherapeutic drugs inhibit ribosome biogenesis at various levels. *J Biol Chem.* 2010;285:12416–25. doi:10.1074/jbc.M109.074211.
434. Boulon S, Westman BJ, Hutten S, Boisvert F-M, Lamond AI. The nucleolus under stress. *Mol Cell.* 2010;40:216–27. doi:10.1016/j.molcel.2010.09.024.
435. Carotenuto P, Pecoraro A, Palma G, Russo G, Russo A. Therapeutic Approaches Targeting Nucleolus in Cancer. *Cells* 2019. doi:10.3390/cells8091090.
436. Ortega-Atienza S, Rubis B, McCarthy C, Zhitkovich A. Formaldehyde Is a Potent Proteotoxic Stressor Causing Rapid Heat Shock Transcription Factor 1 Activation and Lys48-Linked Polyubiquitination of Proteins. *Am J Pathol.* 2016;186:2857–68. doi:10.1016/j.ajpath.2016.06.022.
437. Guerra-Moreno A, Isasa M, Bhanu MK, Waterman DP, Eapen VV, Gygi SP, Hanna J. Proteomic Analysis Identifies Ribosome Reduction as an Effective Proteotoxic Stress Response. *J Biol Chem.* 2015;290:29695–706. doi:10.1074/jbc.M115.684969.
438. Zhang F, Bartels MJ, Pottenger LH, Gollapudi BB. Differential adduction of proteins vs. deoxynucleosides by methyl methanesulfonate and 1-methyl-1-nitrosourea in vitro. *Rapid Commun Mass Spectrom.* 2005;19:438–48. doi:10.1002/rcm.1806.
439. Zhang J, Wang X, Vikash V, Ye Q, Wu D, Liu Y, Dong W. ROS and ROS-Mediated Cellular Signaling. *Oxid Med Cell Longev.* 2016;2016:4350965. doi:10.1155/2016/4350965.
440. Milo-Cochavi S, Pareek M, Delulio G, Almog Y, Anand G, Ma L-J, Covo S. The response to the DNA damaging agent methyl methanesulfonate in a fungal plant pathogen. *Fungal Biol.* 2019;123:408–22. doi:10.1016/j.funbio.2019.03.007.
441. Spuches AM, Kruszyna HG, Rich AM, Wilcox DE. Thermodynamics of the As(III)-thiol interaction: arsenite and monomethylarsenite complexes with glutathione, dihydrolipoic acid, and other thiol ligands. *Inorg Chem.* 2005;44:2964–72. doi:10.1021/ic048694q.

442. Braicu C, Buse M, Busuioc C, Drula R, Gulei D, Raduly L, et al. A Comprehensive Review on MAPK: A Promising Therapeutic Target in Cancer. *Cancers (Basel)* 2019. doi:10.3390/cancers11101618.
443. Andrew AS, Mason RA, Memoli V, Duell EJ. Arsenic activates EGFR pathway signaling in the lung. *Toxicol Sci.* 2009;109:350–7. doi:10.1093/toxsci/kfp015.
444. Zhuang S, Schnellmann RG, Zhougang S. H₂O₂-induced transactivation of EGF receptor requires Src and mediates ERK1/2, but not Akt, activation in renal cells. *Am J Physiol Renal Physiol.* 2004;286:F858-65. doi:10.1152/ajprenal.00282.2003.
445. Paulsen CE, Truong TH, Garcia FJ, Homann A, Gupta V, Leonard SE, Carroll KS. Peroxide-dependent sulfenylation of the EGFR catalytic site enhances kinase activity. *Nat Chem Biol.* 2011;8:57–64. doi:10.1038/nchembio.736.
446. Romeo Y, Zhang X, Roux PP. Regulation and function of the RSK family of protein kinases. *Biochem J.* 2012;441:553–69. doi:10.1042/BJ20110289.
447. Wurzinger B, Mair A, Pfister B, Teige M. Cross-talk of calcium-dependent protein kinase and MAP kinase signaling. *Plant Signal Behav.* 2011;6:8–12. doi:10.4161/psb.6.1.14012.
448. Zhou J, Du T, Li B, Rong Y, Verkhatsky A, Peng L. Crosstalk Between MAPK/ERK and PI3K/AKT Signal Pathways During Brain Ischemia/Reperfusion. *ASN Neuro* 2015. doi:10.1177/1759091415602463.
449. Reinhardt HC, Yaffe MB. Kinases that control the cell cycle in response to DNA damage: Chk1, Chk2, and MK2. *Curr Opin Cell Biol.* 2009;21:245–55. doi:10.1016/j.ceb.2009.01.018.
450. Soni S, Anand P, Padwad YS. MAPKAPK2: the master regulator of RNA-binding proteins modulates transcript stability and tumor progression. *J Exp Clin Cancer Res.* 2019;38:121. doi:10.1186/s13046-019-1115-1.
451. Köpper F, Bierwirth C, Schön M, Kunze M, Elvers I, Kranz D, et al. Damage-induced DNA replication stalling relies on MAPK-activated protein kinase 2 activity. *Proc Natl Acad Sci U S A.* 2013;110:16856–61. doi:10.1073/pnas.1304355110.
452. Rabalski AJ, Gyenis L, Litchfield DW. Molecular Pathways: Emergence of Protein Kinase CK2 (CSNK2) as a Potential Target to Inhibit Survival and DNA Damage Response and Repair Pathways in Cancer Cells. *Clin Cancer Res.* 2016;22:2840–7. doi:10.1158/1078-0432.CCR-15-1314.
453. Junttila MR, Li S-P, Westermarck J. Phosphatase-mediated crosstalk between MAPK signaling pathways in the regulation of cell survival. *FASEB J.* 2008;22:954–65. doi:10.1096/fj.06-7859rev.
454. Whitmarsh AJ. Casein kinase 2 sends extracellular signal-regulated kinase nuclear. *Mol Cell Biol.* 2011;31:3512–4. doi:10.1128/MCB.05916-11.
455. Isaeva AR, Mitev VI. CK2 is acting upstream of MEK3/6 as a part of the signal control of ERK1/2 and p38 MAPK during keratinocytes autocrine differentiation. *Z Naturforsch C J Biosci.* 2011;66:83–6.
456. Sampadi B, Pines A, Munk S, Mišovic B, Groot AJ de, van de Water B, et al. Quantitative phosphoproteomics to unravel the cellular response to chemical stressors with different modes of action. *Arch Toxicol.* 2020;94:1655–71. doi:10.1007/s00204-020-02712-7.
457. Tam LM, Price NE, Wang Y. Molecular Mechanisms of Arsenic-Induced Disruption of DNA Repair. *Chem Res Toxicol.* 2020;33:709–26. doi:10.1021/acs.chemrestox.9b00464.
458. Muenyi CS, Ljungman M, States JC. Arsenic Disruption of DNA Damage Responses-Potential Role in Carcinogenesis and Chemotherapy. *Biomolecules.* 2015;5:2184–93. doi:10.3390/biom5042184.
459. Hu Y, Li J, Lou B, Wu R, Wang G, Lu C, et al. The Role of Reactive Oxygen Species in Arsenic Toxicity. *Biomolecules* 2020. doi:10.3390/biom10020240.
460. Zhao L, Liu X, Xu G, Guo Y, Sun L, Zhang C, et al. Arsenic induces mTOR-dependent autophagy, whereas it impairs the autophagy-lysosome pathway and the potential role of TFEB in cultured dendritic cells. *Metallomics.* 2020;12:1230–45. doi:10.1039/D0MT00057D.
461. Bolt AM, Byrd RM, Klimecki WT. Autophagy is the predominant process induced by arsenite in human lymphoblastoid cell lines. *Toxicol Appl Pharmacol.* 2010;244:366–73. doi:10.1016/j.taap.2010.01.019.
462. Wu C-W, Lin P-J, Tsai J-S, Lin C-Y, Lin L-Y. Arsenite-induced apoptosis can be attenuated via depletion of mTOR activity to restore autophagy. *Toxicol Res (Camb).* 2019;8:101–11. doi:10.1039/C8TX00238J.

463. Yasuda S, Tsuchiya H, Kaiho A, Guo Q, Ikeuchi K, Endo A, et al. Stress- and ubiquitylation-dependent phase separation of the proteasome. *Nature*. 2020;578:296–300. doi:10.1038/s41586-020-1982-9.
464. Lee J, Levin DE. Intracellular mechanism by which arsenite activates the yeast stress MAPK Hog1. *Mol Biol Cell*. 2018;29:1904–15. doi:10.1091/mbc.E18-03-0185.
465. Samikkannu T, Chen C-H, Yih L-H, Wang ASS, Lin S-Y, Chen T-C, Jan K-Y. Reactive oxygen species are involved in arsenic trioxide inhibition of pyruvate dehydrogenase activity. *Chem Res Toxicol*. 2003;16:409–14. doi:10.1021/tx025615j.
466. Guidarelli A, Fiorani M, Cerioni L, Scotti M, Cantoni O. Arsenite induces DNA damage via mitochondrial ROS and induction of mitochondrial permeability transition. *Biofactors*. 2017;43:673–84. doi:10.1002/biof.1375.
467. Yang W-C, Mirzaei H, Liu X, Regnier FE. Enhancement of amino acid detection and quantification by electrospray ionization mass spectrometry. *Anal Chem*. 2006;78:4702–8. doi:10.1021/ac0600510.
468. Mädler S, Bich C, Touboul D, Zenobi R. Chemical cross-linking with NHS esters: a systematic study on amino acid reactivities. *J Mass Spectrom*. 2009;44:694–706. doi:10.1002/jms.1544.
469. Delmotte N, Lasaosa M, Tholey A, Heinzle E, Huber CG. Two-dimensional reversed-phase x ion-pair reversed-phase HPLC: an alternative approach to high-resolution peptide separation for shotgun proteome analysis. *J Proteome Res*. 2007;6:4363–73. doi:10.1021/pr070424t.
470. Villén J, Gygi SP. The SCX/IMAC enrichment approach for global phosphorylation analysis by mass spectrometry. *Nat Protoc*. 2008;3:1630–8. doi:10.1038/nprot.2008.150.
471. Batth TS, Francavilla C, Olsen JV. Off-line high-pH reversed-phase fractionation for in-depth phosphoproteomics. *J Proteome Res*. 2014;13:6176–86. doi:10.1021/pr500893m.
472. Udeshi ND, Mani DC, Satpathy S, Fereshetian S, Gasser JA, Svinkina T, et al. Rapid and deep-scale ubiquitylation profiling for biology and translational research. *Nat Commun*. 2020;11:359. doi:10.1038/s41467-019-14175-1.
473. Rose CM, Isasa M, Ordureau A, Prado MA, Beausoleil SA, Jedrychowski MP, et al. Highly Multiplexed Quantitative Mass Spectrometry Analysis of Ubiquitylomes. *Cell Syst*. 2016;3:395-403.e4. doi:10.1016/j.cels.2016.08.009.
474. Swearingen KE, Moritz RL. High-field asymmetric waveform ion mobility spectrometry for mass spectrometry-based proteomics. *Expert Rev Proteomics*. 2012;9:505–17. doi:10.1586/epr.12.50.
475. Sonnett M, Yeung E, Wühr M. Accurate, Sensitive, and Precise Multiplexed Proteomics Using the Complement Reporter Ion Cluster. *Anal Chem*. 2018;90:5032–9. doi:10.1021/acs.analchem.7b04713.
476. Johnson A, Stadlmeier M, Wühr M. TMTPro Complementary Ion Quantification Increases Plexing and Sensitivity for Accurate Multiplexed Proteomics at the MS2 Level; 2020.
477. Li KW, Gonzalez-Lozano MA, Koopmans F, Smit AB. Recent Developments in Data Independent Acquisition (DIA) Mass Spectrometry: Application of Quantitative Analysis of the Brain Proteome. *Front Mol Neurosci*. 2020;13:564446. doi:10.3389/fnmol.2020.564446.
478. Singhmar P, Kumar A. Angelman syndrome protein UBE3A interacts with primary microcephaly protein ASPM, localizes to centrosomes and regulates chromosome segregation. *PLoS ONE*. 2011;6:e20397. doi:10.1371/journal.pone.0020397.
479. Mishra A, Godavarthi SK, Jana NR. UBE3A/E6-AP regulates cell proliferation by promoting proteasomal degradation of p27. *Neurobiol Dis*. 2009;36:26–34. doi:10.1016/j.nbd.2009.06.010.
480. Zhou X, Deng S, Liu H, Liu Y, Yang Z, Xing T, et al. Knockdown of ubiquitin protein ligase E3A affects proliferation and invasion, and induces apoptosis of breast cancer cells through regulation of annexin A2. *Mol Med Rep*. 2015;12:1107–13. doi:10.3892/mmr.2015.3549.
481. Jiang Y-H, Armstrong D, Albrecht U, Atkins CM, Noebels JL, Eichele G, et al. Mutation of the Angelman Ubiquitin Ligase in Mice Causes Increased Cytoplasmic p53 and Deficits of Contextual Learning and Long-Term Potentiation. *Neuron*. 1998;21:799–811. doi:10.1016/s0896-6273(00)80596-6.
482. Tomaić V, Banks L. Angelman syndrome-associated ubiquitin ligase UBE3A/E6AP mutants interfere with the proteolytic activity of the proteasome. *Cell Death Dis*. 2015;6:e1625. doi:10.1038/cddis.2014.572.

483. Wang Y, Liu X, Zhou L, Duong D, Bhuripanyo K, Zhao B, et al. Identifying the ubiquitination targets of E6AP by orthogonal ubiquitin transfer. *Nat Commun.* 2017;8:2232. doi:10.1038/s41467-017-01974-7.
484. Wu A, Wu B, Guo J, Luo W, Wu D, Yang H, et al. Elevated expression of CDK4 in lung cancer. *J Transl Med.* 2011;9:38. doi:10.1186/1479-5876-9-38.
485. Dobashi Y, Goto A, Fukayama M, Abe A, Ooi A. Overexpression of cdk4/cyclin D1, a possible mediator of apoptosis and an indicator of prognosis in human primary lung carcinoma. *Int J Cancer.* 2004;110:532–41. doi:10.1002/ijc.20167.
486. Lei M. The MCM complex: its role in DNA replication and implications for cancer therapy. *Curr Cancer Drug Targets.* 2005;5:365–80. doi:10.2174/1568009054629654.
487. Li Z, Xu X. Post-Translational Modifications of the Mini-Chromosome Maintenance Proteins in DNA Replication. *Genes (Basel)* 2019. doi:10.3390/genes10050331.
488. Fuchs J, Cheblal A, Gasser SM. Underappreciated Roles of DNA Polymerase δ in Replication Stress Survival. *Trends Genet.* 2021;37:476–87. doi:10.1016/j.tig.2020.12.003.
489. Debnath S, Sharma S. RECQ1 Helicase in Genomic Stability and Cancer. *Genes (Basel)* 2020. doi:10.3390/genes11060622.
490. Guo E, Ishii Y, Mueller J, Srivatsan A, Gahman T, Putnam CD, et al. FEN1 endonuclease as a therapeutic target for human cancers with defects in homologous recombination. *Proc Natl Acad Sci U S A.* 2020;117:19415–24. doi:10.1073/pnas.2009237117.
491. Coster G, Goldberg M. The cellular response to DNA damage: a focus on MDC1 and its interacting proteins. *Nucleus.* 2010;1:166–78. doi:10.4161/nucl.1.2.11176.
492. Xie S, Mortusewicz O, Ma HT, Herr P, Poon RYC, Poon RRY, et al. Timeless Interacts with PARP-1 to Promote Homologous Recombination Repair. *Mol Cell.* 2015;60:163–76. doi:10.1016/j.molcel.2015.07.031.
493. Cubillos-Rojas M, Schneider T, Bartrons R, Ventura F, Rosa JL. NEURL4 regulates the transcriptional activity of tumor suppressor protein p53 by modulating its oligomerization. *Oncotarget.* 2017;8:61824–36. doi:10.18632/oncotarget.18699.
494. Mohiuddin, Kobayashi S, Keka IS, Guilbaud G, Sale J, Narita T, et al. The role of HERC2 and RNF8 ubiquitin E3 ligases in the promotion of translesion DNA synthesis in the chicken DT40 cell line. *DNA Repair (Amst).* 2016;40:67–76. doi:10.1016/j.dnarep.2016.02.002.
495. Bekker-Jensen S, Rendtlew Danielsen J, Fugger K, Gromova I, Nerstedt A, Lukas C, et al. HERC2 coordinates ubiquitin-dependent assembly of DNA repair factors on damaged chromosomes. *Nat Cell Biol.* 2010;12:80–6; sup pp 1–12. doi:10.1038/ncb2008.
496. Al-Hakim AK, Bashkurov M, Gingras A-C, Durocher D, Pelletier L. Interaction proteomics identify NEURL4 and the HECT E3 ligase HERC2 as novel modulators of centrosome architecture. *Mol Cell Proteomics.* 2012;11:M111.014233. doi:10.1074/mcp.M111.014233.
497. Yuan J, Luo K, Deng M, Li Y, Yin P, Gao B, et al. HERC2-USP20 axis regulates DNA damage checkpoint through Claspin. *Nucleic Acids Res.* 2014;42:13110–21. doi:10.1093/nar/gku1034.
498. Furumai R, Tamada K, Liu X, Takumi T. UBE3A regulates the transcription of IRF, an antiviral immunity. *Hum Mol Genet.* 2019;28:1947–58. doi:10.1093/hmg/ddz019.
499. Lopez SJ, Dunaway K, Islam MS, Mordaunt C, Vogel Ciernia A, Meguro-Horike M, et al. UBE3A-mediated regulation of imprinted genes and epigenome-wide marks in human neurons. *Epigenetics.* 2017;12:982–90. doi:10.1080/15592294.2017.1376151.
500. Martínez-Noël G, Galligan JT, Sowa ME, Arndt V, Overton TM, Harper JW, Howley PM. Identification and proteomic analysis of distinct UBE3A/E6AP protein complexes. *Mol Cell Biol.* 2012;32:3095–106. doi:10.1128/MCB.00201-12.
501. Mishra A, Godavarthi SK, Maheshwari M, Goswami A, Jana NR. The ubiquitin ligase E6-AP is induced and recruited to aggregates in response to proteasome inhibition and may be involved in the ubiquitination of Hsp70-bound misfolded proteins. *J Biol Chem.* 2009;284:10537–45. doi:10.1074/jbc.M806804200.
502. Maheshwari M, Samanta A, Godavarthi SK, Mukherjee R, Jana NR. Dysfunction of the ubiquitin ligase Ube3a may be associated with synaptic pathophysiology in a mouse model of Huntington disease. *J Biol Chem.* 2012;287:29949–57. doi:10.1074/jbc.M112.371724.
503. Burette AC, Judson MC, Burette S, Phend KD, Philpot BD, Weinberg RJ. Subcellular organization of UBE3A in neurons. *J Comp Neurol.* 2017;525:233–51. doi:10.1002/cne.24063.

504. Burette AC, Judson MC, Li AN, Chang EF, Seeley WW, Philpot BD, Weinberg RJ. Subcellular organization of UBE3A in human cerebral cortex. *Mol Autism*. 2018;9:54. doi:10.1186/s13229-018-0238-0.
505. Su H, Fan W, Coskun PE, Vesa J, Gold J-A, Jiang Y-H, et al. Mitochondrial dysfunction in CA1 hippocampal neurons of the UBE3A deficient mouse model for Angelman syndrome. *Neurosci Lett*. 2011;487:129–33. doi:10.1016/j.neulet.2009.06.079.
506. Zeng XR, Hao H, Jiang Y, Lee MY. Regulation of human DNA polymerase delta during the cell cycle. *J Biol Chem*. 1994;269:24027–33.
507. Park SH, Kang N, Song E, Wie M, Lee EA, Hwang S, et al. ATAD5 promotes replication restart by regulating RAD51 and PCNA in response to replication stress. *Nat Commun*. 2019;10:5718. doi:10.1038/s41467-019-13667-4.
508. Dungrawala H, Rose KL, Bhat KP, Mohni KN, Glick GG, Couch FB, Cortez D. The Replication Checkpoint Prevents Two Types of Fork Collapse without Regulating Replisome Stability. *Mol Cell*. 2015;59:998–1010. doi:10.1016/j.molcel.2015.07.030.
509. Zhang S, Zhou Y, Sarkeshik A, Yates JR, Thomson TM, Zhang Z, et al. Identification of RNF8 as a ubiquitin ligase involved in targeting the p12 subunit of DNA polymerase δ for degradation in response to DNA damage. *J Biol Chem*. 2013;288:2941–50. doi:10.1074/jbc.M112.423392.
510. Terai K, Shibata E, Abbas T, Dutta A. Degradation of p12 subunit by CRL4Cdt2 E3 ligase inhibits fork progression after DNA damage. *J Biol Chem*. 2013;288:30509–14. doi:10.1074/jbc.C113.505586.
511. Daraba A, Gali VK, Halmai M, Haracska L, Unk I. Def1 promotes the degradation of Pol3 for polymerase exchange to occur during DNA-damage--induced mutagenesis in *Saccharomyces cerevisiae*. *PLoS Biol*. 2014;12:e1001771. doi:10.1371/journal.pbio.1001771.
512. Yi JJ, Paranjape SR, Walker MP, Choudhury R, Wolter JM, Fragola G, et al. The autism-linked UBE3A T485A mutant E3 ubiquitin ligase activates the Wnt/ β -catenin pathway by inhibiting the proteasome. *J Biol Chem*. 2017;292:12503–15. doi:10.1074/jbc.M117.788448.
513. Chan A-L, Grossman T, Zuckerman V, Di Campigli Giammartino D, Moshel O, Scheffner M, et al. c-Abl phosphorylates E6AP and regulates its E3 ubiquitin ligase activity. *Biochemistry*. 2013;52:3119–29. doi:10.1021/bi301710c.
514. Sionov RV, Coen S, Goldberg Z, Berger M, Bercovich B, Ben-Neriah Y, et al. c-Abl regulates p53 levels under normal and stress conditions by preventing its nuclear export and ubiquitination. *Mol Cell Biol*. 2001;21:5869–78. doi:10.1128/MCB.21.17.5869-5878.2001.
515. Olabarria M, Pasini S, Corona C, Robador P, Song C, Patel H, Lefort R. Dysfunction of the ubiquitin ligase E3A Ube3A/E6-AP contributes to synaptic pathology in Alzheimer's disease. *Commun Biol*. 2019;2:111. doi:10.1038/s42003-019-0350-5.
516. Mulherkar SA, Sharma J, Jana NR. The ubiquitin ligase E6-AP promotes degradation of alpha-synuclein. *J Neurochem*. 2009;110:1955–64. doi:10.1111/j.1471-4159.2009.06293.x.
517. Mishra A, Dikshit P, Purkayastha S, Sharma J, Nukina N, Jana NR. E6-AP promotes misfolded polyglutamine proteins for proteasomal degradation and suppresses polyglutamine protein aggregation and toxicity. *J Biol Chem*. 2008;283:7648–56. doi:10.1074/jbc.M706620200.
518. Dindot SV, Antalffy BA, Bhattacharjee MB, Beaudet AL. The Angelman syndrome ubiquitin ligase localizes to the synapse and nucleus, and maternal deficiency results in abnormal dendritic spine morphology. *Hum Mol Genet*. 2008;17:111–8. doi:10.1093/hmg/ddm288.
519. Zampeta FI, Sonzogni M, Niggel E, Lendemeijer B, Smeenk H, Vrij FMS de, et al. Conserved UBE3A subcellular distribution between human and mice is facilitated by non-homologous isoforms. *Hum Mol Genet*. 2020;29:3032–43. doi:10.1093/hmg/ddaa194.
520. Cho KF, Branon TC, Udeshi ND, Myers SA, Carr SA, Ting AY. Proximity labeling in mammalian cells with TurboID and split-TurboID. *Nat Protoc*. 2020;15:3971–99. doi:10.1038/s41596-020-0399-0.
521. Nguyen TMT, Kim J, Doan TT, Lee M-W, Lee M. APEX Proximity Labeling as a Versatile Tool for Biological Research. *Biochemistry*. 2020;59:260–9. doi:10.1021/acs.biochem.9b00791.
522. Sirois CL, Bloom JE, Fink JJ, Gorka D, Keller S, Germain ND, et al. Abundance and localization of human UBE3A protein isoforms. *Hum Mol Genet*. 2020;29:3021–31. doi:10.1093/hmg/ddaa191.

523. Chu BW, Kovary KM, Guillaume J, Chen L, Teruel MN, Wandless TJ. The E3 ubiquitin ligase UBE3C enhances proteasome processivity by ubiquitinating partially proteolyzed substrates. *J Biol Chem.* 2013;288:34575–87. doi:10.1074/jbc.M113.499350.
524. Uchiki T, Kim HT, Zhai B, Gygi SP, Johnston JA, O'Bryan JP, Goldberg AL. The ubiquitin-interacting motif protein, S5a, is ubiquitinated by all types of ubiquitin ligases by a mechanism different from typical substrate recognition. *J Biol Chem.* 2009;284:12622–32. doi:10.1074/jbc.M900556200.
525. Morris CR, Vichinsky EP, van Warmerdam J, Machado L, Kepka-Lenhart D, Morris SM, Kuypers FA. Hydroxyurea and arginine therapy: impact on nitric oxide production in sickle cell disease. *J Pediatr Hematol Oncol.* 2003;25:629–34. doi:10.1097/00043426-200308000-00008.
526. Singh A, Xu Y-J. The Cell Killing Mechanisms of Hydroxyurea. *Genes (Basel)* 2016. doi:10.3390/genes7110099.
527. Cokic VP, Beleslin-Cokic BB, Noguchi CT, Schechter AN. Hydroxyurea increases eNOS protein levels through inhibition of proteasome activity. *Nitric Oxide.* 2007;16:371–8. doi:10.1016/j.niox.2007.01.001.
528. Marshall RS, Vierstra RD. Dynamic Regulation of the 26S Proteasome: From Synthesis to Degradation. *Front Mol Biosci.* 2019;6:40. doi:10.3389/fmolb.2019.00040.
529. Dantuma NP, Lindsten K, Glas R, Jellne M, Masucci MG. Short-lived green fluorescent proteins for quantifying ubiquitin/proteasome-dependent proteolysis in living cells. *Nat Biotechnol.* 2000;18:538–43. doi:10.1038/75406.
530. Longo PA, Kavran JM, Kim M-S, Leahy DJ. Transient mammalian cell transfection with polyethylenimine (PEI). *Methods Enzymol.* 2013;529:227–40. doi:10.1016/B978-0-12-418687-3.00018-5.
531. Quan J, Tian J. Circular polymerase extension cloning. *Methods Mol Biol.* 2014;1116:103–17. doi:10.1007/978-1-62703-764-8_8.
532. Kwon Y, Ju S, Kaushal P, Lee J-W, Lee C. Neutralizing the Detrimental Effect of an N-Hydroxysuccinimide Quenching Reagent on Phosphopeptide in Quantitative Proteomics. *Anal Chem.* 2018;90:3019–23. doi:10.1021/acs.analchem.7b04678.
533. Rappsilber J, Mann M, Ishihama Y. Protocol for micro-purification, enrichment, pre-fractionation and storage of peptides for proteomics using StageTips. *Nat Protoc.* 2007;2:1896–906. doi:10.1038/nprot.2007.261.
534. Gamell C, Gulati T, Levav-Cohen Y, Young RJ, Do H, Pilling P, et al. Reduced abundance of the E3 ubiquitin ligase E6AP contributes to decreased expression of the INK4/ARF locus in non-small cell lung cancer. *Sci Signal* 2017. doi:10.1126/scisignal.aaf8223.
535. Wiśniewski JR, Zougman A, Mann M. Combination of FASP and StageTip-based fractionation allows in-depth analysis of the hippocampal membrane proteome. *J Proteome Res.* 2009;8:5674–8. doi:10.1021/pr900748n.
536. Michalski A, Damoc E, Hauschild J-P, Lange O, Wiegand A, Makarov A, et al. Mass spectrometry-based proteomics using Q Exactive, a high-performance benchtop quadrupole Orbitrap mass spectrometer. *Mol Cell Proteomics.* 2011;10:M111.011015. doi:10.1074/mcp.M111.011015.
537. Cox J, Mann M. MaxQuant enables high peptide identification rates, individualized p.p.b.-range mass accuracies and proteome-wide protein quantification. *Nat Biotechnol.* 2008;26:1367–72. doi:10.1038/nbt.1511.
538. Cox J, Neuhauser N, Michalski A, Scheltema RA, Olsen JV, Mann M. Andromeda: a peptide search engine integrated into the MaxQuant environment. *J Proteome Res.* 2011;10:1794–805. doi:10.1021/pr101065j.
539. Elias JE, Gygi SP. Target-decoy search strategy for increased confidence in large-scale protein identifications by mass spectrometry. *Nat Methods.* 2007;4:207–14. doi:10.1038/nmeth1019.
540. Smyth GK. Linear models and empirical bayes methods for assessing differential expression in microarray experiments. *Stat Appl Genet Mol Biol.* 2004;3:Article3. doi:10.2202/1544-6115.1027.
541. McInnes L, Healy J, Saul N, Großberger L. UMAP: Uniform Manifold Approximation and Projection. *JOSS.* 2018;3:861. doi:10.21105/joss.00861.
542. Eden E, Navon R, Steinfeld I, Lipson D, Yakhini Z. GOrilla: a tool for discovery and visualization of enriched GO terms in ranked gene lists. *BMC Bioinformatics.* 2009;10:48. doi:10.1186/1471-2105-10-48.

543. Tyanova S, Cox J. Perseus: A Bioinformatics Platform for Integrative Analysis of Proteomics Data in Cancer Research. *Methods Mol Biol.* 2018;1711:133–48. doi:10.1007/978-1-4939-7493-1_7.
544. Saito R, Smoot ME, Ono K, Ruscheinski J, Wang P-L, Lotia S, et al. A travel guide to Cytoscape plugins. *Nat Methods.* 2012;9:1069–76. doi:10.1038/nmeth.2212.
545. Casado P, Rodriguez-Prados J-C, Cosulich SC, Guichard S, Vanhaesebroeck B, Joel S, Cutillas PR. Kinase-substrate enrichment analysis provides insights into the heterogeneity of signaling pathway activation in leukemia cells. *Sci Signal.* 2013;6:rs6. doi:10.1126/scisignal.2003573.

8 Acknowledgments

9 *Curriculum Vitae* **Matthias Ostermaier**

